Synthesis, Characterization and Polymerization Kinetic Study of Long Chain Branched Polyolefins Made with Two Single-Site Catalysts

by

Saeid Mehdiabadi

A thesis
presented to the University of Waterloo
in fulfillment of the
thesis requirement for the degree of
Doctor of Philosophy
in
Chemical Engineering

Waterloo, Ontario, Canada, 2011

AUTHOR'S DECLARATION

I hereby declare that I am the sole author of this thesis. This is a true copy of the thesis, including any required final revisions, as accepted by my examiners.

I understand that my thesis may be made electronically available to the public.

Abstract

Recent advances in polyolefin manufacture have focused on the production of differentiated commodity polyolefins, specialty polyolefins, and polyolefins hybrids. What differentiates these new polyolefin types from commodity polyolefins is that their molecular architectures are much more complex and often contain long chain branches (LCBs), leading to unique properties that make them competitive with specialty polymers. This is an exciting new research area in the polyolefin industry because it promises to open new markets for polyolefins that have been thus far restricted to other polymers.

One approach to produce these novel polyolefins is to use one or two single-site catalysts in two CSTRs in series. The first CSTR is used to make semicrystalline polymer chains, some of which must be vinyl-terminated (macromonomers). These macromonomers are then incorporated, via terminal branching, onto the chains growing in the second CSTR, becoming LCBs. If the backbone and the macromonomer have different compositions, they are called cross-products. Since it is not possible to incorporate all macromonomers, the final polymer will consist of a complex mixture of linear chains made by the two catalysts, homogeneous-branched chains (that is, chains where the backbone and all LCBs are of the same type), and cross-product macromolecules. The cross-product will add rather special properties to the polymer and, depending on its molecular architecture, the final product may act as a thermoplastic elastomer (TPE). Developing polymer reactor models for different catalyst combinations can help understand the details of these complex syntheses and to control the properties and fractions of linear chains, homogeneous-branched chains, and cross-products.

Two mathematical models were developed in this thesis for the solution polymerization of olefins with two single-site catalysts to predict the microstructure of long chain branched polyolefins. The first model was developed for a semi-batch reactor and the second one for two CSTRs in series. The models can predict the fractions of different polymer populations made in CSTRs and semibatch reactors, as well as their average chain lengths and LCB densities. Simulation results show that CSTRs are more efficient than semi-batch reactors to make polymers with high LCB densities and/or cross product fraction.

Simulation results also show that to increase the weight percent of cross-product using a linear-catalyst and a LCB-catalyst, the rate of macromonomer formation of the linear-catalyst should be high. The fraction of cross-product can be increased even further when both catalysts are capable of

incorporating macromonomers to form LCB-chains because; in this case, both catalysts can form cross-product chains. Monomer concentration has no effect on cross-product mass fraction and polydispersity index, but increasing monomer concentration will decrease LCB density and increase the average chain lengths. Catalyst deactivation also has a great impact on polymer properties: LCB density, polydispersity index, cross-product fraction, and average chain lengths will all decrease by increasing the catalyst deactivation rate of both catalysts.

Simulation results for two CSTRs in series shows that increasing residence time in the second CSTR will lead to higher cross-product formation and LCB density. This rate of increase is more significant if the residence time in the second CSTR is similar to that of the first CSTR. The catalyst feed policy also has a great impact on polymer properties. We found out that feeding the linear-catalyst and the LCB-catalyst in equal amounts to the first CSTR and just adding the LCB-catalyst to the second CSTR is the preferred catalyst injection method for making polymer with a high mass fraction of cross-product, high chain length averages, and lower polydispersity index (PDI).

These simulation studies indicate that detailed polymerization kinetics for each catalyst is needed in order to synthesize these novel polyolefins. In the experimental part of this thesis, ethylene polymerization kinetics studies were performed first with two individual metallocene catalysts, then with both of them simultaneously.

First, ethylene polymerization with *rac*-Et$(Ind)_2ZrCl_2$/MAO was carried out in a semi-batch solution reactor. Reaction temperature, monomer, MAO, and catalyst concentrations were the factors studied to establish a framework to predict catalyst decay, polymer yield and molecular weight averages. The polymerization order with respect to ethylene and catalyst concentration was found to be first order. Chain transfer to monomer was the dominating chain transfer reaction while β-hydride elimination was negligible. An increase in MAO concentration led to a decrease in molecular weight. Catalyst decay could be described with a first order mechanism. At low MAO concentration this catalyst could make polymer with about one vinyl group per chain.

A similar ethylene polymerization kinetics study using dimethylsilyl(N-tert-butylamido)-(tetramethylcyclopentadienyl)-titanium dichloride (CGC-Ti)/MAO system showed that the polymerization order with respect to catalyst concentration was first order, but first order catalyst decay failed to explain catalyst deactivation. The polymerization order with respect to ethylene concentration was not unity for the whole range of ethylene concentration. The trigger mechanism, along with reversible first order activation and deactivation with MAO and first order thermal decay,

could explain the effect of time, monomer and catalyst concentration on the rate of polymerization. Decrease in MAO concentration increased the amount of polymer chains with terminal vinyl groups and consequently led to polymers with LCBs. Decreasing monomer concentration at low MAO concentration also led to production of polymer chain with more long chain branching.

Ethylene homopolymerization and copolymerization with 1-octene were conducted using combined catalysts system at low and high MAO concentrations. Reactivity ratios were calculated and polymer samples with bimodal MWDs were obtained but no increase in LCB frequency or cross product formation was detected using carbon-13 nuclear magnetic resonance (^{13}C NMR) and high-temperature gel permeation chromatography (GPC) coupled with a viscosity detector.

In order to promote the formation of cross-product macromolecules, 1,9-decadiene was copolymerized with ethylene using the $Et(Ind)_2ZrCl_2$/MAO to make tailored macromonomers with pendant 1-octenyl branches. The macromonomers ranged from having 1 to 6.5 vinyl groups per chain. These macromonomers were then incorporated into growing ethylene/1-butene or ethylene/1-octene copolymer chains using a titanium-based constrained geometry catalyst (CGC-Ti) to form branch block polymer chains with amorphous main backbone having short chain branch density (SCBD) up to 50 per 1 000 carbon atoms, and high crystalinity long chain branches with SCBD up to 3/1000 C atoms (cross product). Increase in polymerization time or catalyst concentration in the second stage of polymerization was observed to increase the cross-product weight fraction. We also observed that an increase in ethylene pressure during the second stage of polymerization, while 1-butene concentration was constant, favoured the formation of cross product. When 1-octene was used as comonomer in the second stage of polymerization, the presence of more pendant vinyl groups in the macromonomer led to increased long chain branching.

Acknowledgements

I would like to express my heartfelt gratitude to my supervisor, Professor Joao Soares, for his guidance, continued encouragement during this work, and support under all situations.

I would like to express my sincere gratitude to my supervisory committee members: Professor Thomas A. Duever, Professor Leonardo Simon and Professor Jean Duhamel.

I would like to express my appreciation to Iran Ministry of Science and Technology for sponsoring my PhD program.

I would like to take this opportunity to thank all University of Waterloo's staff members, who are behind the scenes; without their collaboration, research would stop.

Finally, last but not least: My deepest gratitude goes to my wife Jalleh, for her love, support, patience, and understanding, and to my daughter and son, Kimia and Bardia, whose love are always my stimulus for life.

Table of Contents

List of Figures

List of Tables

Chapter 1
Introduction

1.1 Motivation

Polyolefins, which include various grades of polyethylene and polypropylene, are the most important thermoplastics today. The global demand for polyethylene and polypropylene represents over 60% of all commodity resins consumed worldwide on an annual basis. Polyethylene, including low-density polyethylene (LDPE), linear low-density polyethylene (LLDPE), and high density polyethylene (HDPE), is the largest cumulative category with 38% market share, while polypropylene is the largest single category with 24% market share[1].

The key points to polyolefin success are low production cost and versatility in application. Polyethylenes are used for blow-molded objects such as bottles (milk, food, and detergents), houseware appliances, toys, grocery bags, pipes, wire, cable insulation, and many other applications. Polypropylene (PP) is used for making pipes, bottle crates, bottle caps and closures, washing machines drums, toys, automotive applications, including battery cases and interior trim, rubber modified PP for impact resistant components, such as bumpers, packaging film for food and non-food applications, syringes and vials for medical use, fibers for carpeting, and many other uses. It is surprising that these, at a first glance, simple polymers could have such diverse applications. The key to this versatility lies in the way monomer molecules are connected to form polymer chains with entirely different macroscopic properties.

In the broadest sense, polyethylene resin properties are determined largely by three fundamental distributions: molecular weight, short chain branching (or chemical composition) and long chain branching. It is the branching degree and type that distinguishes between the three major types of polyethylene, that is, LDPE, HDPE and LLDPE. High pressure low-density polyethylene (LDPE) has certain properties which are difficult to obtain by low pressure technologies. One of these properties is long chain branching, which allows easy processing at high molecular weights and makes the resin especially useful for extrusion coating. In addition to long chain branches (LCB), high pressure polyethylene contains a reasonably high amount of short chain branches (SCB) which decreases crystallinity and affects the stiffness of the material in the solid state. On the other hand, the high pressure free radical process needed to make LDPE is expensive to build and maintain, and the broad molecular weight distribution (MWD) of LDPE is responsible for inferior mechanical properties,

being a disadvantage as compared to polyethylene resins made with metallocene catalysts having much narrower MWD.

Polyethylenes made with metallocene catalysts have narrow MWD with greatly improved mechanical properties. Processing these polymers, however, is more difficult than LDPE because of poor shear thinning. Adding a few LCBs to linear polyethylene chains can improve its rheological behavior. Although, LCB increases the resin viscosity at low shear rates (because of chain entanglement) at high shear rates, the branch entanglements relax and more shear thinning is observed compared to linear polyethylene.[2] Fortunately, some metallocene catalysts can make polyethylenes with LCBs. These polymers combine good mechanical properties with easy processability. The mechanism of LCB formation with metallocenes involves the incorporation of a dead polymer chain containing a terminal vinyl group (macromonomer), generated in situ via β-hydride elimination or transfer to ethylene, as a LCBs into a growing polymer chain.

One typical example of metallocene catalysts with the ability of producing polymers with LCB are the family of constrained geometry catalysts (CGCs). However, the LCB levels in CGC resins are relatively low because macromonomers produced in situ have only one reactive double bond per chain. One way to increase LCB levels in CGC resins is to copolymerize ethylene with linear unconjugated dienes. The resulting copolymers have an average of more than one vinyl groups per polymer chains, opening the possibility for developing new products with improved processability and mechanical properties.

It is also possible to increase LCB levels a using combination of metallocene catalysts.When two metallocene catalysts are combined in the same reactor, with at least one being able to form LCBs, the polymer produced may contain a variety of chain architectures: linear chains, homogeneous branched chains, and heterogeneous branched chains (cross product). A heterogeneous branched chain is made when a macromonomer made by one of the catalysts in the reactor is incorporated as a LCB onto the chain growing on the other catalyst present in the reactor. Even a small amount of such cross products can significantly alter the polymer property profile. For instance, these polymers may behave as thermoplastic elastomers if the proper catalysts and monomers are chosen.

Developing polymer reactor models for different catalyst combinations is also very helpful because we can understand the details of these complex syntheses and to control the properties and fractions of these cross-products .

1.2 Research plan and objectives

The main objective of this thesis is to make polyolefins with complex branched structures for potential new applications using dual metallocene catalysts. The product components involved in the complex branched structures are macromonomers (semicrystalline polymer chains with terminal or pendant vinyl groups) amorphous polymer chains (ethylene\1-butene or ethylene\1-octene copolymers with high α-olefin fraction), and cross-products (made by incorporating macromonomers into amorphous polymer chains).

The steps followed in this thesis were:

1) Develop mathematical models to better understand the kinetics of cross-product formation in semi-batch and continuous reactors using dual metallocene catalysts;

2) Synthesize macromonomers with *rac*-Et(Ind)$_2$ZrCl$_2$ and model its polymerization kinetics;

3) Produce ethylene homopolymers using CGC-Ti and model its polymerization kinetics;

4) Produce amorphous ethylene/a-olefin copolymer using CGC-Ti;

5) Combine *rac*-Et(Ind)$_2$ZrCl$_2$ and CGC-Ti to make branched polyolefins with complex molecular architectures containing cross products;

6) Since efforts to make cross products using the approach in 5) were unsuccessful, produce polyethylene macromonomers containing 1,9-decadiene using *rac*-Et(Ind)$_2$ZrCl$_2$ in the first step, followed by the terpolymerizations of ethylene/1-butene/1,9-diene macromonomer or ethylene/1-octene/1,9-diene macromonomer with CGC-Ti to make branch-bock polymer chains having amorphous backbones and semicrystalline LCBs.

The objectives of this thesis can be summarized as follows:

- Develop a mathematical model to describe the solution polymerization of olefins with two single-site catalysts in a semi-batch reactor.
- Develop a mathematical model to describe the solution polymerization of olefins with two single-site catalysts in a series of two continuous stirred tank reactors.
- Perform an ethylene polymerization kinetics study using *rac*-Et(Ind)$_2$ZrCl$_2$/MAO and estimate reaction rate constants.

- Perform an ethylene polymerization kinetics study using dimethylsilyl(N-tert-butylamido)-(tetramethylcyclopentadienyl)-titanium dichloride (CGC-Ti) and MAO and estimate reaction rate constants .
- Investigate the simultaneous use of *rac*-Et$(Ind)_2ZrCl_2$ and CGC-Ti to increase LCB frequency of ethylene/α-olefin copolymers.
- Investigate the use of macromonomers of ethylene and unconjugated dienes to produce polymers with large fraction of branch-block chains.

1.3 Thesis outline

This thesis consists of 10 chapters and is organized as follows:

Chapter 1 presents the introduction, research objectives, and thesis outline.

Chapter 2 contains a literature review including polyethylene types, catalyst types and processes used for making polyethylene. This is followed by a literature review on the kinetics of polymerization with coordination catalysts. Polyolefin characterization techniques are also reviewed at the end of this chapter.

Chapters 3 and 4 develop general mathematical models and present simulation results for the solution polymerization of olefins in semi-batch and continuous stirred tank reactors using the method of moments.

Chapter 5 describes the experimental procedures used in this thesis, including polymerization methods and apparatuses, and polymer characterization techniques.

Chapter 6 discusses the in-depth homopolymerization kinetics study of ethylene with *rac*-Et$(Ind)_2ZrCl_2$/MAO in a semi-batch solution reactor; Chapter 7 shows a similar result for CGC-Ti/MAO.

An attempt to use the combined *rac*-Et$(Ind)_2ZrCl_2$ and CGC-Ti system to increase LCB frequency in the final polymer is described in Chapter 8.

In Chapter 9, we provide results on copolymerization of ethylene and 1,9-decadiene using *rac*-Et$(Ind)_2ZrCl_2$ catalyst to produce macromonomers with different concentration of pendant vinyl groups. Macromonomers were then terpolymerized with ethylene and 1-butene or 1-octene using

CGC-Ti to produce branch-block polymers. The rest of the chapter deals with the effect of reaction parameters on the microstructure of the branch-block polymers produced.

Finally, Chapter 10 summarizes the significant finding of this research and provides some recommendations for future work.

Chapter 2

Literature Review and Background

2.1 Polyolefins

Polyolefins are the largest group of thermoplastics, often referred to as commodity thermoplastics. They are polymers made of simple olefins such as ethylene, propylene and higher α-olefins. The two most common polyolefins are polyethylene (PE) and polypropylene (PP); they have a wide range of applications due to their low cost and versatility.

2.1.1 Polyethylene Types

The three major types of polyethylene are: low density polyethylene (LDPE), linear or high density polyethylene (HDPE), and linear low-density polyethylene (LLDPE). Figure 2-1 compares the molecular structures of these types of polyethylene resins made by coordination (HDPE and LLDPE) and free-radical polymerization (LDPE).

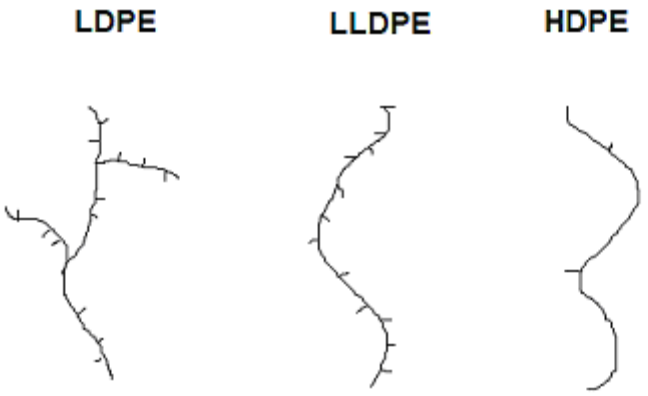

Figure 2-1. Polyethylene molecular structures.

2.1.1.1 Low Density Polyethylene (LDPE)

Low-density polyethylene is produced by free radical bulk polymerization using traces of oxygen (≤300 ppm) as initiator, often in combination with an alkyl or acyl peroxide or hydroperoxide in a

high–pressure (120-300 MPa) and high-temperature (140-325 ^{o}C) process in either autoclave or tubular reactors.[3]

This oldest type of polyethylene resin differs structurally from linear polyethylenes by being highly branched and containing both long chain branches (LCBs) and short chain branches (SCBs) of different lengths, with butyl groups as the dominating SCB.[4-7] The LCBs can be of the same average length as the polymer backbones. Branches, principally SCBs, act as defects and determine the degree of crystallinity which in turn affects a number of polymer properties. The number of SCBs in LDPE may be as high as 15-25 per 1000 carbon atoms.[3]

The degree of crystallinity in LDPE is in the range of 40-60%, the melting temperature varies from 100 to 120^{o}C, and the density is approximately 910-930 kg/m^{3}. The physical properties of LDPE depend on three structural factors: degree of crystallinity (density), molecular weight average, and molecular weight distribution (MWD). The degree of crystallinity and, therefore, density of polyethylene, is dictated primarily by the number of SCBs on the chains. Properties such as opacity, rigidity (stiffness), tensile strength, tear strength, chemical resistance and upper use temperature, which depend on crystallinity, increase as density increases. On the other hand, permeability to liquids and gases, elongation and resistance to stress cracking decreases with increasing crystallinity.[8-9]

Commercial LDPE have number average molecular weights in the range of 20,000-100,000. Melt index (MI), which designates the weight (in grams) of polymer extruded through a standard capillary at 190 ^{o}C in 10 min and is inversely related to molecular weight, is used as a convenient measure of average molecular weights. Typical melt index values for LDPE are in the range of 0.1 to 109. As molecular weight increases, tensile and tear strength, softening temperature, stress cracking resistance, and chemical resistance increase, while processability worsens.[9] The polydispersity index (PDI) also affects LDPE properties. Polyethylene with low PDI has high impact strength, reduced shrinkage and warpage, enhanced toughness and environmental stress cracking resistance, but poor processability. Typical values of PDI for commercial LDPE resins are in the range of 3-20.

Since LDPE possesses the desired combination of low density, flexibility, resilience, high tear strength, and moisture and chemical resistance, which are characteristics of a good film material, thin film packaging comprises its major use. Other uses include wire and cable insulation and extrusion coating. Both film and extrusion coating applications require good processability, meaning balanced

melt strength and flow properties, to be able to extrude the material and form a film or coating layer as desired.

2.1.1.2 High-Density Polyethylene (HDPE)

High-density polyethylene was discovered approximately 20 years after LDPE. It was first made by Karl Ziegler using aluminum alkyl/transition metal halide catalyst complexes. As an example, HDPE can be prepared by bubbling ethylene into a suspension of $Al(C_2H_5)_3$ and $TiCl_4$ in hexane at room temperature.[10] This type of polyethylene has few or no short chain branches, and its crystallinity falls in the range 70-90 % with densities from 940 to 975 kg/m^3. Most HDPEs have number average molecular weights of 50,000 to 250,000 and crystalline melting temperature in the range of 133-138^{o}C.[8]

Various specialty ultra-high molecular weight polyethylenes (UHMWPE), with molecular weights in the range of 250,000-1,500,000, are also produced for pressure piping in mining, industrial, sewer, gas, oil, and water applications. Increased molecular weight results in increased tensile strength, elongation, low-temperature impact resistance, and stress crack resistance, although processing is more expensive because of increased melt viscosity.[8]

2.1.1.3 Linear Low-Density Polyethylene (LLDPE)

Linear-low density polyethylene is a copolymer of ethylene and α-olefins (generally 1-butene, 1-hexene, or 1-octene) with densities in the range 915-940 kg/m^3. Products with even lower densities, down to 880 kg/m^3, are sometimes called very low-density polyethylene (VLDPE) but are chemically identical to LLDPE. Copolymerization of ethylene with increasing amounts of α-olefins disrupts the order of linear polyethylene chains by introducing SCBs. As a consequence, the density, crystallinity, and rigidity of LLDPE are lower than those of HDPE.[11] LLDPE is frequently blended with LDPE for film and sheet production.[10] LLDPE was in the market development stages as early as the 1960s, but the major driving force for the development of LLDPE processes in the late 1970s and early 1980s was the desire to reduce the capital required to construct a high-pressure plants to produce LDPE and to reduce the costs associated with the maintenance and operation of complex mechanical equipments at pressures in the range 15,000 40,000 psi.[12]

2.2 Catalysts for Polyethylene Polymerization

Today, polyethylenes are commercially produced using free-radical initiators, Ziegler-Natta catalysts, chromium oxide (Phillips) catalysts and, more recently, metallocene and late transition metal catalysts. Each type of catalyst will be discussed briefly below.

2.2.1 Ziegler- Natta Catalysts

In general, a Ziegler- Natta catalyst is a complex of a metal cation from groups I-III in the periodic table, such as triethylaluminum, $Al(C_2H_5)_3$, and a transition metal compound from groups IV-VIII, such as titanium tetrachloride ($TiCl_4$). The former component is usually known as the co-catalyst or activator and the latter as the catalyst. For industrial use, most Ziegler- Natta catalysts are based on titanium salts and aluminum alkyls. These types of catalysts have improved considerably since their discovery by K. Ziegler and G. Natta in the late fifties. The first commercial Ziegler-Natta catalyst was a $TiCl_3/Et_2AlCl$ system with low polymer yield requiring a step for removing the catalyst residue (de-ashing) for the commercial production of polyolefins. Modern Ziegler-Natta catalysts are $TiCl_4$ supported on $MgCl_2$ and use Et_3Al as activator. These catalysts are more active and have better control of active sites and particle morphology, enabling them to meet the increasing demands of high performance polyolefin materials. Nevertheless, due to their multi-sited nature, the polymer structure can be controlled only to a limited degree.[13]

2.2.2 Phillips Catalysts

A traditional Phillips catalyst is based on chromium (VI) oxide supported on silica (SiO_2) or aluminosilicates (mixed SiO_2/Al_2O_3). The support is sometimes modified with titania (TiO_2). This catalyst is prepared by impregnating the finely divided support with an aqueous solution of CrO_3. The chromium loading is in the range 0.5-5 wt%, typically 1 wt%. Unlike Ziegler- Natta catalysts, it does not necessarily require a cocatalyst for activation. Activation is carried out by heat treatment (calcination) which fixes the CrO_3 on the support surface. This catalyst is very stable and useful in gas-phase polymerization but unable to polymerize propene to isotactic polypropylene.[14] Due to their multi-sited nature, both Phillips and Ziegler- Natta catalysts produce ethylene homo- and copolymers with broad MWD and broad chemical composition distribution.

2.2.3 Metallocene Catalysts

Metallocene catalysts are as old as Ziegler-Natta catalysts, but they were found to have very low activity when alkylaluminums were used as cocatalysts.[15-16] Their potential was fully realized when methylaluminoxane (MAO) was used as a cocatalyst in the early 1980s.[17] In contrast to heterogeneous Ziegler-Natta catalysts, most metallocenes have only one type of active site and are, therefore, classified as single site catalysts. They offer superior control over the polymer molecular architecture and produce chains with narrow MWD and polydispersity index close to 2.0. In addition, their catalytic activity is higher than that of classical Ziegler-Natta systems; for instance, for a standard zirconocene/MAO catalyst system, the activity is 10 to 100 times higher than that of a typical Ziegler-Natta catalysts.[18]

Metallocene catalysts have a sandwich structure in which a π-bonded metal atom is situated between two aromatic rings, but this definition has been expanded to include structures having only one C_5 ring. Figure 2-2 shows the general structure of a bridged metallocene catalyst precursor. In the Cp_2MXY complex shown, M, is the transition metal and X and Y are usually Cl or CH_3. The η_5-bonded "tilted sandwich" cyclopentadienyl (Cp) ligands can be substituted and/or connected by an inter-annular bridge.

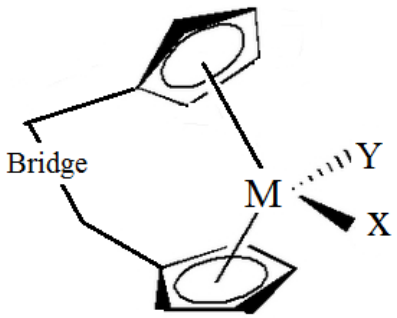

Figure 2-2. General structure of a bridged metallocene catalyst precursor.

Slight structural variations of the bridging groups and ring constituents, as well as transition metal type, can significantly affect the activity and stereoselectivity of olefin polymerization catalysts.[19-20] Generally, zirconium catalysts are more active than hafnium or titanium systems.[19] The first metallocene catalysts were unsubstituted or substituted bis-cyclopentadienyl ligands and they were

activated by methylalumoxane (MAO). Today, numerous families of different single-site catalysts have been developed for the production of polyethylenes and other polyolefins.[21-25]

One of the drawbacks of metallocene catalysts (as well as Ziegler-Natta and Phillips catalysts) is that they are unable to polymerize polar molecules, such as common acrylics or vinyl chloride. This is due to the metallocene's oxophilicity, their propensity for binding to oxygen. Introduction of a polar monomer into an olefin polymerization reactor will reduce the catalyst activity to almost zero. Late transition metal catalysts, discussed in the next section, are much less sensitive to polar comonomers.

2.2.4 Late Transition Metal Catalysts

Polymerization catalysts using late transition metals – those metals from groups 8, 9 and 10 in the periodic table of elements – have attracted a lot of attention lately. These compounds have good polymerization activity, although slightly less than metallocenes. The lower oxophilicity, and therefore more tolerance towards functionalized monomers, and presumed greater functional group tolerance of late transition metals relative to early metals make them likely targets for the development of catalysts for the copolymerization of ethane with polar monomers under mild conditions.[23] The last property is very attractive for modifying the chemical composition of polyolefins by copolymerization with vinyl alcohols, acrylates, or other vinyl polymers. A few functional groups can significantly increase the hydrophobicity of polyolefins, adhesion, and compatibility with hydrophilic materials.[11] Commercially, these catalysts still have not had a significant impact. The most commercially relevant late-transition metal catalysts are the Brookhart catalysts, which are diimine complexes of palladium or nickel with an interesting polymerization mechanism step called chain walking.[26]

2.3 Processes for Polyethylene Manufacture

Ethylene polymerization processes with coordination catalysts can be classified into solution, slurry and gas phase. Solution and slurry processes are based on polymerizing ethylene in a liquid carrier. Depending on whether the temperature at which the polymerization is carried out is below or above the polyethylene melting point, the process will be a slurry or solution process, respectively.

Following polymerization, the catalyst is killed and the polymer separated from the liquid carrier. Solution processes are performed in autoclave, tubular, and loop reactors.[12]

In slurry processes, the polymer is separated as a powder or crumb by a combination of centrifugation, filtration, or steam stripping, followed by drying, melting, extruding, and pelletizing to get polymer pellets. In solution processes, the polymer is separated from the carrier as a molten mass by a combination of distillation or flashing of the carrier, and devolatilization extrusion, followed by pelletization to beads or granules.

In gas phase polymerization, ethylene is circulated through a fluidized bed forming polyethylene powder that is removed continuously from the reactor via a sequence of valves to a product discharge vessel. The advantage of the gas phase process is the elimination of the liquid carrier and the unit operations necessary to separate, recover, and purify it.

2.4 Polymerization Kinetics with Metallocene Catalysts

The mechanism for coordination polymerization can be divided into five main classes of reactions: catalyst activation with cocatalyst, catalysts initiation with monomer, chain propagation, chain transfer, and poisoning and deactivation.[11], [27-32] Each of these steps will be described briefly below.

2.4.1 Catalyst Activation

Metallocene catalysts need to be activated by a suitable cocatalyst before they can be used for polymerization. MAO is the most commonly used metallocene activator; it also acts as a scavenger for catalyst poisons by reacting with impurities such as oxygen and water that may be present in the reactor.[33] MAO is prepared from the controlled hydrolysis of trimethylaluminum (TMA), usually in toluene. The main suppliers of MAO (Akzo Nobel, Albemarle and Witco) add water to TMA by use of either moist nitrogen or a marginally wet aromatic solvent.[25] About 5-30% of the Al atoms in MAO solutions are in the form of TMA. The solubility of MAO in hydrocarbon solvents is possible through the use of an excess of TMA during synthesis and any attempt to completely remove this excess TMA results in MAO precipitation.[33]

Despite intense research efforts, the structure of MAO, the mechanism by which it activates metallocenes, and the polymerization mechanism at the active site are still not fully understood.

Generally, MAO consists of basic units of $Al_4O_3(CH_3)_6$.[34] These units can combine to form cage structures of preferentially four units. This cage is complexed with differing amounts of TMA which could be the active form for MAO.

When zirconocene dichloride is treated with MAO, monomethylation takes place within seconds.[35] Excess MAO leads to formation of dimethylated species. In order for the active site to form, it is at least necessary that one alkyl group is bonded to the metallocene.[36] The site activation mechanism below has been proposed by Kaminsky:[18]

Complexation

$$L_2ZrCl_2 + MAO \rightleftharpoons L_2ZrCl_2.MAO \quad (2\text{-}1)$$

Methylation

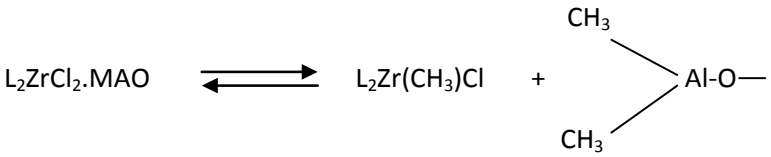

$$L_2ZrCl_2.MAO \rightleftharpoons L_2Zr(CH_3)Cl + \begin{matrix} CH_3 \\ \diagdown \\ \text{Al-O—} \\ \diagup \\ CH_3 \end{matrix} \quad (2\text{-}2)$$

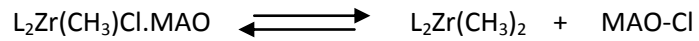

$$L_2Zr(CH_3)Cl.MAO \rightleftharpoons L_2Zr(CH_3)_2 + MAO\text{-}Cl \quad (2\text{-}3)$$

The MAO complex can seize a methyl anion, a Cl anion, or an OR^- anion from the metallocene forming an MAO anion which can distribute the electrons over the whole cage, thus stabilizing the charged system.[37] The appearance of alkylated metallocene cations, generally regarded as the active centres in olefin polymerization, as described in Equation (2-4), was confirmed by ^{13}C-NMR.[38]

Activation

$$L_2Zr(CH_3)Cl + MAO \rightleftharpoons L_2Zr(CH_3)Cl.MAO \rightleftharpoons [L_2ZrCH_3]^+ + [MAO\text{-}Cl]^- \quad (2\text{-}4)$$

MAO is needed in large excess: [Al]/[metal] ratios of 1000 to10,000 are often used for metallocene activation in solution.[39] The relatively high aluminoxane concentration can be partly explained by the fact that MAO acts as an impurities scavenger.[18]

Catalyst deactivation may be caused by α-hydrogen transfer reactions from a zirconium methyl bond to a MAO methyl group or another zirconium complex, as shown in Equation (2-5). A high MAO

excess is necessary to reactivate the Zr-CH_2-Al- structure formed during the inactivation reaction,[35] as proposed in Equation (2-6), which may also explain the need for high MAO concentration.[18]

Deactivation

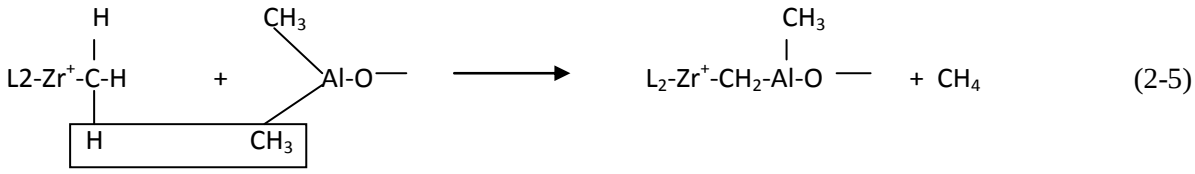

(2-5)

Reactivation

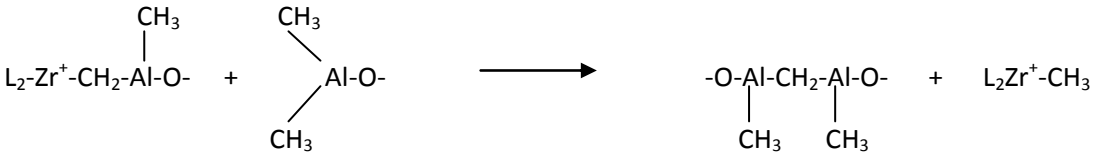

(2-6)

Unfortunately, the TMA also appears to inhibit the catalytic activity of metallocene/alkylalumoxane catalyst system through complexation with the metallocene.[40]

The high Al/Zr ratios required to obtain high catalyst activity and relatively stable kinetic profiles, and the high MAO cost are among some of the disadvantages of this type of cocatalyst.

2.4.2 Catalysts Initiation with Monomer and Chain Propagation

After the catalyst is activated by reaction with the cocatalyst, monomer reacts with the active site to form a living polymer chain of length 1,

$$C^* + M \xrightarrow{k_i} P_1^* \tag{2-7}$$

where M is the monomer, P_1^* is a polymer chain containing one monomer unit attached to a catalyst site, and k_i is the rate constant for chain initiation for catalyst type i. Since in practice it is very difficult to determine the rate constants for initiation and propagation separately, most polymerization kinetics model use the same rate constant for initiation and propagation.[11] This simplifying

assumption seems reasonable because they both involve the addition of an ethylene molecule to the catalyst site.

The addition of monomer species to a growing polymer chain of length *r*, increases its length to *r*+1, as shown below,

$$P_r^* + M \xrightarrow{k_p} P_{r+1}^* \tag{2-8}$$

Propagation reactions are usually assumed to be first order on monomer concentration, but this generalization does not hold for every coordination catalyst.

2.4.3 Chain Transfer Reactions

The most common transfer reactions in metallocene catalyzed polymerization are: (1) β-hydride elimination, (2) β-methyl elimination, (3) transfer to monomer, (4) transfer to co-catalyst, and (5) transfer to hydrogen.[11]

In β-hydride elimination, the hydrogen atom attached to the β-carbon in the living chain is abstracted by the active center, forming a dead polymer chain with a terminal vinyl unsaturation ($P_r^=$) , and a metal hydride center, C_H^* ,

$$P_r^* \xrightarrow{k_{\beta H}} P_r^= + C_H^* \tag{2-9}$$

In a density functional study,[41] this reaction was detailed to locate its transition state, but the reaction profile revealed that the process was endothermic and that the energy steadily increased during the course of the reaction until the products were formed. For this reason, it was difficult to locate a transition state in this case (Figure 2-3). The theoretically obtained reaction enthalpy of ΔH = 176 kJ/mol, is in agreement with other estimates for the β-hydride elimination enthalpy obtained experimentally from neutral scandocene complexes.[42-43] .

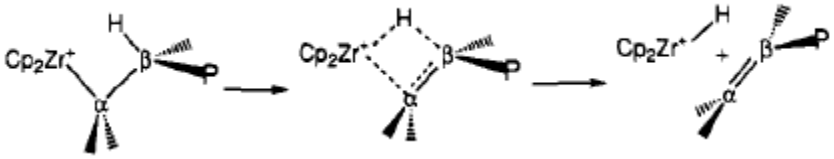

Figure 2-3. Detailed mechanism for β-hydride elimination.[41]

For propene polymerization, β-hydride elimination will produce a dead polymer chain with a vinyldine chain end. On the other hand, β-methyl elimination can also take place during propene polymerization with some catalyst systems in which a methyl group from the beta carbon of the living chain is abstracted by the active center, forming a dead polymer chain with a terminal vinyl unsaturation ($P_r^=$) , and a metal methyl center, $C_{CH_3}^*$,[44-46]

$$P_r^* \overset{k_{\beta-CH_3}}{\rightarrow} P_r^= + C_{CH_3}^* \tag{2-10}$$

Transfer to monomer also occurs during olefin polymerization, leading to vinyl-terminated chains for the case of polyethylene and vinylidine-terminated chain for the case of polypropylene,

$$P_r^* + M \overset{k_M}{\rightarrow} P_r^= + P_1^* \tag{2-11}$$

In the absence of hydrogen, β-hydride elimination and chain transfer to monomer are the dominant chain transfer reactions in olefin polymerization.[47]

Chain transfer to hydrogen produces a dead chain with a saturated chain end,

$$P_r^* + H_2 \overset{k_H}{\rightarrow} C_H^* + P_r \tag{2-12}$$

A number of papers have been published in which hydrogen has been used as chain transfer agent;[48] however, hydrogen was seen to be far more reactive in metallocene-catalyzed polymerization than in Ziegler-Natta polymerization[43, 49] and significantly increases the productivity of some metallocene catalysts,[50-51] so its effect very often goes beyond that of mere chain transfer agent.

The cocatalyst can also act as chain transfer agent. If the cocatalyst is trimethylaluminum, a methylated active center can be formed along with the formation of an Al-CH_2-R compound which by

treatment with HCl/EtOH, a standard laboratory post-polymerization washing procedure, results in a saturated end group in the polymer chain,[52]

$$P_r^* + Al \xrightarrow{k_{Al}} C_{CH_3}^* + P_{r,Al} \tag{2-13}$$

2.4.4 Poisoning and Deactivation

First order deactivation is a plausible deactivation mechanism for metallocene catalysts. This behavior was observed in both solution and gas phase polymerization of ethylene,[53-55]

$$P_r^* \xrightarrow{k_d} C_d + P_r \tag{2-14}$$

Reactions with polar impurities, also leads to the formation of a deactivated site,

$$P_r^* + I \xrightarrow{k_{dI}} C_d + P_r \tag{2-15}$$

where I and P_r refer to impurity and dead polymer chain of length r respectively.

2.4.5 Long Chain Branch Formation

Terminal branching has been considered to be the most probable long chain branch formation mechanism with coordination polymerization catalysts.[28, 30, 56-58] In this mechanism, chains containing terminal double bonds (also called macromonomers), which are formed through β-hydride elimination or chain transfer to monomer are inserted into the growing polymer chains yielding LCBs,

$$P_{m,i}^* + P_{n,j}^{=} \xrightarrow{k_b} P_{m+n,i+j+1}^* \tag{2-16}$$

In Equation (2-16), the first subscript refers to chain length, while the second one shows the number of LCBs per chain.

2.5 Effect of Long Chain Branches on Rheological and Solution Properties of Polethylene

The rheological and processing behavior of polyethylene depends mainly on its molecular weight averages, MWD, and LCB density and distribution.[59-66] LCB affects melt viscosity, zero shear viscosity, shear thinning, activation energy, die swell and many other rheological properties, whereas SCB has little or no effect on the rheological behavior of polyethylenes.[67]

Molten polyethylene is a pseudoplastic fluid, that is, its apparent viscosity decreases with increasing shear stress (shear-thinning). The viscosity-shear rate relationship depends on the molecular structure, especially on long chain branching. As the shear rate increases, the viscosity of the long chain-branched polyethylene chains decreases more rapidly than that of linear chains; as a result, under practical extrusion condition of high shear rate, polyethylene resins containing LCBs can be extruded at a higher rate with a lower energy consumption. At very low shear rates the zero-shear viscosity of long chain-branched polyethylenes is higher than that of linear polyethylene because long chain branches hinder polymer chain movement when they become entangled,[3, 67-68] whereas at high shear rates, the branch entanglements relax and shear-thinning behavior is observed.

Previous works[69-70] on the viscoelastic behavior of linear HDPE fractions at 190 ^{0}C using a series of nearly monodisperse polyethylenes obtained by hydrogenation of anionic polybutadienes showed that there is an empirical relation between zero-shear viscosity and molecular weight,

$$\eta_0 = 3.4 \times 10^{-15} M_w^{3.6} \tag{2-17}$$

Where η_0 is the zero-shear viscosity in Pa.s and M_w is the weight average molecular weight in g/mol.

Vega et al.[71] found a similar relationship for HDPE. However, for metallocene-catalyzed polyethylenes, the relationship was the same in form, but had a different exponent,

$$\eta_0 = 3.2 \times 10^{-15} M_w^{3.6} \quad \text{Ziegler-Natta HDPE} \tag{2-18}$$

$$\eta_0 = 2.3 \times 10^{-17} M_w^{4.2} \quad \text{Metallocene HDPE} \tag{2-19}$$

Since η_0 of long chain-branched HDPE is greater than of linear HDPE, η_0 can, in principle, be used to detect the presence of LCBs.[67, 72-78]

Rodriguez et al.[79] studied some commercial LDPE and HDPE resins with PDI varying from 2.2 to 3.3 and found out the following correlations for zero-shear viscosity,

$$\log \eta_0 = -4.19501 + 1.9489[\log(M_w g^{3/2})] \quad \text{for HDPE} \quad (2\text{-}20)$$

$$\log \eta_0 = -4.443 + 1.9239[\log(M_w g^{3/2})] \quad \text{for LDPE} \quad (2\text{-}21)$$

where g is the branching parameter defined as the ratio of the mean radius of gyration for the branched molecule over the linear molecule with the same molecular weight.

LCBs also influence the flow activation energy of polyethylene.[73, 80] Increasing LCB frequency increases the flow activation energy, which was shown to be a good indicator of the presence of LCBs.[66]

Molten polyethylene also exhibits elastic properties over a wide temperature range, such as die swell and elastic recovery when stress is removed. When molten polyethylene emerges under pressure from the die of an extruder, the strand increases in diameter or thickness. This phenomenon is known as die swell. At low shear rate, die swell increases as molecular weight and LCB frequency increase.[3]

The solution properties of polyethylene are also influenced by the presence of LCBs. For linear chains, the intrinsic viscosity, η, is related to molecular weight according to the Mark-Houwink equation,

$$[\eta] = KM^{a} \quad (2\text{-}22)$$

where K and a are empirical constant that depend on solvent type and temperature for a given polymer. For a solution of polyethylene in 1,2,4 trichlorobenzene (TCB) at 140°C, K and a are, 39×10^{-3} mL/g and 0.725, respectively.[81-82]

Introducing LCBs into linear polymer chains decreases their intrinsic viscosity, which can be used to confirm the presence of LCBs.[83-84]

2.6 Thermoplastic Elastomers

Thermoplastic elastomers (TPEs) are materials with functional properties of conventional thermoset rubbers and processing characteristic of thermoplastics. They do not have the chemical cross-links present in vulcanized elastomers. Instead, elastomeric properties are the result of physical crosslinks

caused by the cocrystallization of semi-crystalline segments of different polymer chains that create a tri-dimensional network structure. The network domain is based on a block copolymer, one block consists of relatively long, flexible polymer chains (soft segment), while the other block is composed of stiff polymer molecules (hard segment). A thermoplastic elastomer is a two phase mixture with a dispersion of the soft rubbery phase in a continuous glassy plastic matrix. Each polymer or major polymer segment or block has its softening temperature, T_s. The useful temperature range for a thermoplastic elastomer lies above the T_s of the elastomeric (soft) phase and below the T_s of the hard phase. Within this temperature range, the polymer molecules in the soft phase can undergo significant segmental motion. The reinforcing action of the hard phase disappears above its softening temperature and the thermoplastic elastomer behaves as a viscous liquid. Upon cooling, the hard phase resolidifies and the TPE becomes rubbery again. Similarly, cooling below T_s of the soft phase changes the material from a rubbery to a hard brittle solid. This process is also reversible. These materials can therefore be processed by conventional molding techniques by heating them above the softening temperature of hard phase.[9] The ability to recycle scrap, and overall lower production costs are significant advantages of TPEs. More details on this subject will be given in the introductions of Chapters 3 and 4.

Typical thermoplastic elastomers derived from propylene and olefins are: isotactic polypropylene grafted to atactic propylene (aPP-*g*-iPP), or polyethylene grafted to ethylene/α-olefin copolymers (PEαO-*g*-PE).[85] In the former case, isotactic polypropylene chains with terminal vinyl groups are produced using a stereoselective catalyst; then, using a aspecific catalyst with high reactivity ratios toward macromonomer incorporation (LCB Catalyst), isotactic blocks are grafted to amorphous backbones (Figure 2-4).

The elastic properties of these polymers are attributed to the crystallization of isotactic blocks, forming physical crosslinks which link the chains to form a long-range network (Figure 2.5).

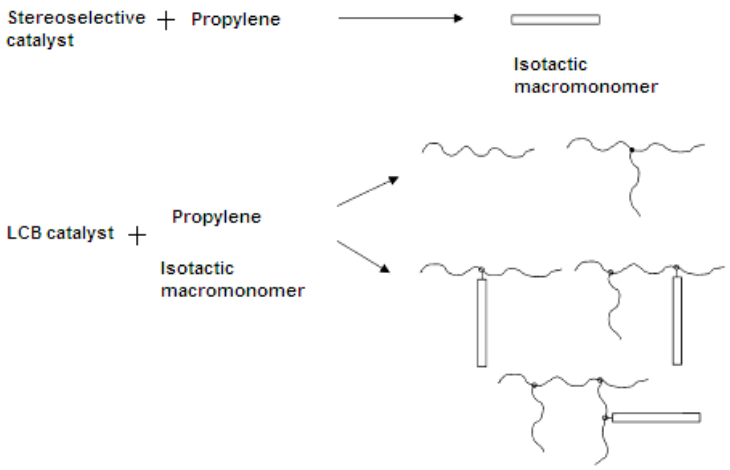

Figure 2-4. Mechanism for TPE formation with dual metallocene systems.

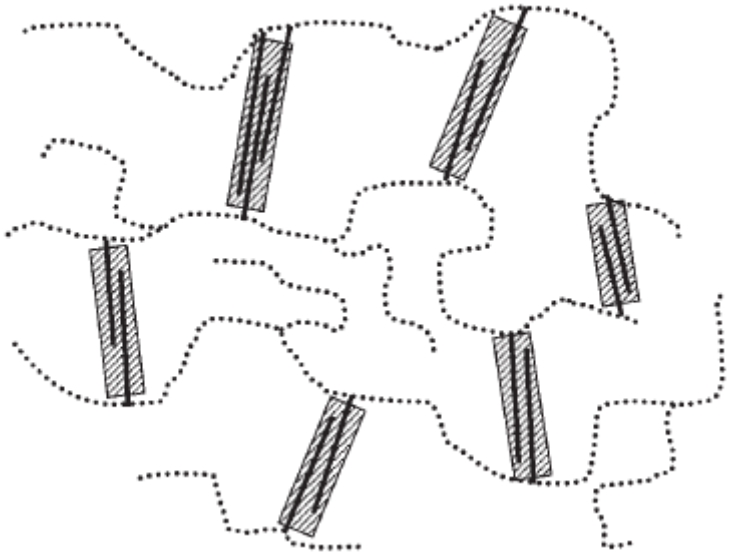

Figure 2-5. Illustration of a branch-block thermoplastic elastomer made via macromonomer incorporation (— isotactic branches, ···· amorphous backbones).[86]

2.7 Polymer Characterization

Molecular weight distribution, degree of long chain branching, and chemical composition distribution are among the microstructural properties needed to describe the TPE samples that will be produced in this thesis. A brief overview of the characterization techniques to measure these properties will be given below.

2.7.1 Molecular Weight Distribution (MWD)

The essential distinguishing characteristic of polymeric materials is their molecular size which can be measured by primary or secondary methods. Primary methods determine molecular masses directly and secondary methods require calibration curves with stardards of known molecular masses. Gel permeation chromatography (GPC) is the most important secondary method for MWD determination.

GPC is a form of liquid chromatography in which the polymer molecules are separated according to their molecular sizes or, more correctly, their hydrodynamic volumes in solution. The procedure involves injecting a dilute solution of a polydisperse polymer into a continuous flow of solvent passing through a column containing tightly packed microporous gel particles. The gel has particle sizes in the range 5-10 μm in order to give efficient packing and typically has a range of pore sizes from 0.5-10^5 nm, which corresponds to the effective size range of polymer molecules.[87] Separation of the molecules occurs by preferential penetration of polymer molecules with different sizes into the pores; small molecules are able to permeate more easily through the pores compared to the large sized molecules so that their rate of passage through the column is correspondingly slower. The continuous flow of the solvent leads to separation of the molecules according to size, with the large molecules being eluted first and the smaller molecules, which have penetrated more deeply into the pores, requiring longer elution times. If the pore sizes are too small to permit penetration by any of the molecules or too large that all molecules can penetrate them with the same relative ease, there would be little or no separation of the molecules. Consequently, selection of the column packing material is crucial and different column packings are usually required for polymers having wide range of molecular masses. The availability of gels of mixed pore sizes has made this a less demanding requirement.

Clearly, if retention volume can be directly related to molecular weight by means of an appropriate calibration curve, then in principle a chromatogram can be made to yield molecular weight averages

and distributions. The simplest type of calibration curve is established experimentally by relating the peak-retention volume to molecular weight for a series of known narrow molecular weight standards. This calibration curve depends on the solvent used for the separation, the structure of the polymer, and the temperature.

Another calibration curve, called the universal calibration curve, is obtained by relating the retention volume to hydrodynamic volume of polymeric molecules calculated by the product of intrinsic viscosity, [η], and molecular weight, M. In general, GPC universal calibrations curves for different types of polymers merge into a single plot when log[η]M is plotted against retention volume.[88] The details of these routine calibration techniques have been discussed elsewhere.[81, 89]

2.7.2 Long Chain Branching Determination

There are three major methods for estimating LCB frequencies: 1)^{13}C-NMR spectroscopy, 2) gel permeation chromatography coupled with online light scattering (LS), and/or viscosity (CV) detectors, and 3) rheological measurements.[78, 90-92]

Melt rheological measurements are the most sensitive methods for detecting very low concentration of LCB. However, the information from melt rheological measurements is indirect because the measured rheological properties result from the combined effects of molecular weight averages, MWD, as well as LCB length, content, and distribution. Furthermore, they provide qualitative information about branching and their interpretations requires a good understanding of branch type and level. Triple detection GPC (LS, CV, plus a mass detector such as a refractometer), on the other hand, gives information on LCB density as well as LCB density distribution across the molecular weight distribution.[83]

2.7.2.1 Long Chain Branching Determination via ^{13}C-NMR

Nuclear magnetic resonance spectroscopy is a powerful analytical tool that can provide a wealth of information on polymer molecular structure. This technique exploits the fact that the atomic nuclei of some elements interact with an external applied magnetic field. Unlike spinning macroscopic bodies, which can be made to spin in any direction, there are quantized limits to the direction of nuclear angular momentum. By applying a magnetic field and radiofrequency to a polymer sample, a

resonance condition is attained which can be envisaged as causing the precessing nuclei to flip from one orientation to the other. However, the resonance frequencies of carbon nuclei located in different electron densities differ, making it possible to distinguish between different carbons in the sample. This phenomenon, known as chemical shift, has been fully exploited by polymer analysts to characterize branching in polyethylene.

Let us begin our discussion of polyethylene long chain branching by examining the ^{13}C-NMR spectra for linear ethylene 1-octene copolymer [5]. The nomenclature, used to designate those polymer backbone and side chain carbons discriminated by ^{13}C-NMR, is given in Figure 2-6.

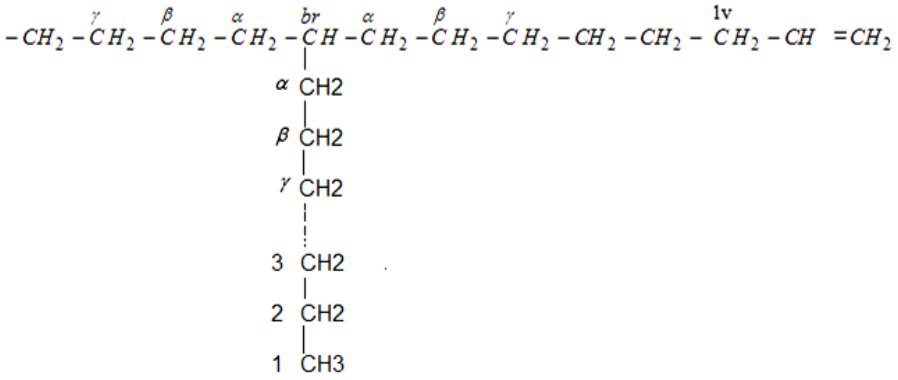

Figure 2-6. Carbon nomenclature for chemical shift assignments.

The distinguishable backbone carbons are designated by Greek symbols while the side-chain branch carbons are numbered consecutively starting with methyl group and ending with methylene carbon bonded to the polymer backbone. The results of NMR studies show that the "6" carbon resonance for the hexyl branch is the same as α, the "5" carbon resonance is the same as β, and the "4" carbon resonance is the same as γ. Resonances 1, 2 and 3, likewise, are the same as the end group resonances observed for linear polyethylene.[5, 93] Thus, a six carbon branch produces the same ^{13}C spectral pattern as any subsequent branch of greater length. Therefore, ^{13}C-NMR, alone, cannot be used to distinguish a linear six-carbon branch from a longer branch.

A survey of ^{13}C-NMR spectra for essentially linear polyethylene samples[30, 94] containing a small degree of long chain branching made by solution polymerization, shows that only 9 resonances are produced. A major resonance at 30 ppm arises from equivalent, recurring methylene carbons, which

are four or more carbon atoms removed from an end group or a branch. Resonances at 14.1, 22.9, 32.3, and 33.9 ppm are from carbons 1, 2, 3, and the allylic carbon, respectively. These five resonances are fundamental to the spectra of all polyethylenes. The other four resonances, observed at 34.6, 27.3, 30.4, and 38.2 ppm are due to α, β, γ, and methine carbons. The γ carbon chemical shifts are often obscured by the major 30 ppm resonance from equivalent, recurring methylene carbons. Thus, in high density polyethylene, where long chain branching is essentially the only branch type present, ^{13}C-NMR can be used to establish unequivocally the presence of branches six carbon long or longer. If no comonomer has been used during polymerization, it is very likely that the presence of such resonances are due to true long chain branching. In any event, ^{13}C-NMR can be used to pinpoint the absence of long chain branching and place an upper limit upon the long chain branch concentration whenever branches with six carbons or longer are detected.

The long chain branch density (LCBD: number of branching points per 1000 carbons), saturated chain end density, (SCED: number of saturated chain ends per 1000 carbons), unsaturated chain end density, (UCED: number of unsaturated chain ends per 1000 carbons), and long chain branch frequency, (LCBF: number of LCBs per polymer chain) can be calculated using the following equations,

$$LCBD = \frac{IA_{\alpha}}{3IA_{Tot}} \times 1000 \tag{2-23}$$

$$SCED = \frac{IA_1 + A_2}{2IA_{Tot}} \times 1000 \tag{2-24}$$

$$UCED = \frac{IA_{1v}}{IA_{Tot}} \times 1000 \tag{2-25}$$

$$LCBF = \frac{2LCBD}{SCED + UCED - LCBD} \tag{2-26}$$

where IA_{α} IA_1, IA_2 , IA_{1v} and IA_{Tot} are the integral areas of α, 1, 2, allylic carbon, and total intensity of carbons, respectively.[30]

2.7.2.2 GPC/LS

When a polymer sample elutes from a GPC column equipped with a multi-angle laser light scattering detector on-line, the radius of gyration and molecular weight of polymer fractions coming out of the

column can be measured. The corresponding radius of gyration of linear chains of same molecular weight can be calculated by the following relation, which correlates the radius of gyration of linear polyethylene to its molecular weight,[83]

$$\left\langle r_g^2 \right\rangle_{lin}^{1/2} = 2.86 \times 10^{-2} M^{.568} \tag{2-27}$$

where $\left\langle r_g^2 \right\rangle_{lin}^{1/2}$ is the radius of gyration of a linear polyethylene chain in nm. This correlation can be easily obtained by injecting a linear polyethylene sample into the GPC column and then performing a simple linear regression to find out the pertinent constants. Since the molecular weight and radius of gyration of the fractions coming out of the GPC column are known, the branching parameter, *g*, of each fraction (the ratio of the mean square radius of gyration of a branched chain to that of a linear chain with same molecular weight) can be calculated with the equation,

$$g = \frac{\left\langle r_g^2 \right\rangle_{br}}{\left\langle r_g^2 \right\rangle_{lin}} \tag{2-28}$$

The following Zimm-Stockmayer equation[95] is then applied to calculate LCBF of fractions exiting from the column,

$$g = \left[\left(1 + \frac{LCBF}{7} \right)^{1/2} + \frac{4LCBF}{9\pi} \right]^{-1/2} \tag{2-29}$$

The average LCBF and LCBD can be calculated by,

$$LCBF_{av} = \frac{\sum LCBF_i \frac{c_i}{M_i}}{\sum \frac{c_i}{M_i}} \tag{2-30}$$

$$LCBF_{av} = \frac{r_n LCBD_{av}}{500} \tag{2-31}$$

The experimental results by Wang[83] showed that LCBF estimates from LS detector were in good agreement with the ^{13}C-NMR measurements for PEs with LCBF greater than 0.08 or LCBD greater than 0.022. Due to sensitivity limitations of the LS technique, errors for samples having LCBF less than 0.08 were quite significant.

Another common measure of LCB arises when the intrinsic viscosity of the polymer is compared with that of a linear chain of the same M_w,[95-96]

$$g' = \frac{[\eta]_{br}}{[\eta]_{lin}} \tag{2-32}$$

One can express the correlation between these two quantities in terms of the exponent ε,

$$g' = g^{\varepsilon} \tag{2-33}$$

The literature quotes values of ε ranging from 0.5 to 1.5.[97-99] Using a value of ε =0.5, Mendelson et al.[100] demonstrated that comparisons made at a constant effective molecular volume, yielded values of zero shear viscosity, η_0, for polymer melts with long branches are always higher than those for linear polymers.

2.7.3 Crystallization Analysis Fractionation (Crystaf)

Crystallization analysis fractionation (Crystaf) is a polymer characterization technique based on the continuous crystallization of polymer chains from a dilute solution.[101] The analysis is carried out by monitoring the polymer solution concentration during crystallization by temperature reduction. Aliquots of the solution are filtered and analyzed by a concentration detector. In fact, the whole process is similar to a classical stepwise fractionation by precipitation, with the exception that in this approach no attention is paid to the polymer precipitated but to the polymer that remains in solution. The first data points, taken at temperatures above crystallization starts to take place, provide a constant concentration equal to the initial polymer solution concentration. As the temperature goes down, the most crystalline fractions, composed of chains without or with very few branches, will precipitate first, resulting in a steep decrease in the solution concentration. This is followed by the precipitation of fractions of increasing branch content as the temperature continues to decrease. The last data point, corresponding to the lowest temperature of the crystallization cycle, represents the fraction that has not crystallized (mainly highly branched material) and remains soluble at room temperature.

For LLDPE, chain crystallizability is mainly controlled by the fraction of noncrystallizable comonomer units in the chain. The chains with fewer comonomer molecules will precipitate at higher

temperatures, whereas the chains with more comonomer content will precipitate at lower temperatures. Consequently, the differential Crystaf profile, together with an appropriate calibration curve, can be used to estimate the copolymer chemical composition distribution (CCD) of an ethylene/α-olefin copolymer.[101-103]

Other factors may affect polymer crystallizability, such as molecular weight and long chain branching. Soares, et. al.[104] showed that long-chain branching had only a very small effect on Crystaf profiles, and that molecular weight effects might be significant for samples with number average molecular weight below 5000, but this effect may be partially corrected if terminal methyl groups are taken into account.

2.7.4 Infrared Spectroscopy

Infrared spectroscopy (IR spectroscopy) is the subset of spectroscopic techniques that deals with the infrared region of the electromagnetic spectrum. The main goal of IR spectroscopic analysis is to determine the chemical functional groups in the sample. When infrared radiation is absorbed by a molecule, it causes atoms in bonds to vibrate back and forth with increased amplitude. Because each functional group has a particular grouping of atoms, there is a characteristic infrared absorption associated with each type of functional group. The infrared spectrum of a sample is collected by passing a beam of infrared light through the sample. If the wavenumber of the incident beam matches one of the characteristic absorptions of the molecule, the sample absorbs the light and hence at that particular wavenumber the intensity of the transmitted beam would be less than that of the reference beam. By varying the wavenumber over time, and monitoring the transmittance of the light passing through the sample, a transmittance infrared spectrum is obtained. In a Fourier transform instrument all frequencies are examined simultaneously.

2.7.4.1 Sample Preparation

Solid samples can be prepared in a variety of ways. One common method is to grind a quantity of the sample with a specially purified salt (usually potassium bromide) finely (to remove scattering effects from large crystals). This powder mixture is then pressed in a mechanical press to form a translucent pellet through which the beam of the spectrometer can pass. The second method is the "cast film" technique, which is used mainly for polymeric materials. The sample is first dissolved in a suitable, non hygroscopic solvent. A drop of this solution is deposited on surface of KBr or NaCl cell. The solution is then evaporated to dryness and the film formed on the cell is analysed directly. The third

method is to make a film of polymer using a hot press and brass shims. The details of this method are described in ASTM D5576.[105]

Chapter 3

Simulation of Polymerization and Long Chain Branch Formation in a Semi-batch Reactor Using Two Single-Site Catalysts

3.1 Summary

We developed a mathematical model for the solution polymerization of olefins in a semi-batch reactor with two single-site catalysts. In the propylene polymerization case, our objective is to study the production of a thermoplastic elastomer using two catalysts, one capable of forming isotactic chains containing terminal vinyl bonds (macromonomers) and the other producing atactic chains while also being able to copolymerize macromonomers to form long chain branches (LCB). A similar thermoplastic elastomer can be produced by polymerizing ethylene and α-olefin comonomers when the α-olefin reactivity ratios of the two catalysts are significantly different. The model can predict the polydispersity index, and the number and weight average chain lengths of different polymer populations: linear chains, homogenous-branched chains, and cross-products, which are polymerization products formed when macromonomers formed on one catalyst are incorporated into chains growing on the other catalyst. The model can also predict the weight and mole percent of the different populations.

3.2 Introduction

Thermoplastic elastomers (TPEs) are a class of polymers or a physical mix of polymers which consist of materials with both thermoplastic and elastomeric properties. TPEs are generally easier to process than conventional thermoset rubbers and easier to be recycled. However, TPEs are generally not as effective as chemically crosslinked elastomers when considering resistance to solvents and deformation at high temperatures and, therefore, are not used in applications such as automobile tires where these properties are important. [106]

There are at least two types of domains present in a TPE: a soft domain, in which flexible chain segments act as springs, and a hard domain, which functions as knots preventing the stretched polymer chains from irreversibly sliding by one another. In a thermoset rubber, the hard domain is created by covalent bonds, for example by vulcanization using sulfur, whereas in TPEs, physical aggregates such as the small crystallites in a semi-crystalline polymer or the glassy domains in a multiphase triblock copolymer[107]form the hard domain.

The four major types of TPEs are polyurethanes, polyester copolymers, styrene copolymers, and olefinics. Olefinic TPEs are classified as multicomponent or single component. Multicomponent olefin TPEs are made through the physical blending of polypropylene and ethylene-propylene-diene terpolymers (EPDM) or ethylene-propylene rubber (EPR), but the latter is preferred because of its lower cost.[106] Single-component olefin TPEs can be prepared through polymerization of propylene using homogenous or heterogeneous organometallic catalysts.

Polypropylene composed of blocks of isotactic and atactic stereosequences forms an interesting family of thermoplastic elastomers.[108] This type of TPE is unusual because it is derived from just a single monomer unit. The stereoregular structure of isotactic polypropylene enables it to form helices that can pack into crystallites. Atactic polypropylene is stereoirregular and amorphous at all temperatures. The elastic properties of elastomeric polypropylene are believed to arise from their stereo-block (isotactic-atactic) microstructure[109-112] that allows the formation of short crystallizable isotactic blocks in a low-tacticity polymer chain.

Long chain-branched polypropylene[113] with elastomeric properties can, alternatively, be synthesized by grafting isotactic blocks of polypropylene containing a terminal vinyl unsaturation (macromonomer) to atactic propylene (aPP-*g*-iPP) using two metallocenes[114]. Some other olefinic thermoplastics such as high-density polyethylene (HDPE) grafted onto ethylene/α-olefin copolymers (PEαO-*g*-PE), have also been made[85]. In the former case, using a stereoselective catalyst, isotactic polypropylene chains with terminal vinyl groups are produced in a first polymerization step. In a second polymerization step, using a non-stereoselective catalyst with high macromonomer incorporation rate (LCB-catalyst), isotactic chains made in the first step are grafted onto the amorphous polypropylene chain, as depicted in Figure 3-1.

Physical crosslinks resulting from crystallization of the isotactic LCBs is the reason for the elastic properties of this polymer. simultaneous or sequential.[115] methods can be used for the synthesis of these materials.

In the simultaneous synthesis method, the catalysts capable of producing isotactic polypropylene macromonomers, such as rac-dimethylsilanediylbis(2-methyl-4-phenylindenyl)zirconium dichloride,[44] and of producing atactic polypropylene chains and incorporating macromonomer, such as a constrained geometry catalyst, are added to the reactor simultaneously to produce polymer that contains a variety of chain architectures: linear chains, homogeneous-branched chains, and heterogeneous-branched chains (also called cross-product). Cross-product chains are generated when

a macromonomer made by one of the catalysts in the reactor is incorporated as a LCB onto the chain growing on the other catalyst present in the reactor. These cross-products chains can be seen as compatibilizers between the purely amorphous or purely semi-crystalline chains made by each catalyst individually.

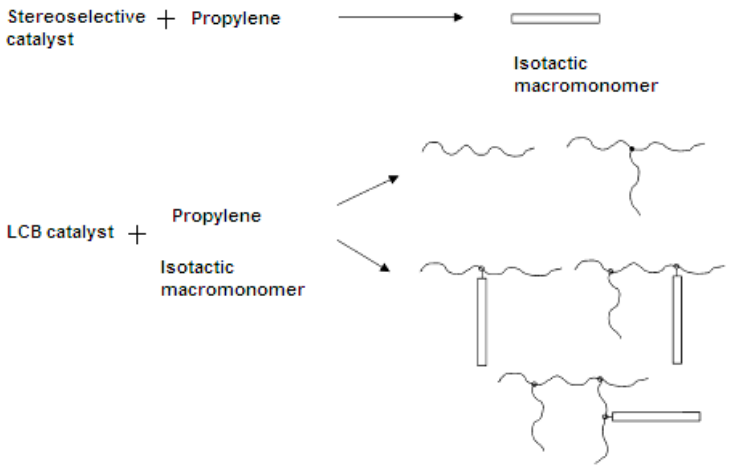

Figure 3-1. Mechanism of branch blocks formation with dual metallocenes.

In the sequential synthesis approach, isotactic polypropylene macromonomers are first produced in the polymerization reactor, then by injecting a non-stereospecific catalyst capable of forming LCBs into the same reactor, isotactic blocks are incorporated onto atactic polypropylene chains.

Both methods can also be used to produce TPEs based on ethylene and α-olefin copolymers. For the simultaneous synthesis method, one of the catalysts must have a low α-olefin comonomer reactivity ratio, thus making HDPE, while the other must have a high α-olefin comonomer reactivity ratio, to produce amorphous ethylene/α-olefin copolymer.

Developing polymer reactor models for different catalyst combinations can help understand the details of these complex syntheses and to control the properties and fractions of linear chains, homogeneous-branched chains and cross-products. In a recently developed mathematical model,[85] only the molar fraction of linear, homogenous-branched and cross-product chains were predicted to explain the differences between polymers made with sequential or simultaneous modes of polymerization. The model was developed for semi-batch polymerization under constant ethylene

pressure for the case where the TPE is formed by HDPE grafting onto amorphous ethylene/α-olefin copolymers.

In the present chapter, we developed a mathematical model for the solution polymerization of olefins in a semi-batch reactor using two single-site catalysts under constant monomer pressure. The model can predict molar and weight percents of the different polymer populations including linear chains, homogenous-branched and cross-products. The model is also able to calculate average LCB frequencies.

This Chapter has been published in Journal of Macromolecular Reaction Engineering.[116]

3.3 Model Development

The model uses population balances and the method of moments to calculate microstructural properties of macromonomers, living and dead chains. Each of these populations is subdivided into linear, homogeneous-branched, and cross-product chains. In homogeneous-branched chains, all LCBs and the backbone were made on the same catalyst. In cross-product chains, at least one of the LCBs and/or the backbone was made on a different catalyst used to produce the other segments. Figure 3-2 illustrates this classification.

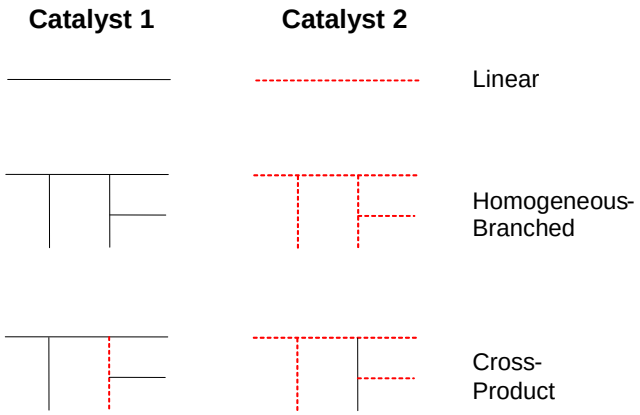

Figure 3-2. Chain classification used in the model. This classification is applied to macromonomers, living and dead polymer chains.

The model can predict the following properties for each of the polymer populations: molar (n %) and weight (w %) percentages, number (r_n) and weight (r_w) average chain lengths, and average LCB per 1000 C atoms (λ) and per chain (B_n).

3.3.1 Polymerization Mechanism

The mechanism for coordination polymerization can be divided into five main reaction classes: catalyst activation with cocatalyst, catalyst initiation with monomer, chain propagation, chain transfer, and poisoning and deactivation.[11, 27-28, 30-32] Terminal branching has been considered to be the most probable branching mechanism with coordination polymerization catalysts.[56, 117] In this mechanism, macromonomers formed through β-hydride elimination and transfer to monomer (polyethylene), or β-methyl elimination (polypropylene), are inserted into the growing polymer chains yielding LCBs. All these steps are included in the model described below.

The following convention was adopted to represent the different chain populations in the model: $x_{i,r}$ is linear; $\bar{x}_{i,r}$ is homogeneous-branched; $\bar{\bar{x}}_{i,r}$ is cross-product; the subscript *i* represents catalyst type; the subscript *r* indicates chains length (number of monomer units in the chain); living polymer chains are denoted by *P*, macromonomers by μ, and dead polymers by *D*.

We have also assumed that catalyst activation with cocatalyst was instantaneous. This hypothesis can be easily relaxed without any significant alteration in the final model equations.

A monomer-free catalyst, C_i, generates a polymer chain of unit length $P_{i,1}$ via insertion of a monomer molecule *M*:

$$C_i + M \xrightarrow{k_{p,i}} P_{i,1} \tag{3-1}$$

Linear, homogeneous-branched, and cross-product chains propagate according to the reactions:

$$P_{i,r} + M \xrightarrow{k_{p,i}} P_{i,r+1} \tag{3-2}$$

$$\bar{P}_{i,r} + M \xrightarrow{k_{p,i}} \bar{P}_{i,r+1} \tag{3-3}$$

$$\bar{\bar{P}}_{i,r} + M \xrightarrow{k_{p,i}} \bar{\bar{P}}_{i,r+1} \tag{3-4}$$

We have assumed, for simplicity's sake, that initiation and propagation reactions have the same rate constants, $k_{p,i}$.

Long chain branches are formed by incorporation of macromonomers of different types:

$$P_{i,r} + \mu_{i,s} \xrightarrow{k_{b,i}} \bar{P}_{i,r+s} \tag{3-5}$$

$$P_{i,r} + \mu_{j,s} \xrightarrow{k_{b,i}} \bar{\bar{P}}_{i,r+s} \tag{3-6}$$

$$P_{i,r} + \bar{\mu}_{i,s} \xrightarrow{k_{b,i}} \bar{P}_{i,r+s} \tag{3-7}$$

$$P_{i,r} + \bar{\mu}_{j,s} \xrightarrow{k_{b,i}} \bar{\bar{P}}_{i,r+s} \tag{3-8}$$

$$P_{i,r} + \bar{\bar{\mu}}_{s} \xrightarrow{k_{b,i}} \bar{\bar{P}}_{i,r+s} \tag{3-9}$$

$$\bar{P}_{i,r} + \mu_{i,s} \xrightarrow{k_{b,i}} \bar{P}_{i,,r+s} \tag{3-10}$$

$$\bar{P}_{i,r} + \mu_{j,s} \xrightarrow{k_{b,i}} \bar{\bar{P}}_{i,r+s} \tag{3-11}$$

$$\bar{P}_{i,r} + \bar{\mu}_{i,s} \xrightarrow{k_{b,i}} \bar{P}_{i,r+s} \tag{3-12}$$

$$\bar{P}_{i,r} + \bar{\mu}_{j,s} \xrightarrow{k_{b,i}} \bar{\bar{P}}_{i,r+s} \tag{3-13}$$

$$\bar{P}_{i,r} + \bar{\bar{\mu}}_{s} \xrightarrow{k_{b,i}} \bar{\bar{P}}_{i,r+s} \tag{3-14}$$

$$\bar{\bar{P}}_{i,r} + \mu_{i,s} \xrightarrow{k_{b,i}} \bar{\bar{P}}_{i,r+s} \tag{3-15}$$

$$\bar{\bar{P}}_{i,r} + \mu_{j,s} \xrightarrow{k_{b,i}} \bar{\bar{P}}_{i,r+s} \tag{3-16}$$

$$\bar{\bar{P}}_{i,r} + \bar{\mu}_{i,s} \xrightarrow{k_{b,i}} \bar{\bar{P}}_{i,r+s} \tag{3-17}$$

$$\bar{\bar{P}}_{i,r} + \bar{\mu}_{j,s} \xrightarrow{k_{b,i}} \bar{\bar{P}}_{i,r+s} \tag{3-18}$$

$$\bar{\bar{P}}_{i,r} + \bar{\bar{\mu}}_{s} \xrightarrow{k_{b,i}} \bar{\bar{P}}_{i,r+s} \tag{3-19}$$

Chain transfer reactions can lead to the formation of either macromonomers or dead polymer chains, according to the chemical equations:

$$P_{i,r} \xrightarrow{k_{\beta,i}} \mu_{i,r} + C_i \tag{3-20}$$

$$P_{i,r} \xrightarrow{k_{\beta-CH_3,i}} \mu_{i,r} + C_i \tag{3-21}$$

$$P_{i,r} + M \xrightarrow{k_{M,i}} \mu_{i,r} + P_{i,1} \tag{3-22}$$

$$P_{i,r} + Al \xrightarrow{k_{Al,i}} D_{i,r} + C_i \tag{3-23}$$

$$P_{i,r} + H_2 \xrightarrow{k_{H,i}} D_{i,r} + C_i \tag{3-24}$$

$$\overline{P}_{i,r} \xrightarrow{k_{\beta,i}} \overline{\mu}_{i,r} + C_i \tag{3-25}$$

$$\overline{P}_{i,r} \xrightarrow{k_{\beta-CH_3,i}} \overline{\mu}_{i,r} + C_i \tag{3-26}$$

$$\overline{P}_{i,r} + M \xrightarrow{k_{M,i}} \overline{\mu}_{i,r} + P_{i,1} \tag{3-27}$$

$$\overline{P}_{i,r} + Al \xrightarrow{k_{Al,i}} \overline{D}_{i,r} + C_i \tag{3-28}$$

$$\overline{P}_{i,r} + H_2 \xrightarrow{k_{H,i}} \overline{D}_{i,r} + C_i \tag{3-29}$$

$$\overline{\overline{P}}_{i,r} \xrightarrow{k_{\beta,i}} \overline{\overline{\mu}}_r + C_i \tag{3-30}$$

$$\overline{\overline{P}}_{i,r} \xrightarrow{k_{\beta-CH_3,i}} \overline{\overline{\mu}}_r + C_i \tag{3-31}$$

$$\overline{\overline{P}}_{i,r} + M \xrightarrow{k_{M,i}} \overline{\overline{\mu}}_r + P_{i,1} \tag{3-32}$$

$$\overline{\overline{P}}_{i,r} + Al \xrightarrow{k_{Al,i}} \overline{\overline{D}}_r + C_i \tag{3-33}$$

$$\overline{\overline{P}}_{i,r} + H_2 \xrightarrow{k_{H,i}} \overline{\overline{D}}_r + C_i \tag{3-34}$$

Finally, a simple first order catalyst deactivation mechanism was assumed to produce the deactivated species, $\hat{C}_i$:

$$P_{i,r} \xrightarrow{k_{d,i}} D_{i,r} + \hat{C}_i \tag{3-35}$$

$$\overline{P}_{i,r} \xrightarrow{k_{d,i}} \overline{D}_{i,r} + \hat{C}_i \tag{3-36}$$

$$\overline{\overline{P}}_{i,r} \xrightarrow{k_{d,i}} \overline{\overline{D}}_r + \hat{C}_i \tag{3-37}$$

$$C_i \xrightarrow{k_{d,i}} \hat{C}_i \tag{3-38}$$

3.3.2 Moment Equations for Living Chains

The n^{th} moment, M^n, of a generic distribution $f(x)$ is given by the equation:

$$\mathrm{M}^n = \sum_{x=0}^{\infty} x^n f(x) \tag{3-39}$$

The following nomenclature convention was adopted for the moments: x_i, x_i^I, x_i^{II} are the zero$^{\text{th}}$, first and second moments of linear chains; $\overline{x}_i, \overline{x}_i^I, \overline{x}_i^{II}$ are the zero$^{\text{th}}$, first and second moments of homogeneous-branched chains; $\overline{\overline{x}}_i, \overline{\overline{x}}_i^I, \overline{\overline{x}}_i^{II}$ are the zero$^{\text{th}}$, first and second moments of cross-product chains; the subscript i indicates catalyst type; moments of living polymer chains are represented by Y, of macromonomers by Θ, and of dead polymers by Q.

The population balance for linear living chains with length larger than 2, $r \geq 2$, is given by:

$$\begin{aligned}\frac{\mathrm{d}P_{i,r}}{\mathrm{d}t} &= k_{p,i}M(P_{i,r-1} - P_{i,r}) - (k_{\beta,i} + k_{\beta-CH_3,i} + k_{Al,i}Al + k_{H,i}H_2 + k_{M,i}M)P_{i,r} \\ &\quad - k_{d,i}P_{i,r} - k_{b,i}P_{i,r}\sum_{s=2}^{\infty}(\mu_{i,s} + \mu_{j,s} + \overline{\mu}_{i,s} + \overline{\mu}_{j,s} + \overline{\overline{\mu}}_s)\end{aligned} \tag{3-40}$$

This equation will be used in a more compact form as,

$$\frac{\mathrm{d}P_{i,r}}{\mathrm{d}t} = k_{p,i}M(P_{i,r-1} - P_{i,r}) - (\sigma_i + k_{b,i}\tilde{\Theta})P_{i,r} \tag{3-41}$$

where the following lumped parameters were defined:

$$\sigma_i = K_{t,i} + k_{d,i} \tag{3-42}$$

$$K_{t,i} = K_{t.i}^{-} + K_{t.i}^{s} \tag{3-43}$$

$$K_{t,i}^{-} = k_{\beta,i} + k_{M,i}M + k_{\beta-CH_3,i} \tag{3-44}$$

$$K_{t,i}^{s} = k_{Al,i}Al + k_{H,i}H_2 \tag{3-45}$$

$$\tilde{\Theta} = \sum_{r=2}^{\infty}(\mu_{i,r} + \mu_{j,r} + \bar{\mu}_{i,r} + \bar{\mu}_{j,r} + \bar{\bar{\mu}}_{r}) \tag{3-46}$$

A slightly different equation is required for chains of unity length, $r = 1$,

$$\frac{dP_{i,1}}{dt} = k_{p,i}M(C_i - P_{i,1}) - (\sigma_i + k_{b,i}\tilde{\Theta})P_{i,1} + \sum_{r=1}^{\infty}(P_{i,r} + \bar{P}_{i,r} + \bar{\bar{P}}_{i,r})k_{M,i}M \tag{3-47}$$

$$\frac{dP_{i,1}}{dt} = k_{p,i}M(C_i - P_{i,1}) - (\sigma_i + k_{b,i}\tilde{\Theta})P_{i,1} + k_{M,i}M\tilde{Y}_i \tag{3-48}$$

where,

$$\tilde{Y}_i = \sum_{r=1}^{\infty}P_{i,r} + \sum_{r=2}^{\infty}\bar{P}_{i,r} + \sum_{r=2}^{\infty}\bar{\bar{P}}_{i,r} \tag{3-49}$$

The dynamic equation for the zero[th] moment of linear living polymer made on catalyst *i* is:

$$\frac{dY_i}{dt} = \frac{dP_{i,1}}{dt} + \sum_{r=2}^{\infty}\frac{dP_{i,r}}{dt} \tag{3-50}$$

Substituting Equations (3-41) and (3-48) into Equation (3-50) and simplifying the resulting expression, we obtain the equation for the zero[th] moment of linear living chains:

$$\frac{dY_i}{dt} = k_{p,i}C_iM - (\sigma_i + k_{b,i}\tilde{\Theta})\,Y_i + k_{M,i}M\tilde{Y}_i \tag{3-51}$$

The equation for the first moment is:

$$Y_i^I = \sum_{r=1}^{\infty} rP_{i,r} \tag{3-52}$$

Differentiating Equation (3-52) yields:

$$\frac{\mathrm{d}Y_i^I}{\mathrm{d}t} = \frac{\mathrm{d}P_{i,1}}{\mathrm{d}t} + \sum_{r=2}^{\infty} r\frac{\mathrm{d}P_{i,r}}{\mathrm{d}t} \tag{3-53}$$

Substituting Equations (3-41) and (3-48) into Equation (3-53):

$$\begin{aligned}\frac{\mathrm{d}Y_i^I}{\mathrm{d}t} &= k_{p,i}(C_i - P_{i,1})M - (\sigma_i + k_{b,i}\widetilde{\Theta})P_{i,1} \\ &+ \sum_{r=2}^{\infty} r[k_{p,i}(P_{i,r-1} - P_{i,r})M - (\sigma_i + k_{b,i}\widetilde{\Theta})P_{i,r}] + k_{M,i}M\widetilde{Y}_i\end{aligned} \tag{3-54}$$

After simplification of Equation (3-54), the expression for the first moment of linear living chains becomes:

$$\frac{\mathrm{d}Y_i^I}{\mathrm{d}t} = k_{p,i}M(C_i + Y_i\ ) - (\sigma_i + k_{b,i}\widetilde{\Theta})\,Y_i^I + k_{M,i}M\widetilde{Y}_i \tag{3-55}$$

Finally, for the second moment:

$$\frac{\mathrm{d}Y_i^{II}}{\mathrm{d}t} = \frac{\mathrm{d}P_{i,1}}{\mathrm{d}t} + \sum_{r=2}^{\infty} r^2\frac{\mathrm{d}P_{i,r}}{\mathrm{d}t} \tag{3-56}$$

Substituting Equations (3-41) and (3-48) into Equation (3-56) we get:

$$\begin{aligned}\frac{\mathrm{d}Y_i^{II}}{\mathrm{d}t} &= k_{p,i}(C_i - P_{i,1})M - (\sigma_i + k_{b,i}\widetilde{\Theta})P_{i,1} + k_{M,i}M\widetilde{Y} + \\ &\sum_{r=2}^{\infty} r^2[k_{p,i}(P_{i,r-1} - P_{i,r})M - (\sigma_i + k_{b,i}\widetilde{\Theta})P_{i,r}]\end{aligned} \tag{3-57}$$

After some algebraic manipulation, the following equation for the second moment of linear living polymer is obtained:

$$\frac{\mathrm{d}Y_i^{II}}{\mathrm{d}t} = k_{p,i}C_iM - (\sigma_i + k_{b,i}\widetilde{\Theta})Y_i^{II} + k_{p,i}(Y_i\ + 2Y_i^I)M + k_{M,i}M\widetilde{Y}_i \tag{3-58}$$

We will consider only chains with $r \geq 2$ as branched chains, since chains with $r = 1$ must necessarily be linear. This is just a convention and does not affect the final calculation results for long chains, but simplifies the next derivation steps.

The population balance for homogenous-branched living chains is:

$$\begin{aligned}\frac{\mathrm{d}\overline{P}_{i,r}}{\mathrm{d}t} &= k_{p,i}M(\overline{P}_{i,r-1} - \overline{P}_{i,r}) - (\sigma_i + k_{b,i}\widetilde{\Theta})\overline{P}_{i,r} \\ &+ k_{b,i}\sum_{s=2}^{r-1}\overline{P}_{i,r-s}(\mu_{i,s} + \overline{\mu}_{i,s}) + k_{b,i}\sum_{s=2}^{r-1}P_{i,r-s}(\mu_{i,s} + \overline{\mu}_{i,s})\end{aligned} \tag{3-59}$$

The equation for the zero[th] moment is obtained by substituting Equation (3-59) into Equation (3-50) and ignoring the first term of the right hand side for $r = 1$:

$$\begin{aligned}\frac{\mathrm{d}\overline{Y}_i}{\mathrm{d}t} &= k_{p,i}M\left(\sum_{r=2}^{\infty}\overline{P}_{i,r-1} - \sum_{r=2}^{\infty}\overline{P}_{i,r}\right) - (\sigma_i + k_{b,i}\widetilde{\Theta})\sum_{r=2}^{\infty}\overline{P}_{i,r} \\ &+ k_{b,i}\sum_{r=2}^{\infty}\sum_{s=2}^{r-1}\overline{P}_{i,r-s}(\mu_{i,s} + \overline{\mu}_{i,s}) + k_{b,i}\sum_{r=2}^{\infty}\sum_{s=2}^{r-1}P_{i,r-s}(\mu_{i,s} + \overline{\mu}_{i,s})\end{aligned} \tag{3-60}$$

This expression can be simplified to obtain the final equation for the zero[th] moment of homogeneous-branched living chains:

$$\frac{\mathrm{d}\overline{Y}_i}{\mathrm{d}t} = k_{b,i}Y_i(\Theta_i + \overline{\Theta}_i) - [\sigma_i + k_{b,i}(\Theta_j + \overline{\Theta}_j + \overline{\overline{\Theta}})]\ \overline{Y}_i \tag{3-61}$$

The equation for the first moment is obtained by substituting Equation (3-59) into Equation (3-53) and summing from $r = 2$ to ∞ and using the identities:

$$\sum_{r=2}^{\infty} r\overline{P}_{i,r-1} - \sum_{r=2}^{\infty} r\overline{P}_{i,r} = \overline{Y}_i \tag{3-62}$$

$$\sum_{r=2}^{\infty}\sum_{s=1}^{r-1} rP_{r-s}D_s = Y\ Q^I + Y^I Q \tag{3-63}$$

Finally, the equation for the first moment of homogeneous-branched living chains is:

$$\frac{\mathrm{d}\overline{Y}_i^I}{\mathrm{d}t} = k_{p,i} M \overline{Y}_i + k_{b,i}[(Y_i + \overline{Y}_i)(\Theta_i^I + \overline{\Theta}_i^I) + Y_i^I(\Theta_i + \overline{\Theta}_i)] - [\sigma_i + k_{b,i}(\Theta_j + \overline{\Theta}_j + \overline{\overline{\Theta}})]\overline{Y}_i^I \tag{3-64}$$

The equation for the second moment is obtained by substituting Equation (3-59) into Equation (3-56) and using the following expressions:

$$\sum_{r=2}^{\infty} r^2 \overline{P}_{i,r-1} - \sum_{r=2}^{\infty} r^2 \overline{P}_{i,r} = \overline{Y}_i + 2\overline{Y}_i^I \tag{3-65}$$

$$\sum_{r=2}^{\infty}\sum_{s=1}^{r-1} r^2 P_{r-s} D_s = Y\ Q^{II} + 2Y^I Q^I + Y^{II} Q \tag{3-66}$$

Finally, the equation for the second moment of homogeneous-branched living chains becomes:

$$\frac{\mathrm{d}\overline{Y}_i^{II}}{\mathrm{d}t} = k_{p,i} M(\overline{Y}_i + 2\overline{Y}_i^I) - [\sigma_i + k_{b,i}(\Theta_j + \overline{\Theta}_j + \overline{\overline{\Theta}})]\overline{Y}_i^{II} + k_{b,i}[(\overline{Y}_i + Y_i)(\Theta_i^{II} + \overline{\Theta}_i^{II}) + 2(\overline{Y}_i^I + Y_i^I)(\Theta_i^I + \overline{\Theta}_i^I) + Y_i^{II}(\Theta_i + \overline{\Theta}_i)] \tag{3-67}$$

For cross-product chains, we will also adopt the convention that $r > 2$ during all derivations.

The population balance for cross-product chains is:

$$\frac{\mathrm{d}\overline{\overline{P}}_{i,r}}{\mathrm{d}t} = k_{p,i} M(\overline{\overline{P}}_{i,r-1} - \overline{\overline{P}}_{i,r}) - (\sigma_i + k_{b,i}\tilde{\Theta})\overline{\overline{P}}_{i,r} + k_{b,i}\sum_{s=2}^{r-1}\left[\begin{array}{l}\overline{\overline{P}}_{i,r-s}(\mu_{i,s} + \mu_{j,s} + \overline{\mu}_{i,s} + \overline{\mu}_{j,s} + \overline{\overline{\mu}}_s) + \\ (\overline{P}_{i,r-s} + P_{i,r-s})(\mu_{j,s} + \overline{\mu}_{j,s} + \overline{\overline{\mu}}_s)\end{array}\right] \tag{3-68}$$

The equation for the zero[th] moment is obtained by substituting Equation (3-68) into Equation (3-50):

$$\frac{\mathrm{d}\overline{\overline{Y}}_i}{\mathrm{d}t} = k_{p,i} M\left(\sum_{r=2}^{\infty}\overline{\overline{P}}_{i,r-1} - \sum_{r=2}^{\infty}\overline{\overline{P}}_{i,r}\right) - (\sigma_i + k_{b,i}\tilde{\Theta})\sum_{r=2}^{\infty}\overline{\overline{P}}_{i,r} + k_{b,i}\sum_{r=2}^{\infty}\sum_{s=2}^{r-1}\left[\begin{array}{l}\overline{\overline{P}}_{i,r-s}(\mu_{i,s} + \mu_{j,s} + \overline{\mu}_{i,s} + \overline{\mu}_{j,s} + \overline{\overline{\mu}}_s) + \\ (\overline{P}_{i,r-s} + P_{i,r-s})(\mu_{j,s} + \overline{\mu}_{j,s} + \overline{\overline{\mu}}_s)\end{array}\right] \tag{3-69}$$

This expression can be reduced to the more convenient form,

$$\frac{\mathrm{d}\overline{\overline{Y}}_i}{\mathrm{d}t} = k_{p,i}M(\overline{\overline{Y}}_i - \overline{\overline{Y}}_i) - (\sigma_i + k_{b,i}\tilde{\Theta})\overline{\overline{Y}}_i + k_{b,i}\begin{bmatrix} \sum_{r=2}^{\infty}\overline{\overline{P}}_{i,r}\sum_{s=2}^{\infty}(\mu_{i,s} + \mu_{j,s} + \overline{\mu}_{i,s} + \overline{\mu}_{j,s} + \overline{\overline{\mu}}_s) + \\ \sum_{r=2}^{\infty}(\overline{P}_{i,r} + P_{i,r})\sum_{s=2}^{\infty}(\mu_{j,s} + \overline{\mu}_{j,s} + \overline{\overline{\mu}}_s) \end{bmatrix} \tag{3-70}$$

or:

$$\frac{\mathrm{d}\overline{\overline{Y}}_i}{\mathrm{d}t} = k_{b,i}(\overline{Y}_i + Y_i)(\Theta_j + \overline{\Theta}_j + \overline{\overline{\Theta}}) - \sigma_i\overline{\overline{Y}}_i \tag{3-71}$$

The equation for the first moment is calculated by substituting Equation (3-68) into Equation (3-53) and simplifying the resulting equation using Equations (3-62) and (3-63):

$$\frac{\mathrm{d}\overline{\overline{Y}}_i^{I}}{\mathrm{d}t} = k_{p,i}M\overline{\overline{Y}}_i - \sigma_i\overline{\overline{Y}}_i^{I} + k_{b,i}\begin{bmatrix} \overline{\overline{Y}}_i(\Theta_i^I + \Theta_j^I + \overline{\Theta}_i^I + \overline{\Theta}_j^I + \overline{\overline{\Theta}}^I) \\ + (\overline{Y}_i + Y_i)(\Theta_j^I + \overline{\Theta}_j^I + \overline{\overline{\Theta}}^I) \\ + (\overline{Y}_i^I + Y_i^I)(\Theta_j + \overline{\Theta}_j + \overline{\overline{\Theta}}) \end{bmatrix} \tag{3-72}$$

The equation for the second moment is derived by substituting Equation (3-68) into Equation (3-56) and then applying Equations (3-62) and (3-63) to simplify the result:

$$\frac{\mathrm{d}\overline{\overline{Y}}_i^{II}}{\mathrm{d}t} = k_{p,i}M(\overline{\overline{Y}}_i + 2\overline{\overline{Y}}_i^{I}) - \sigma_i\overline{\overline{Y}}_i^{II} + k_{b,i}\begin{bmatrix} \overline{\overline{Y}}_i(\Theta_i^{II} + \Theta_j^{II} + \overline{\Theta}_i^{II} + \overline{\Theta}_j^{II} + \overline{\overline{\Theta}}^{II}) + 2\overline{\overline{Y}}_i^{I}(\Theta_i^I + \Theta_j^I + \overline{\Theta}_i^I + \overline{\Theta}_j^I + \overline{\overline{\Theta}}^I) \\ + (\overline{Y}_i + Y_i)(\Theta_j^{II} + \overline{\Theta}_j^{II} + \overline{\overline{\Theta}}^{II}) + 2(\overline{Y}_i^I + Y_i^I)(\Theta_j^I + \overline{\Theta}_j^I + \overline{\overline{\Theta}}^I) \\ + (\overline{Y}_i^{II} + Y_i^{II})(\Theta_j + \overline{\Theta}_j + \overline{\overline{\Theta}}) \end{bmatrix} \tag{3-73}$$

3.3.3 Moment Equations for Macromonomers

The population balance for linear macromonomers is given by:

$$\frac{\mathrm{d}\mu_{i,r}}{\mathrm{d}t} = K_{t,i}^{=} P_{i,r} - k_{b,i}(Y_i + \overline{Y}_i + \overline{\overline{Y}}_i)\mu_{i,r} - k_{b,j}(Y_j + \overline{Y}_j + \overline{\overline{Y}}_j)\mu_{i,r} \tag{3-74}$$

Defining $\tilde{\tilde{Y}}_i$ as the zero[th] moment of the population of all living chains growing on catalyst type *i*,

$$\tilde{\tilde{Y}}_i = Y_i + \overline{Y}_i + \overline{\overline{Y}}_i \tag{3-75}$$

leads to a more compact representation of the population balance of linear macromonomers:

$$\frac{\mathrm{d}\mu_{i,r}}{\mathrm{d}t} = K_{t,i}^{=} P_{i,r} - (k_{b,i}\tilde{\tilde{Y}}_i + k_{b,j}\tilde{\tilde{Y}}_j)\ \mu_{i,r} \tag{3-76}$$

Substitution of Equation (3-76) into Equation (3-50) leads to the expression for the zero[th] moment of linear macromonomers:

$$\frac{\mathrm{d}\Theta_i}{\mathrm{d}t} = K_{t,i}^{=} Y_i - (k_{b,i}\tilde{\tilde{Y}}_i + k_{b,j}\tilde{\tilde{Y}}_j)\ \Theta_i \tag{3-77}$$

Similarly, substitution of Equation (3-76) into Equation (3-53) results in the expression for the first moment:

$$\frac{\mathrm{d}\Theta_i^I}{\mathrm{d}t} = K_{t,i}^{=} Y_i^I - (k_{b,i}\tilde{\tilde{Y}}_i + k_{b,j}\tilde{\tilde{Y}}_j)\ \Theta_i^I \tag{3-78}$$

Finally, combining Equations (3-76) and (3-56) leads to the expression for the second moment:

$$\frac{\mathrm{d}\Theta_i^{II}}{\mathrm{d}t} = K_{t,i}^{=} Y_i^{II} - (k_{b,i}\tilde{\tilde{Y}} + k_{b,j}\tilde{\tilde{Y}}_j)\ \Theta_i^{II} \tag{3-79}$$

The population balance for homogeneous-branched macromonomers is:

$$\frac{\mathrm{d}\overline{\mu}_{i,r}}{\mathrm{d}t} = K_{t,i}^{=} \overline{P}_{i,r} - (k_{b,i}\tilde{\tilde{Y}}_i + k_{b,j}\tilde{\tilde{Y}}_j)\overline{\mu}_{i,r} \tag{3-80}$$

Substituting Equation (3-80) into Equations (3-50), (3-53) and (3-56) leads to the expressions for the zero[th], first and second moments of homogeneous-branched macromonomers:

$$\frac{\mathrm{d}\overline{\Theta}_i}{\mathrm{d}t} = \overline{\overline{K}}_{t,i}\overline{Y}_i - (k_{b,i}\widetilde{Y}_i + k_{b,j}\widetilde{Y}_j)\,\overline{\Theta}_i \tag{3-81}$$

$$\frac{\mathrm{d}\overline{\Theta}_i^I}{\mathrm{d}t} = \overline{\overline{K}}_{t,i}\overline{Y}_i^I - (k_{b,i}\widetilde{Y}_i + k_{b,j}\widetilde{Y}_j)\,\overline{\Theta}_i^I \tag{3-82}$$

$$\frac{\mathrm{d}\overline{\Theta}_i^{II}}{\mathrm{d}t} = \overline{\overline{K}}_{t,i}\overline{Y}_i^{II} - (k_{b,i}\widetilde{Y}_i + k_{b,j}\widetilde{Y}_j)\,\overline{\Theta}_i^{II} \tag{3-83}$$

Similarly, the population balance for cross-product macromonomers is:

$$\frac{\mathrm{d}\overline{\overline{\mu}}_r}{\mathrm{d}t} = \overline{\overline{K}}_{t,i}\overline{\overline{P}}_{i,r} + \overline{\overline{K}}_{t,j}\overline{\overline{P}}_{j,r} - (k_{b,i}\widetilde{Y}_i + k_{b,j}\widetilde{Y}_j)\overline{\overline{\mu}}_r \tag{3-84}$$

Consequently, the equations for the zero[th], first, and second moments are:

$$\frac{\mathrm{d}\overline{\overline{\Theta}}}{\mathrm{d}t} = \overline{\overline{K}}_{t,i}\overline{\overline{Y}}_i + \overline{\overline{K}}_{t,j}\overline{\overline{Y}}_j - (k_{b,i}\widetilde{Y}_i + k_{b,j}\widetilde{Y}_j)\,\overline{\overline{\Theta}} \tag{3-85}$$

$$\frac{\mathrm{d}\overline{\overline{\Theta}}^I}{\mathrm{d}t} = \overline{\overline{K}}_{t,i}\overline{\overline{Y}}_i^I + \overline{\overline{K}}_{t,j}\overline{\overline{Y}}_j^I - (k_{b,i}\widetilde{Y}_i + k_{b,j}\widetilde{Y}_j)\,\overline{\overline{\Theta}}^I \tag{3-86}$$

$$\frac{\mathrm{d}\overline{\overline{\Theta}}^{II}}{\mathrm{d}t} = \overline{\overline{K}}_{t,i}\overline{\overline{Y}}_i^{II} + \overline{\overline{K}}_{t,j}\overline{\overline{Y}}_j^{II} - (k_{b,i}\widetilde{Y}_i + k_{b,j}\widetilde{Y}_j)\,\overline{\overline{\Theta}}^{II} \tag{3-87}$$

3.3.4 Moment Equations for Dead Chains

The derivation of population balance and moment equations for dead polymers follows the same approach used for the macromonomers. Only the final equations are shown below.

$$\frac{\mathrm{d}D_{i,r}}{\mathrm{d}t} = (K_{t,i}^s + k_{d,i})P_{i,r} \tag{3-88}$$

$$\frac{\mathrm{d}Q_i}{\mathrm{d}t} = (K_{t,i}^s + k_{d,i})Y_i \tag{3-89}$$

$$\frac{\mathrm{d}Q_i^I}{\mathrm{d}t} = (K_{t,i}^s + k_{d,i})Y_i^I \tag{3-90}$$

$$\frac{\mathrm{d}Q_i^{II}}{\mathrm{d}t} = (K_{t,i}^s + k_{d,i})Y_i^{II} \tag{3-91}$$

$$\frac{\mathrm{d}\overline{D}_{i,r}}{\mathrm{d}t} = (K_{t,i}^s + k_{d,i})\overline{P}_{i,r} \tag{3-92}$$

$$\frac{\mathrm{d}\overline{Q}_i}{\mathrm{d}t} = (K_{t,i}^s + k_{d,i})\,\overline{Y}_i \tag{3-93}$$

$$\frac{\mathrm{d}\overline{Q}_i^I}{\mathrm{d}t} = (K_{t,i}^s + k_{d,i})\,\overline{Y}_i^I \tag{3-94}$$

$$\frac{\mathrm{d}\overline{Q}_i^{II}}{\mathrm{d}t} = (K_{t,i}^s + k_{d,i})\,\overline{Y}_i^{II} \tag{3-95}$$

$$\frac{\mathrm{d}\overline{\overline{D}}_r}{\mathrm{d}t} = (K_{t,i}^s + k_{d,i})\,\overline{\overline{P}}_{i,r} + (K_{t,j}^s + k_{d,j})\,\overline{\overline{P}}_{j,r} \tag{3-96}$$

$$\frac{\mathrm{d}\overline{\overline{Q}}}{\mathrm{d}t} = (K_{t,i}^s + k_{d,i})\,\overline{\overline{Y}}_i + (K_{t,j}^s + k_{d,j})\,\overline{\overline{Y}}_j \tag{3-97}$$

$$\frac{\mathrm{d}\overline{\overline{Q}}^I}{\mathrm{d}t} = (K_{t,i}^s + k_{d,i})\,\overline{\overline{Y}}_i^I + (K_{t,j}^s + k_{d,j})\,\overline{\overline{Y}}_j^I \tag{3-98}$$

$$\frac{\mathrm{d}\overline{\overline{Q}}^{II}}{\mathrm{d}t} = (K_{t,i}^s + k_{d,i})\,\overline{\overline{Y}}_i^{II} + (K_{t,j}^s + k_{d,j})\,\overline{\overline{Y}}_j^{II} \tag{3-99}$$

3.3.5 Other Moment Equations and Molar Balances

The equation for the zero[th] moment of all living chains growing on catalyst type *i* is given by the expression:

$$\frac{\mathrm{d}\widetilde{Y}_i}{\mathrm{d}t} = k_{p,i}C_iM - (K_{t,i} + k_{d,i})\widetilde{Y}_i + k_{M,i}M\widetilde{Y} = k_{p,i}C_iM - \sigma_i\widetilde{Y}_i + k_{M,i}M\widetilde{Y}_i \tag{3-100}$$

The molar balance for catalytic active sites of type *i* is given by,

$$\frac{\mathrm{d}C_i}{\mathrm{d}t} = (k_{\beta,i} + K^s_{t.i})\tilde{Y}_i - (k_{p,i}M + k_{d,i})\,C_i \tag{3-101}$$

or,

$$\frac{\mathrm{d}C_i}{\mathrm{d}t} = (k_{\beta,i} + K^s_{t.i})(Y_i + \bar{Y}_i + \bar{\bar{Y}}_i) - (k_{p,i}M + k_{d,i})\,C_i \tag{3-102}$$

The molar balance for monomer is given by the expression,

$$\begin{aligned}\frac{\mathrm{d}M}{\mathrm{d}t} = {} & \frac{F_{M,in}}{v} - k_{p,i}C_i\,M - k_{p,j}C_j M - k_{p,i}M\sum_{i=1}^{\infty}P_{i,r} - k_{p,j}M\sum_{j=1}^{\infty}P_{j,r} \\ & - k_{p,i}M\sum_{i=2}^{\infty}\bar{P}_{i,r} - k_{p,j}M\sum_{j=2}^{\infty}\bar{P}_{j,r} - k_{p,i}M\sum_{i=2}^{\infty}\bar{\bar{P}}_{i,r} - k_{p,j}M\sum_{j=2}^{\infty}\bar{\bar{P}}_{j,r} - \\ & k_{M,i}M\sum_{i=1}^{\infty}P_{i,r} - k_{M,j}M\sum_{j=1}^{\infty}P_{j,r} - k_{M,i}M\sum_{i=2}^{\infty}\bar{P}_{i,r} - k_{M,j}M\sum_{j=2}^{\infty}\bar{P}_{j,r} - \\ & k_{M,i}M\sum_{i=2}^{\infty}\bar{\bar{P}}_{i,r} - k_{M,j}M\sum_{j=2}^{\infty}\bar{\bar{P}}_{j,r}\end{aligned} \tag{3-103}$$

where $F_{M,in}$ is the molar flow rate of monomer into the reactor and v is the reactor volume. The equation above can be expressed more compactly:

$$\begin{aligned}\frac{\mathrm{d}M}{\mathrm{d}t} = {} & -[k_{p,i}C_i + k_{p,j}C_j]M - k_{p,i}M\tilde{Y}_i - k_{p,j}M\tilde{Y}_j - k_{M,i}M\tilde{Y}_i \\ & - k_{M,j}M\tilde{Y}_j + \frac{F_{M,in}}{v}\end{aligned} \tag{3-104}$$

Since the monomer concentration is kept constant in the reactor, Equation (3-104) simplifies to:

$$M = \frac{\dfrac{F_{M,in}}{v}}{+[k_{p,i}C_i + k_{p,j}C_j] + k_{p,i}\tilde{Y}_i + k_{p,j}\tilde{Y}_j + k_{M,i}\tilde{Y}_i + k_{M,j}\tilde{Y}_j} \tag{3-105}$$

3.3.6 Chain Length Averages

Number and weight average Chain lengths, r_n and r_w , are given by the ratio of two moments. For living linear chains made on catalyst *i*:

$$r_n = \frac{Y_i^I}{Y_i} \tag{3-106}$$

$$r_w = \frac{Y_i^{II}}{Y_i^I} \tag{3-107}$$

$$pdi = \frac{r_w}{r_n} \tag{3-108}$$

Similar equations are used to calculate the chain length averages of other polymer populations present in the reactor.

3.3.7 Molar and Weight Percentages

Molar percentages are calculated from the zero[th] moments. For instance, the molar percentage of linear living chains made on catalyst *i* is given by:

$$n\ \% = \frac{Y_i}{\left(\begin{array}{l} Y_i + Y_j + \overline{Y}_i + \overline{Y}_j + \overline{\overline{Y}}_i + \overline{\overline{Y}}_j + \\ \Theta_i + \Theta_j + \overline{\Theta}_i + \overline{\Theta}_j + \overline{\overline{\Theta}}_i + \overline{\overline{\Theta}}_j + \\ Q_i + Q_j + \overline{Q}_i + \overline{Q}_j + \overline{\overline{Q}}_i + \overline{\overline{Q}}_j \end{array}\right)} \times 100\ \% \tag{3-109}$$

Similarly, weight percentages are calculated using the first moments:

$$w\ \% = \frac{Y_i^I}{\left(\begin{array}{l} Y_i^I + Y_j^I + \overline{Y}_i^I + \overline{Y}_j^I + \overline{\overline{Y}}_i^I + \overline{\overline{Y}}_j^I + \\ \Theta_i^I + \Theta_j^I + \overline{\Theta}_i^I + \overline{\Theta}_j^I + \overline{\overline{\Theta}}_i^I + \overline{\overline{\Theta}}_j^I + \\ Q_i^I + Q_j^I + \overline{Q}_i^I + \overline{Q}_j^I + \overline{\overline{Q}}_i^I + \overline{\overline{Q}}_j^I \end{array}\right)} \times 100\ \% \tag{3-110}$$

Analogous expressions are used to calculate the molar and weight percentages of the other polymer populations in the reactor.

3.3.8 Long Chain Branch Averages

The number of LCBs per 1000 C atoms, λ, is calculated with the expression:

$$\lambda = 500\,\frac{\int_0^t \text{rate of long chain branch formation. dt}}{\int_0^t \text{rate of polymerization. dt}} = 500\,\frac{\int_0^t (k_{b,1}\tilde{Y}_1 + k_{b,2}\tilde{Y}_2)\tilde{\Theta}dt}{\int_0^t (k_{p,1}\tilde{Y}_1 + k_{p,2}\tilde{Y}_2)Mdt} \qquad (3\text{-}111)$$

3.3.9 Solution of the Differential Equations

The Gear method was used to solve the simultaneous system of differential equations above which includes the zero[th], first and second moment equations of the linear, homogeneous-branched and cross-products of the living, macromonomer and dead chains to get the concentration of different populations versus time.

3.4 Results and Discussion

Our main objective with this model is to study how different catalyst combinations and polymerization conditions affect the microstructure of the TPEs produced with dual metallocenes. We divided our investigation into four case studies to investigate some of the most important parameters affecting these systems: 1) macromonomer formation rate; 2) LCB incorporation rate; 3) monomer concentration; and 4) catalyst deactivation. Each of these case studies will be discussed in detail below. All simulations were done for the simultaneous synthesis approach, but the model equations could be equally applied to the sequential method.

3.4.1 Case Study 1: Effect of the Rate of Macromonomer Formation

In Case Study 1, a system of two single-site catalysts, one linear (Catalyst 2, linear-catalyst) and the other capable of forming LCBs (Catalyst 1, LCB-catalyst), was studied while varying the macromonomer formation rate of the linear-catalyst by changing the parameter $k_{\beta,2}+k_{M,2}[M]$. Table 3-1 shows the initial conditions and typical reaction rate constants used in the simulations. As shown in Table 3-1, Catalyst 2 does not form LCBs since $k_{b,2} = 0$.

In Figures 3-3 to 3-8, the parameter *a* is the ratio $(k_{\beta,2}+k_{M,2}[M])/ (k_{\beta,1}+k_{M,1}[M])$, that is, the ratio between the rates of macromonomer formation of the linear catalyst and the LCB-catalyst.

Table 3-1. Initial conditions and reaction rate constants used for Case Study 1.

Rate constant	**Catalyst 1**	**Catalyst 2**	**Process Conditions**	
Propagation rate constant, k_p ($L \cdot mol^{-1} \cdot s^{-1}$)	5000	5000	Monomer concentration ($mol \cdot L^{-1}$)	0.5
Deactivation rate constant, k_d (s^{-1})	0.005	0.005	Polymerization time (s)	600
Transfer to monomer rate constant, k_M ($L \cdot mol^{-1} \cdot s^{-1}$)	0.4	0.4		
β-hydride elimination rate constant, k_β (s^{-1})	1	1		
β-methyl elimination rate constant, $k_{\beta\text{-}CH3}$ (s^{-1})	0	0		
LCB rate constant, k_b ($L \cdot mol^{-1} \cdot s^{-1}$)	400	0		

Figures 3-3 and 3-4 show that increasing the value of $k_{\beta,2}+k_{M,2}[M]$ (increasing a) of the linear-catalyst results in more cross-products and shifts the locus of the catalyst ratio corresponding to the maximum cross-product fraction. This behavior is expected, since an increase in the concentration of macromonomers made by the linear-catalyst will favor the incorporation of these macromonomers by the LCB-catalyst, thus increasing the molar and mass fractions of cross-product. We also notice that the mass fraction of cross-product is higher than its molar fraction since the cross-product is formed by LCB-chains that have, in average, higher weights than linear and homogeneously-branched chains.

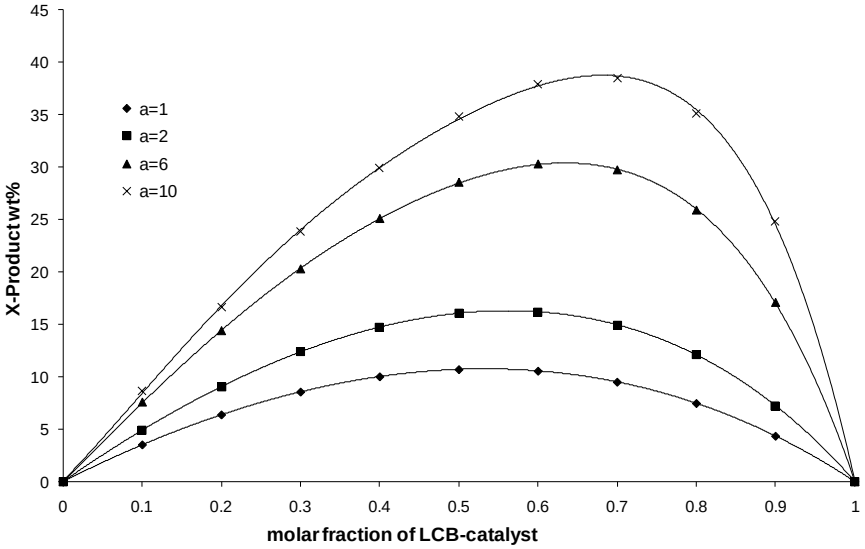

Figure 3-3. Effect of the rate of macromonomer formation of the linear-catalyst on the cross-product weight percent as a function of molar fraction of the LCB-catalyst. In Figures 3-3 to 3-14, the parameter a is the ratio $(k_{\beta,2}+k_{M,2}[M])/ (k_{\beta,1}+k_{M,1}[M])$.

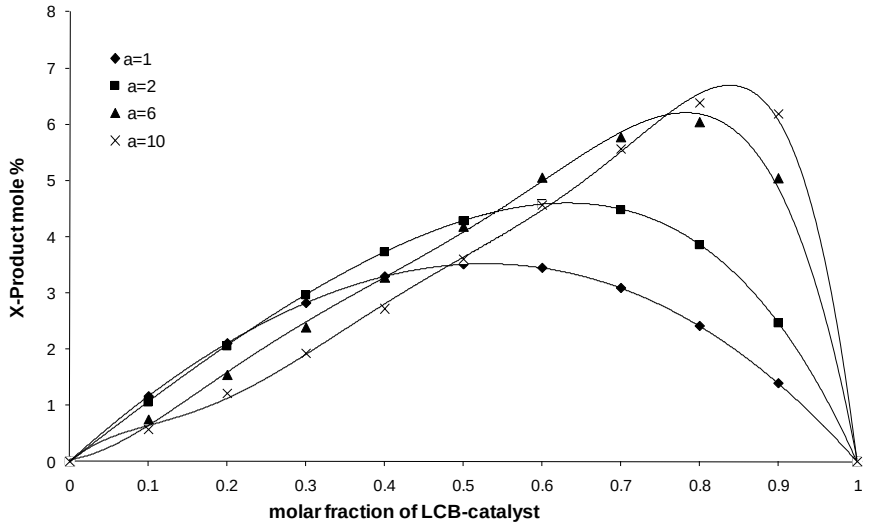

Figure 3-4. Effect of the rate of macromonomer formation of the linear-catalyst on the mole percent of cross-product as a function of the molar fraction of the LCB-catalyst.

Figure 3-5 shows that the LCB density, λ, also passes through a maximum by varying the catalyst ratio but, differently from Figures 3-3 and 3-4, this maximum always occurs at the same catalyst ratio.

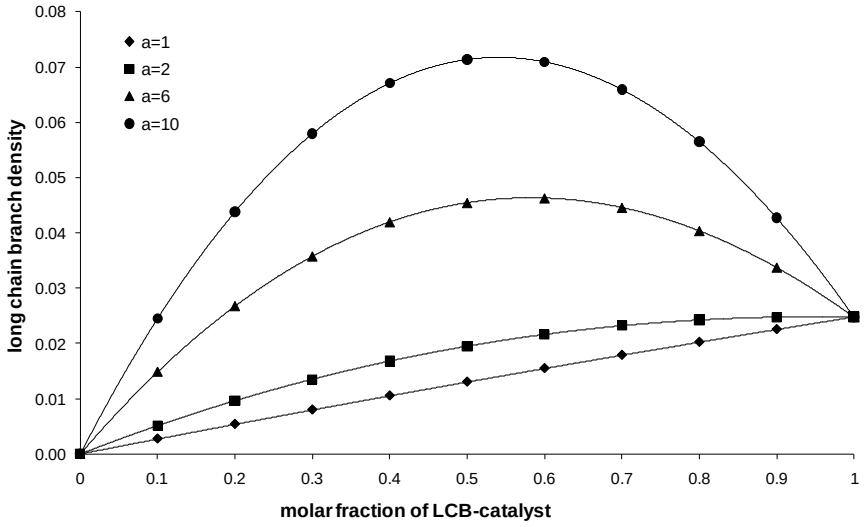

Figure 3-5. Effect of the rate of macromonomer formation of the linear catalyst on the LCB density as a function of the molar fraction of the LCB-catalyst.

The polydispersity index increases as the value of $k_{\beta,2}+k_{M,2}[M]$ for the linear-catalyst increases, as illustrated in Figure 3-6; since the linear-catalyst makes smaller and smaller chains as $k_{\beta,2}+k_{M,2}[M]$ increases, the overall chain length distribution must necessarily broaden as indicated in the simulation results.

Similarly, as the linear catalyst makes more macromonomer, the number and weight average chain lengths decreases, as depicted in Figures 3-7 and 3-8. A very interesting behavior and, to our knowledge, unreported thus far, is that a linear relationship is observed for the weight average chain length of the overall polymer as a function of the fraction of LCB-catalyst in the reactor. Curiously, this seems to be a general property of these dual-catalyst systems, as it was observed in all simulations described in this chapter.

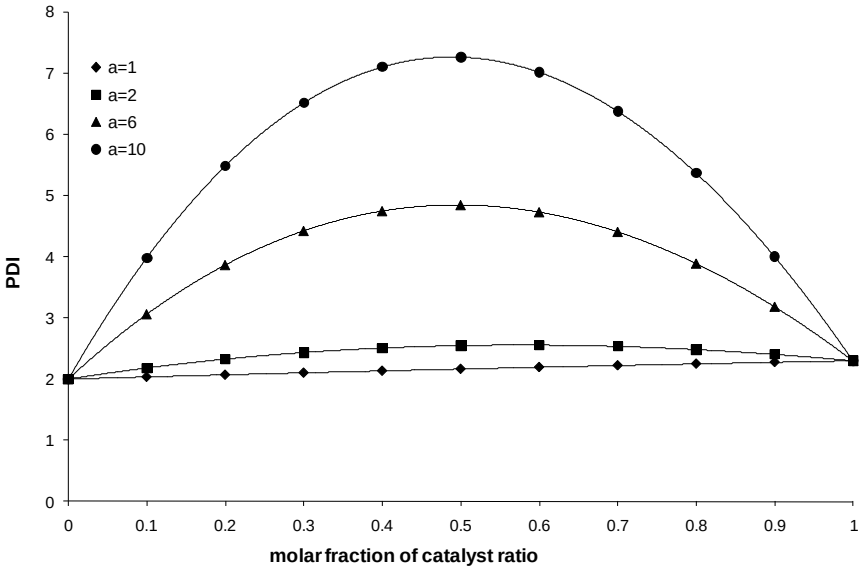

Figure 3-6. Effect of the rate of macromonomer formation of the linear catalyst on polydispersity index as a function of the molar fraction of the LCB-catalyst.

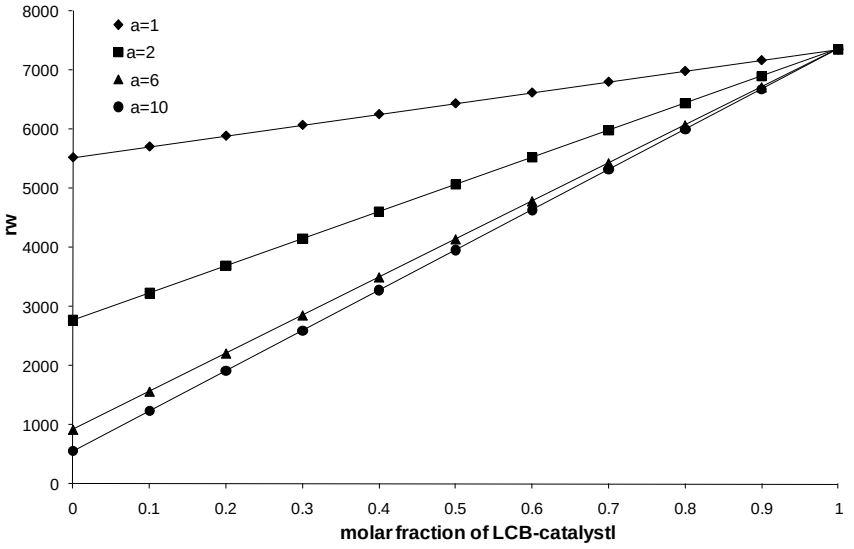

Figure 3-7. Effect of the rate of macromonomer formation of the linear catalyst on the weight average chain length as a function of the molar fraction of LCB-catalyst.

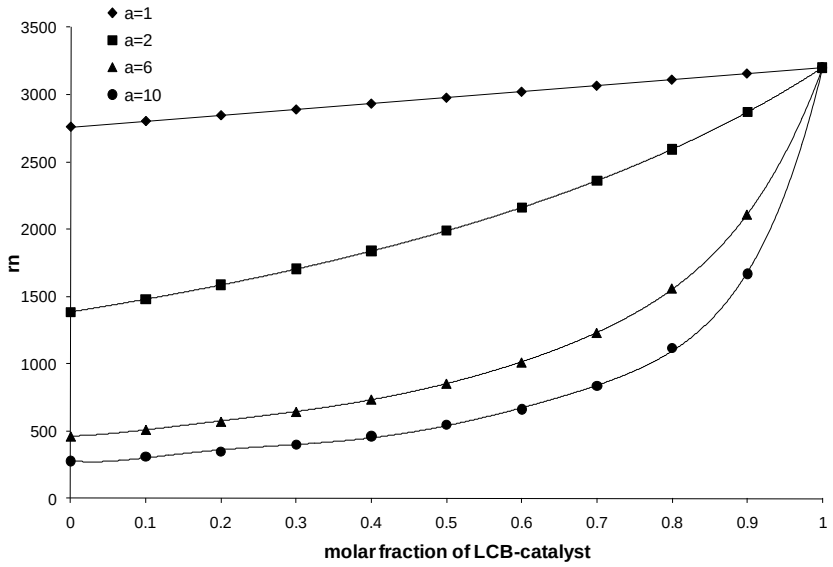

Figure 3-8. Effect of the rate of macromonomer formation of the linear catalyst on the number average chain length as a function of the molar fraction of LCB-catalyst.

The results shown in Figures 3-3 to 3-8 clearly indicate that the selection of the linear-catalyst, guided by its ability to produce macromonomers, is a very important step when designing the microstructure of TPEs made with dual metallocenes, since this property will have a significant effect on the fraction of each polymer population, as well as in their chain length averages and LCB densities.

3.4.2 Case Study 2: Effect of the Rate of LCB formation of Catalyst 2 ("Linear"-Catalyst)

In Case Study 2, the value of the LCB formation rate constant ($k_{b,2}$) for the linear-catalyst fed to the reactor was increased from 0 to 400; therefore, the "linear"-catalyst becomes a LCB-catalyst (as effective as Catalyst 1) and we will call it simply Catalyst 2 in Case Study 2. All other parameters used in the simulations were the same as those for Case Study 1. We superimposed the simulation results from Case Study 1 (solid lines), to the results from Case Study 2 (dashed lines) in Figures 3-9 to 3-14 to show the effect on the polymer microstructure when $k_{b,2}$ is changed from 0 to 400 $L \cdot mol \cdot^{-1} s^{-1}$.

Figure 3-9 shows that, as $k_{b,2}$ increases, the weight percent of cross-product increases because Catalyst 2 now incorporates macromonomers made by Catalyst 1 and can also make cross-product chains. In addition, as $k_{b,2}$ increases, the locus for the maximum of cross-product fraction increases

towards catalyst mixtures richer in Catalyst 1. A similar trend is observed for the mole percent of the cross-product (Figure 3-10).

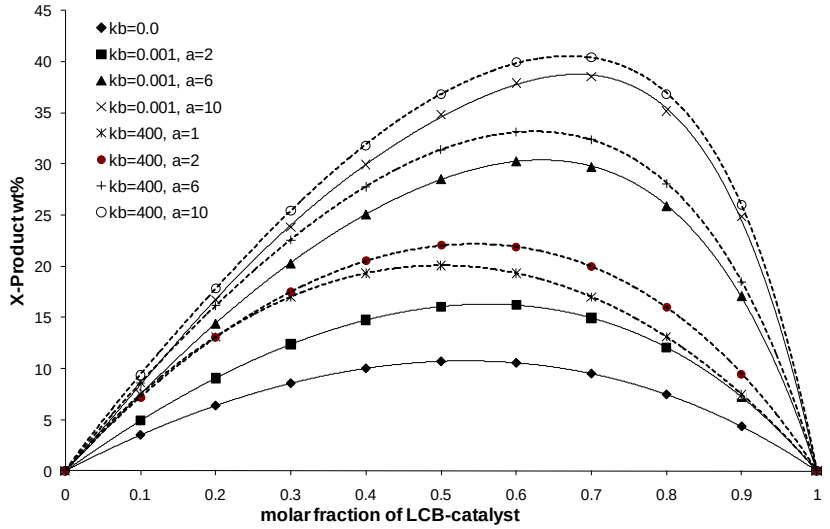

Figure 3-9. Effect of the rate of LCB formation by Catalyst 2 on the weight percent of cross-product as a function of the molar fraction of the LCB-catalyst. In Figures 3- 9 to 3-14, the dashed and solid curves are simulation results for Case Study 2 and 1, respectively.

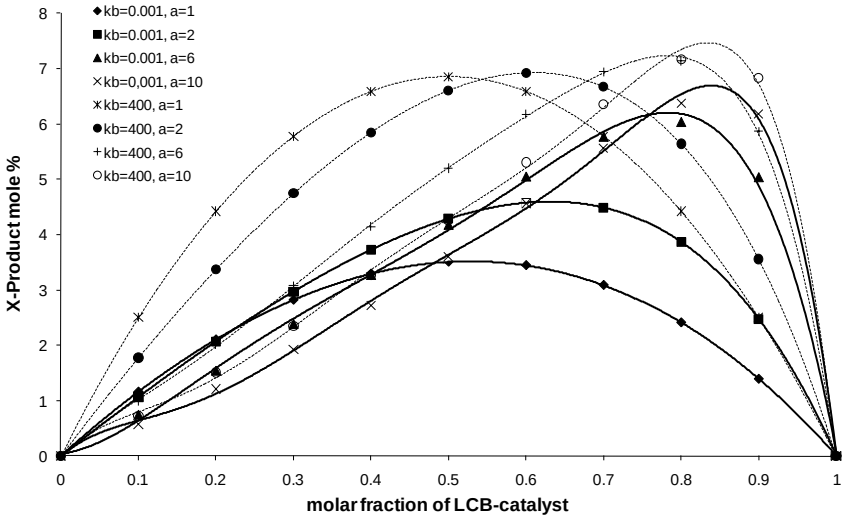

Figure 3-10. Effect of the rate of LCB formation by Catalyst 2 on the mole percent of cross-product as a function of the molar fraction of the LCB-catalyst.

Figure 3-11 shows a behavior that departs markedly from that observed in Case Study 1, when Catalyst 2 only produced linear chains: in the former case study, λ passed through a maximum for a given catalyst ratio, but now we observe a linear relationship between λ and catalyst ratio. Both catalysts have the same LCB-forming rate constant ($k_{b,1}=k_{b,2}$); therefore, when they produce the same amount of macromonomer (that is, $k_{\beta,1} + k_{m,1}[M] = k_{\beta,2} + k_{m,2}[M]$), λ is unaffected by the catalyst ratio (the catalysts are, from a modeling point of view, the same). However, as Catalyst 2 starts making more macromonomer, that is $k_{\beta,2} + k_{m,2}[M] > k_{\beta,1} + k_{m,1}[M]$, it is always more advantageous to have only Catalyst 2 in the reactor if our only objective it to maximize λ. Adding Catalyst 1 will only reduce the overall LCB density. Of course, this conclusion is not valid if the objective it to maximize the fraction of cross-product.

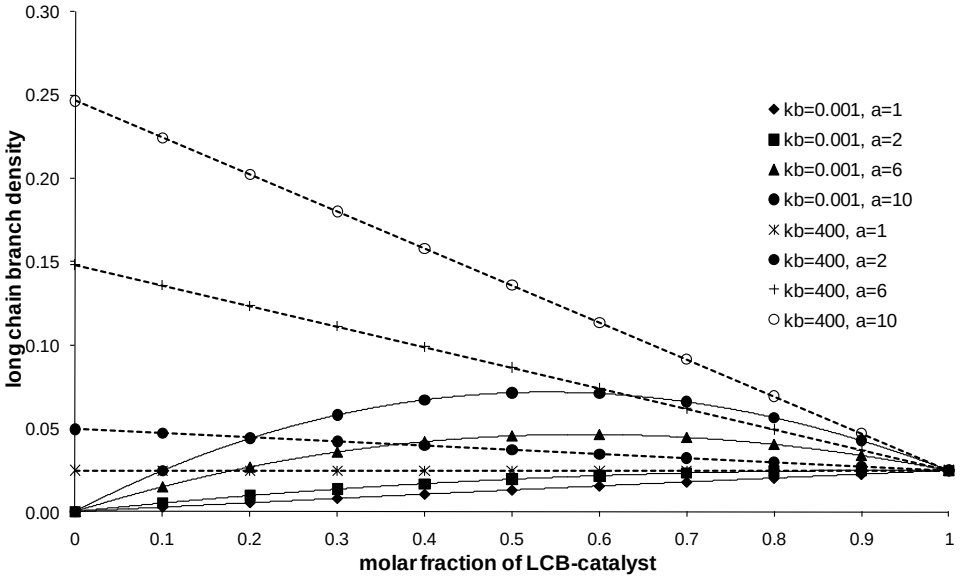

Figure 3-11. Effect of the rate of LCB formation by Catalyst 2 on the LCB density as a function of molar fraction of LCB-catalyst.

Figure 3-12 shows how the polydispersity index reaches a maximum for a catalyst ratio of 0.5, which is a rather usual feature in dual single-site catalyst systems if propagation rate are the same. Polydispersity indexes will be slightly lower when both catalysts form LCB-chains, due to the intrinsic chain-length averaging trends of LCB formation through terminal branching.

Finally, Figures 3-13 and 3-14 show how the average chain lengths are affected by the simulation parameters. We notice again the surprising linear relation between the weight average chain length and catalyst ratio, even in this case study when both catalyst are capable of forming LCBs.

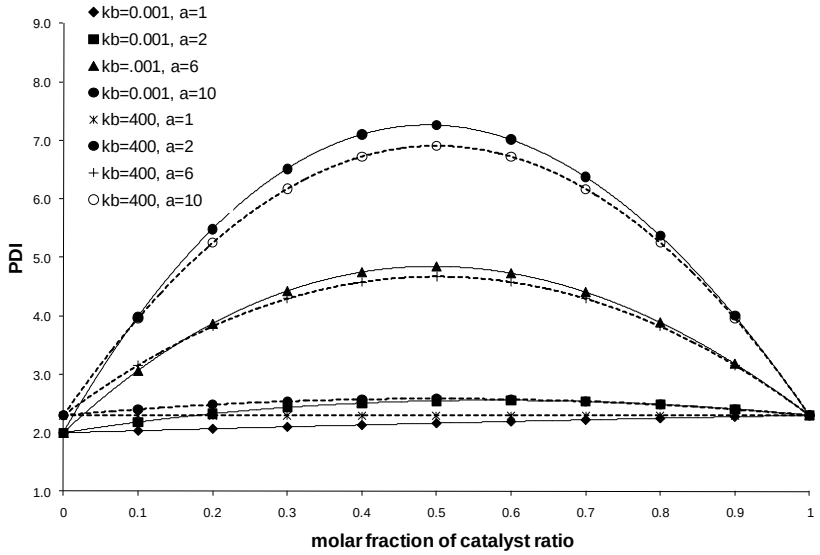

Figure 3-12. Effect of the rate of LCB formation by Catalyst 2 on the polydispersity index as a function of molar fraction of LCB-catalyst.

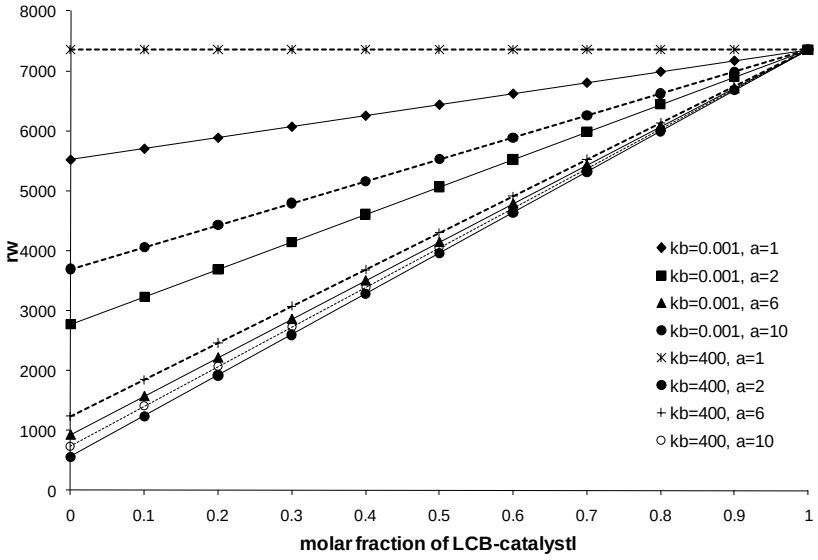

Figure 3-13. Effect of the rate of LCB formation by Catalyst 2 on the weight average chain length as a function of the molar fraction of the LCB-catalyst.

A few observations are worth summarizing at this point: 1) When Catalyst 2 is also a LCB-forming catalyst, the molar and weight fractions of cross-products increase (Figures 3-9 and 3-10); 2) No maximum is observed in the LCB density curve when both catalysts can form LCBs at the same rate (Figure 3-11); 3) The general trends for number and weight average chain lengths are the same when Catalyst 2 makes only linear chains or when it is also capable of making LCB-chains (Figures 3-13 and 3-14).

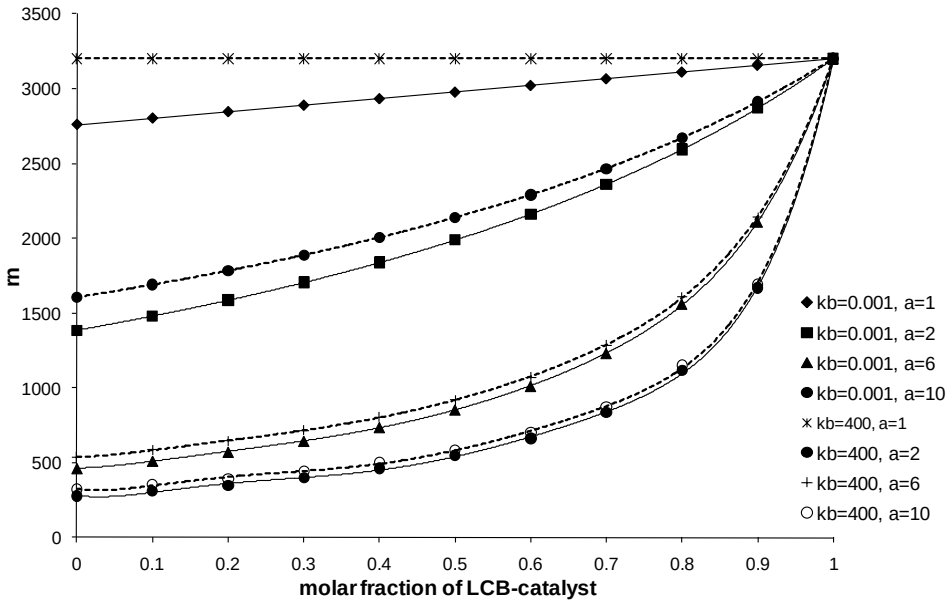

Figure 3-14. Effect of the rate of LCB formation by Catalyst 2 on the number average chain length as a function of the molar fraction of the LCB-catalyst.

3.4.3 Case Study 3: Effect of Monomer Concentration

In Case Study 3, we investigated the effect of monomer concentration on polymer properties. In this case study, Catalyst 2 is once more a linear-catalyst ($k_{b,2}$ = 0) and cannot incorporate macromonomers. Initial conditions and parameters used for simulation in this case are the same as before, except that the transfer rate constants for Catalyst 2 are six times higher than for Catalyst 1, as given in Table 3-2. Four monomer concentrations, 0.25, 0.5, 2 and 4 mol·L^{-1} were studied.

Table 3-2. Transfer reactions rate constants for Case Study 3.

	Catalyst 1	**Catalyst 2**
Transfer to monomer rate constant	0.4	2.4
β-hydride elimination rate constant	1	6

Figures 3-15 and 3-16 show that monomer concentration does not influence the fraction of cross-product, since monomer concentration neither affects the rate of macromonomer formation, nor the rate of macromonomer incorporation by Catalyst 1. Inspection of Figure 3-17 also shows that the polydispersity index is not altered by monomer concentration.

On the other hand, the LCB density increases as monomer concentration decreases, as illustrated in Figure 3-18, since LCB formation is a competitive mechanism between macromonomer and monomer insertion.

Weight average chain length also changes with monomer concentration, as shown in Figure 3-19; we notice again the intriguing linear relationship between weight average chain length and catalyst ratio.

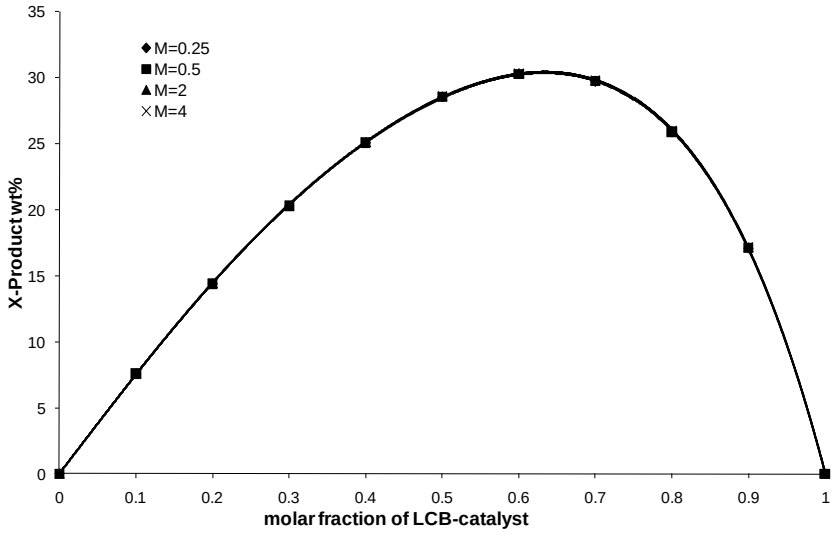

Figure 3-15. Effect of monomer concentration on the weight percent of cross-product as a function of the molar fraction of the LCB-catalyst. In Figures 3-15 to 3-19, monomer concentration is given in mol·L-1.

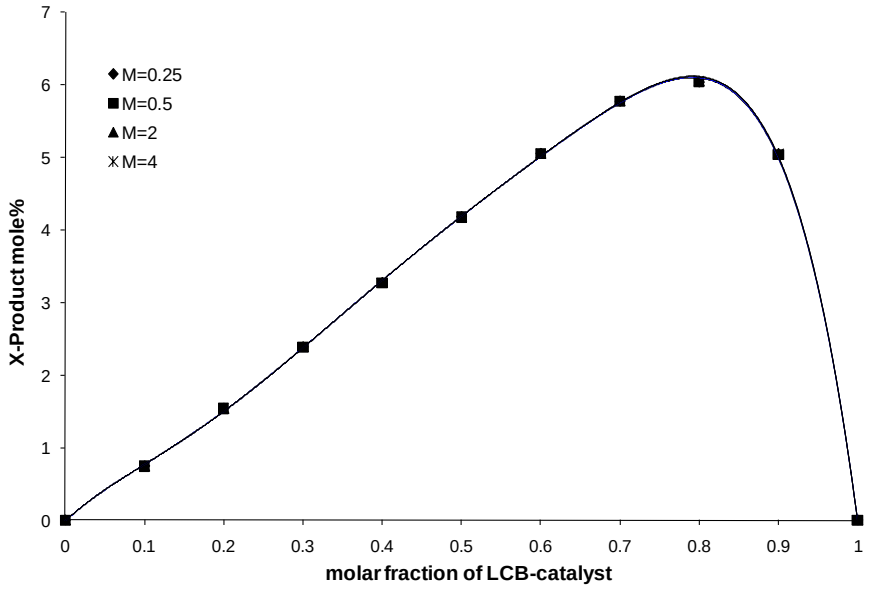

Figure 3-16. Effect of monomer concentration on the mole percent of cross-product as a function of the molar fraction of the LCB LCB-catalyst.

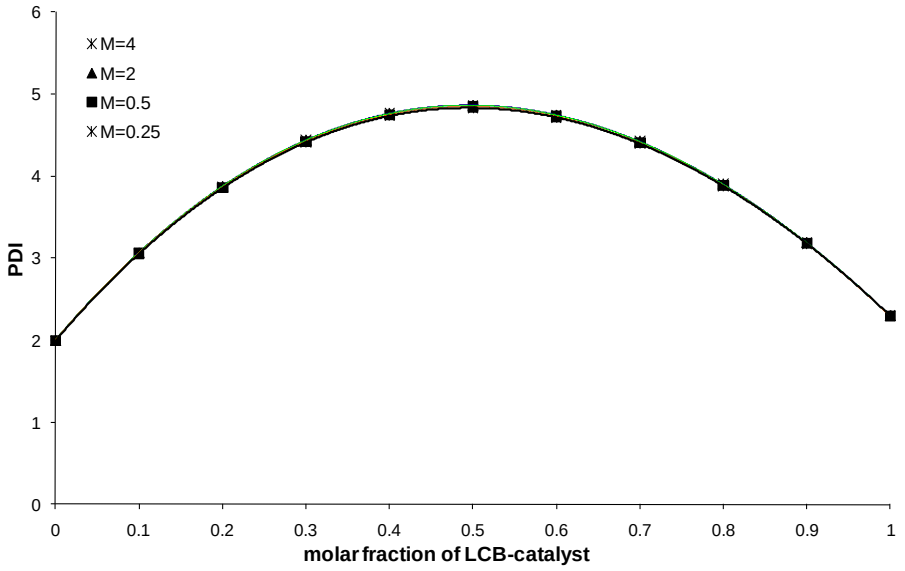

Figure 3-17. Effect of monomer concentration on the polydispersity index as a function of the molar fraction of the LCB-catalyst.

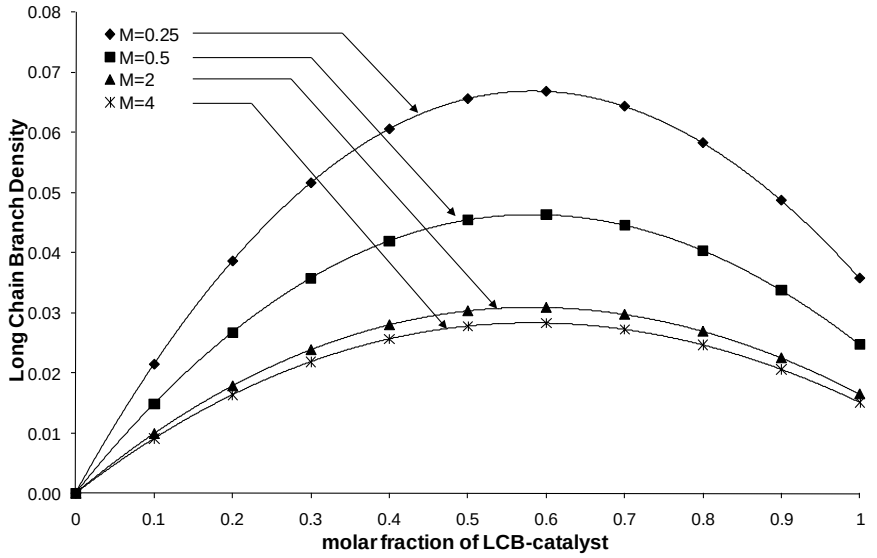

Figure 3-18. Effect of monomer concentration on the LCB density as a function of the molar fraction of the LCB-catalyst.

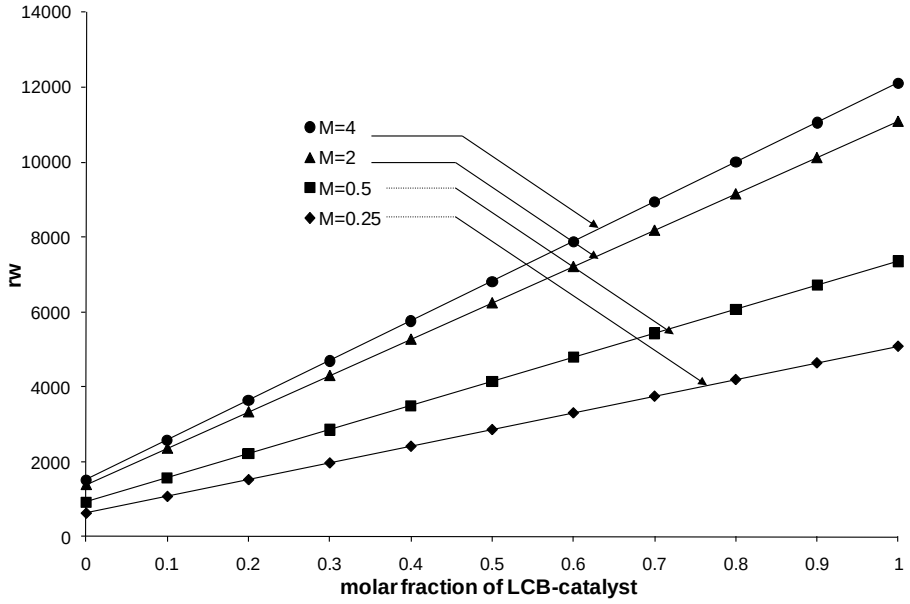

Figure 3-19. Effect of monomer concentration on the weight average chain length as a function of the molar fraction of the LCB-catalyst.

3.4.4 Case Study 4: Effect of Catalyst Deactivation

Finally, Case Study 4 analyzes the effect of catalyst deactivation by varying the deactivation rate constant of both catalysts, $k_{d,i}$, simultaneously. Higher deactivation rates will lead to lower concentrations of macromonomer, living and dead chains in the reactor. The immediate effect is a decrease in the production of LCB-species, either homogeneous-branched or cross-product and, consequently, a decrease in chain length averages. Accordingly, we notice that, with increasing catalyst deactivation rates: the weight fractions of the cross-product decrease (Figure 3-20); the LCB density decreases (Figure 3-21); and the polydispersity and chain length averages decreases (Figures 3-22 and 3-23).

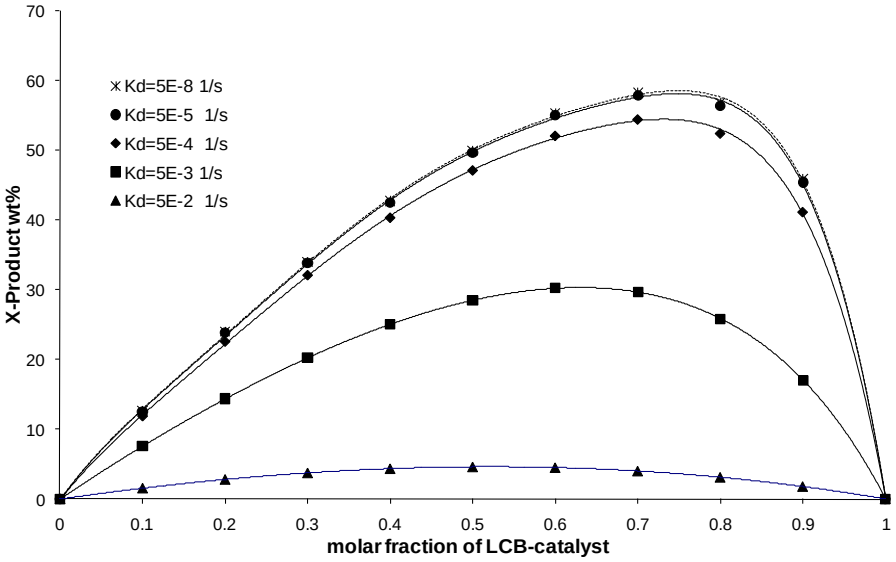

Figure 3-20. Effect of catalyst deactivation on weight percent of cross-product as a function of the molar fraction of the LCB-catalyst.

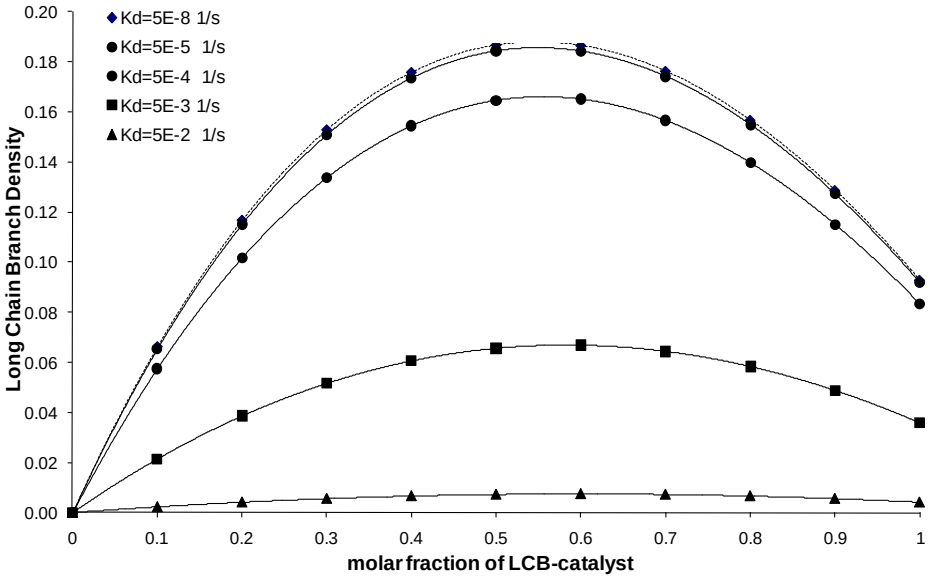

Figure 3-21. Effect of catalyst deactivation on long chain branch density as a function of the molar fraction of the LCB-catalyst.

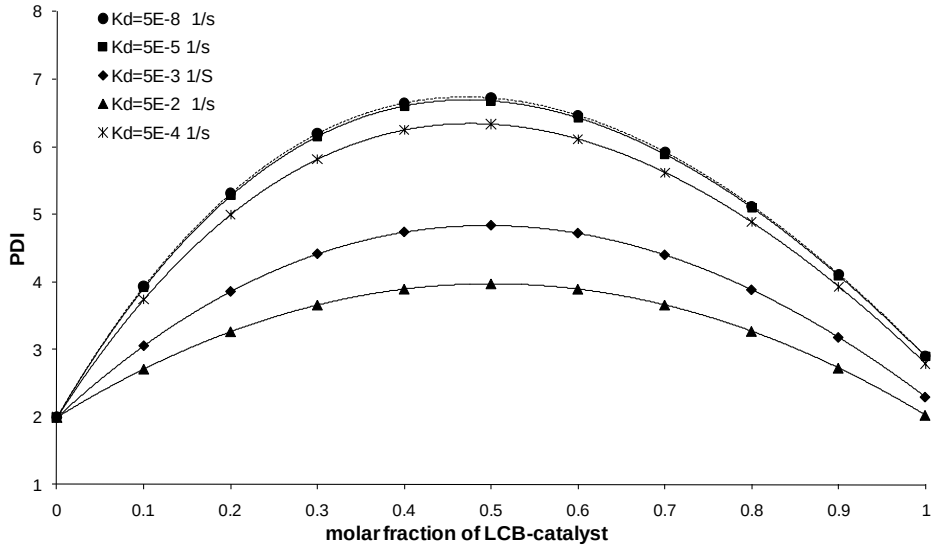

Figure 3-22. Effect of catalyst deactivation on polydispersity index as a function of the molar fraction of the LCB-catalyst.

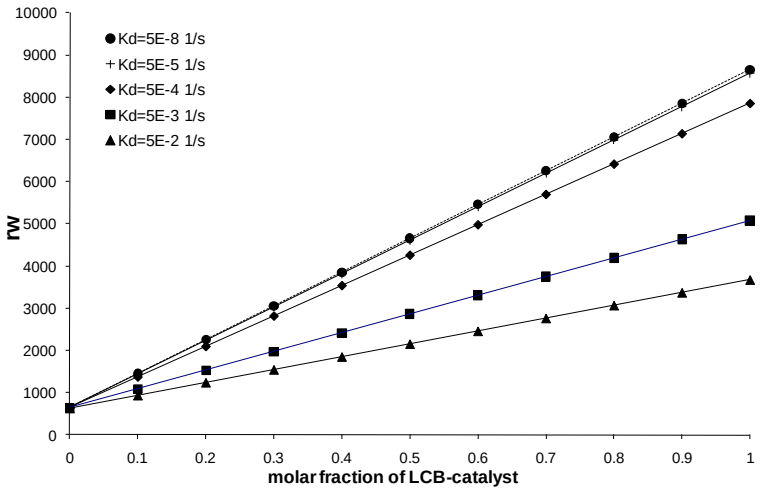

Figure 3-23. Effect of catalyst deactivation on the weight average chain length as a function of the molar fraction of the LCB-catalyst.

3.5 Concluding Remarks

We have developed a mathematical model that can describe the microstructure of polyolefins with LCBs made with two metallocenes in a semi-batch reactor. In one of its applications, these dual-metallocene systems are used to produce olefinic TPEs. The model can predict the fractions of different polymer populations in the reactor as well as their average chain lengths and branching densities.

Simulation results show that to increase the weight percent of cross-product using a linear-catalyst and a LCB-catalyst, the rate of macromonomer formation of the linear-catalyst should be high. The fraction of cross-product can be increased even further when both catalysts are capable of incorporating macromonomers to form LCB-chains because, in this case, both catalysts can form cross-product chains.

Monomer concentration has no effect on cross-product fraction and polydispersity index, but increasing monomer concentration will decrease LCB density and increase the average chain lengths.

Catalyst deactivation also has a great impact on polymer properties: LCB density, polydispersity index, cross-product fraction, and average chain lengths will all decrease by increasing the catalyst deactivation rate of both catalysts.

Finally, an intriguing linear relationship between weight average chain length and LCB-catalyst fraction appears in all simulations done in this investigation.

Chapter 4

Production of Long Chain Branched Polyolefins with Two Single-Site Catalysts: Comparing CSTR and Semi-Batch Performance

4.1 Summary

We developed a mathematical model to describe the solution polymerization of olefins with two single-site catalysts in a series of two continuous stirred-tank reactors (CSTRs). The model was used to simulate processes where semicrystalline macromonomers produced in the first reactor are incorporated as long chain branches (LCBs) onto amorphous (or lower crystallinity) chains in the second reactor (cross-products). The simulation results show that CSTRs are more efficient to make chains with high LCB density and high weight percent of cross-products. The model can also predict the polydispersity index, average chain lengths, and fractions of the different polymer populations, and help the polymer reactor engineer formulate new products with complex microstructures.

4.2 Introduction

The polyolefins demand comprises two-thirds of the total demand for thermoplastics which was over 110 million metric tons in 2007[118] with the low cost of raw materials as being the main reason for their high demand. The same reason and the potential of metallocene catalysts to make polymers with tailored microstructures have attracted industry to invest on research for production of differentiated commodity polyolefins, specialty polyolefins, and polyolefin hybrids. What make these new polyolefin types different from commodity polyolefins are their much more complex molecular architectures which often contain long chain branches (LCBs). This is an exciting new research area because it promises to open new markets for polyolefins that have been restricted to other polymers.

One approach to produce these novel polyolefins is to use one or two single-site catalysts in two CSTRs in series. The first CSTR is used to make semicrystalline polymer chains, some of which must be vinyl-terminated (macromonomers). These macromonomers are then incorporated, via terminal branching, onto the chains growing in the second CSTR, becoming LCBs. If the backbone and the macromonomer have different compositions, we call these chains cross-products. Since it is not possible to incorporate all macromonomers, the final polymer will consist of a complex mixture of linear chains made by the two catalysts, homogeneous-branched chains (that is, chains where the

backbone and all LCBs are of the same type), and cross-products. The cross-product will add rather special properties to the polymer and, depending on its molecular architecture, it may act as a viscosity modifier, a thermoplastic elastomer (TPE), or a polymer blend compatibilizer, as illustrated in Figure 4-1.[119] It is important to keep in mind that the structures shown in Figure 4-1 represent only typical cross-product structures and that, in reality, the cross-products are composed of a distribution of chains with different molecular weights and branching frequencies.

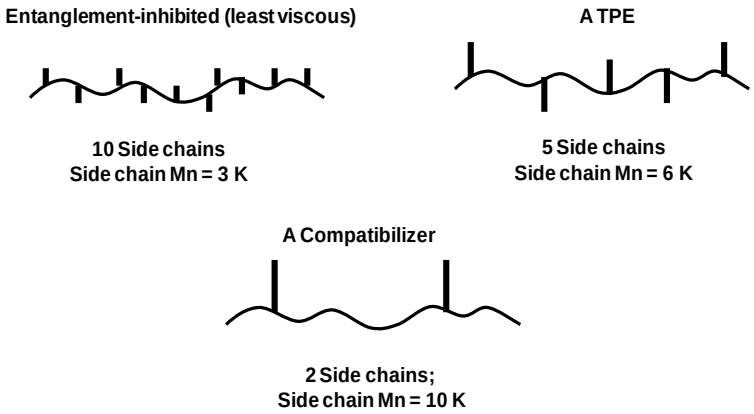

Figure 4-1. Shape-functionality schematic for cross-product structures

Thermoplastic elastomers constitute a commercially relevant class of polymeric materials that combines some of the advantages of thermoplastic polymers and thermoset elastomers. Thermoplastic polymers soften and can be made to flow when they are heated, but harden upon cooling. This heating and cooling cycle can usually be repeated many times without significant degradation if the polymer is properly compounded with stabilizers.[9, 107] Block polyolefin TPEs can be prepared through non-living alkene polymerization catalysts such as Ziegler-Natta catalyst,[120] asymmetric metallocenes,[121] oscillating metallocenes[122] or employing living catalysts and changing the monomer or reaction conditions during chain formation to control block formation.[123]An interesting block polyolefin, composed of blocks of isotactic and atactic stereosequences, is derived from propylene alone.[108] The elastic properties of elastomeric polypropylene are believed to arise from their stereo-block (isotactic-atactic) microstructure that allows the formation of short crystallizable isotactic blocks in a low-tacticity polymer chain.[109-110, 112, 120]

An isotactic/atactic catalyst pair, acting on a propylene-only feed, would produce a reactor product comprising isotactic and atactic linear polypropylene chains, homogeneous-branched isotactic and atactic chains, and cross-product chains such as aPP-*g*-iPP and linear diblock copolymers consisting

of an amorphous backbone with terminal isotactic polypropylene LCB (Figure 3-1). Another interesting catalyst pair consists of one catalyst with high and the other with low comonomer incorporation ratios acting on a mixture of ethylene and α-olefin to produce a reactor product in which amorphous blocks (with high α-olefin fraction) and macromonomer-derived crystalline LCBs (with low α-olefin fraction) are coupled in unique ways to make cross-products among other reactor components. Depending on the compositional details and the amount of such cross-product, these materials may exhibit characteristics of a TPE, as illustrated in Figure 4-1.[85, 113-114]

Two procedures can be used for the synthesis of these materials: simultaneous or sequential synthesis.[115] In the simultaneous synthesis method, two different catalysts are added to the reactor at the beginning of the polymerization. One catalyst, such as rac-dimethylsilanediylbis(2-methyl-4-phenylindenyl)zirconium dichloride,[44] produces isotactic polypropylene macromonomers, while the other, such as a constrained geometry catalyst, produces atactic polypropylene chains and incorporates the macromonomer. Due to macromonomer incorporating ability of this catalyst, cross-product chains are formed in addition to linear chains and homogeneous-branched chains.

In the sequential synthesis procedure, isotactic polypropylene macromonomers are first produced in the polymerization reactor. These macromonomers are then incorporated onto atactic polypropylene chains by injecting a non-stereospecific catalyst capable of forming LCBs in the reactor.

Developing polymer reactor models for different catalyst combinations can help understand the details of these complex syntheses and to control the properties and fractions of linear chains, homogeneous-branched chains, and cross-products. Recently we developed a mathematical model,[116] for semi-batch polymerization reactors under constant olefin pressure to explain how different catalyst combinations and polymerization conditions affect the molecular properties and fractions of the different populations. In the present article, we extended our model to simulate the solution polymerization of olefins with two single-site catalysts in a series of two continuous stirred-tank reactors (CSTR) operated at steady state. This model is essential for the scale-up of laboratory semi-batch reactors, to industrial scale CSTRs used in the polyolefin industry.

This Chapter with some modification has been published in the Journal Macromolecular Reaction Engineering.[124]

4.3 Model Development

Our model describes the solution polymerization of olefins in a series of two CSTRs operated at steady state using two single-site catalysts (Figure 4-2). The following notation was used to represent the relevant parameters in Figure 4-2: $F_{M,in,1}$ and $F_{M,out,1}$ are molar flow rates of monomer entering and leaving CSTR 1, respectively; $F_{M,in,2}$ and $F_{M,out,2}$ are the respective values for CSTR 2. Parameters $\lambda_{overall,out,1}$ and $\lambda_{overall,out,2}$ are the LCB density (number of branch points per 1000 carbon atoms) for the polymer exiting CSTR 1 and CSTR 2 . The volumes of CSTR 1 and CSTR 2 are represented by v_1 and v_2, respectively, and were assumed to be the same with no change in the volume of the reaction mixtures during the polymerization. C_1^{in}, C_2^{in} *are* molar flow rates of catalysts 1 and 2 per unit volume of the reactor. The volumetric flow rates entering and leaving CSTR 1 are denoted by $\dot{\upsilon}_{in,1}$ and $\dot{\upsilon}_{out,1}$ and for CSTR 2 by $\dot{\upsilon}_{in,2}$ and $\dot{\upsilon}_{out,2}$.

Population balances and the method of moments were used to calculate microstructural properties of macromonomers, living and dead chains. Each of these populations was subdivided into linear, homogeneous-branched, and cross-product chains. In homogeneous-branched chains, all LCBs and the backbone are made by the same catalyst. In cross-product chains, at least one of the LCBs and/or the backbone is made on a different catalyst from that used to make the other segments. Figure 4-3 illustrates this classification.

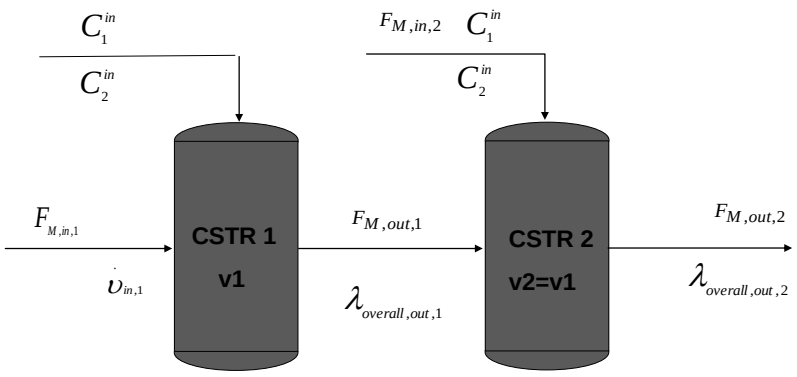

Figure 4-2. Two CSTRs in series.

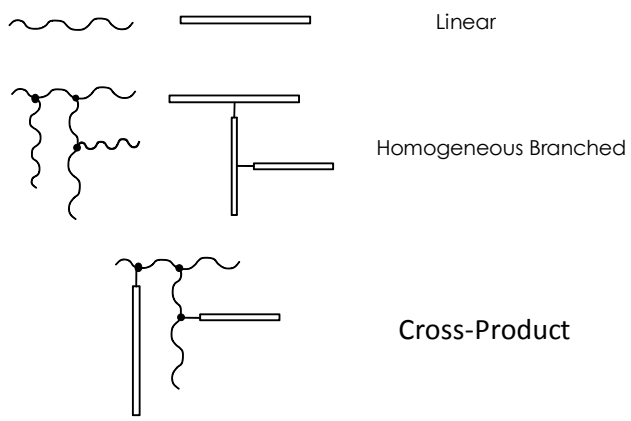

Figure 4-3. Chain classification used in the model.

The model can predict the following properties for each of the polymer populations: molar (*n*%) and weight (*w*%) percentages, number (r_n) and weight (r_w) average chain lengths, and average LCB per 1000 C atoms (λ) and per chain (B_n).

4.3.1 Polymerization Mechanism

The polymerization mechanism assumed to develop the rate equations for different chain populations is exactly the same one used in Chapter 3. The convention adopted to represent the different chain populations in the model is also the same as one used in Chapter 3. (see Section 3.3.1).

Population balances and moment equations for the polymerization mechanism described by Equations (3-1) to (3-38) are presented in Appendix A for the first CSTR (CSTR 1). The steady-state solution of the moment equations derived in Appendix A is discussed in Appendix B. Appendix C lists the model equations for the second CSTR in series. Appendix D lists equations to calculate chain length averages and LCB frequencies in the CSTR 1 and fractions of the different polymer populations in both CSTRs. Finally, Appendix E shows the equations used to calculate LCB averages in CSTR 2.

4.4 Results and Discussion

We used our model to study how different catalyst combinations and polymerization conditions affect the microstructure of the polymers produced with dual metallocenes. We divided our investigation into four case studies: 1) Comparison of CSTR and semi-batch reactor operation; 2) Effect of

residence time in CSTR 2; 3) Effect of the LCB formation rate constant ($k_{b,1}$) for the catalyst fed to CSTR 2; and 4) Catalyst feeding policy.

Each of these case studies will be discussed in detail below.

4.4.1 Case Study 1: Comparing a CSTR versus a Semi-Batch Reactor

In Case Study 1 we compared the simulation results for one CSTR and one semi-batch reactor (simultaneous synthesis method). The methodology used to simulate semi-batch reactors was presented in Chapter 3 and published in an article.[116]

A system of two single-site catalysts, one linear (catalyst 2, a catalyst with very low macromonomer incorporation rate) and one capable of forming LCBs (catalyst 1), was investigated while varying the macromonomer formation rate of the linear-catalyst by changing the value of the parameter $k_{\beta,2}+k_{M,2}[M]$. It should be mentioned that we kept $k_{\beta,1}+k_{M,1}[M]$ constant. The two catalysts fed simultaneously to the CSTR and the semi-batch reactor. Table 4-1 lists the process conditions and reaction rate constants used in the simulations. As shown in Table 4-1, catalyst 2 does not form appreciable amount of LCBs since $k_{b,2} = 0.001$ is so small compared to $k_{b,1} = 400$.

Table 4-1. Process conditions and reaction rate constants used in Case Study 1.

Rate constants	Units	Catalyst 1	Catalyst 2	Process Conditions	
Propagation, k_p	$L\cdot mol^{-1}\cdot s^{-1}$	5000	5000	Monomer concentration	0.5 $mol\cdot L^{-1}$
Deactivation, k_d	s^{-1}	0.005	0.005	Polymerization time	600 s
Transfer-to-monomer, k_M	$L\cdot mol^{-1}\cdot s^{-1}$	0.4	0.4		
β-hydride elimination, k_β	s^{-1}	1	1		
β-methyl elimination, $k_{\beta\text{-}CH3}$	s^{-1}	0	0		
LCB formation, k_b	$L\cdot mol^{-1}\cdot s^{-1}$	400	0.001		

The catalyst molar flow rate per CSTR volume for simulations was adjusted such that the amount of catalyst fed into the CSTR over one average reactor residence time, was equal to the initial amount of catalyst in the semi-batch reactor. For example, if the initial concentration of one of the catalysts in the semi-batch reactor was 2×10^{-6} mol/L and the polymerization time was 600 s, the catalyst molar flow rate per unit volume to the CSTR was calculated as $\frac{2\times10^{-6}\,\text{mol/L}}{600\ \text{s}} = 3.33333\times10^{-9}\,\text{mol/L}\cdot\text{s}$. Thus, in 600 seconds, the same amount of catalyst was fed to the CSTRs and the semi-batch reactor. Monomer concentration was also kept the same for both reactor types.

In Figures 4-4 to 4-10, the parameter a is defined as the ratio $(k_{\beta,2}+k_{M,2}[M])/(k_{\beta,1}+k_{M,1}[M])$. Therefore, it quantifies the ratio of the macromonomer formation frequencies of the linear-catalyst and the LCB-catalyst. A value of $a = 2$ indicates that the linear-catalyst has a macromonomer formation frequency that is twice that of the LCB-catalyst.

Figures 4-4 and 4-5 show that the polymer made in one CSTR have both higher LCB density (LCBD) – measured as number of LCB per 1000 C atoms –and cross-product weight fractions than polymers made in a semi-batch reactor under equivalent conditions. Macromonomers are always present in a CSTR operated at steady-state, whereas it takes a certain time for macromonomers to accumulate in a semi-batch reactor before significant LCB formation occurs. It is also interesting to notice that the LCBD and the weight fraction of cross-product increases when the value of the parameter a is raised. This simply indicates that a higher production of macromonomers by the linear-catalyst will increase the formation of cross-product chains by the LCB-catalyst, as expected.

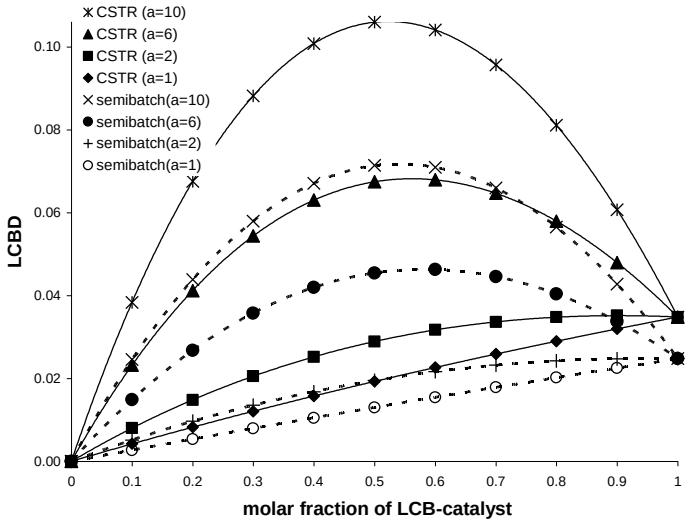

Figure 4-4. Effect of reactor type and rate of macromonomer formation of the linear-catalyst on long chain branch density (LCB/1000 C) as a function of the molar fraction of the LCB-catalyst. (Dashed curves are simulation results for semi-batch reactors and solid curves for CSTR.)

Consequently, weight and number average chain lengths are also higher when CSTRs are used due to increased LCB formation, as shown in Figures 4-6 and 4-7. We also note an intriguing linear relationship between weight average chain length and the molar fraction on LCB-catalyst in the reactor, firstly observed in our simulation of semi-batch reactors.[116] Evidently, as the parameter a

increases, the number average chain lengths, r_n and r_w, decrease due to the increased rates of transfer to monomer and β-hydride elimination of the linear-catalyst.

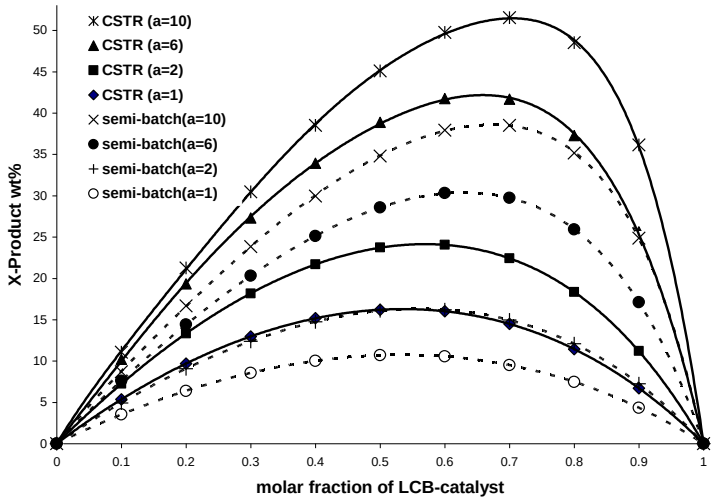

Figure 4-5. Effect of reactor type and rate of macromonomer formation of the linear-catalyst on weight percent of cross-product as a function of the molar fraction of the LCB-catalyst. (Dashed curves are simulation results for semi-batch reactors and solid curves for CSTR.)

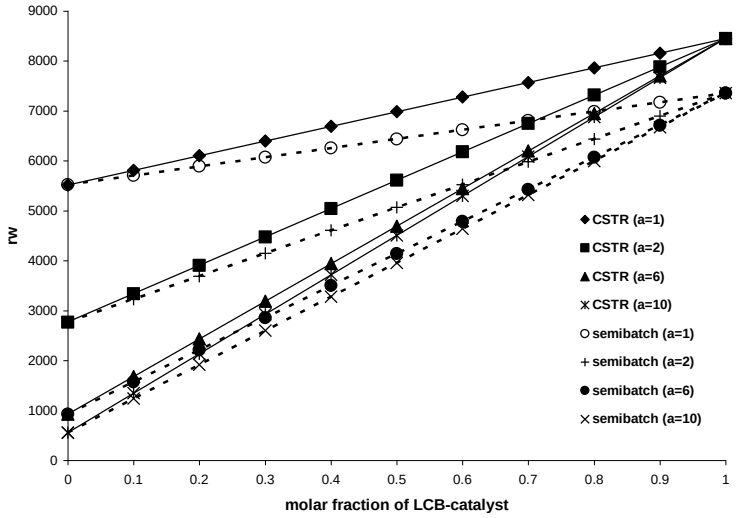

Figure 4-6. Effect of reactor type and rate of macromonomer formation of the linear-catalyst on weight average molecular weight. (Dashed curves are simulation results for semi-batch reactors and solid curves for CSTR.**)**

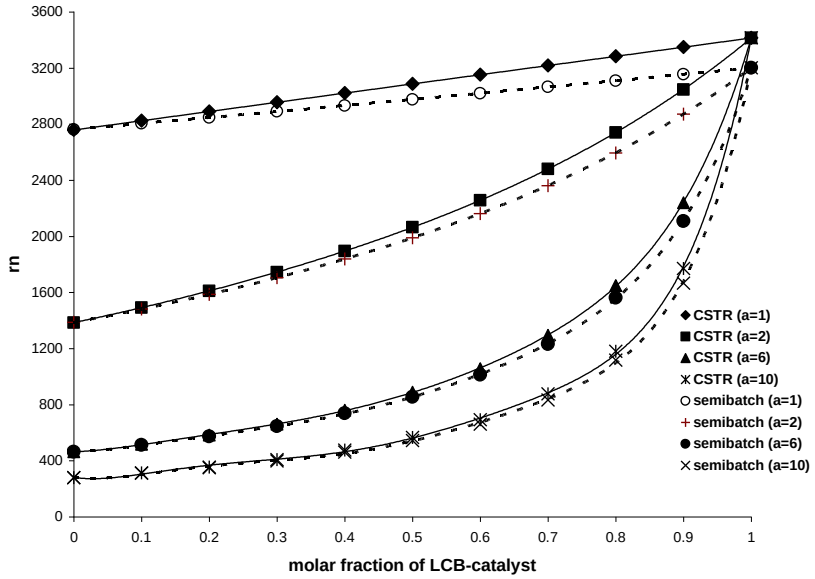

Figure 4-7. Effect of reactor type and rate of macromonomer formation of the linear-catalyst on number average molecular weight. (Dashed curves are simulation results for semi-batch reactor and solid curves for CSTR.)

Figure 4-8 shows that the polydispersity index (PDI) of polymer made in CSTRs is also higher, which is, once again, related to the increased LCB formation in these reactors.

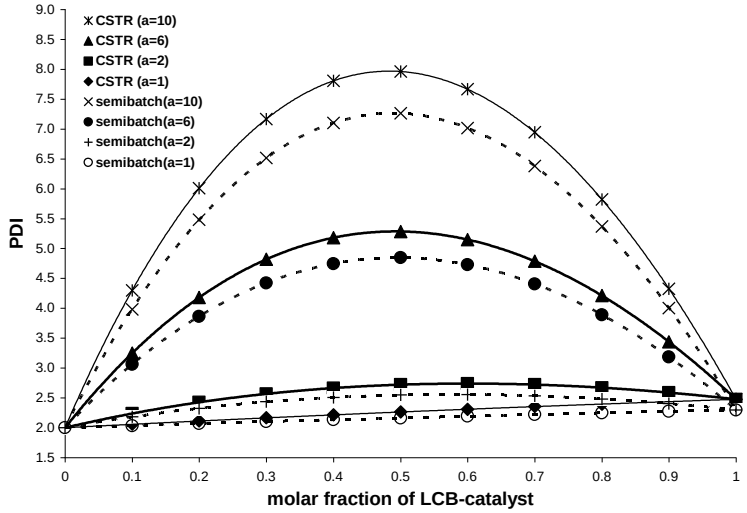

Figure 4-8. Effect of reactor type and rate of macromonomer formation of the linear-catalyst on the polydispersity index. (Dashed curves are simulation results for semi-batch reactor and solid curves for CSTR.)

As discussed above, the LCBD and weight fraction of cross-product depends strongly on the type of polymerization reactor, being always higher when CSTRs are used. If we calculate the percent increase for these variables between CSTRs and semi-batch reactors and plot them versus the fraction of LCB-catalyst in the reactor, some interesting trends are observed. Figure 4-9 shows how the increase in the weight fraction of cross-product is affected by the parameter *a*.

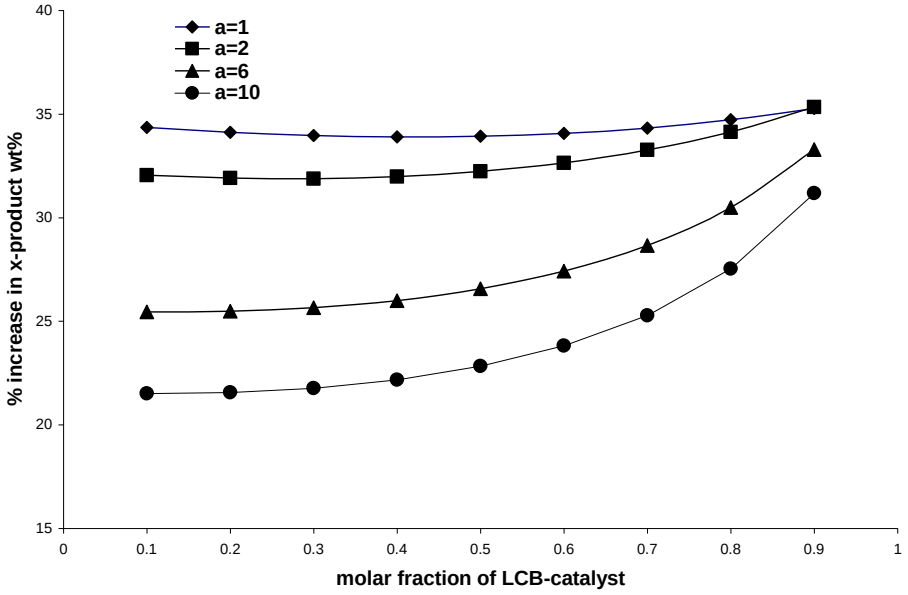

Figure 4-9. Effect of the rate of macromonomer formation of the linear-catalyst on percent increase in cross-product weight percent from semi-batch reactor to CSTR.

The higher the macromonomer formation rate of the linear-catalyst (large *a*), the lower the difference between CSTR and semi-batch reactor operation. In other words, when both catalyst have the same macromonomer formation rate, CSTR is more efficient than semi-batch reactor in producing polymer with more cross-product content. Contrarily, the macromonomer formation rate of the linear-catalyst has no effect on the percent increase in LCBD, as depicted in Figure 4-10. Moreover, it shows that the difference between a CSTR and a semi-batch reactor is more pronounced at lower molar fraction of LCB-catalyst. This conclusion is expected because as aforementioned; macromonomers are always present in CSTR,whereas some time is needed for macromonomers build up before significant LCB formation occurs.

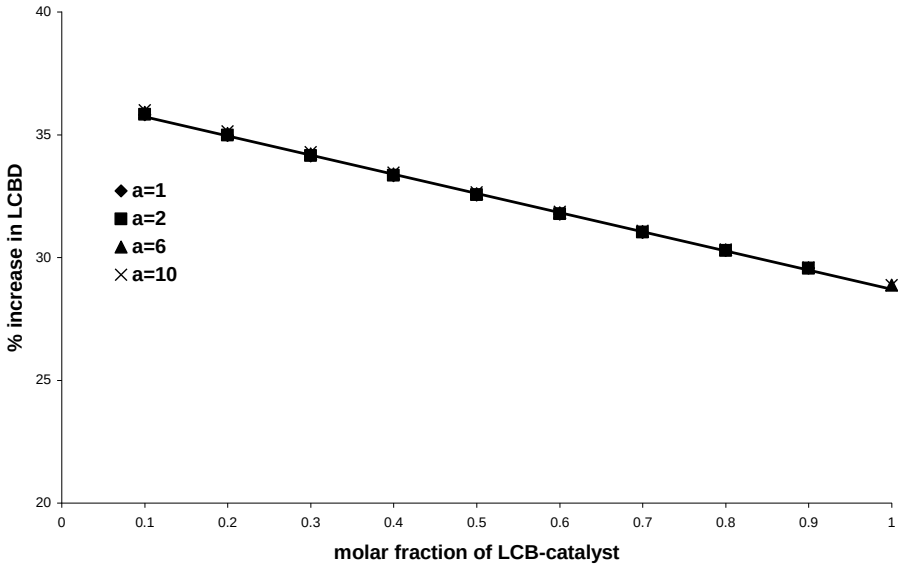

Figure 4-10. Effect of the rate of macromonomer formation of the linear-catalyst on percent increase in LCBD from semi-batch reactors to CSTRs.

4.4.2 Case Study 2: Effect of Residence Time in the Second CSTR on Polymer Microstructural Properties

In Case Study 2, the effect of residence time CSTR 2 was studied by varying it from 0 to 4000 seconds. Linear-catalyst was fed to CSTR 1, and the LCB-catalyst was fed to CSTR 2. Reaction variables, kinetic rate constants, and all other parameters used in simulation are given in Tables 4-2 and 4-3.

Figure 4-11 shows that increasing the residence time in CSTR 2 leads to an increase in the weight fraction of cross-product. This increase is accompanied by a decrease in the weight fraction of linear chains, showing that linear chains are mostly converted to cross-product chains. Since most of the linear chains formed by the linear-catalyst (catalyst 2) are made in CSTR 1, their corresponding decrease is more pronounced at lower residence time in CSTR 2.

Table 4-2. Reaction variables used for Case Study 2.

Reactor	**1**	**2**	**Description**
$[C_1]^{in}$ (mol·L^{-1}·s^{-1})	0	4×10^{-9}	Molar flow rate of LCB-catalyst per CSTR volume
$[C_2]^{in}$ (mol·L^{-1}·s^{-1})	4×10^{-9}	0	Molar flow rate of linear-catalyst per CSTR volume
[M] (mol·L^{-1})	0.5	0.5	Monomer concentration
[H_2] (mol·L^{-1})	0.0	0.0	Hydrogen concentration
[Al] (mol·L^{-1})	0.0	0. 0	Cocatalyst concentration
t_r (s)	400	0.0-4000	Residence time
Molar fraction of LCB-catalyst	0.0	1	

Table 4-3. Reaction rate constants used for Case Study 2.

Reactor	**1**	**1**	**2**	**2**	**Description**
Catalyst	**1**	**2**	**1**	**2**	
k_p (L.mol^{-1}.s^{-1})	-	5000	5000	5000	Propagation rate constant
k_b (L.mol^{-1}.s^{-1})	-	0.001	400	0.001	LCB formation rate constant
k_d (s^{-1})	-	0.005	0.005	0.005	Deactivation rate constant
k_β (s^{-1})	-	2.4	0.4	2.4	β-hydride elimination rate constant
k_M (L.mol^{-1}.s^{-1})	-	6	1	6	Transfer to monomer rate constant
k_{Al} (L.mol^{-1}.s^{-1})	-	0.0	0.0	0.0	Transfer to cocatalyst rate constant
k_H (L.mol^{-1}.s^{-1})	-	0.0	0.0	0.0	Transfer to hydrogen rate constant
$k_\beta+k_M[M]$ (s^{-1})	-	5.4	0.9	5.4	Macromonomer formation frequency

Figure 4-12 shows that the weight average chain length of the cross-product and of the overall polymer increases with increasing residence time in CSTR 2. This result is consistent with the decrease in weight percent of linear chains because cross-product chains result from LCB-forming reactions. Finally, Figures 4-13 and 4-14 show how the LCBD and PDI for the different polymer populations are affected by changes in residence time in CSTR 2. Figure 4-13 shows that increase in the residence time of the CSTR 2 leads to increase in LCBD of the overall polymer, cross-product and homogenous LCB product formed on catalyst 1 and since catalyst 2 has no macromonomer incorporating ability, LCBD for LCB 2 (homogenous LCB polymer formed on catalyst 2) is nearly zero.

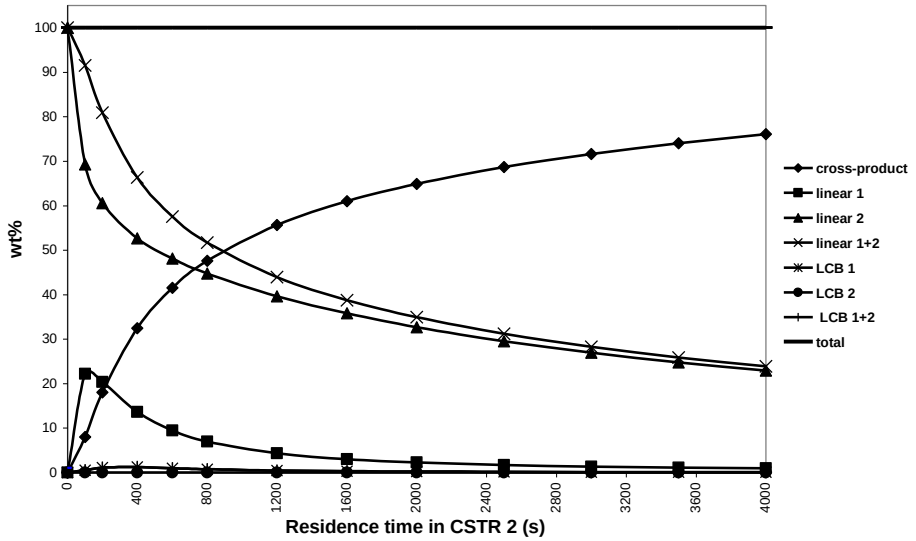

Figure 4-11. Effect of average residence time in CSTR 2 on the weight fraction of different polymer populations.

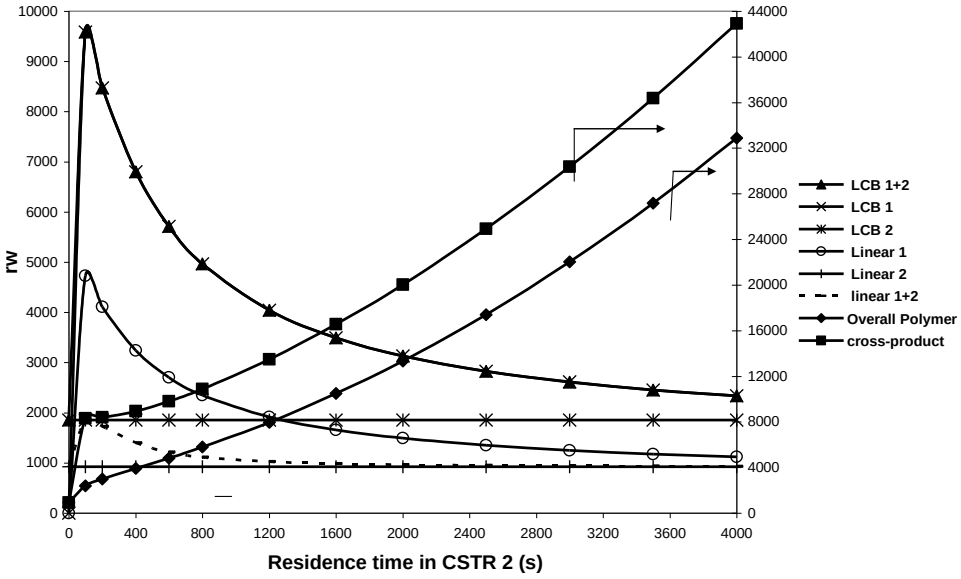

Figure 4-12. Effect of average residence time in CSTR 2 on the weight average chain lengths of different polymer populations. Values for cross-product and overall polymer are read from the right vertical axis.

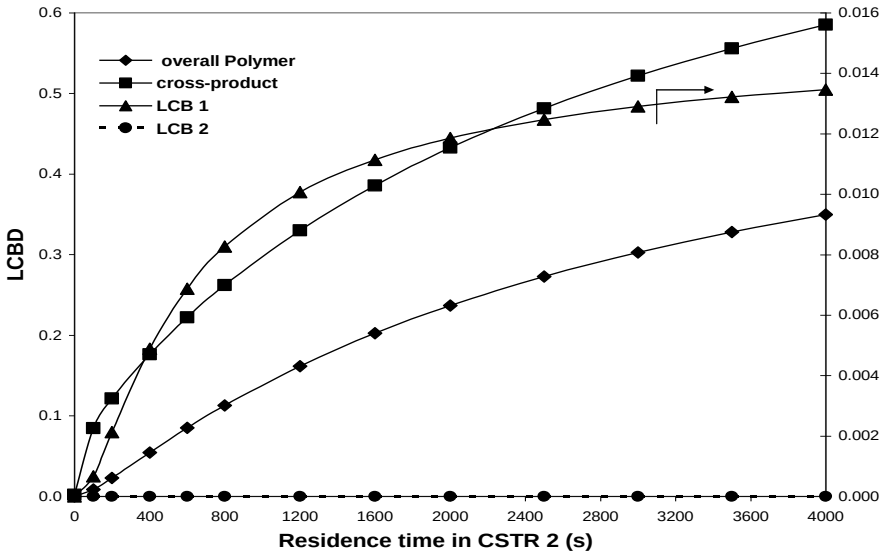

Figure 4-13. Effect of average residence time in CSTR 2 on the LCBD of different polymer populations. LCBD values for homogenous product formed on catalyst 1 (LCB 1) is read from the right vertical axis .

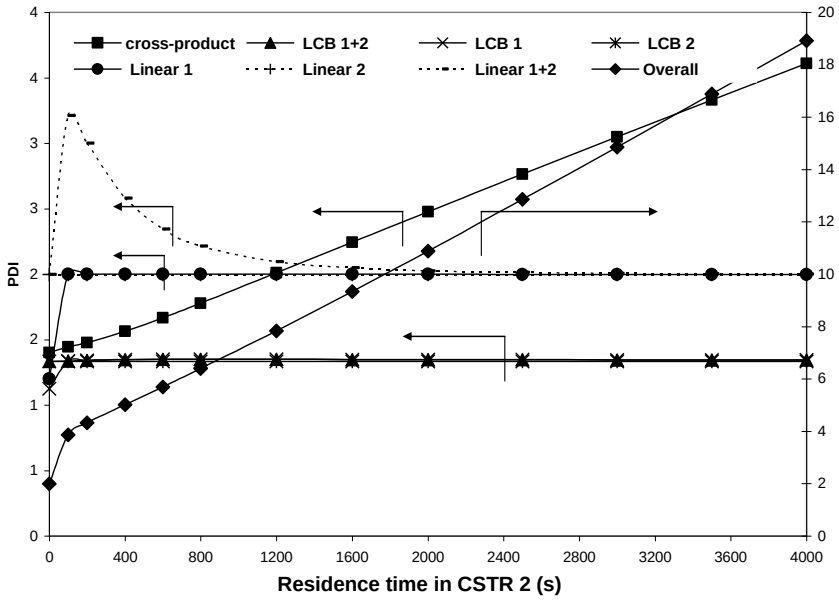

Figure 4-14. Effect of average residence time in CSTR 2 on the PDI of different polymer populations. Arrows show which axis should be used for reading PDI.

4.4.3 Case Study 3: Effect of the LCB Formation Rate Constant ($k_{b,1}$) for Catalyst 1 Fed to CSTR 2

In Case Study 3, we investigated the effect of changing the value of the LCB formation rate constant for the LCB-catalyst ($k_{b,1}$) by varying its value from 1×10^{-3} to 600 s^{-1}. The average residence times in both CSTRs were fixed at 400 seconds and, as for Case Study 2, the linear-catalyst is fed to CSTR 1 and the LCB-catalyst is fed to CSTR 2. All the other simulation parameters are the same as for Case Study 2.

Figure 4-15 shows that, as $k_{b,1}$ increases, the fraction of cross-product exiting CSTR 2 increases. Macromonomers formed by both catalysts are converted into cross-products, as indicated by the decrease in the weight fraction of linear chains in the reactor. However, since the linear-catalyst has a six times higher macromonomer formation rate constant than the LCB-catalyst, the decrease in the fraction of linear chains made in the LCB-catalyst is more pronounced. Therefore, the higher the LCB formation rate constant of the catalyst fed to CSTR 2, the higher will be the weight fraction of cross-product.

Figure 4-16 illustrates how the weight average chain length of the cross-product increases, due to higher LCB formation in the reactor, the value of $k_{b,1}$ increases. Figure 4-17 shows similar results for the LCBD.

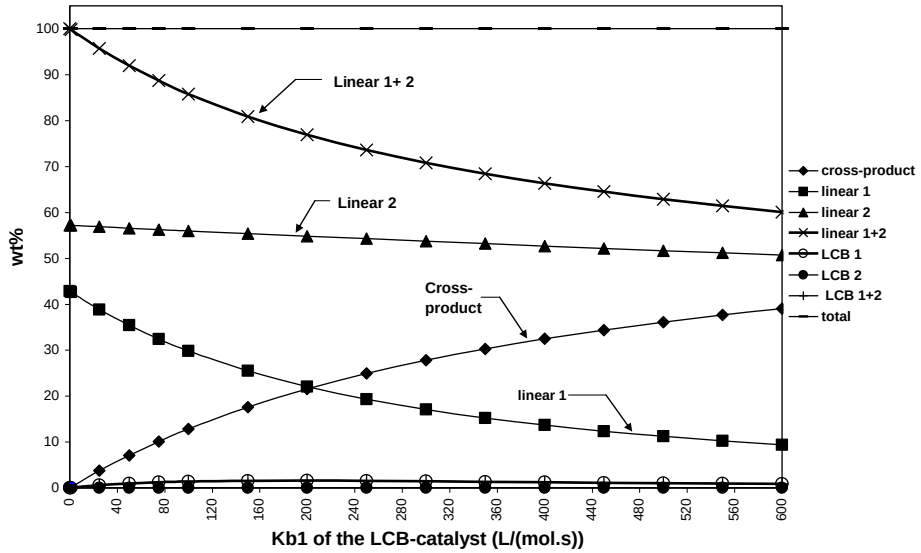

Figure 4-15. Effect of the LCB formation rate constant for the LCB-catalyst (kb,1) on the weight percent of the different polymer populations exiting CSTR 2.

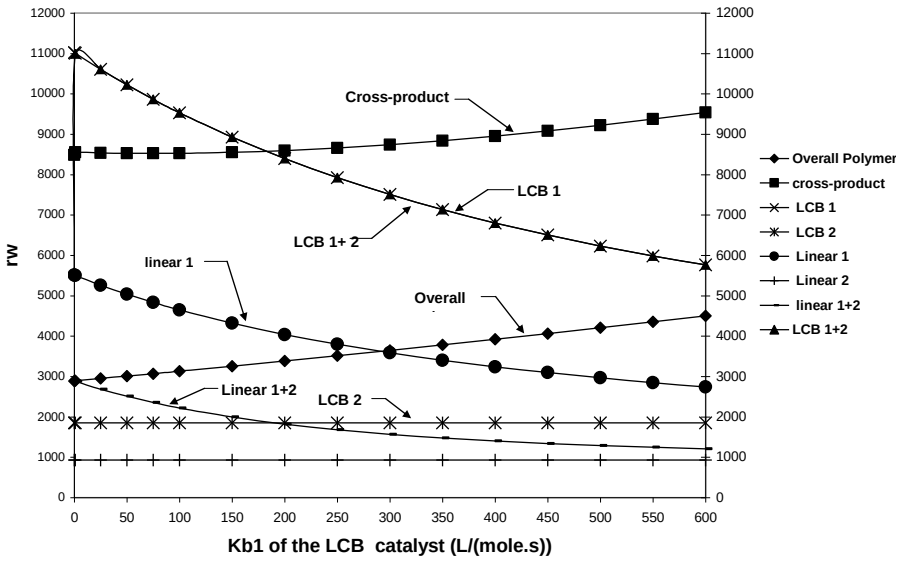

Figure 4-16. Effect of the LCB formation rate constant for the LCB-catalyst ($k_{b,1}$) on the weight average chain length of the different polymer populations exiting CSTR 2.

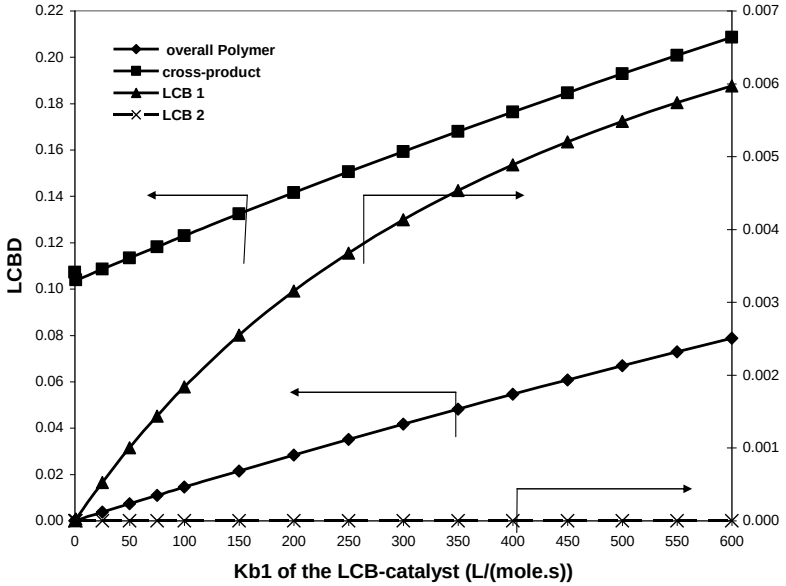

Figure 4-17. Effect of the LCB formation rate constant for the LCB-catalyst ($k_{b,1}$) on the LCBD of the different polymer populations exiting CSTR 2. Arrow direction shows which axis should be used for reading LCB.

4.4.4 Case Study 4: Catalyst Feed Policy

Case Study 4 compares four different methods of catalyst addition to the CSTRs:

- Method A: Both catalysts are added to the CSTR 1. No catalyst is added to CSTR 2.
- Method B: The linear-catalyst (catalyst 2) is added to CSTR 1; the LCB-catalyst (catalyst 1) is added to CSTR 2.
- Method C: The catalyst flow rates used in Methods A and B are halved and both catalysts are added to both CSTRs.
- Method D: Same as method C, except that only the LCB-catalyst is added to CSTR 2.

The overall catalyst flow rates were the same for all four methods, as described in Table 4-4. All the reaction rate constants and reaction parameters used in the simulations were the same as those used in Case Study 2, but the average reactor residence time of both CSTRs was increased to 600 seconds.

Table 4-4. Catalyst feeding policies for Case Study 4.

Method	Catalyst	Catalyst Flow Rate ($mol \cdot L^{-1} \cdot s^{-1}$)	
		CSTR 1	CSTR 2
A	Linear	8×10^{-9}	0
	LCB	8×10^{-9}	0
B	Linear	0	8×10^{-9}
	LCB	8×10^{-9}	0
C	Linear	4×10^{-9}	4×10^{-9}
	LCB	4×10^{-9}	4×10^{-9}
D	Linear	4×10^{-9}	8×10^{-9}
	LCB	4×10^{-9}	0

Figure 4-18 shows that the composition of the products exiting CSTR 1 are completely different when Method A and B are employed. However, the composition of the product exiting CSTR 2 is very similar when Methods A and B are used, as illustrated in Figure 4-19. For method A, only a little more cross-product was produced in CSTR 2 when compared to method B (55.47 vs. 52.31 wt%). When all the four simulations are compared, Method D is clearly the preferred approach for maximizing the weight fraction of cross-product. The polydispersity index of the overall polymer

made according to Method D is also the lowest of all catalyst feed policies (Figure 4-20) and the weight average chain length is the highest (Figure 4-21).

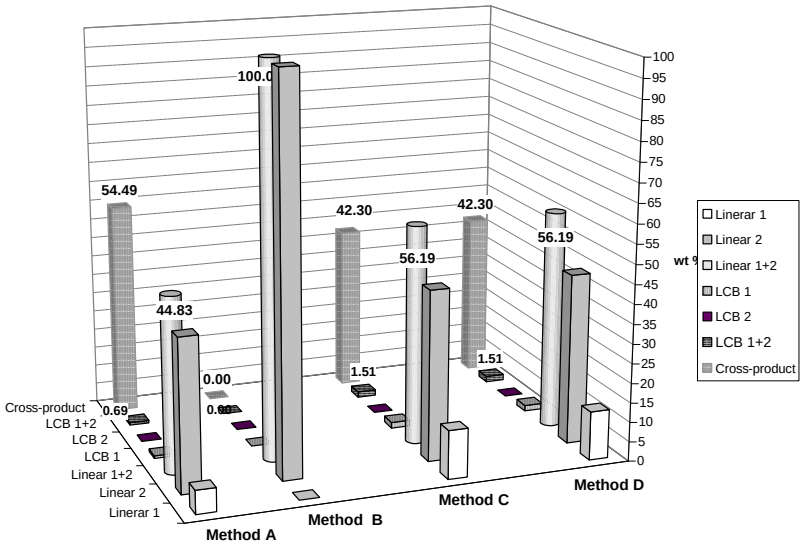

Figure 4-18. Weight percent of different polymer populations exiting CSTR 1. Numbers on the columns are their corresponding wt%.

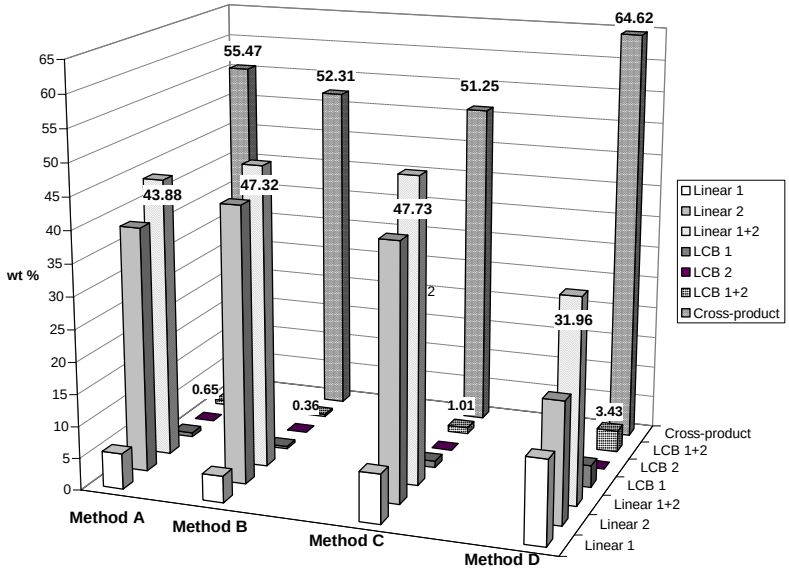

Figure 4-19. Weight percent of different polymer populations exiting CSTR 2. Numbers on the columns are their corresponding wt% .

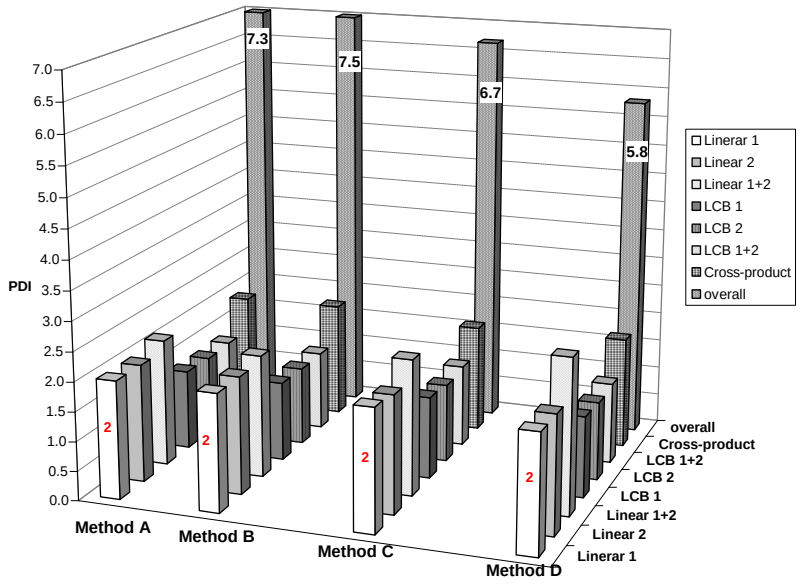

Figure 4-20. Polydispersity index of different populations exiting CSTR 2.

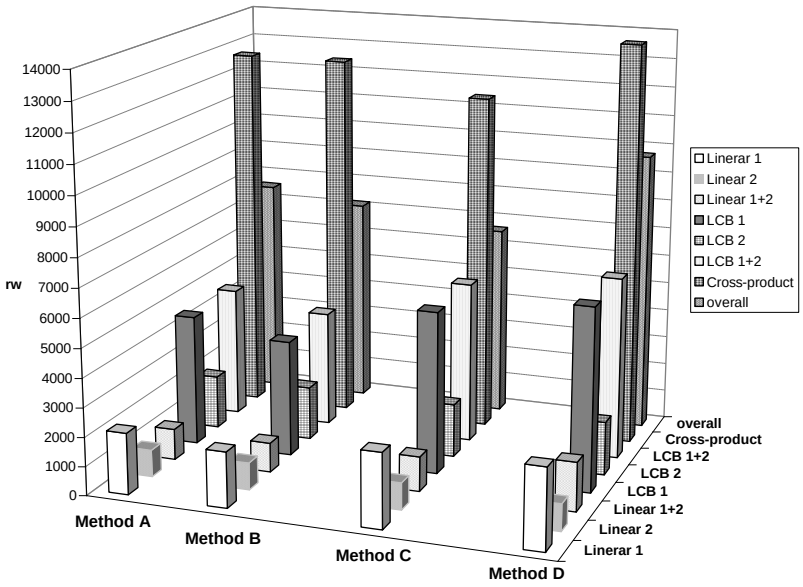

Figure 4-21. Weight average chain length of different populations exiting CSTR 2.

4.5 Concluding Remarks

We have developed a mathematical model that describes the microstructure of long-chain branched polyolefins made with two metallocenes in two CSTRs in series. In one of its applications, these dual-metallocene systems are used to produce olefinic TPEs. The model can predict the fractions of different polymer populations made in both reactors, as well as their average chain lengths and LCB densities.

Simulation results show that CSTRs are more efficient than semi-batch reactors when higher long chain branch densities or more cross-product is required. To increase the weight percent of cross-product using a linear-catalyst and a LCB-catalyst in sequential mode, the rate of macromonomer formation of the linear-catalyst should be higher than that of the LCB-catalyst. Increasing residence time in the second CSTR will also lead to higher cross-product formation and LCB density. This rate of increase is more significant if the residence time in the second CSTR is similar to that of the first CSTR.

The catalyst feed policy also has a great impact on polymer properties. We found out that feeding the linear-catalyst and the LCB-catalyst in equal amounts to the first CSTR and just adding the LCB-catalyst to the second CSTR (Method D) is the preferred catalyst injection method for making polymer with a high mass fraction of cross-product, high chain length averages, and lower PDI.

Chapter 5

Materials and Methods

5.1 Reagents and Apparatus

5.1.1 Reagents

Reagents used in each set of polymerization runs will be described in the relevant chapters.

5.1.2 Polymerization Apparatus

A 500-ml semi-batch reactor, illustrated in Figure 5-1, was used for all polymerizations. The reactor was equipped with stirrer, heating mantle, and cooling coil for controlling the temperature of the reaction media during polymerization. Two independent proportional-integral derivative control loops were used to control the cold water flow in the cooling coil and the power input to the electric heater. The monomer mass flow rate was monitored using an in-line mass flow meter installed in the monomer feed line. The reactor pressure was adjusted by an in-line pressure regulator installed in the ethylene feed line. The process control calculations were performed by a personal computer running a Labview program. Excellent temperature control was achieved using this control scheme as the reactor temperature was maintained within ±0.5 ^{o}C of the set point for most typical polymerizations.

5.1.2.1 Polymerization Procedure

Details of experiments and materials that are specific for each chapter will be described separately in those chapters.

5.2 Polymer Characterization

A general review of polymer characterization techniques was presented in Chapter 2, Section 2.8. In the following sections, some specific polymer characterization techniques not mentioned in Chapter 2 but used in this thesis, will be presented.

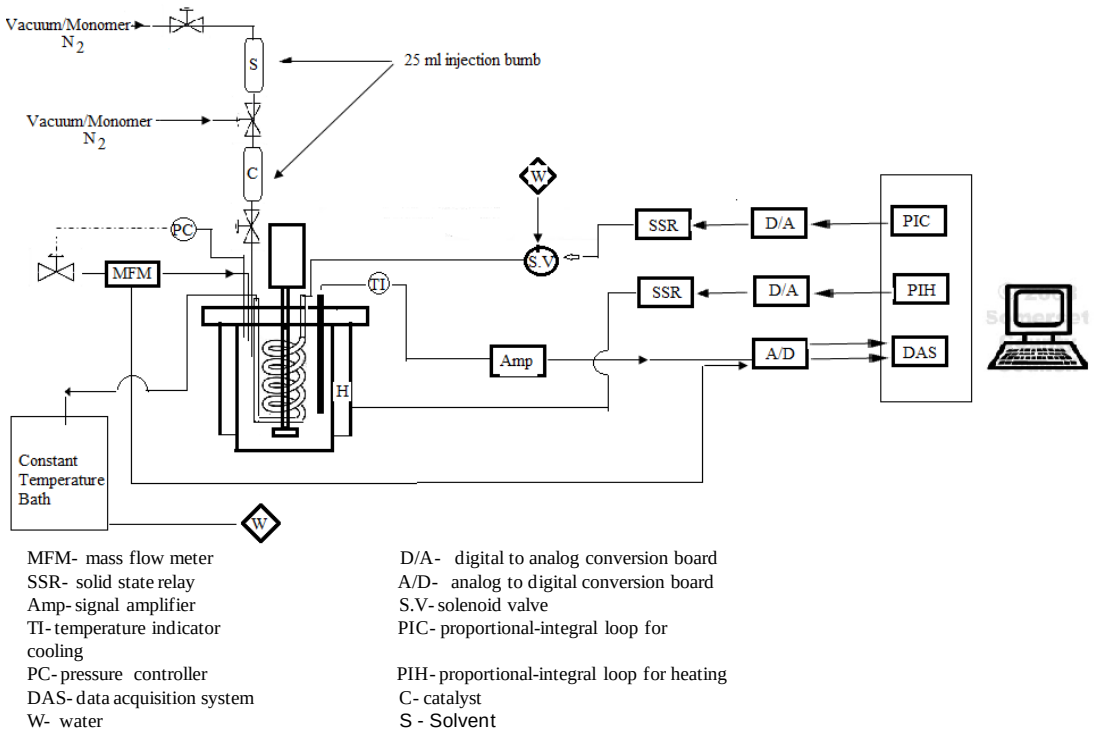

Figure 5-1. Semi-batch polymerization reactor and control system

5.2.1 ^{13}C-NMR Spectroscopy

^{13}C-NMR was used to measure comonomer content, (1-octene, 1-butene, 1,9 decadiene) or long-chain branching of the samples. The ^{13}C NMR spectra were obtained using a Bruker 500 MHz system. 100 mg of polymer sample was placed in a 5-mm NMR tube followed by addition of 0.65-0.7 g deuterated ortho dichlorobenzene. The content of the sample tube was homogenized in a heating block at 135 ^{o}C for 4-5 h and then transferred into an NMR magnet. The probe temperature was set to 120 ^{o}C. Acquisition parameters were 14 microsecond 90^{o} pulses, 2.6 s acquisition time, 7.5 s relaxation delay time between pulses. Inverse gated proton decoupling was applied. The biggest peak was referenced to 30.0 ppm. Peak assignments will be explained in the relevant chapters.

5.2.2 Estimation of comonomer Content by Crystalization Analysis Fractionation (Crystaf).

The main idea for using Crystaf as a means for comonomer determination is to make a calibration curve relating crystallization peak temperature of the Crstaf profiles to comonomer content of the

copolymer samples determined by ^{13}C NMR. In the following paragraphs, we explain how the calibration curve for 1-octene determination of the copolymer samples was obtained.

Eight ethylene/1-octene copolymer samples with different 1-octene fractions were synthesized by copolymerization of ethylene and 1-octene using CGC-Ti in the semi-batch reactor. Table 5-1 summarizes polymerization conditions for these samples.

The samples were analyzed using ^{13}C-NMR spectroscopy to determine their 1-octene content. 3000 scans were used for data averaging. A representative spectrum of an ethylene/1-octene copolymer, sample EO-9.02 (Table 5-1), is shown in Figure 5-2 with chemical shift assignments. The comonomer content of the samples were calculated using the procedure proposed by DePooter et al.[125] Calculation using this procedure takes into account branches separated by one ethylene unit and two or three branches next to each other in addition to isolated branches. These two latter structures were seen when comomoner content was higher than 4 mole percent. Chemical shifts at 40.98 and 40.26 ppm are related to these structures. The integration limits used to determine the molar composition of ethylene/1-octene copolymers are listed in Table 5-2. Table 5-3 lists the total area integrated under all the peaks in each region of interest and the calculated 1-octene mole percent of the samples.

Table 5-1. Polymerization conditions for 1-octene copolymerization

Sample	**1-octene concentration in the feed (mol.L^{-1})**
EO-9.02	0.64
EO-6.43	0.48
EO-5.25	0.4
EO-4.08	0.32
EO-3.03	0.24
EO-1.87	0.16
EO-0.85	0.08
EO-0.0	0.00

Total reactor pressure=120 psig, Reaction temperature=120 ^{o}C, Catalyst concentration= 6×10^{-7} mol/L.

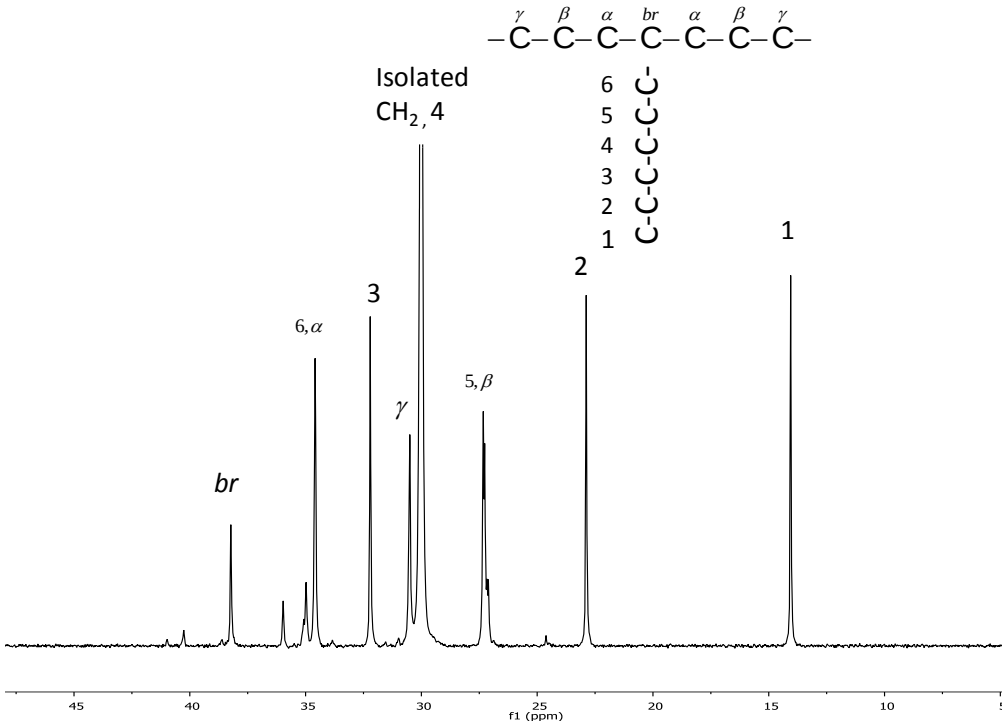

Figure 5-2. ^{13}C-NMR spectrum for the sample EO-9.02 listed in Table 5-2.

Table 5-2. Integration limits for ethylene/1-octene copolymers

Area	Region (ppm)
A	41.5 to 40.5
B	40.5 to 39.5
C	39.5 to 37
D	Peak at 36
D+E	36.8 to33.2
F+G+H	33.2 to-25.5
H	28.5 to 26.5
I	25 to24
P	24 to 22

Table 5-3. List of integrated areas under the picks given in Table 5-1.

Sample	Value of integral in region									1-octene mole%
	A	B	C	D	D+E	F+G+H	H	I	P	
EO-9.02	1.00	2.75	20.24	7.00	76.97	612.38	71.24	1.76	42.67	9.02
EO-6.43	1.00	3.26	30.95	9.22	128.80	1326.30	121.86	1.98	62.03	6.43
EO-5.25	1.00	3.91	40.08	10.51	154.20	1975.40	147.70	2.03	72.10	5.25
EO-4.08	0.00	1.00	14.00	2.68	47.21	796.70	46.85	0.49	21.98	4.08
EO-3.03	0.00	1.00	21.54	2.78	75.55	1638.48	73.60	1.17	34.57	3.03
EO-1.87	0.00	0.00	1.00	0.07	3.61	120.72	3.50	0.00	1.53	1.87
EO-0.85	0.00	0.00	1.00	0.00	3.10	240.12	3.70	0.00	1.58	0.85
EO-0.0	0.00	0.00	0.00	0.00	1.48	1483.9	0.00	0.0	1.0	0.0

The molar composition of the copolymer samples was calculated using the following formulas,[125]

$$O_1 = \frac{(A + 2C + 2D)}{2} \tag{5-1}$$

$$O_2 = (1.5A + 2B + (D + E) - D) \tag{5-2}$$

$$O' = \frac{(O_1 + \frac{O_2}{3})}{2} \tag{5-3}$$

$$E' = \left\{[(F + G + H) - (3A + 3B + H + P + I)]/2 + O'\right\} \tag{5-4}$$

where O' is average moles of 1-octene . O_1 , O_2 and E' are moles of branch , α carbons and ethylene, respectively.

$$1-octene \quad mol\% = \frac{O'}{(O' + E')} \times 100 \tag{5-5}$$

The samples were also analyzed by Crystaf using a PolymerChar Crystaf model 200. Polymer samples were dissolved in 47 ml 1,2,4 trichlorobenzene at a concentration of 0.6 mg/ml. The polymer solution was heated to 160 ^{o}C, held for 2 hours to ensure complete dissolution, followed by decreasing the temperature to 105 ^{o}C and stabilizing for another 55 minutes. A constant cooling rate of 0.1^{o}C/min was applied during all analyses until the temperature reached 30 ^{o}C. Polymer

concentration in the solution phase was monitored using an in-line IR detector. The Crystaf profiles for all the samples in Table 5-1 are shown in Figure 5-3. Their Crystaf profiles show that CGC-Ti makes copolymer with unimodal SCBD, as expected for single site catalysts. Due to the high 1-octene of sample EO-9.02, its Crystaf peak is below 30 ^{o}C, the lowest temperature used during Crystaf analysis; therefore, it could not be included in the Crystaf calibration curve.

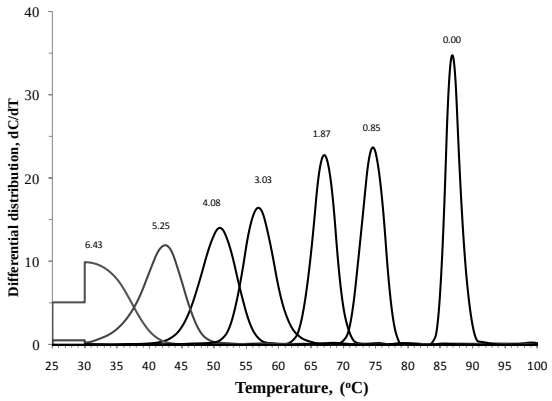

Figure 5-3. Crystaf profiles for ethylene/1-octene copolymers made with CGC-Ti. The labels on the curves are the 1-octene mole % in the copolymer.

Table 5-4 summarizes the results for 1-octene fraction in the copolymer and crystallization peak temperature (T_{peak}) for all samples listed in Table 5-1. T_{peak} is the Crystaf profile peak temperature. The Crystaf analyses for some of the samples were replicated to estimate the standard deviation for T_{peak} shown in Table 5-4.

Table 5-4. Crystaf and ^{13}C-NMR measurements for ethylene/1-octene copolymers.

Sample	**1-octene mole %**	**T_{peak} (^{o}C)**				**Standard deviation (^{o}C)**
EO-9.02	9.02	<30				
EO-6.43	6.43	30				
EO-5.25	5.25	42.9	42.7	42.1	42.8	0.36
EO-4.08	4.08	50.9	51.5			0.4
EO-3.03	3.03	57.9	58.8			0.63
EO-1.87	1.87	67.1	66	67		0.64
EO-0.85	0.85	74.6	75.6	74.6		0.58
EO-0.0	0.0	86.9	87.5	86.8		0.38

Since the standard deviations at different 1-octene molar fractions are nearly the same (see last column of Table 5-4), they were pooled to get a better estimate of the standard deviation, which was found to be 0.5 ^{o}C (For more details on pooled standard deviations, see Appendix I, at the end of this thesis).

An estimate of the standard deviation for 1-octene mole % in the copolymer was obtained by using three ^{13}C-NMR analysis replicates of sample EO-4.08, and was found to be 0.032 mole %. Both variables, T_{peak} and 1-octene mole %, are random variables and the complete analysis of the problem would, in principle, require an error in variable approach. This could be verified by examining the equation below relating 1-octene mole % to T_{peak}, obtained using linear regression.

$$\text{1-octene mole \%} = -0.1201 T_{peak}(\text{in } ^{o}\text{C}) + 10.116 \quad (5\text{-}6)$$

Table 5-5 shows the results of a sensitivity analysis for sample EO-4.08, by changing T_{peak} within two standard deviations and calculating the respective 1-octene mole % using Equation (5-6).

Table 5-5. Sensitivity in 1-octene mole % due to variability in T_{peak}.

T_{peak}	**1-octene mole % calculated using Equation (5-6)**
50.2	4.087
51.2	3.967
52.2	3.847

The difference between the maximum and minimum 1-octene mole % in Table 5-5 is 0.24, which is nearly twice of the four standard deviations for 1-octene mole % measured by ^{13}C-NMR (0.24~2×4×0.032). Although, variability in 1-octene mole% is higher than variability in T_{peak} but this difference is not in the range of order of magnitude. Therefore, we cannot assume that one of the variables can be approximated as a fixed variable and apply linear regression. This means that using linear regression is not a correct approach to obtain slope and intercept of equation 5-6 and Error in variable model should be invoked but Equation 5-6 can still be used to obtain a point estimate of the 1-octene mole % in ethylene/1-octene copolymers as we did in Chapter 8.

The linear relationship between Crystaf peak temperature, T_{peak} , and the 1-octene mole % of the samples measured by ^{13}C-NMR is illustrated in Figure 5-4. Crystaf peak temperature decreases with increasing amount of 1-octene, indicating that polymer chains with higher content of short chain branches crystallize at lower temperatures, as expected.

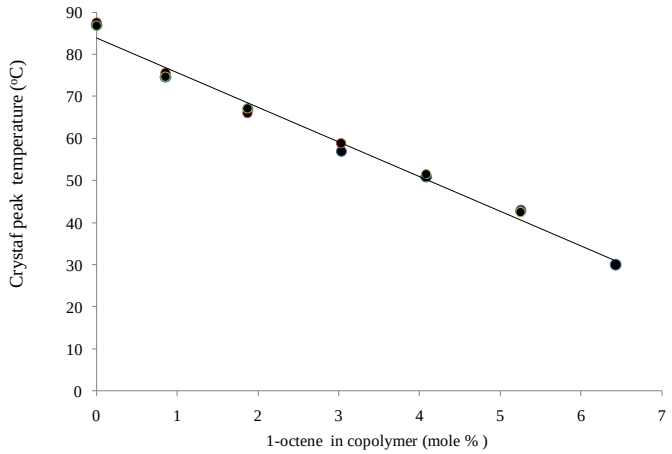

Figure 5-4. Plot of Crystaf peak temperaute (T_{peak}) versus 1-octene mole % in ethylene/1-octene copolymer samples.

5.2.3 Determination of Unsaturated Chain End Density by FT-IR (UCED)

Five polyethylene samples were made with different unsaturated chain end densities (UCED, (1000 C)$^{-1}$). To make theses samples, ethylene was copolymerized with 1,9-decadiene using CGC-Ti. The detailed procedure for making these copolymers and analyzing them by ^{13}C-NMR to determine their UCED is given in Chapter 9.

The samples were melt-pressed at 150 ^{o}C into 0.1 to 0.3 mm disks using a table press and their thickness were measured with a micrometer with thimble graduations of 0.001 mm. In the FTIR measurements, 32 scans were collected from 400 to 4000 cm^{-1} with 2 cm^{-1} resolution. Figure 5-5 shows the IR spectrum for these samples. The absorption band at 910 cm^{-1}, which is indicative of terminal vinyl group, was used for construction of the calibration curve. The area under this peak was measured by choosing a baseline between the valleys on either side of the peak. Table 5-6 summarizes the results for the areas under the 910 cm^{-1} peak and thickness measurements for these samples.

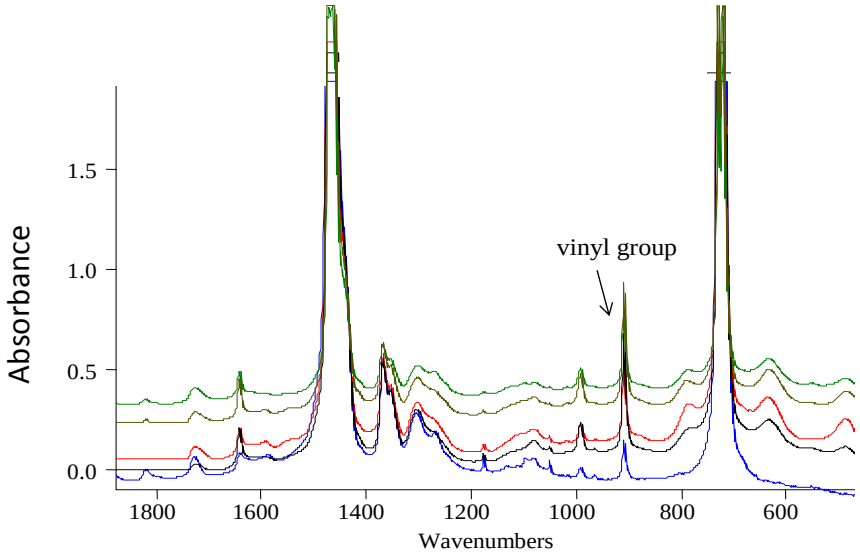

Figure 5-5. FTIR spectra for polyethylene films with different UCED.

Table 5-6. FTIR analysis summary for ethylene/1,9-decadiene copolymers.

Sample	**UCED×10**	**Area under the peak A_λ (940.6 - 871.4 cm^{-1})**	**Thickness (mm)**	A_λ/b (cm^{-1}/mm)
PE554A	5.95	1.714	0.306	5.60
PE558B	14.69	3.588	0.207	17.34
PE556C	22.76	5.226	0.195	26.80
PE557C	29.84	3.901	0.107	36.46
PE559C	37.92	5.569	0.125	44.55

5.2.3.1 Calibration

Transmittance, τ_λ, is defined as,

$$\tau_\lambda = \frac{I}{I_0} \tag{5-7}$$

where I_0 is the intensity of the incident radiation and I is the intensity of the radiation coming out of the sample.

Absorbance, A_λ, is defined as,

$$A_\lambda = -Log_{10}(\tau_\lambda) \tag{5-8}$$

According to Beer's law, absorbance is related to functional group concentration (c), in our case UCED, as follows,

$$A_\lambda = a \times b \times c \tag{5-9}$$

where a is a proportionality constant called extinction coefficient and b is the path length of the radiation through the absorbing medium (sample thickness). Substituting c with UCED in Equation (5-9) and rearranging gives,

$$UCED = \frac{1}{a}\frac{A_\lambda}{b} \tag{5-10}$$

Therefore, a plot of UCED versus A_λ/b is expected to be linear and can be used as the calibration curve for measuring UCED (Figure 5-6). As expected, a linear relationship with slope 0.08421 UCED.cm.mm was observed. In Chapter 7, Figure 5-6 will be used to estimate UCED in polymer samples made with CGC-Ti.

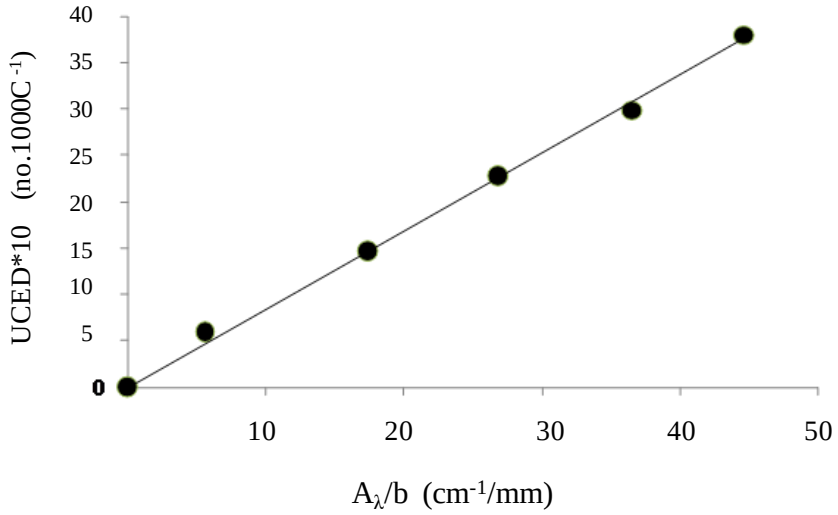

Figure 5-6. FTIR calibration curve used to measure UCED.

5.2.4 Short chain branch determination by online FTIR spectroscopy coupled with GPC

FTIR detection of short chain branching for PE in trichlorobenzene solutions relies on methyl and methylene absorption bands found at 2855 and 2928 cm^{-1}.[126-128] This dependence of the FTIR spectra on the presence of $-CH_3$ and $-CH_2-$ groups can be used to measure the level of short chain branching (SCB) in polyethylene. In this region of the spectrum, the GPC solvent, trichlorobenzene, does not interfere with the infra-red absorption peaks.[126] This technique is coupled with GPC and can significantly enhance the characterization of polyolefins by determining short chain branch distribution across molecular weight.

5.2.5 Short Chain Branch Distribution Determination

5.2.5.1 Ethyl and Hexyl Branch Distribution

The number of ethyl and hexyl branches per 1,000 carbon atoms as a function of molecular weight was measured with an online dual wavelength infrared detector (Polymer Char, Valencia, Spain), using the above mentioned wavelengths. A calibration curve was constructed using three ethylene/1-butene and nine ethylene/1-octene copolymer samples of known ethyl and hexyl branch content made with CGC-Ti. In addition to those samples, three ethylene homopolymers made with CGC-Ti under high Al/Ti ratio and two linear polyethylene standard samples (NBS 1475) were used as the reference point for zero SCBD. The SCBD of the CGC-Ti copolymers was measured by ^{13}C NMR. The procedure for calculation of 1-butene and 1-octene content was adopted from the article by Depooter et.al.[125]

Figure 5-7 shows the IR calibration curve used in this study. The x-axis is the ratio of the area under the methyl signal to the area under the methylene signal for all the samples. The lowest points on the curve are for ethylene homopolymers made with CGC and the linear polyethylene standards (NBS 1475). The calibration curve for both 1-butene and 1-octene are coincident, as expected.

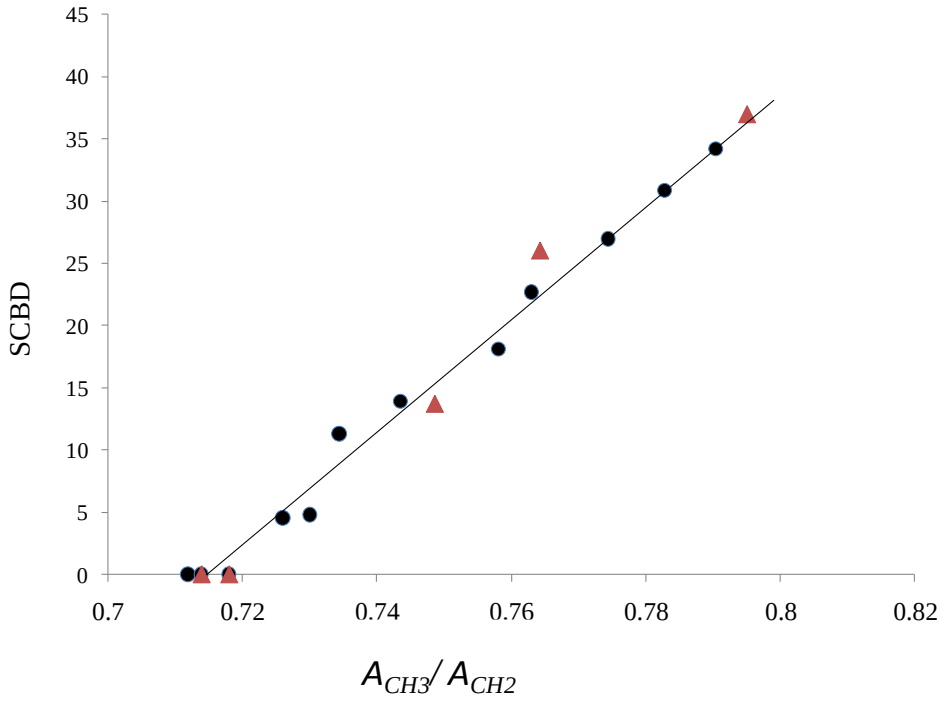

Figure 5-7. IR calibration curve for number of ethyl branches per 1,000 carbon atoms. The triangular and circular symbols refer to 1-butene/ethylene and 1-octene /ethylene copolymer samples, respectively.

The following equation was obtained by linear regression of the data relating SCBD to the ratio of the intensities of methyl to methylene signals, CH_3/CH_2,

$$SCBD = 451.83\left(\frac{A_{CH_3}}{A_{CH_2}}\right) - 322.92 \qquad (5\text{-}11)$$

5.2.6 Long Chain Branch Estimation

It is possible to estimate the degree of long chain branching of a polymer with a viscosity detector that measures the intrinsic viscosity across the molecular weight distribution obtained by GPC using the Zimm-Stockmayer equation. This approach is based on the fact that polymer chains having LCBs have smaller sizes in solution, and consequently lower intrinsic viscosities, than linear molecules of the same molecular weight.

The intrinsic viscosity branching factor, g', is the ratio of the intrinsic viscosities of branched and linear chains with the same molecular weight,

$$g' = \left(\frac{[\eta]_b}{[\eta]_l} \right)_M \tag{5-12}$$

where $[\eta]_b$ and $[\eta]_l$ are the intrinsic viscosities of branched and linear chains, respectively. The parameter g' is related to the branching factor, g, which is the ratio of the mean square radius of gyrations of branched and linear polymers of the same molecular weight,

$$g' = g^{\varepsilon} \tag{5-13}$$

where the value of ε is a function of the long chain branching structure and the number of LCBs per chain.[95] If an on-line multiangle light scattering detector is available, the value of g can be measured directly during the GPC analysis and ε does not need to be estimated.

Theoretically estimated values for ε vary from 0.5 to 1.5 for several branching configurations.[95, 129] For star polymers, a value of ε = 0.5 has been estimated,[97-98] while studies for comb polymers indicate a value of 1.5.[99] Randomly-branched polymers have ε values ranging between those for comb and star polymers. A values of ε = 0.75 was reported for randomly-branched polyethylene in 1,2,4-trichlobenzene.[130]

To include the SCB contraction effect on the coil dimension, the parameter g'_{SCB} introduced by Sun[82] was used. This parameter is defined as,

$$g'_{SCB} = \frac{[\eta]_{SCB}}{[\eta]_l} \tag{5-14}$$

where $[\eta]_{SCB}$ and$[\eta]_l$ are the intrinsic viscosities of samples of the same molecular weight with and without short chain branches, respectively.

The intrinsic viscosity of linear polymer solutions is described by the Mark-Houwink[131] equation,

$$[\eta]_l = kM^a \tag{5-15}$$

where the constants k and a depend on the type of polymer, solvent, and temperature. Since the constant a is not affected by SCB frequency,[82] Equation (5-14) can also be expressed as,

$$g'_{SCB} = \frac{k_{SCB}}{k} \tag{5-16}$$

where k_{SCB} and k are the Mark-Houwink coefficients for the ethylene/ α-olefin copolymer (in our case, ethylene/1-butene or ethylene/1-octene copolymers), and ethylene homopolymer, respectively.

For the ethylene/1-butene and ethylene/1-octene copolymers reported by Sun,[82] an empirical relation was found between g'_{SCB} and 1-butene or 1-octene weight fractions, W_b or W_o, in the copolymer. For ethylene/1-butene copolymer the relation is given by,,

$$g'_{SCB} = 1 - 0.72\ W_b \tag{5-17}$$

Similarly, for ethylene/1-octene copolymers,

$$g'_{SCB} = 1 - 0.77\ W_o \tag{5.18}$$

The following Mark-Houwink constants were obtained at 135 ^{o}C for the standard linear polyethylene sample NBS 1475 using our GPC on-line intrinsic viscosity measurements,

$$[\eta]_l = 0.000527\ [M]^{0.7049} \tag{5-19}$$

where $[\eta]$ is in dL/g. These Mark-Houwink constants were obtained by averaging the results of 7 samples. The standard deviations for *k* and *a* are 0.00004 and 0.007, respectively. These estimates are consistent with those found by Sun[131] for linear polyethylene at 135 ^{o}C in TCB,

$$[\eta]_l = 0.0004934[M]^{0.705} \tag{5-20}$$

Substituting Equation (5-17) into Equation (5-16) and then using Equations (5-19) and (5-14), we obtain the following equation for intrinsic viscosity of linear polyethylenes with ethyl branches,

$$[\eta]_{SCB} = (1 - 0.00288 \cdot EBD) \cdot 0.000527 \cdot M^{0.7049} \tag{5-21}$$

where *EBD* is the number of ethyl branches per 1000 carbon atoms in the chain. EBD can be measured for each GPC slice using the in-line IR detector, as explained in Section 5.2.5.1

Combining Equations (5-21) and (5-12) leads to the following equation for the intrinsic viscosity branching factor, when ethyl branches are also present,

$$g' = \frac{[\eta]_b}{(1 - 0.00288 \cdot EBD) \cdot 0.000527 \cdot M^{0.7049}} \tag{5-22}$$

Analogously, the corresponding equation for linear ethylene/1-octene copolymers is,

$$g' = \frac{[\eta]_b}{(1 - 0.00616 \cdot HBD) \cdot 0.000527 \cdot M^{0.7049}} \tag{5-23}$$

where *HBD* is the number of hexyl branches per 1000 carbon atoms in the chain.

The next step is to relate g or g' to the number of long chain branches in the polymer chains. Zimm and Stockmayer formulated several equations to quantify the number of long chain branches in a polymer based on how it compares to a linear (non-branched) variant of the same polymer. For a monodispersed polymer mixture with n randomly distributed trifunctional branch units per molecule, the g factor is given by the expression,[95]

$$g = \frac{1}{\sqrt{(1+n/7)^{1/2} + 4n/9\pi}} \tag{5-24}$$

Since the intrinsic viscosity and EBD or HBD are known for each slice of the GPC chromatogram, we can calculate g' using Equation (5-22) or (5-23), and estimate g with Equation (5-13), setting ε = 0.75. Finally, Equation (5-23) can be used to calculate the number of LCBs per polymer chain for each GPC slice.

The number average LCB frequency (LCBF) and LCB density (LCBD) for the whole polymer can then be estimated with the following equations,

$$LCBF = \frac{\sum n_i \frac{c_i}{M_i}}{\sum \frac{c_i}{M_i}} \tag{5-25}$$

$$LCBD = \frac{14{,}000 \cdot LCBF}{M_n} \tag{5-26}$$

Chapter 6

In-Depth Investigation of Ethylene Polymerization Kinetics with *rac*-Et(Ind)$_2$ZrCl$_2$ in a Solution Reactor

6.1 Summary

Ethylene polymerization with rac-Et(Ind)$_2$ZrCl$_2$/MAO was studied in a semi-batch solution reactor using a systematic statistical approach. The factors investigated were ethylene concentration, polymerization temperature, MAO and catalyst concentrations. The ethylene polymerization kinetics with rac-Et(Ind)$_2$ZrCl$_2$/MAO is first order with respect to ethylene and catalyst concentration. Catalyst deactivation is also a first order reaction. Chain transfer to monomer is the dominant chain transfer reaction in this system, but transfer to MAO also happens to a lesser extent. On the other hand, β-hydride elimination is negligible for the conditions investigated in this study.

6.2 Introduction

The use of two single-site catalysts to synthesize polymers with complex microstructures is a very promising way to create novel polyolefins. For instance, dual metallocene systems have been used to produce polyolefins with bimodal distributions of molecular weight[132] and chemical composition,[133] and to maximize the formation of long chain branches in polyethylene.[28] Dual single-site catalysts have also been used to produce branched[85,116,124,134] or linear olefin block copolymers through terminal branching and the chain shuttling process, respectively.[135]

The use of two (or more) metallocene catalysts simultaneously requires a detailed knowledge of the kinetics of polymerization of both catalysts in order to make polymers with the proper balance of the two (or more) components. For instance, a polyolefin with bimodal molecular weight distribution will be produced only if the mass fractions and ratios of molecular weight averages of the polymers made by the two catalysts are within a specified range.[136-138] Since these variables are sensitive to polymerization temperature, monomer pressure, catalyst and hydrogen concentrations, a polymerization kinetics model is essential for property control of polymers made with dual single-site catalysts.

In this chapter, we investigate the ethylene polymerization kinetics with *rac*-Et(Ind)$_2$ZrCl$_2$/MAO in a solution reactor to determine its main reaction kinetic constants. Part of this Chapter has been published in Journal of Macromolecular Symposia[139].

6.3 Experimental

6.3.1 Materials

Methylaluminoxane (MAO, 10 wt % in toluene, Sigma-Aldrich) was used as received. Ethylene and nitrogen (Praxair) were purified by passing through molecular sieves (3 and 4-Å) and copper(II)oxide packed beds. Toluene (EMD) was purified by distillation over an n-butyllithium/styrene/sodium system and then passed through two packed columns in series filled with molecular sieves (3, 4, and 5-Å) and Selexorb for further purification. All air-sensitive compounds were handled under inert atmosphere in a glove box.

The catalyst, *rac*-ethenebis(indenyl) zirconium dichloride (rac-Et[Ind]$_2$ZrCl$_2$), was purchased in powder form from Sigma-Aldrich. It was dissolved in toluene at concentration of 1×10^{-8} mol/g before polymerization. The toluene was distilled and passed through molecular sieves before being added to the catalysts to assure that it contained no catalyst poisons.

6.3.2 Polymer Synthesis

All polymerizations were performed in the semi-batch reactor described in Chapter 5, Section 5.1.2. The reaction medium was mixed using a pitched-blade impeller connected to magneto-driver stirrer, rotating at 2000 rpm. Prior to use, the reactor was heated to 125^{o}C, evacuated, and refilled with nitrogen six times to reduce the oxygen level, before being charged with 250 ml of toluene and 0.5 g of AliBu$_3$ as a scavenger. The temperature was then increased to 120^{o}C and kept constant for 20 minutes. Finally, the reactor contents were blown out under nitrogen pressure. This procedure ensures excellent removal of impurities from the reactor walls.

In a typical polymerization run, 200 ml of toluene were charged into the reactor, followed by an appropriate amount of MAO, introduced via a 5 ml tube and a 20 ml sampling cylinder connected in series with an ethylene pressure differential of 20 psig. A specified volume of toluene was placed in the sampling cylinder before injection to wash the tube wall from any MAO solution. The same method was applied to inject the catalyst solution into the reactor. Monomer was supplied on demand to maintain a constant reactor pressure of 120 psig and monitored with a mass flow meter. With the exception of a 1–2^{o}C exotherm upon catalyst injection, the temperature was kept at 120^{o}C ± 0.15^{o}C throughout the reaction. After 15 minutes, the polymerization was stopped by closing the monomer valve and immediately blowing out the reactor contents into a 1-L beaker filled with 400 ml of

ethanol. The polymer produced was then kept overnight, filtered, washed with ethanol, dried in air, and further dried under vacuum.

6.3.3 Polymer characterization

Molecular weight distributions (MWD) were determined with a Polymer Char high-temperature gel permeation chromatographer (GPC), at 145^{o}C under a flow rate of trichlorobenzene of 1 ml/min. The GPC is equipped with three detectors in series (infra-red, light scattering, and differential viscosimeter) and was calibrated with polystyrene narrow standards using the universal calibration curve.

6.4 Results and Discussion

To estimate the ethylene polymerization kinetic constants during solution polymerization, the ethylene concentration in solution as a function of ethylene partial pressure and reaction temperature needs to be determined first. The method used for measuring ethylene concentration in toluene is explained below.

6.4.1 Estimation of Ethylene Concentration in Toluene

A volume of 200 ml of toluene at 25^{o}C was introduced into the reactor using a calibrated sight glass. The reactor was heated up to the desired temperature and ethylene was fed until the desired pressure was established, while recording its flow rate with the in-line volume flow meter. The total moles of ethylene transferred to the reactor were obtained by integrating with time the ethylene volume flow rate into the reactor and converting it to number of moles using the ideal gas law. Ideal gas behavior was also assumed for calculating the total number of moles in the vapor phase. Assuming Ideal gas behavior is appropriate because calculation of the compressibility factor using Lee/Kesler correlation[140] gives Z values 0.97-0.99 for the range of temperatures and pressures used in the polymerizations.

Therefore, we can write for toluene,

$$(1-y_E)P = (1-x_E)P_{tol}^{sat} \tag{6-1}$$

where y_E and x_E and are the mole fractions of ethylene in the vapor and liquid phases, respectively, and P and P_{tol}^{sat} are the total reactor pressure and toluene vapor pressure, respectively.

Ethylene mole fractions in the vapor and liquid phases, and the number of moles of toluene in the vapor phase were calculated with the expressions,

$$y_E = \frac{N_E^g RT}{P(V_T - V_l)} \tag{6-2}$$

$$x_E = \frac{N_E^T - N_E^g}{N_E^T + N_T^T - (N_E^g + N_T^g)} \tag{6-3}$$

$$N_T^g = \frac{P(V_T - V_l)}{RT} - N_E^g \tag{6-4}$$

where V_T is the total reactor volume, V_l is the volume of liquid phase in the reactor, N_E^g and N_T^g are the number of moles of ethylene and toluene in the gas phase, respectively, and N_E^T and N_T^T are the total number of moles of ethylene and toluene fed into the reactor. Substituting Equations (6-2), (6-3) and (6-4) into Equation (6-1) gives

$$\left(P - \frac{N_E^g RT}{V_T - V_l}\right) = \left(1 - \frac{N_E^T - N_E^g}{N_E^T + N_T^T - \frac{P(V_T - V_l)}{RT}}\right) P_{tol}^{sat} \tag{6-5}$$

Solving Equation (6-5) yields the value of N_E^g at the specified temperature and pressure. The other unknowns are obtained with the expressions,

$$N_E^l = N_E^T - N_E^g \tag{6-6}$$

$$N_T^l = N_T^T - N_E^g \tag{6-7}$$

$$N_T^g = \frac{P(V_T - V_l)}{RT} - N_E^g \tag{6-8}$$

Finally, the ethylene concentration was calculated using the equation,

$$C_E = \frac{N_E^l}{\nu_l (N_E^L + N_T^L)} \tag{6-9}$$

where ν_l is the specific volume of the liquid phase and C_E is the ethylene concentration in the liquid phase. ASPEN PLUS was used to estimate the specific volumes of the liquid phase at different ethylene mole fractions. The reactor volume was determined by filling it with toluene at room temperature. The volume of toluene was calculated by measuring its mass using a precision scale, with accuracy of ±0.001 g, and knowing its accurate density, 866.96 ± 0.09 Kg/m^3 at 95 % confidence limit at 20^{o}C.[141] Five replicate reactor volume measurements resulted in an average reactor volume of V_T = 608.7 ml, with standard deviation of 0.7 ml.

Wagner equation[142] was used to calculate vapor pressures of toluene at different temperatures,

$$\ln P_r^{sat} = \frac{A\tau + B\tau^{1.5} + C\tau^3 + D\tau^6}{1-\tau} \quad (6\text{-}10)$$

$$\tau = 1 - \frac{T}{T_C} \quad (6\text{-}11)$$

$$P_r^{sat} = \frac{P^{sat}}{P_C} \quad (6\text{-}12)$$

where *A*, *B*, *C*, and *D* are empirical constants, and T_C and P_C are the critical temperature and pressure. For toluene, *A* = - 7.28607, *B* = 1.38091, *C* = - 2.83433, *D* = - 2.79168, T_C = 591.8 K , P_c = 41.06 bar.[142]

Ethylene concentrations at five different temperatures, from 100 to 140^{o}C, and at constant pressure of 120 psig, were measured using the method explained above. Three replicates at 120^{o}C were performed to estimate standard deviation for ethylene concentration, and found to be 0.0046 mol/L. Table 6-1 summarizes the result of these calculations and Figure 6-1 depicts the ethylene concentration in toluene versus temperature. An almost linear relationship was observed for the studied range of temperatures. Ethylene concentrations in toluene were also measured for eleven different ethylene pressures at 120^{o}C (Table 6-2). A linear relation represents the dependency reasonably well, as depicted in Figure 6-2.

Table 6-1. Ethylene concentration in toluene at 120 psig and different temperatures.

Temperature (^{o}C)	**Ethylene Concentration (mol/L)**	**Temperature (^{o}C)**	**Ethylene Concentration (mol/L)**
120	0.451	120	0.451
120	0.459	110	0.489
100	0.528	130	0.412
140	0.373		

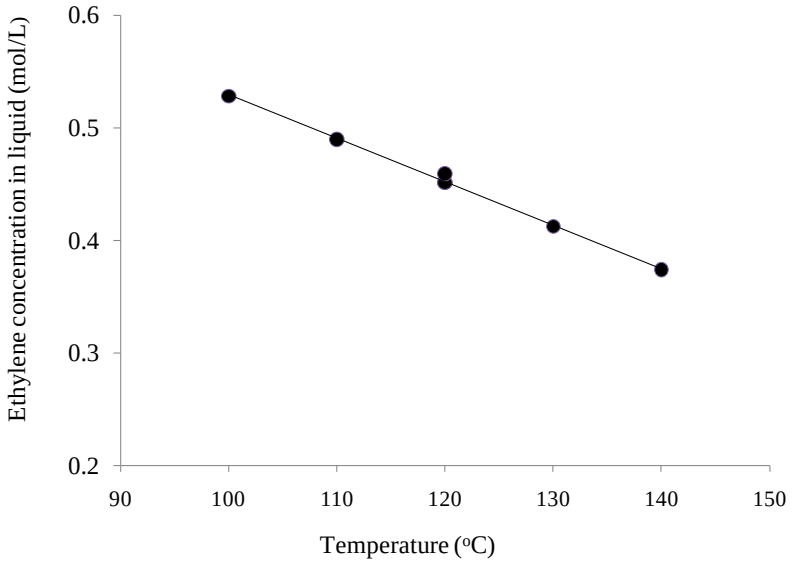

Figure 6-1. Concentration of ethylene in toluene as a function of temperature at total pressure of 120 psig.

Table 6-2. Ethylene concentration in toluene at 120°C and different total pressures.

Pressure (psig)	**Ethylene Concentration (mol/L)**	**Pressure (psig)**	**Ethylene Concentration (mol/L)**
35.6	0.110	162.5	0.631
58.4	0.203	184	0.717
80	0.292	205.2	0.805
99.2	0.370	227.2	0.901
120.7	0.459	240	0.950
141.6	0.541		

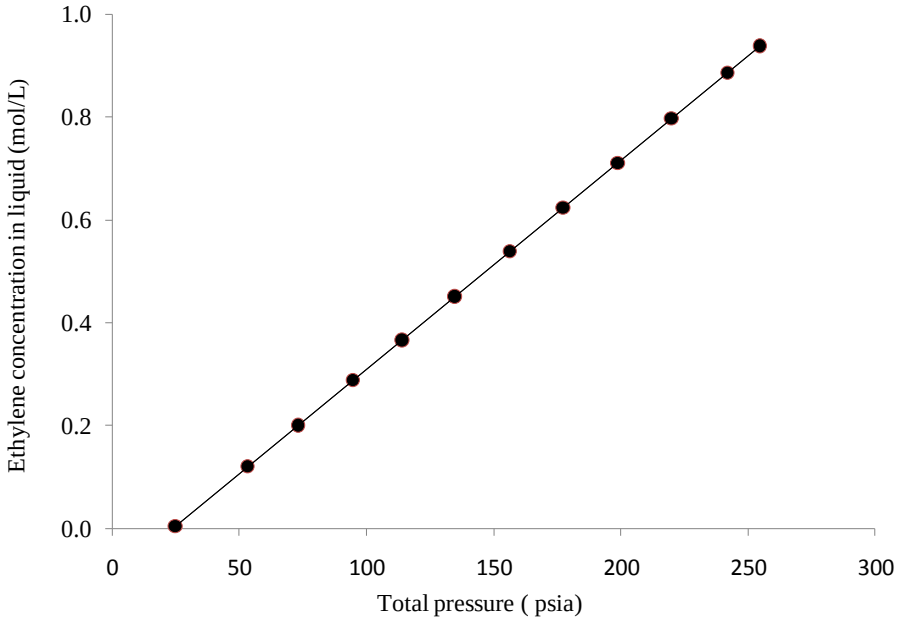

Figure 6-2. Concentration of ethylene in toluene as a function of total pressure at 120°C.

6.4.2 Effect of Catalyst Concentration

A complete randomized design with seven catalyst concentration levels and two replicates at each level was used to investigate the kinetics of *rac*-Et(Ind)$_2$ZrCl$_2$ deactivation. All polymerizations were performed at 120°C and 120 psig ethylene pressure with the same solvent volume (222.8 ml toluene) and MAO mass (1.6258 g). Figure 6-3 shows the ethylene volumetric consumption rates versus polymerization time for these set of runs.

Several elementary reactions take place during coordination polymerization: initiation, propagation, long chain branch formation, chain transfer reactions, and catalyst deactivation. For catalyst deactivation studies, however, just the initiation, propagation and deactivation steps need to be considered, as described below,

Initiation $$C_i + M \xrightarrow{k_p} P^* \quad (6\text{-}13)$$

Propagation $$P^* + M \xrightarrow{k_p} P^* \quad (6\text{-}14)$$

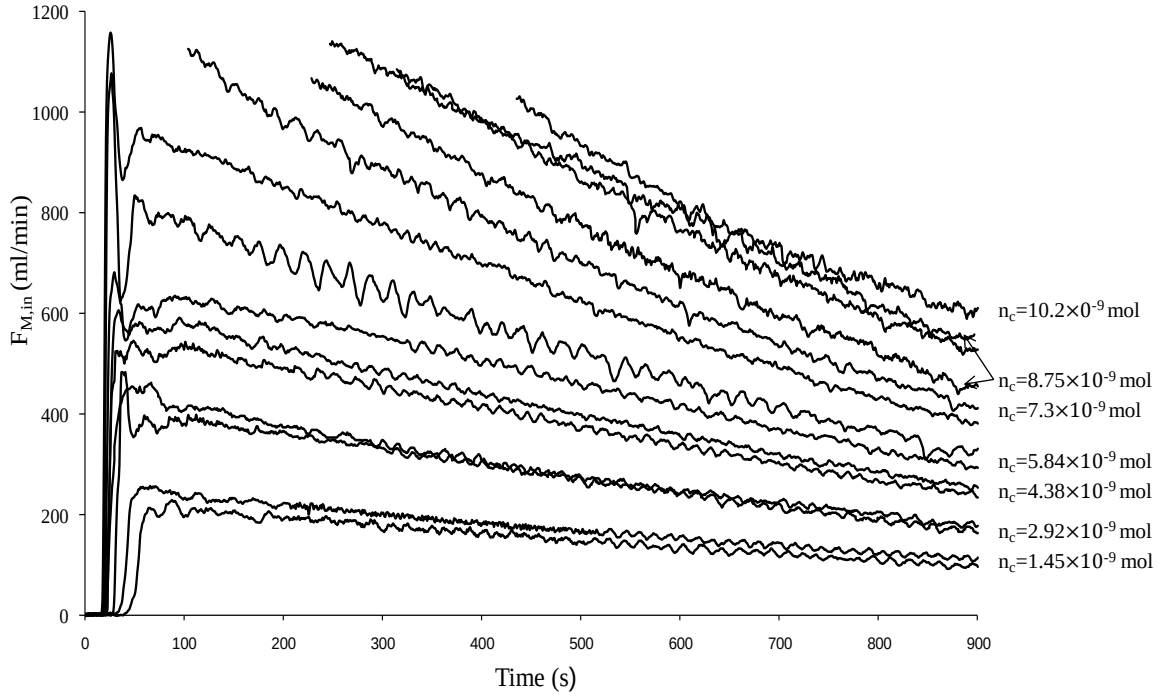

Figure 6-3. Ethylene consumption rates versus polymerization time for different catalyst concentrations. Labels on the side shows moles of catalyst injected into the reactor.

Deactivation

$$P^* \xrightarrow{k_d} D + \hat{C}_i \tag{6-15}$$

$$C_i \xrightarrow{k_d} \hat{C}_i \tag{6-16}$$

where, P^* represents living chains, D dead chains, C_i, monomer-free active sites, and $\hat{C}_i$ deactivated catalyst sites. We have also assumed that the initiation and propagation constants, k_p, have the same value and that the two catalyst deactivation steps, shown in Equations (6-15) and (6-16), also share the same kinetic constant, k_d.

The molar balances for active catalyst sites and living chains are given by,

$$\frac{\mathrm{d}[C_i]}{\mathrm{d}t} = -k_p[C_i][M] - k_d[C_i] \tag{6-17}$$

$$\frac{\mathrm{d}[P^*]}{\mathrm{d}t} = k_p[C_i][M] - k_d[P^*] \tag{6-18}$$

Solving these simultaneous differential equations with the initial conditions (at t = 0) $[C_i]=[C_i]_0$ and $[P^*]=0$ yields

$$[P^*]=[C_i]_0[e^{-k_d t}-e^{-(k_d+k_p[M])t}] \tag{6-19}$$

$$[C_i]=[C_i]_0 e^{-k_d t}-[P^*] \tag{6-20}$$

The second exponential term in Equation (6-19) is negligible because it contains the large term $k_p[M]$. Thus, Equation (6-19) simplifies to,

$$[P^*]=[C_i]_0 e^{-k_d t} \tag{6-21}$$

The molar balance for monomer is given by,

$$\frac{\mathrm{d}[M]}{\mathrm{d}t}=\frac{F_{M,in}}{V_R}-k_p[P^*][M] \tag{6-22}$$

where $F_{M,in}$ is the molar flow rate of ethylene to the reactor and V_R is the volume of the reaction medium.

Substituting Equation (6-21) into Equation (6-22) and solving the resulting equation using the assumption that monomer concentration is constant, we conclude that, for a first order catalyst decay, the kinetic data obeys the following relation,

$$\ln\left(\frac{F_{M,in}}{V_R}\right)=\ln(k_p[C_i]_0[M])-k_d t \tag{6-23}$$

Consequently, a plot of $\ln\left(\frac{F_{M,in}}{V_R}\right)$ versus polymerization time should have a constant slope equal to k_d and an intercept equal to $\ln(k_p[C_i]_0[M])$ for catalysts that follow first order catalyst decay kinetics and first order propagation rate with respect to monomer concentration. This is exactly what is illustrated in Figure 6-4 for ethylene polymerization runs with *rac*- Et(Ind)$_2$ZrCl$_2$. Table 6-3 shows the values estimated for k_d and $k_p[M]$, using this approach, as well as the experimental values for polymer yield.

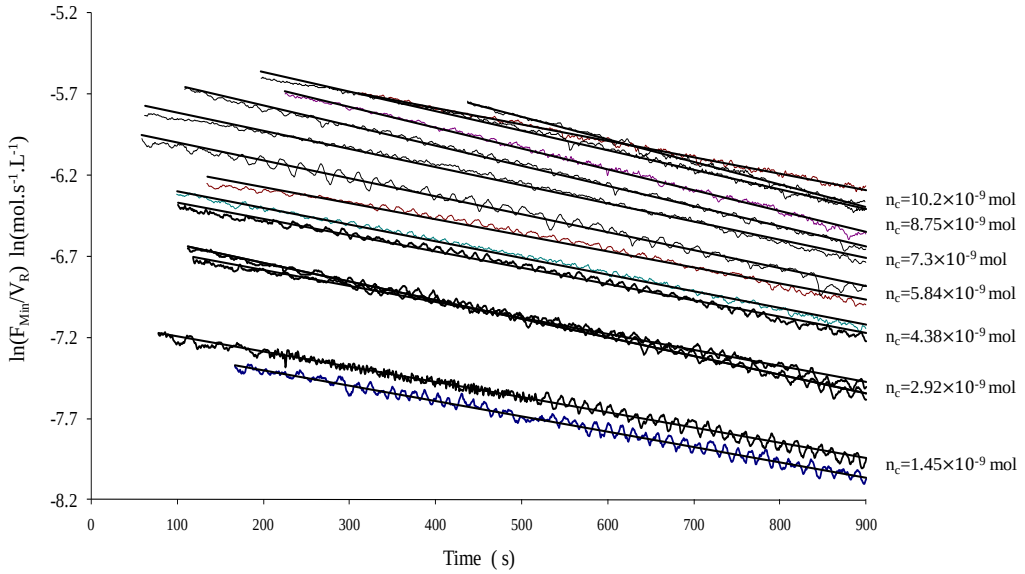

Figure 6-4. Ethylene polymerization with rac-Et(Ind)$_2$ZrCl$_2$ with several catalysts concentrations.

Table 6-3. Reaction rate constant for rac-Et(Ind)$_2$ZrCl$_2$ (varying catalyst concentration).

Run	Moles of Catalyst	Slope	Intercept	$k_p[M]$ (s^{-1})	k_d (s^{-1})	Polymer Yield (g)	*Activity* (tonne PE/(mol Zr.hr))[a]
8	5.84×10^{-9}	-0.00102	-6.05543	89 462	1.02×10^{-3}	8.60	5 885
4	4.38×10^{-9}	-0.00104	-6.24759	98 339	1.04×10^{-3}	7.15	6 524
14	1.02×10^{-8}	-0.00119	-5.33151	105 384	1.19×10^{-3}	16.20	6 335
3	7.30×10^{-9}	-0.00116	-5.67598	104 540	1.16×10^{-3}	11.74	6 429
11	2.92×10^{-9}	-0.001	-6.57702	104 638	1.00×10^{-3}	5.17	6 970
12	8.76×10^{-9}	-0.00129	-5.39051	116 070	1.29×10^{-3}	14.36	6 559
6	5.84×10^{-9}	-0.00114	-5.86786	108 863	1.14×10^{-3}	9.78	6 754
7	4.38×10^{-9}	-0.00105	-6.18042	104 731	1.05×10^{-3}	7.45	6 762
1	2.92×10^{-9}	-0.00116	-6.50186	113 912	1.16×10^{-3}	5.32	7 247
9	1.45×10^{-9}	-0.00098	-7.19717	114 745	1.1×10^{-3}	2.91	8 012
11	1.02×10^{-8}	-0.00112	-5.1405	127 723	1.11×10^{-3}	17.37	6 801
2	7.30×10^{-9}	-0.00124	-5.52014	121 843	1.24×10^{-3}	13.10	7 152
5	1.45×10^{-9}	-0.00095	-7.0934	127 091	0.95×10^{-3}	3.25	8 925
13	8.76×10^{-9}	-0.00101	-5.38016	117 216	1.01×10^{-3}	15.18	6 933

a: One tonne is equivalent to 1000 Kg

Theoretically, it is preferred to estimate the kinetic parameters via nonlinear regression on the untransformed data; therefore, Equation (6-23) is expressed below in a form suitable for nonlinear regression,

$$F_{M,in} = V_R k_p [C_i]_0 [M] e^{-k_d t} \tag{6-24}$$

or

$$F_{M,in} = a e^{-k_d t} \tag{6-25}$$

Where,

$$a = n_c \times k_p [M] \tag{6-26}$$

$$n_c = V_R [C_0] \tag{6-27}$$

and n_c is the number of moles of catalyst injected into the reactor.

Nonlinear regression on the monomer consumption rate × time data using Equation (6-25) gives the results for k_d and a listed in Table 6-4. Equation (6-26) was used to obtain $k_p[M]$ from a. The parameters k_d and $k_p[M]$ were also estimated through linear regression and are reproduced in the last two columns of Table 6-4. Rate constant estimates using linear and nonlinear regression are practically the same.

We can describe the values estimated for k_d and k_p with the single-factor ANOVA model,

$$Y_{i,j} = \mu + \tau_i + \varepsilon_{i,j} \tag{6-28}$$

where $Y_{i,j}$ is the $i \times j^{\text{th}}$ measurement, μ is the overall mean, τ_i is a parameter associated with the i^{th} treatment level (called the treatment effect; in the present case, catalyst concentration) and $\varepsilon_{i,j}$ is a random error component arising from all sources of variability. The null hypothesis is $H_0 : \tau_1 = \tau_2 = ... \tau_n = 0$ (where n = 7 catalyst concentration levels) and the alternative hypothesis is $H_1 : \tau_i \neq 0$ for at least one value of i.

Table 6-4. Summary of reaction rate constants for rac-Et(Ind)$_2$ZrCl$_2$ using nonlinear and linear regression.

Run	Moles of Catalyst	a	k_d (s^{-1})[a]	$k_p[M]$ (s^{-1})[a]	k_d (s^{-1})[b]	$k_p[M]$ (s^{-1})[b]
8	5.84×10^{-9}	5.15×10^{-4}	0.99×10^{-3}	88 228	1.02×10^{-3}	89 462
4	4.38×10^{-9}	4.22×10^{-4}	1.00×10^{-3}	96 358	1.04×10^{-3}	98 339
14	10.2×10^{-9}	9.97×10^{-4}	1.21×10^{-3}	97 540	1.19×10^{-3}	105 384
3	7.30×10^{-9}	7.55×10^{-4}	1.14×10^{-3}	103 400	1.16×10^{-3}	104 540
11	2.92×10^{-9}	3.08×10^{-4}	0.99×10^{-3}	105 637	1.00×10^{-3}	104 638
12	8.76×10^{-9}	10.05×10^{-4}	1.27×10^{-3}	114 744	1.29×10^{-3}	116 070
6	5.84×10^{-9}	6.25×10^{-4}	1.12×10^{-3}	107 004	1.14×10^{-3}	108 863
7	4.38×10^{-9}	4.57×10^{-4}	1.03×10^{-3}	104 355	1.05×10^{-3}	104 731
1	2.92×10^{-9}	3.32×10^{-4}	1.14×10^{-3}	113 766	1.16×10^{-3}	113 912
9	1.45×10^{-9}	1.66×10^{-4}	1.01×10^{-3}	114 029	0.98×10^{-3}	114 745
11	10.2×10^{-9}	13.03×10^{-4}	1.11×10^{-3}	127 503	1.11×10^{-3}	127 723
2	7.30×10^{-9}	8.83×10^{-4}	1.22×10^{-3}	120 939	1.24×10^{-3}	121 843
5	1.45×10^{-9}	1.84×10^{-4}	0.94×10^{-3}	126 607	0.95×10^{-3}	127 091
13	8.76×10^{-9}	10.29×10^{-4}	1.02×10^{-3}	117 484	1.01×10^{-3}	117 216

[a] Estimated using nonlinear regression; [b] Estimated using linear regression.

The analysis of variance for the parameter k_d, estimated through nonlinear regression, is summarized in Table 6-5. The test statistic F_0, which is the ratio of treatment mean square to error mean square, was used to test the null hypothesis. Since $F_0 = 1.55$ is less than $F_{0.05\ 6,\ 7} = 3.866$, we accept the null hypothesis. This means that each k_d measurement consists of the overall mean plus a realization of the random error component $\varepsilon_{i,j}$. This is equivalent to saying that all 14 k_d estimates are taken from a normal distribution with mean μ and variance σ^2. Consequently, catalyst concentration does not influence the value of k_d, as expected from the first order deactivation processes proposed in Equations (6-15) and (6-16). The normal probability plot for k_d, shown in Figure 6-5, confirms the normal distribution of the k_d estimates with confidence level of 95% and a value of

$k_d = 1.081\times10^{-3}\pm6\times10^{-5}\ s^{-1}$.

A similar analysis of variance, repeated for k_p[M] (Table 6-6) shows that the values estimated for $k_p[M]$ (109 828±6 660 s^{-1}) are also independent of catalyst concentration.

Figure 6-6 shows plot of $k_p[M]$ and k_d versus catalyst concentration. The normal probability plot for $k_p[M]$ is shown in Figure 6-7.

The use of analysis of variance to test for no difference in treatment means requires that the measurement errors be normally and independently distributed with mean zero and a constant (but unknown) variance σ^2.[143] In Figure 6-8, the normal probability plot for the residuals of k_d was constructed, indicating that they are normally distributed. No pattern was seen either in the plot of residuals versus run order and concentration, confirming independent distribution of the residuals. The same test was repeated for k_p[M] to test normal distribution of the residuals, as shown in Figure 6-9.

Table 6-5. Analysis of variance for k_d (varying catalyst concentration).

Source of Variation	**Sum of Squares**	**Degrees of Freedom**	**Mean Square**	F_0	**P-Value**
Catalyst Concentration	8.1×10^{-8}	6	1.35×10^{-8}	1.55	0.29
Error	6.1×10^{-8}	7	8.73×10^{-9}		
Total	1.42×10^{-7}	13			

Table 6-6. Analysis of variance for $k_p[M]$ (varying catalyst concentration).

Source of Variation	**Sum of Squares**	**Degrees of Freedom**	**Mean Square**	F_0	**P-value**
Catalyst Concentration	8.02×10^{8}	6	1.337×10^{8}	1.01	0.487
Error	9.27×10^{8}	7	1.324×10^{8}		
Total	1.73×10^{9}	13			

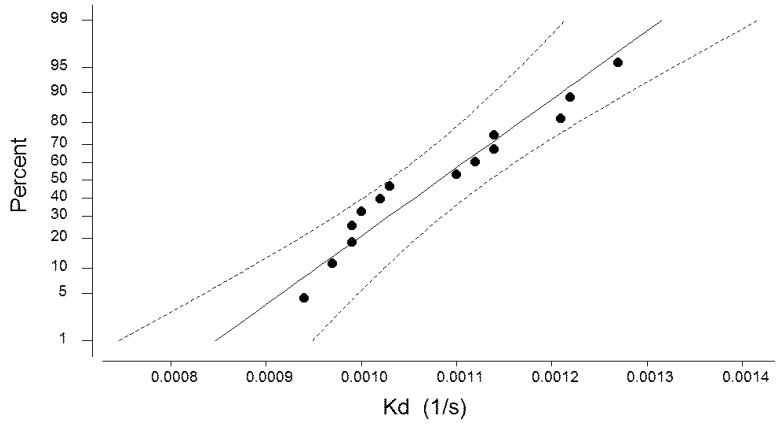

Figure 6-5. Normal probability plot for k_d with 95% confidence limits (varying catalyst concentration).

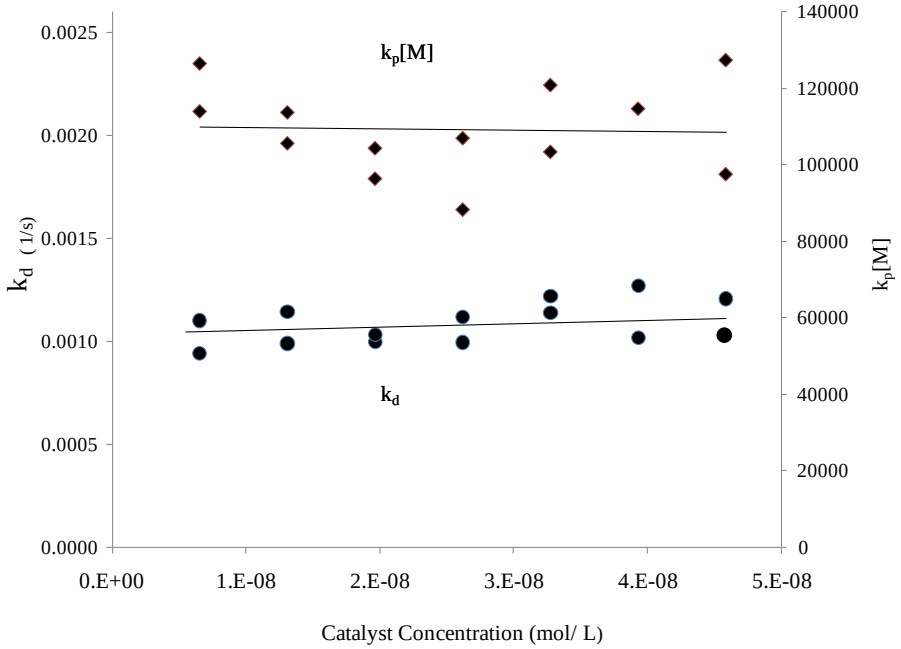

Figure 6-6. Plot of $k_p[M]$ and k_d versus catalyst concentration.

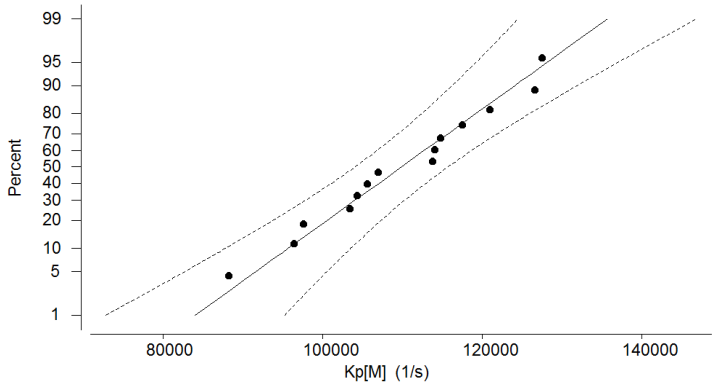

6-7. Normal probability plot for $k_p[M]$ with 95% confidence limits (varying catalyst concentration). (Minitab output).

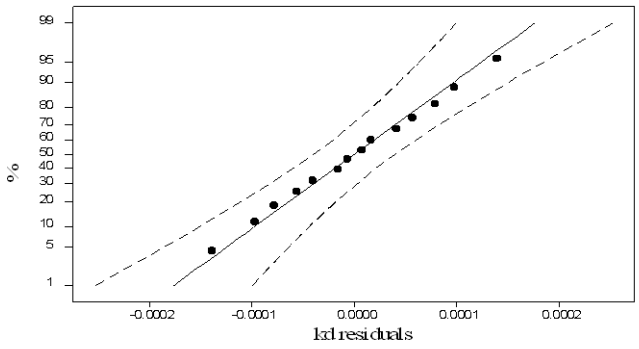

Figure 6-8. Normal probability plot for k_d residuals (varying catalyst concentration).

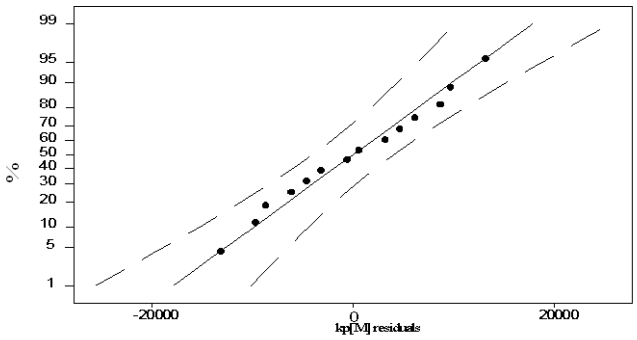

Figure 6-9. Normal probability plot for $k_p[M]$ residuals (varying catalyst concentration).

Another point worth mentioning is that, although the k_d or $k_p[M]$ values estimated by nonlinear regression are not exactly the same as those estimated using the slope and intercept of semi-log graph plot for monomer consumption rate versus time (Figure 6-4), their average values and variances are the same (Table 6-7), which can be verified using basic statistics.[144] The 95 % confidence interval on the difference between the two means, knowing that variances are equal is (see Appendix I),

$$-6.7\times10^{-5} \leq k_{d,l} - k_{d,nl} \leq 9.5\times10^{-5}\ s^{-1} \quad (6\text{-}29)$$

where $k_{d,l} - k_{d,nl}$ are the deactivation rate constant estimated by linear and nonlinear regression, respectively. Since the confidence interval includes zero, it is unlikely that these two means are different. A similar confidence interval estimation for the difference between the two means for $k_p[M]$ leads to the same conclusion,

$$-9903 \leq k_p[M]_l - k_p[M]_{nl} \leq 7480\ s^{-1} \quad (6\text{-}30)$$

where $k_p[M]_l$ and $k_p[M]_{nl}$ are the linear and nonlinear regression estimates of $k_p[M]$, respectively (Appendix I gives more details on how confidence intervals for difference between two means were calculated).

Table 6-7. Comparison of k_d and $k_p[M]$ estimated using linear and nonlinear regression methods.

Parameter	Sample mean	Sample standard deviation
k_d	1.096×10^{-3}	1.04×10^{-4}
$k_p[M]$	111040	10830
k_d[a]	1.081×10^{-3}	1.05×10^{-4}
$k_p[M]$[a]	109828	11533

[a] Estimated using nonlinear regression with Equation (6-24).

Estimates for k_p and k_d can also be obtained by computing the mass of polymer (m_p) produced as a function of catalyst concentration

$$m_p = \left(28\frac{\text{g}}{\text{mol}}\right) \times \int_0^t F_{M,in}\,\text{d}t \tag{6-31}$$

Substituting Equation (6-24) into Equation (6-31), we find,

$$m_p = 28\frac{k_p}{k_d} n_c [M](1 - e^{-k_d t}) \tag{6-32}$$

Therefore, a plot of polymer yield (m_p) versus catalyst concentration should be linear with a slope $28k_p V_R[M](1-e^{-k_d t})/k_d$, as confirmed in Figure 6-10. If we estimate the value of $k_p[M]$ from the slope of the line in Figure 6-10 and the previously estimated value of k_d, we obtain $k_p[M]$ = 1.04×10^5 s^{-1}, which is in good agreement with the value estimated using nonlinear or linear regression of monomer consumption rate×time data given in Table 6.7.

Results of molecular weight measurements using GPC are summarized in Table 6-8. Analysis of variance for number and weight average molecular weights (M_n and M_w), as well as the polydispersity index (*PDI*) are presented in Tables 6-9, 6-10 and 6-11, respectively, demonstrating that none of them are affected by catalyst concentration. Figure 6-11 plots M_w, M_n and *PDI* versus catalyst concentration.

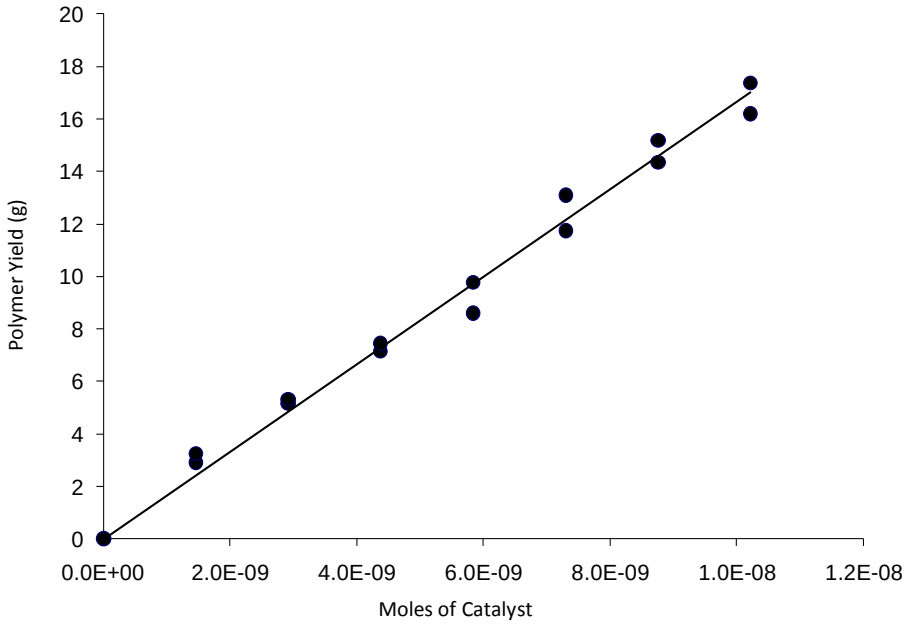

Figure 6-10. Polymer yield versus catalyst concentration.

Table 6-8.Summary of molecular weight measurement (varying catalyst concentration)

Run	Moles of Catalyst	M_n	M_w	PDI
8	5.84×10^{-9}	23 200	46 900	2.02
4	4.38×10^{-9}	23 800	47 600	2.00
14	1.02×10^{-9}	23 700	48 200	2.03
3	7.30×10^{-9}	23 400	47 200	2.02
11	2.92×10^{-9}	22 600	45 400	2.01
12	8.76×10^{-9}	23 500	46 500	1.98
6	5.84×10^{-9}	23 500	47 000	2.00
7	4.38×10^{-9}	22 700	46 000	2.03
1	2.92×10^{-9}	22 600	47 400	2.09
9	1.45×10^{-9}	23 100	46 000	1.99
11	1.02×10^{-9}	23 3005	46 600	2.00
2	7.30×10^{-9}	23 800	47 200	1.99
5	1.45×10^{-9}	22 200	45 000	2.03
13	8.76×10^{-9}	23 000	46 000	2.00

Table 6-9. Analysis of variance for M_n (varying catalyst concentration).

Source of Variation	Sum of Squares	Degrees of Freedom	Mean Square	F_0	P-value
Catalyst Concentration	1928 856	6	321 476	1.63	0.267
Error	1365 870	7	195 117		
Total	3294 676	13			

Table 6-10. Analysis of variance for M_w (varying catalyst concentration).

Source of Variation	Sum of Squares	Degrees of Freedom	Mean Square	F_0	P-value
Catalyst Concentration	5 249 117	6	874 853	1.24	0.388
Error	4 933 852	7	704 836		
Total	10 182 969	13			

Table 6-11. Analysis of variance for PDI (varying catalyst concentration).

Source of Variation	Sum of Squares	Degrees of Freedom	Mean Square	F_0	P-value
Catalyst Concentration	0.01029	6	0.00171	0.62	0.713
Error	0.01940	7	0.00277		
Total	0.02969	13			

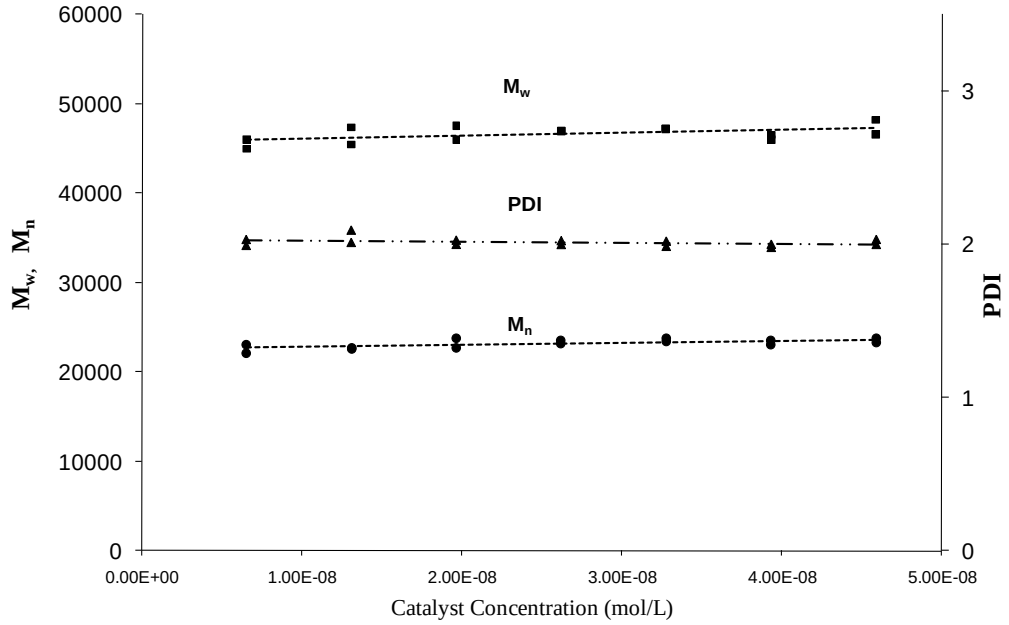

Figure 6-11. Molecular weight averages and PDI versus catalyst concentration.

6.4.3 Effect of Ethylene Pressure

A complete randomized design with 19 polymerization runs at 9 different, equally spaced, levels of ethylene pressure (40 to 200 psig), comprising three replicates at 140 psig and two replicates at other pressure levels was chosen to test the effect of monomer pressure on polymer yield, molecular weight, and reaction rate constants. All other polymerization conditions were kept constant: polymerization temperature = 120^{o}C, solvent type = toluene, solvent volume = 222.8 ml, catalyst concentration in the reactor = 1.316×10^{-8} mol/L, MAO mass = 1.6247 g.

Figure 6-12 shows the plot of monomer consumption versus time for several ethylene pressures. Similarly to the treatment adopted in Figure 6-4, we plotted $\ln\left(\frac{F_{M,in}}{V_R}\right)$ versus time in Figure 6-13 and estimated k_d and $k_p[M]$ from the curves intercept and slope. We also used nonlinear regression with Equation (6-25) to estimate k_d and $k_p[M]$. Table 6-12 summarizes the parameter estimate results and average molecular weight measurements.

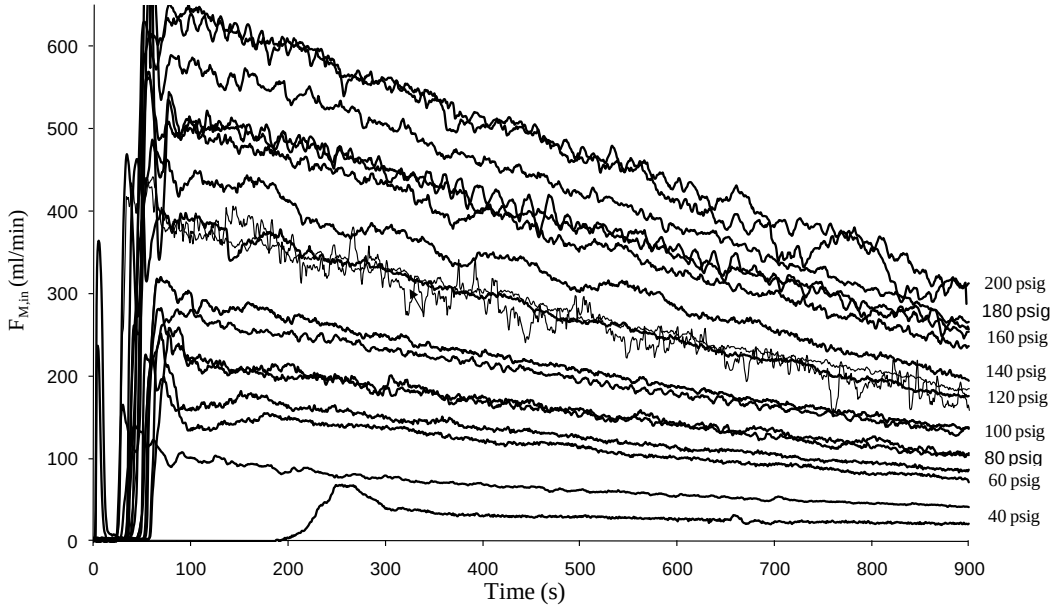

Figure 6-12. Ethylene consumption rate (ml/min) versus polymerization time for different ethylene pressures. (The numbers at the right-end of the curves refer to total pressures at which the polymerizations were performed).

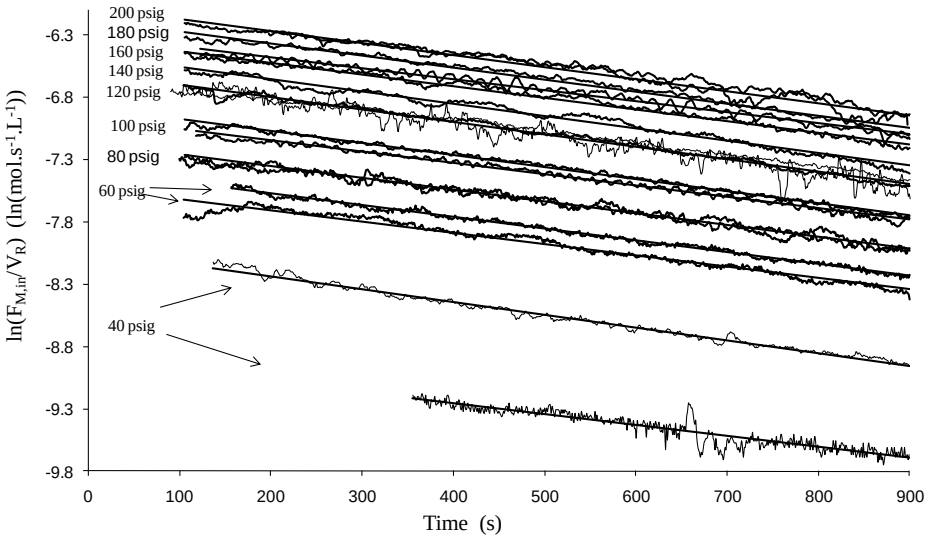

Figure 6-13. Ethylene polymerization with rac-Et(Ind)$_2$ZrCl$_2$ under several ethylene pressures (see Figure 6-12).

Table 6-12. Summary of reaction rate constant estimates and average molecular weight measurements for ethylene polymerization with rac-Et(Ind)$_2$ZrCl$_2$ (varying ethylene pressure).

Pressure (psig)	**Slope**	**Intercept**	$k_p[M]$ (s^{-1})[a]	k_d (s^{-1})[a]	$k_p[M]$ (s^{-1})[b]	k_d (s^{-1})[b]	M_n	M_w	***PDI***
120	-0.001004	-6.596	104 254	0.001004	104 361	0.000999	22 300	45 300	2.03
140	-0.000997	-6.453	119 867	0.000997	117 674	0.000960	23 600	47 200	2.00
60	-0.000975	-7.481	42 967	0.000975	42 876	0.000971	21 200	44 000	2.07
160	-0.000934	-6.339	134 295	0.000934	132 763	0.000908	24 200	47 600	1.96
200	-0.000994	-6.058	177 329	0.000994	174 545	0.000960	23 600	49 500	2.10
80	-0.000940	-7.167	58 502	0.000940	58 034	0.000920	23 000	45 500	1.98
180	-0.000996	-6.157	161 849	0.000996	159 466	0.000965	24 700	48 400	1.96
100	-0.000981	-6.868	78 853	0.000981	78 414	0.000970	22 500	46 100	2.05
180	-0.000924	-6.288	140 726	0.000924	139 567	0.000907	23 800	47 500	2.00
80	-0.000939	-7.172	58 019	0.000939	57 774	0.000930	22 000	45 800	2.08
140	-0.000937	-6.607	103 009	0.000937	102 314	0.000923	24 000	48 100	2.01
60	-0.000945	-7.381	47 382	0.000945	47 452	0.000947	21 100	44 200	2.09
160	-0.000882	-6.302	138 579	0.000882	137 109	0.000859	23 300	46 800	2.01
100	-0.000936	-6.946	72 904	0.000936	72 367	0.000922	22 800	46 100	2.02
120	-0.001024	-6.602	102 808	0.001024	102 143	0.001008	24 300	47 700	1.96
200	-0.000909	-6.087	172 872	0.000909	170 929	0.000886	24 000	47 600	1.99
39.5	-0.000909	-8.883	10 559	0.000909	10 741	0.000936	21 000	42 500	2.02
39	-0.001048	-8.021	24 993	0.001048	25 446	0.001041	NA	NA	NA
140	-0.000948	-6.593	104 232	0.000948	103 473	0.000934	22 800	46 600	2.04

a: Estimated using linear regression, b:Estimated using nonlinear regression with Equation (6-25).

Table 6-13 gives the analysis of variance for k_d (estimated by nonlinear regression). Since $F_0 = 1.93$ is less than test statistic $F_{0.05\ 8,\ 10} = 3.072$, we can conclude that k_d is not affected by monomer pressure, as expected from the proposed deactivation mechanism. This also indicates that the monomer feed does not introduce significant amounts of catalyst poisons in the reactor, in which case we should detect an apparent increase in k_d with increasing monomer pressure.

Table 6-13. Analysis of variance for k_d (varying ethylene pressure).

Source of Variation	Sum of Squares	Degrees of Freedom	Mean Square	F_0	P-value
Monomer Concentration	2.0625×10^{-8}	8	2.578×10^{-9}	1.94	0.164
Error	1.328×10^{-8}	10	1.328×10^{-9}		
Total	3.391×10^{-8}	18			

The normal probability plot for k_d (estimated by nonlinear regression), shown in Figure 6-14, confirms the normal distribution of the k_d estimates. The average value for k_d with confidence level of 95% is $k_d = 9.5\times10^{-4} \pm 2\times10^{-5}$ s^{-1}. The corresponding average value for k_d estimated by linear regression is the same $k_d = 9.6\times10^{-4} \pm 2.1\times10^{-5}$ s^{-1}. Figure 6-15 plots k_d versus total pressure, showing that k_d does not depend on monmer concentration, again confirming that the proposed first order decay is the correct choice for this polymerization system.

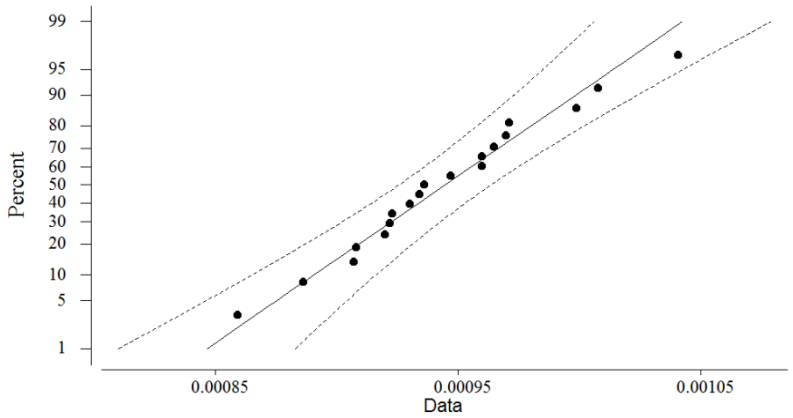

Figure 6-14. Normal probability plot for k_d with 95% confidence limit 95% (varying ethylene pressure).

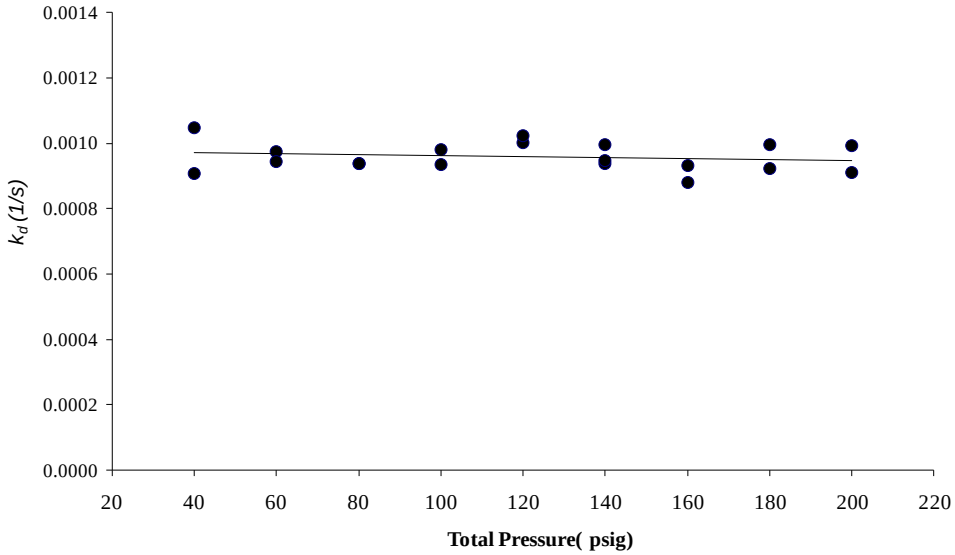

Figure 6-15. Plot of k_d versus total pressure.

When we compare the sample mean for k_d estimated when the catalyst concentration was changed ($k_{d,C=}1.08\times10^{-3}\pm6\times10^{-5}$ s^{-1}) and the one obtained when pressure was varied ($k_{d,P}=9.5\times10^{-4}\pm2\times10^{-5}$ s^{-1}), we notice that they disagree slightly. To determine the difference between these two means, we need to determine, first, whether their sample variances are equal or different. Hypothesis testing on ratio of the sample variances[144] of these two samples shows that their variances are different (see Appendix I). Using basic statistics, the 95 % confidence interval of the difference between the means is $8.3\times10^{-5} \leq k_{d,C} - k_{d,P} \leq 1.9\times10^{-4}$ s^{-1}. This difference is small and may be associated to batch-to-batch solvent purity variation, since we used two different solvent batches for the catalyst concentration and ethylene pressure investigations.

The dependency of $k_p[M]$ on total reactor pressure and ethylene concentration in toluene are shown in Figures 6-16 and 6-17, respectively. A clear first order dependency with respect to ethylene concentration is noticed, and the slope of the curve in Figure 6-17 gives a point estimate of k_p =213,000 $L\cdot mol^{-1}\cdot s^{-1}$. (Experimental ethylene concentrations data in Table 6-2 were used to estimate ethylene concentrations at different pressures.)

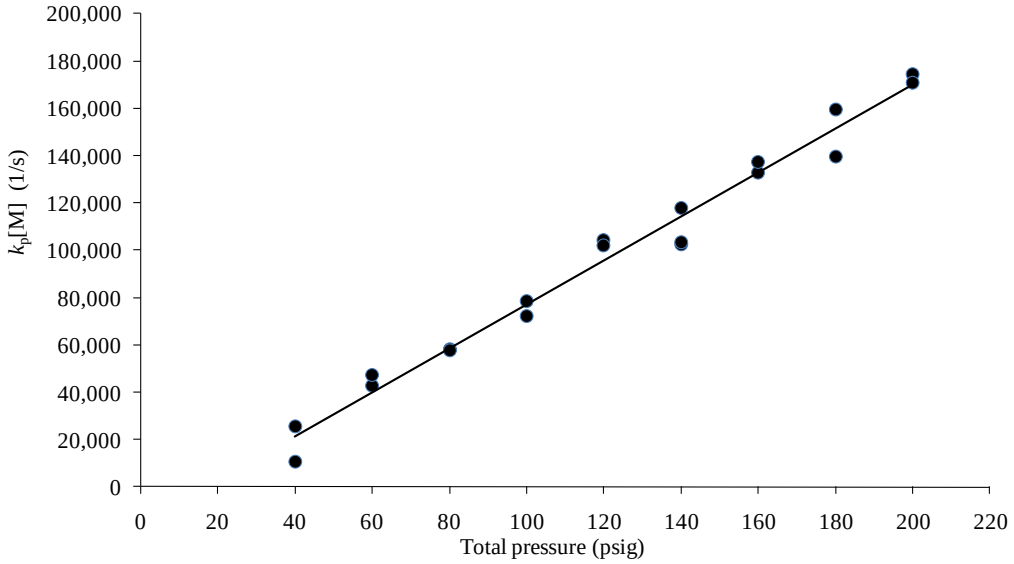

Figure 6-16. Plot of $k_p[M]$ versus total pressure.

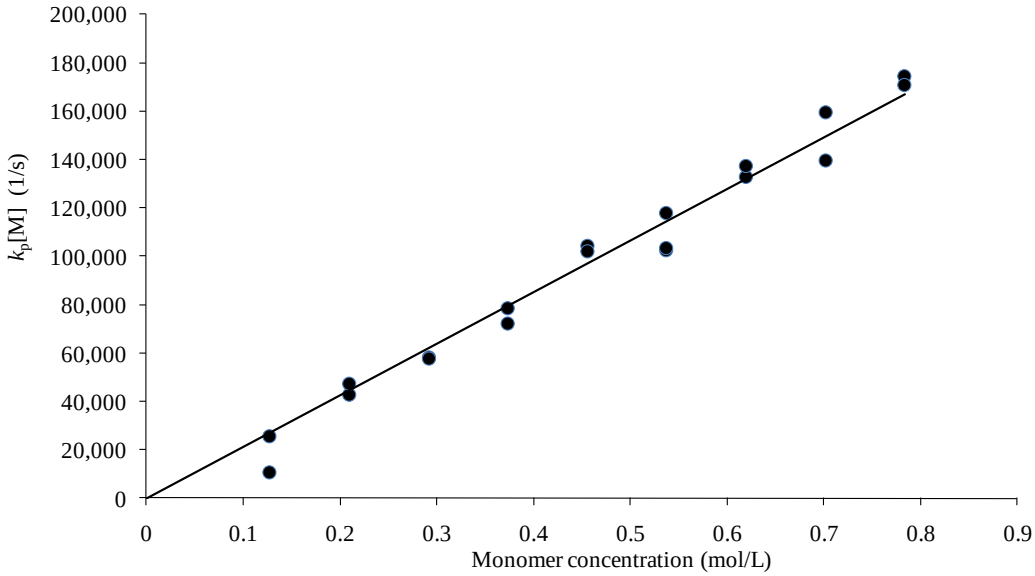

Figure 6-17. Plot of $k_p[M]$ versus monomer concentration.

Curve fitting of the $k_p[M]$, ethylene concentration data using linear regression model gives the following 95% confidence intervals on slope, k_p, and intercept, assuming that the ethylene concentration variable is error-free:

Intercept=-7526±8400 1/s

k_p= 226600±16600 L/(mol.s)

The confidence interval for intercept includes zero, meaning that this term is not significant in the model and we expect this because at zero ethylene concentration $k_p[M]$ should be zero. Figure 6-17 is, in fact, the no-intercept fit of the $k_p[M]$ data versus ethylene concentration. Assuming that the ethylene concentration variable is error-free, we can estimate 95% confidence interval for k_p, which is 213000±7300 L/(mol.s). This assumption is not too much unrealistic because the variability in $k_p[M]$ data is much higher than the variability in the regressor variable, ethylene concentration. Calculation of pooled standard deviation based on all $k_p[M]$ data estimated using nonlinear regression (Table 6-12) gives an estimate of 7096 s^{-1}, while standard deviation for ethylene concentration is 0.0046 mol/L. If we perturb ethylene concentration by one standard deviation, 0.0046 mol/L, the change in $k_p[M]$ would be 213000×0.0046=980 s^{-1}, which is one order of magnitude less than 7096 s^{-1}, the pooled standard deviation of $k_p[M]$ data. This implies that measurement error in ethylene concentration can be ignored and standard least squares methods applied.

The analysis of variance for M_w and M_n is summarized in Tables 6-14 and 6-15. Since F_0 = 7.6 for M_w and F_0 = 4.72 for M_n are both greater than $F_{0.05\ 8,\ 9}$ = 3.23, we accept that M_w and M_n are affected by the monomer concentration, as expected. As shown in Figure 6-18, both M_w and M_n increase linearly with pressure, but the increase in M_w is more pronounced than the increase in M_n, as implied by their P and F_0 values[145].

Table 6-14. Analysis of variance for M_w (varying ethylene pressure).

Source of Variation	**Sum of Squares**	**Degrees of Freedom**	**Mean Square**	F_0	***P*-value**
Monomer Concentration	4.459×10^7	8	5.573×10^6	7.6	0.003
Error	6.601×10^6	9	7.335×10^5		
Total	5.119×10^7	17			

Table 6-15. Analysis of variance for M_n (varying ethylene pressure).

Source of Variation	Sum of Squares	Degree of freedom	Mean Square	F_0	*P*-value
Monomer Concentration	1.781×10^7	8	2.226×10^6	4.72	0.016
Error	4.245×10^6	9	4.717×10^5		
Total	2.205×10^7	17			

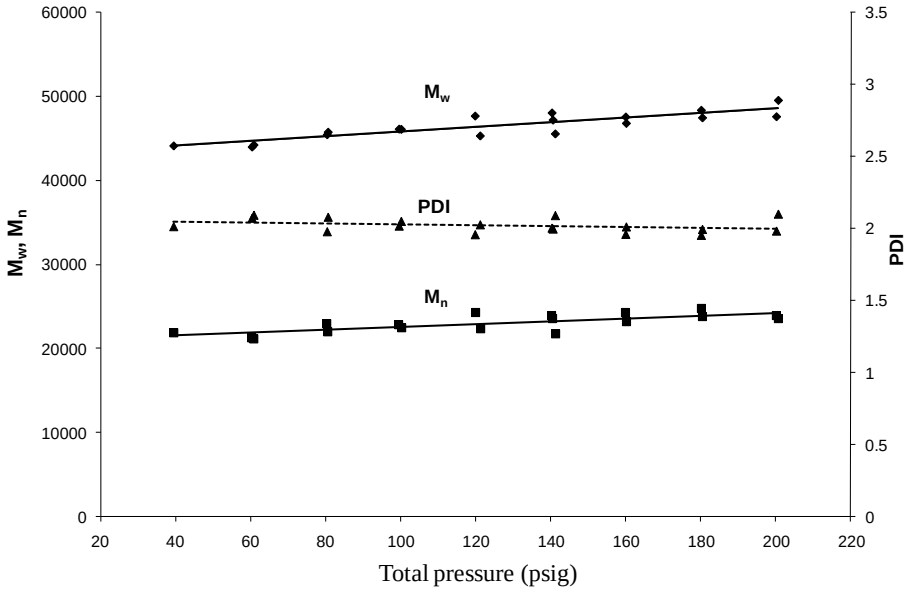

Figure 6-18. Effect of ethylene pressure on M_w, M_n and *PDI*.

Figures 6-19 shows that the polymer yield varies linearly with ethylene concentration. This linear relationship confirms that the rate of polymerization is first order with respect to ethylene concentration for $Et(Ind)_2ZrCl_2$ under this range of experimental conditions.

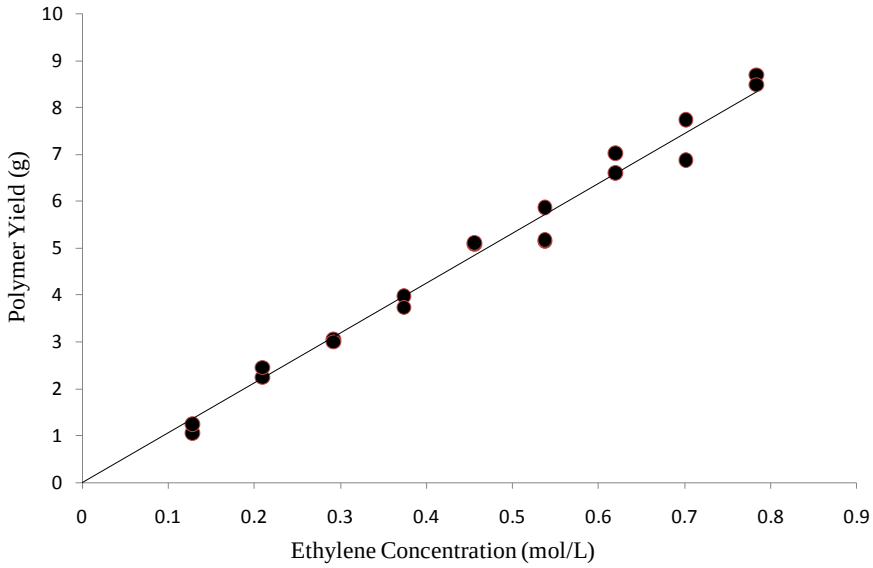

Figure 6-19. Polymer yield as a function of ethylene concentration in toluene.

6.4.4 Estimation of Rate Transfer Constants

The molecular weight distribution of polyolefins made with single site catalysts follows Flory's most probable distribution,

$$w(r) = r\tau^2 \exp(-r\tau) \tag{6-28}$$

where r is the chain length and $w(r)\mathrm{d}r$ is the weight fraction of chains with length in the interval [r, r + dr]. For linear chains, the parameter τ is the reciprocal of the number average chain length,

$$\tau = \frac{1}{r_n} \tag{6-29}$$

$$\tau = \frac{mw}{M_n} \tag{6-30}$$

where r_n is number average chain length and mw is monomer molecular weight.

The parameter τ can also be expressed as,

$$\tau = \frac{R_{tM} + R_{t\beta H} + R_{CTA}}{R_P} \tag{6-31}$$

where R_P is the rate of propagation, and R_{tM}, $R_{t\beta H}$ and R_{CTA} are the rates of transfer to monomer, β-hydride elimination, and transfer to chain transfer agent (in our case, transfer to MAO), respectively. Substituting the relevant rate terms in Equation (6-31) gives,

$$\frac{1}{M_n} = \frac{k_{tM}[M] + k_{t\beta H} + k_{tAl}[Al]}{mw\ k_p[M]} \tag{6-32}$$

or,

$$\frac{1}{M_n} = \frac{k_{tM}}{mw\ k_p} + \frac{k_{t\beta H} + k_{tAl}[Al]}{mw\ k_p} \times \frac{1}{[M]} \tag{6-33}$$

or, equivalently,

$$M_n = \frac{[M]}{\frac{k_{tM}}{mw\ k_p}[M] + \frac{k_{t\beta H} + k_{tAl}[Al]}{mw\ k_p}} \tag{6-34}$$

where [*Al*] denotes concentration of MAO. Equation (6-33) is appropriate for linear curve fitting, while Equation (6-34) is suitable for nonlinear regression. We performed both types of regression on the data collected in the present study.

Figure 6-20 shows the plot of the reciprocal of the number average molecular weight versus the reciprocal of monomer concentration for the set of data related to the pressure effect. Figure 6-21 shows the nonlinear curve fitting over the untransformed data by minimizing the sum of squares of the residuals. Assuming that the variability in monomer concentration is negligible, the approximate confidence interval for the parameters can also be calculated. Table 6-16 summarizes the results for the 95% confidence interval calculations for the parameters using linear regression and the corresponding approximate ones using nonlinear regressions. The next section explains how those confidence intervals were calculated.

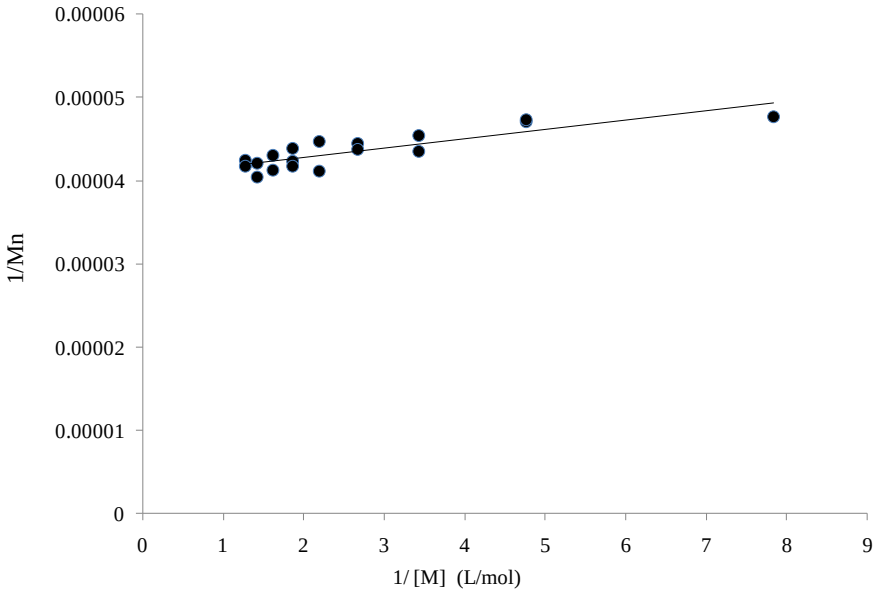

Figure 6-20. Plot of $1/M_n$ versus $1/[M]$.

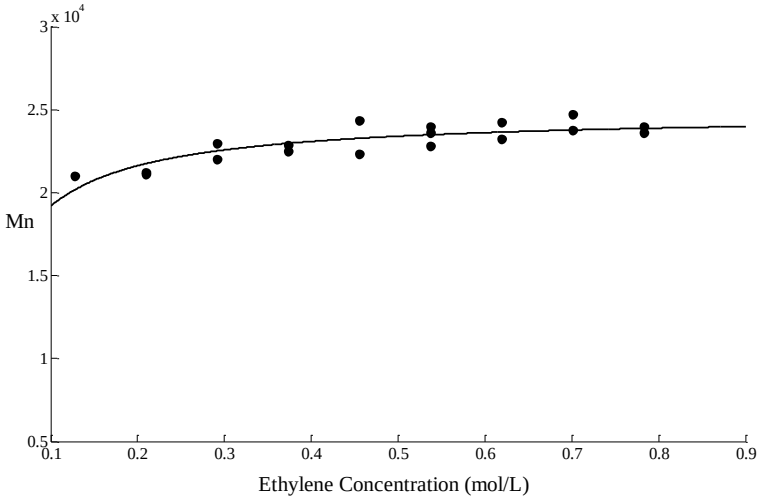

Figure 6-21. Curve fitting for M_n data using Equation (6-34).

Table 6-16. Parameter estimates with 95% confidence intervals using linear and nonlinear regression (varying ethylene concentration).

	Linear regression		Nonlinear regression	
Parameter	**Mean with 95% C.I**	**Standard Error**	**Mean with 95% C.I**	**Standard Error**
$k_M / mw\ k_p$ (mol/g)	$4.06\times10^{-5}\pm1.15\times10^{-6}$	5.44×10^{-7}	$4.04\times10^{-5}\pm1.18\times10^{-6}$	5.6×10^{-7}
$(k_{\beta H}+k_{Al}[Al])/(mw\ k_p)$ (mol^2/L.g)	$1.11\times10^{-6}\pm3.68\times10^{-7}$	1.73×10^{-7}	$1.17\times10^{-6}\pm4.21\times10^{-7}$	2×10^{-7}

6.4.4.1 Approximate Confidence Interval for Nonlinear Model and Confidence Interval for Linear Model

Despite lack of theoretical reliability, asymptotic confidence interval estimation of model parameters using the t-test statistic is commonly used in nonlinear regression.[146] Confidence intervals estimated based on this method are approximate and may be underestimated; however, the estimation is computationally expedient and conceptually appealing. Consider the general regression model,

$$g(y_i) = f(\underline{x}_i, \underline{\theta}) + \varepsilon_i \tag{6-35}$$

where y_i (i = 1,….,n) are response variables observed with unknown error ε_i (i = 1, ….,n) and x_i are the fixed predictor variables. For a particular confidence level, the confidence region for an individual parameter θ_i is given by,[147]

$$\theta_i \pm t_{\alpha/2,n-p}\, s\sqrt{\left(X^{'}X\right)^{-1}_{ii}} \tag{6-36}$$

where n and p are the number of data points and parameters, respectively. The term $t_{\alpha/2,n-p}$ is the upper 100×α/2 percentage point of the t-distribution with n-p degrees of freedom.[11] For nonlinear models, X is the Jacobian evaluated at the optimum values of parameters,

$$X = \left[\frac{\partial f(\underline{x}_i, \underline{\theta})}{\partial(\theta_j)}\right] \quad \text{(i,j)}^{\text{th}} \text{ element} \tag{6-37}$$

When dealing with linear models, X would be a matrix of the form below with dimension $n \times p$,

$$X = [f_j(\underline{x}_i)] \qquad (i,j)^{\text{th}} \text{ element} \tag{6-38}$$

and f_j is the function acting as the coefficient for the parameter θ_j.

$\left(X^{'}X\right)_{ii}^{-1}$ is the i^{th} diagonal element of the $\left(X^{'}X\right)^{-1}$ matrix, and s can be calculated from the equation below,

$$s^2 = \frac{S(\hat{\theta})}{n-p} \tag{6-39}$$

where $S(\hat{\theta})$ is the sum of squares of residuals calculated at the optimum value of the parameters. An estimate of the standard deviation (estimated standard error) for parameter θ_i was obtained by calculating $\sqrt{\left(X'\ X\right)_{ii}^{-1} s^2}$.

6.4.4.2 Joint Confidence Region

Confidence intervals estimate the variability of each parameter alone, ignoring the interaction between the parameters, whereas a joint confidence region encompasses all combinations of values for the parameters that are simultaneously acceptable at the specified level of confidence. Therefore, the joint confidence region of the parameters gives more information about their accuracy. The joint confidence region of the parameters, k_{tM}/mwk_p and $(k_{t\beta H}+k_{tAl}[Al])/(mwk_p)$, having the correct shape but approximate probability content was constructed by solving the equation below,[147]

$$S(\theta) \le S(\hat{\theta})\left[1 + \frac{p}{n-p} F_{p,n-p,\alpha}\right] \tag{6-40}$$

where n and p are number of data points and parameters, respectively. $F_{p,n\text{-}p,\alpha}$ is the upper critical value of the $F_{p,n\text{-}p}$ distribution. $S(\theta)$ is the sum of the square of the residuals, which is a function of the parameters, and $S(\hat{\theta})$ is the corresponding value at the optimum values of the parameters $\hat{\theta}$.

Equation (6-40) was solved iteratively using Excel to construct the joint confidence contour bounding. Figure 6-22 compares the 95% joint confidence region obtained using Equation 6-40 with the confidence intervals estimated using linear and nonlinear regression (Table 6-15).

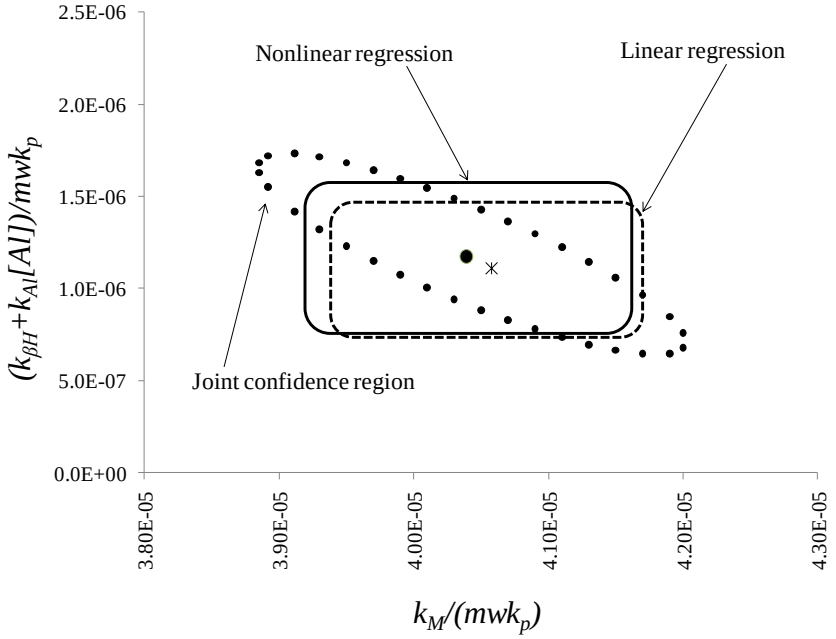

Figure 6-22. Plot of 95 % joint confidence region and individual confidence intervals for k_M/mwk_p and $(k_{\beta H}+k_{Al}[Al])/(mwk_p)$. The solid point in the middle of ellipse shows the average of the parameters calculated using nonlinear regression while the star points shows the average value of the parameters calculated by linear regression.

The joint confidence region stretches from 3.88×10^{-5} to 4.2×10^{-5} for k_M/mwk_p and from 6.0×10^{-7} to 1.75×10^{-6} for $(k_{\beta H}+k_{Al}[Al])/(mwk_p)$. These confidence intervals are greater than the corresponding intervals estimated through linear and nonlinear regressions (Table 6-16), as expected. Despite lack of theoretical support for using linear regression, which causes transformation of the residuals, the confidence intervals for linear and nonlinear regression are nearly the same. The tilted elliptical joint confidence region is possibly due to high variances in M_n data or high nonlinearity of the function.

Using our previous estimate for k_p, and knowing that the relative standard deviation of a fraction is obtained by summing the squares of their relative standard deviations and extracting the square root of the sum given that variables involved are independent, we can estimate confidence interval for k_M and $k_{\beta H}+k_{Al}[Al]$. The 95% confidence intervals estimates for k_M and $k_{\beta H}+k_{Al}[Al]$ are given in Table 6.17. Appendix F gives more detail on how these confidence intervals were calculated.

Table 6-17. Estimates for k_M and $k_{\beta H} + k_{Al}[Al]$

Parameter	Mean value and 95% confidence interval
k_M	240.94±10.83
$k_{\beta H} + k_{Al}[Al]$	6.98±2.53

Later in this chapter we will show how to estimate k_{Al} independently of $k_{\beta H}$ using a set of polymerizations performed under different MAO concentrations.

6.4.5 Effect of Temperature

Ten polymerization runs were conducted randomly at five temperature levels, with two replicates at each level, to study effect of temperature on the rate constants. The experimental conditions are given in Table 6-18. Except for the temperature, all other variables were kept constant in all polymerizations.

Table 6-18. Summary of experimental conditions (polymerization temperature effect).

Temperature	120 to 140^{o}C	Catalyst Concentration	1.31× 10^{-8} mol/L
Pressure	120 psig	Polymerization time	15 min
Solvent	Toluene	MAO (10 wt% in toluene)	2 g
Solvent volume	222.8 ml		

The polymerization procedure was the same as the one used for the previous runs. Temperature control for one of the runs at 140 ^{o}C was poor (140±0.6 ^{0}C) and, therefore, only molecular weight data was considered for that run. A change in temperature of ±0.6 ^{0}C causes significant fluctuations in the monomer consumption rate curve, but has a minor effect on polymer molecular weight. Figure 6-23 shows the plot of ethylene consumption rates versus time at different temperatures, while Figure 6-24 depicts the plot of ln($F_{M,in}/V_R$) versus time, showing good agreement with the 1st order decay model developed above.

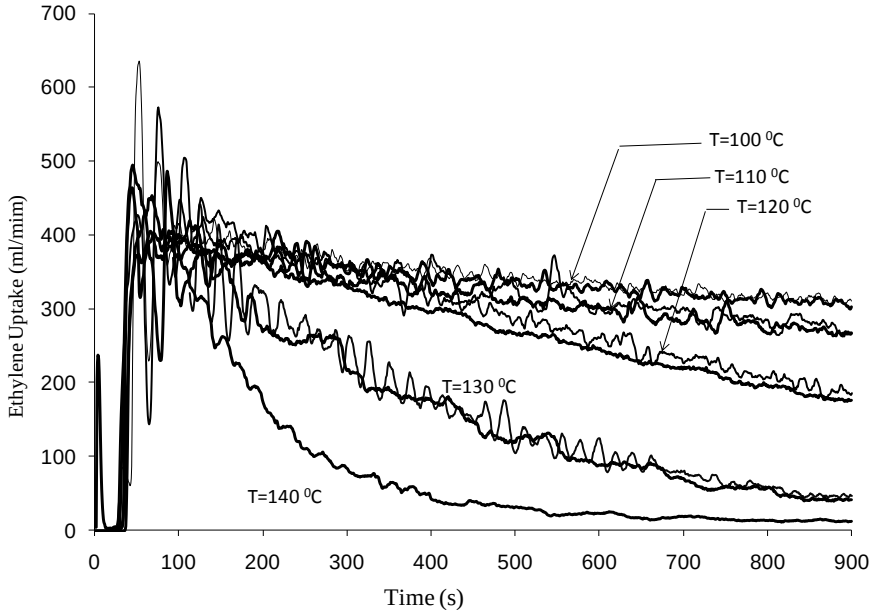

Figure 6-23. Ethylene uptake curves for polymerization runs at different temperatures.

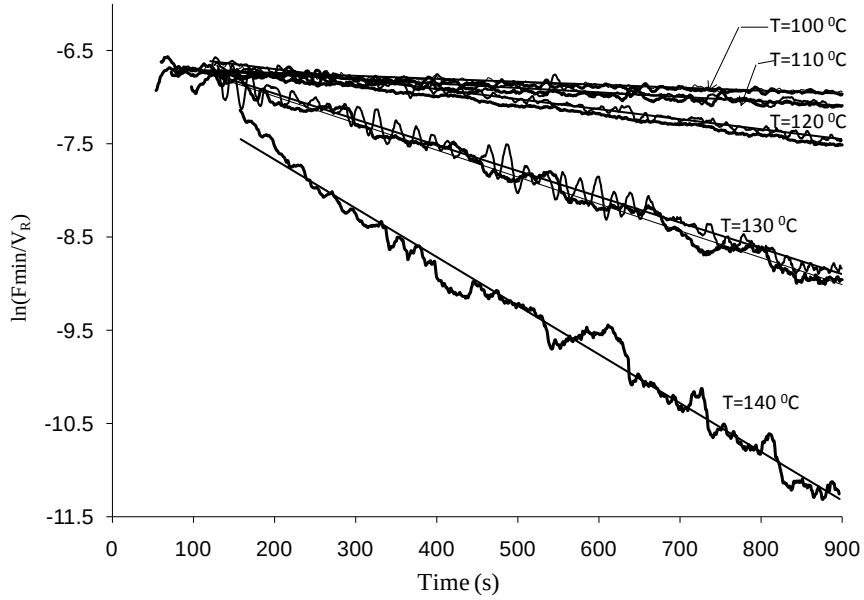

Figure 6-24. Effect of temperature on the plot of $\ln(F_{M,in}/V_R)$ versus time.

The values of k_d and $k_p[M]$ shown in Table 6-19 were calculated using the slopes and intercepts in Figure 6-24, and also by curve fitting of the monomer uptake data using Equation (6-24), as done previously for the ethylene pressure study in Section 6.4.3.

Table 6-19. Summary of polymerization rate constants (polymerization temperature effect).

Temperature (^oC)	**$k_p[M]$ (s^{-1})[a]**	**k_d (s^{-1})[a]**	**$k_p[M]$ (s^{-1})[b]**	**k_d (s^{-1})[b]**	**M_w**	**M_n**	***PDI***	**Polymer Yield(g)**
140	NA	NA	NA	NA	18 800	40 200	2.14	1.30
140	113 200	0.00518	114 040	0.00532	17 400	38 400	2.21	1.49
110	96 894	0.00048	97 298	0.00048	22 800	49 100	2.16	6.19
130	126 425	0.00278	124 746	0.00274	20 500	42 800	2.09	3.75
100	94 974	0.00031	95 278	0.00032	24 900	52 500	2.11	6.48
120	115 039	0.00107	114 701	0.00106	22 100	46 000	2.09	5.87
120	104 795	0.00100	103 860	0.00100	22 400	45 300	2.03	5.00
110	93 815	0.00046	94 258	0.00047	23 300	48 000	2.06	5.91
130	125 968	0.00291	123 413	0.00286	19 200	42 000	2.19	3.49
100	90 752	0.00026	90 895	0.00027	25 400	51 600	2.03	6.22

[a] Estimated using linear regression; [b] Estimated using nonlinear regression

Figure 6-25 shows the Arrhenius plot for k_d. The point estimate for the activation energy for catalyst deactivation was calculated using the slope of the line in Figure 6-25 and the Arrhenius law, to obtain E_a = 96 KJ/mol. Using a similar approach, we obtained the point estimate for the activation energy for propagation to be E_{aP} = 20.52 KJ/mol (Figure 6-26). To calculate k_p from $k_p[M]$ data, the monomer concentration data shown in Table 6-1 were used.

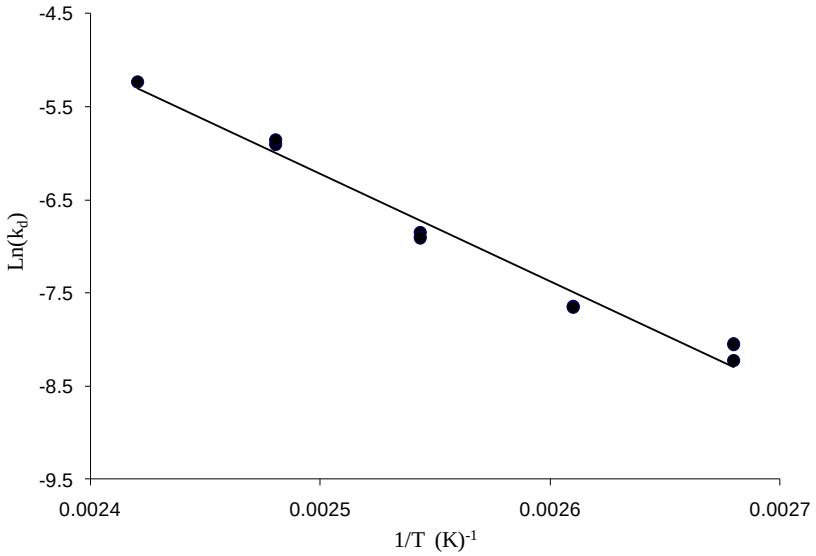

Figure 6-25. Arrhenius plot, for k_d. The k_d values were calculated by nonlinear regression.

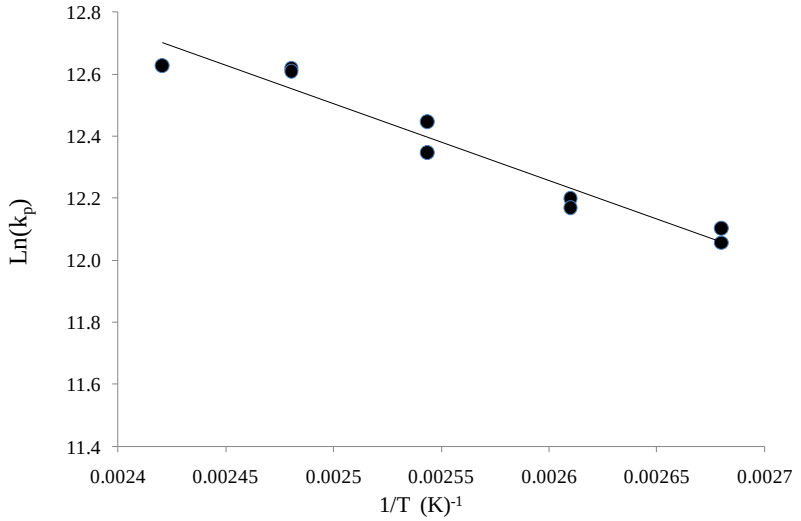

Figure 6-26. Arrhenius plot for k_p. The k_p values were calculated by nonlinear regression.

Figure 6-27 show how the molecular weight averages and polydispersity index depend on the polymerization temperature. The molecular weight averages decrease with increasing temperature, while the PDI remains practically the same.

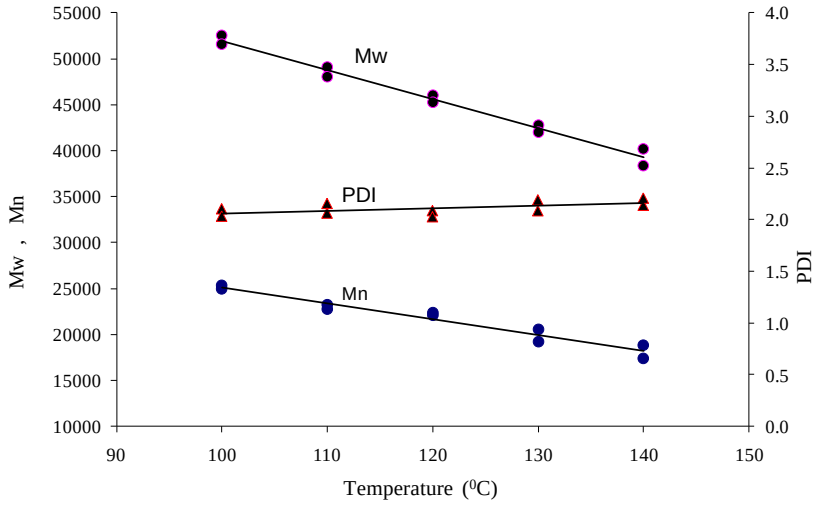

Figure 6-27. Effect of polymerization temperature on molecular weight averages and polydispersity. index.

6.4.6 Effect of MAO concentration

In order to investigate the effect of MAO concentration on polymerization kinetics and polymer molecular weight, sixteen polymerization runs were performed, randomly, at eight equally spaced levels of MAO concentrations at 120 ^{0}C with two replicates at each level.

The summary of experimental conditions is listed in Table 6-20. Except for MAO concentration, all other variables were kept constant during the polymerizations. Figure 6-28 provides plots of the ethylene consumption rate versus time for all these runs.

Table 6-20. Summary of experimental conditions (Study of MAO concentration).

Temperature:	120 ^{o}C	Catalyst Concentration:	1.31×10^{-8} mol/L
Pressure:	120 psig	Polymerization time:	15 min
Solvent:	Toluene	MAO (10 wt% in toluene)	0.138-2.57 g
Solvent volume:	222.8 ml		

Like the treatment we adopted in the previous sections in this chapter, $\ln(F_{M,in}/V_R)$ versus time was plotted in Figure 6-29 and used to estimate k_d and $k_p[M]$ from the curves intercept and slope. However, nonlinear regression was not used to estimate the kinetic parameters this time because this procedure leads to practically the same values, as demonstrated in the previous sections. Table 6-21

summarizes the results of these calculations along with the results of the molecular weight measurements using GPC and polymer yields for all runs.

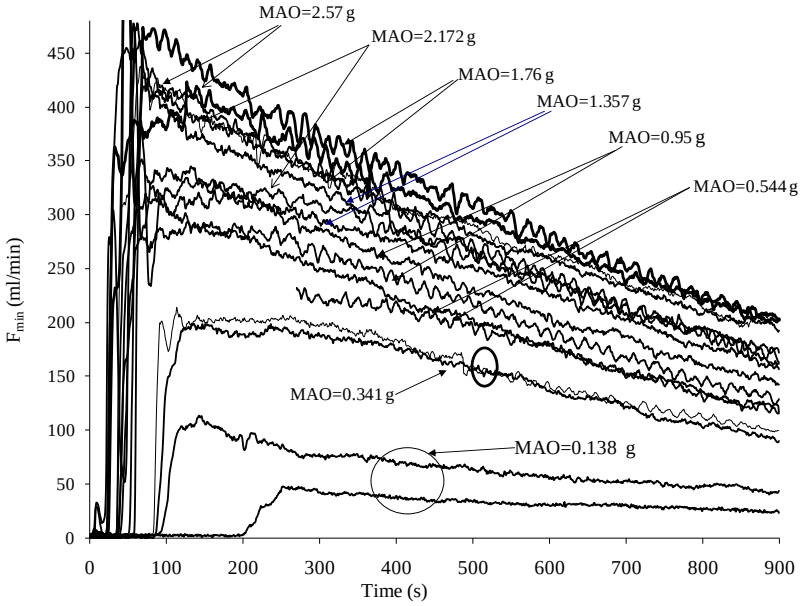

Figure 6-28. Ethylene uptake curves for polymerization runs at different MAO concentrations.

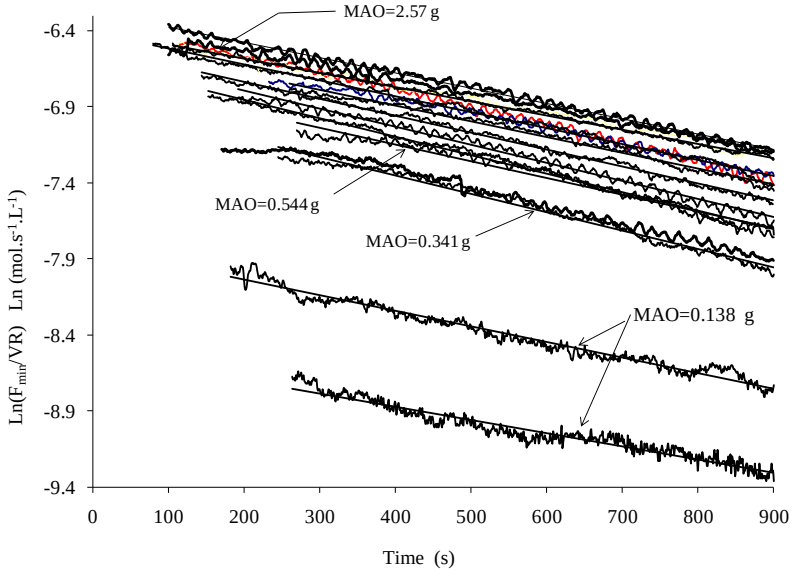

Figure 6-29. Plots of $\ln(F_{M,in}/V_R)$ versus time (effect of MAO concentration).

Table 6-21.Summary of kinetic parameters, molecular weight average measurements, and polymer yield results.

Run	Weight of MAO solution (g)	Al Concentration (Mol/L)	Al/Zr	$k_p[M]$ (s^{-1})	k_d (s^{-1})	M_n	M_w	*PDI*	Polymer Yield (g)
1-M	1.764	0.0122	1 038 300	113 100	0.00115	NA	NA	NA	5.32
2-M	0.951	0.0066	559 700	85 400	0.00110	23 700	48 300	2.04	4.04
3-M	0.544	0.0038	320 200	77 600	0.00110	25 500	50 400	1.97	3.21
4-M	2.173	0.0150	1 279 000	98 800	0.00096	22 100	45 800	2.07	4.85
5-M	0.341	0.0024	200 700	65 600	0.00119	23 700	51 800	2.19	2.72
6-M	1.356	0.0094	798 100	97 000	0.00102	22 900	47 200	2.06	4.44
7-M	0.341	0.0024	200 700	70 000	0.00123	22 700	50 300	2.22	2.75
8-M	1.764	0.0122	1 038 300	119 800	0.00100	22 600	45 200	2.00	5.83
9-M	0.138	0.0010	81 200	12 800	0.00089	24 600	53 200	2.17	0.69
10-M	0.951	0.0066	559 700	93 800	0.00111	22 400	47 000	2.10	4.39
11-M	2.576	0.0178	1 516 200	112 600	0.00096	20 600	44 800	2.18	5.40
12-M	0.544	0.0038	320 200	85 200	0.00121	22 900	49 100	2.14	3.81
13-M	0.138	0.0010	81 200	25 800	0.00106	24 500	53 500	2.18	1.19
14-M	1.356	0.0094	798 100	104 900	0.00105	21 900	46 000	2.10	5.02
15-M	2.576	0.0178	1 516 200	105 400	0.00091	21 000	44 800	2.14	5.51
16-M	2.173	0.0150	1 279 000	105 900	0.00093	22 500	46 500	2.07	5.27
17-M	5.01	0.0346	2 950 600	101 500	0.00076	20400	44000	2.16	5.79

Figures 6-30 and 6-31 show how k_d and k_p vary with MAO concentration, respectively. The last point (polymerization at high MAO concentration, Run 17-M) was not in the initial design of the experiments; it was performed at the end of the polymerization set to confirm some trends observed in the original design. The value of k_d decreases with increasing MAO concentration. This implies that MAO reduces the rate of catalyst deactivation, perhaps by stabilizing the active sites.

Inspection of Figure 6-31 shows that k_p increases until reaching a plateau value at MAO concentration of approximately 0.012 mol/L (Al/Zr ratio of about 1×10^6), remaining essentially constant up to MAO concentration of 0.035 mol/L, the highest MAO concentration studied (Al/Zr ratio 3×10^6). MAO is believed to alkylate the transition metal-chloride bond followed by abstraction of the second chloride to yield a metalloceinum cation.[8] The maximum k_p value observed in Figure 6-31 may correspond to the amount of MAO that completely converts the metallocene to the active metallocenium cation species. A similar trend was seen in the plot of polymer yield versus MAO

concentration (Figure 6-32). If we define the *catalyst activation efficiency* as the ratio of actual polymer yield to the maximum polymer yield (the polymer yield at the plateau part of the polymer yield versus Al/catalyst ratio curve), this efficiency would depend on the Al/Zr ratio, with its maximum value at Al/Zr about 1×10^6 for the catalyst studied.

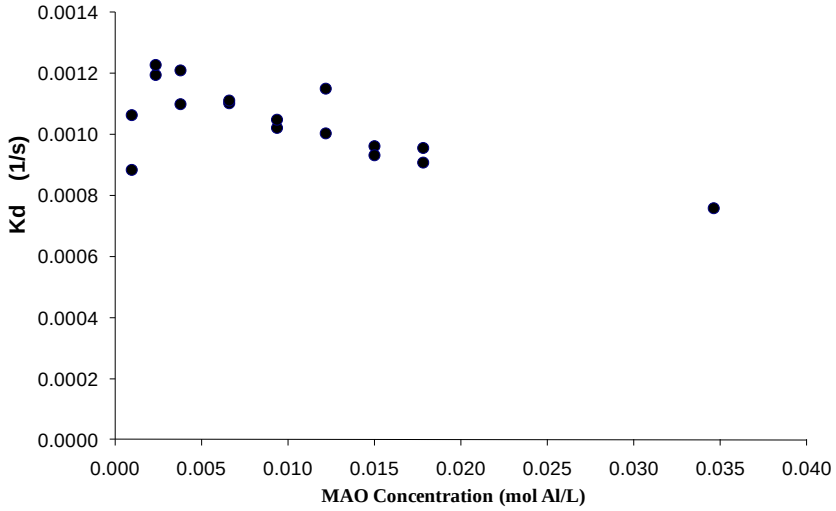

Figure 6-30. Plot of k_d versus MAO concentration.

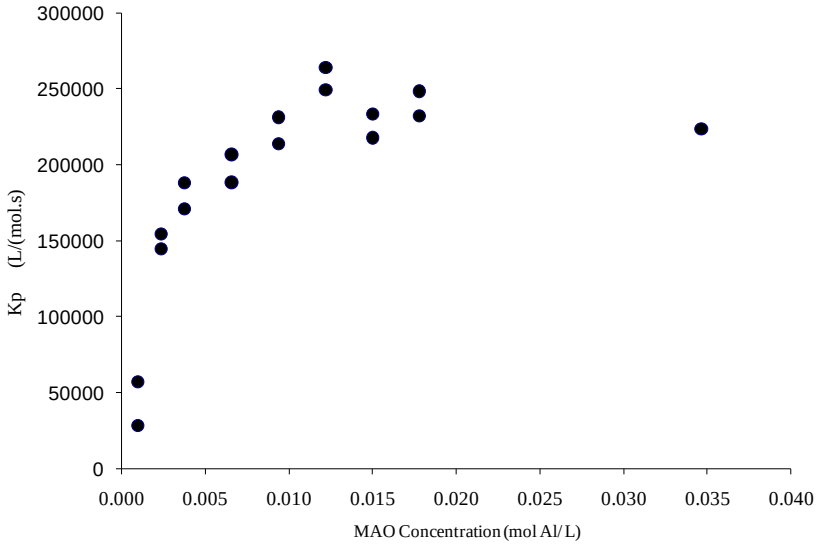

Figure 6-31. Plot of k_p versus MAO concentration.

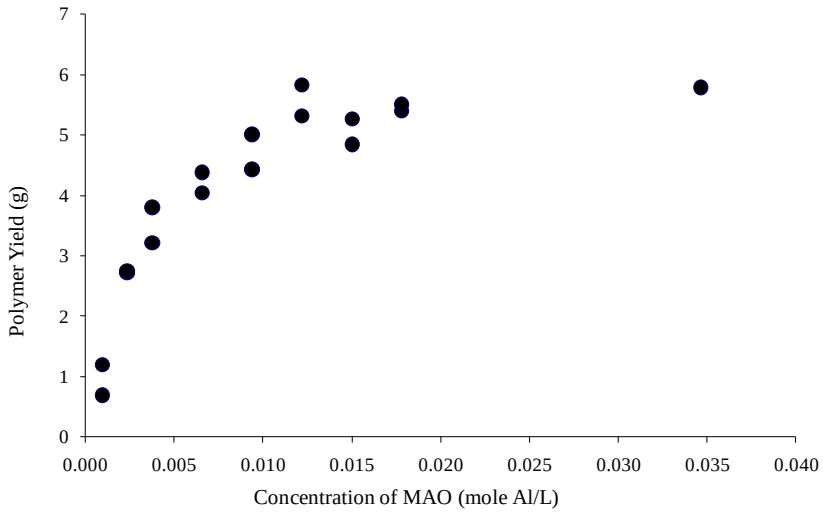

Figure 6-32. Polymer yield versus MAO concentration.

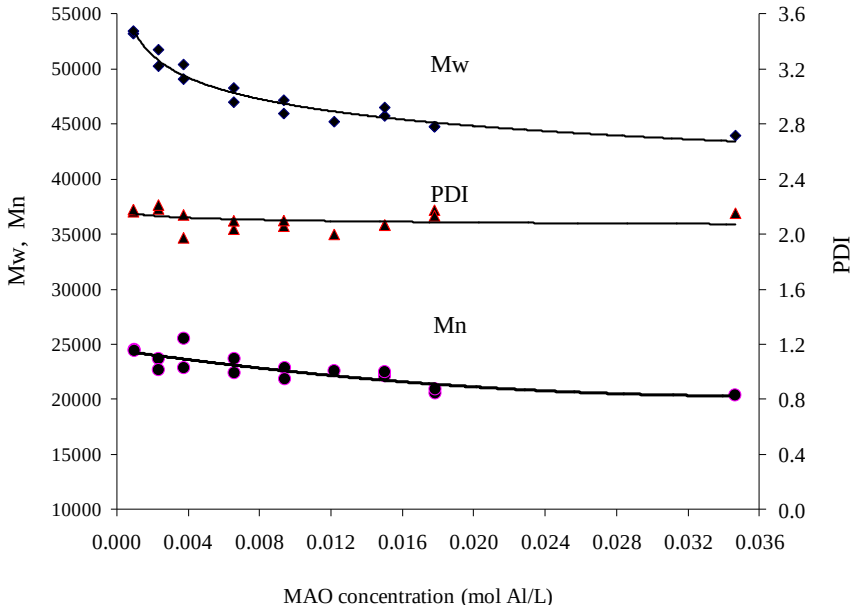

Figure 6-33. Effect of MAO concentration on molecular weight averages and PDI.

Increase in MAO concentration decreases molecular weight averages but it does not affect PDI (Figure 6-33). The decrease in molecular weight is likely due to chain transfer to MAO, most likely to

trimethyl aluminum ($AlMe_3$) contained in the MAO solution.[48] This type of chain transfer has also been reported in propylene polymerization using TMA.[45]

6.4.6.1 Estimation of transfer to MAO rate constant

Equation (6-34) can be rearranged to the following form,

$$M_n = \frac{1}{\frac{k_M}{mwk_p} + \frac{k_{\beta H}}{mwk_p[M]} + \frac{k_{Al}[Al]}{mwk_p[M]}} \tag{6-41}$$

A nonlinear least squares fit of Equation (6-41) over the M_n data shown in Figure 6-34 gives the estimates for the transfer to propagation constants with their corresponding approximate 95% confidence interval limits and estimated standard errors shown in Table 6-22.

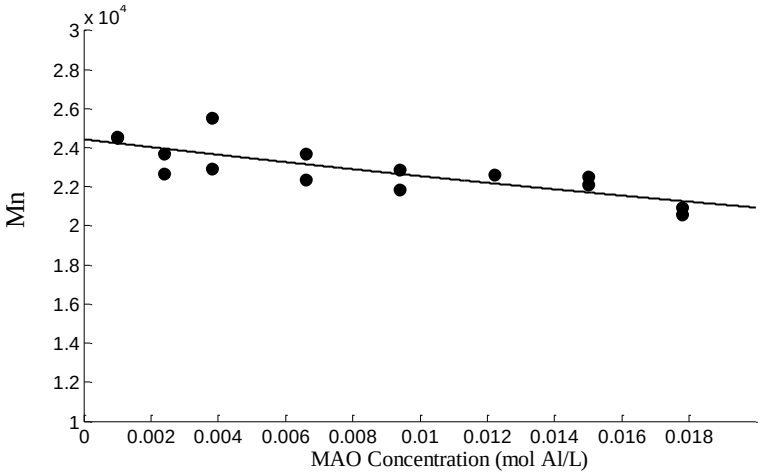

Figure 6-34. Curve fitting of M_n data using Equation (6-41).

Table 6-22. Parameter estimation with 95% confidence intervals using nonlinear regression (varying MAO concentration).

Parameter	Mean with 95% C.I	Standard Error
$k_M / mwk_p + k_{\beta H}/(mw\, k_p[M])$ (mol/g)	$4.092\times10^{-5}\pm1.44\times10^{-6}$	6.67×10^{-7}
$k_{Al}/(mwk_p[M])$ (L/g)	$3.419\times10^{-4}\pm1.57\times10^{-4}$	7.27×10^{-5}

Since the value of k_M/mwk_p, $4.04\times10^{-5}\pm1.18\times10^{-6}$ mol/g, is known from previous calculations (Table 6-16), we can calculate $k_{\beta H}/(\ mw\ k_p[M])$ and its approximate 95% confidence interval using propagation of errors,

$$\frac{k_{\beta H}}{mwk_p[M]} = 5.2\times10^{-7} \pm 17.1\times10^{-7} \qquad \frac{mol}{g} \tag{6-42}$$

Since its confidence interval includes zero, we conclude that transfer by β-hydride elimination is negligible with this catalyst under the polymerization conditions investigated herein.

Similarly, using the previously estimated value of k_p, 213000 $L.mol^{-1}.s^{-1}$, the approximate 95 % confidence interval for the kinetic parameter k_{Al} is,

$$k_{Al} = 925 \pm 420 \qquad \frac{L}{mol.s} \tag{6-43}$$

Appendix G shows how these confidence intervals were calculated.

Linear regression can also be used to estimate the transfer to propagation constants. Rearranging Equation (6-41) yields the expression below which is suitable for linear regression,

$$\frac{1}{M_n} = \frac{k_M}{mwk_p} + \frac{k_{\beta H}}{mwk_p[M]} + \frac{k_{Al}[Al]}{mwk_p[M]} \tag{6-44}$$

The plot of $1/M_n$ versus [Al] is shown in Figure 6-35. Intercept and slope of the line with their 95% confidence intervals are,

$$\frac{k_M}{mwk_p} + \frac{k_{\beta H}}{mwk_p[M]} = 4.1\times10^{-5} \pm 1.49\times10^{-6} \tag{6-45}$$

$$\frac{k_{Al}}{mwk_p[M]} = 3.44\times10^{-4} \pm 1.47\times10^{-4} \tag{6-46}$$

These means and confidence intervals are very close to individual confidence intervals estimated by nonlinear regression.

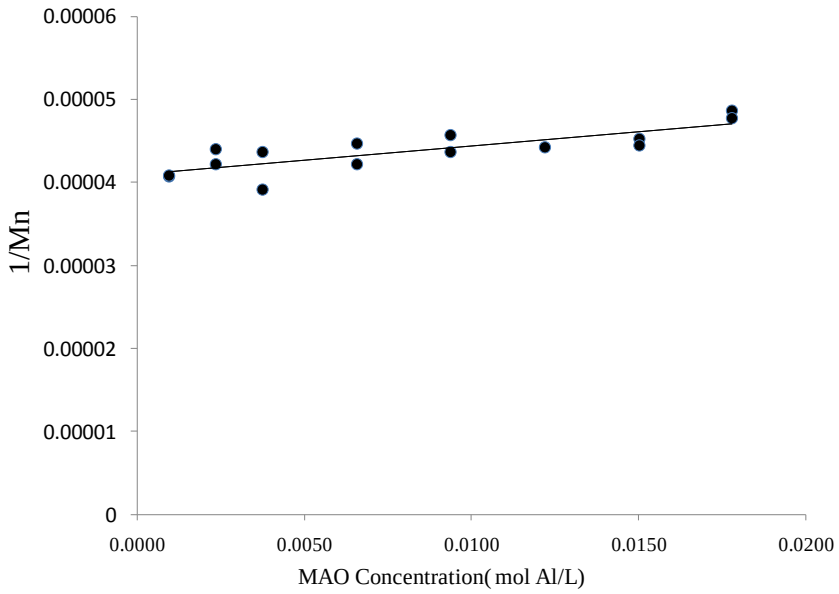

Figure 6-35. Plot of 1/Mn versus MAO concentration

Equation (6-40) was also used to construct the correct shape for the joint confidence region. Figure 6-36 compares the 95% joint confidence region with the confidence intervals estimated using linear and nonlinear regressions (The solid and dashed rectangles are confidence intervals obtained by nonlinear and linear regressions, respectively). Note that the ellipse-shaped joint confidence region is not parallel to horizontal axis and is elongated in that direction, this implies that $\frac{k_{Al}}{mwk_p[M]}$ is not estimated as precisely as $\frac{k_M}{mwk_p} + \frac{k_{\beta H}}{mwk_p[M]}$.

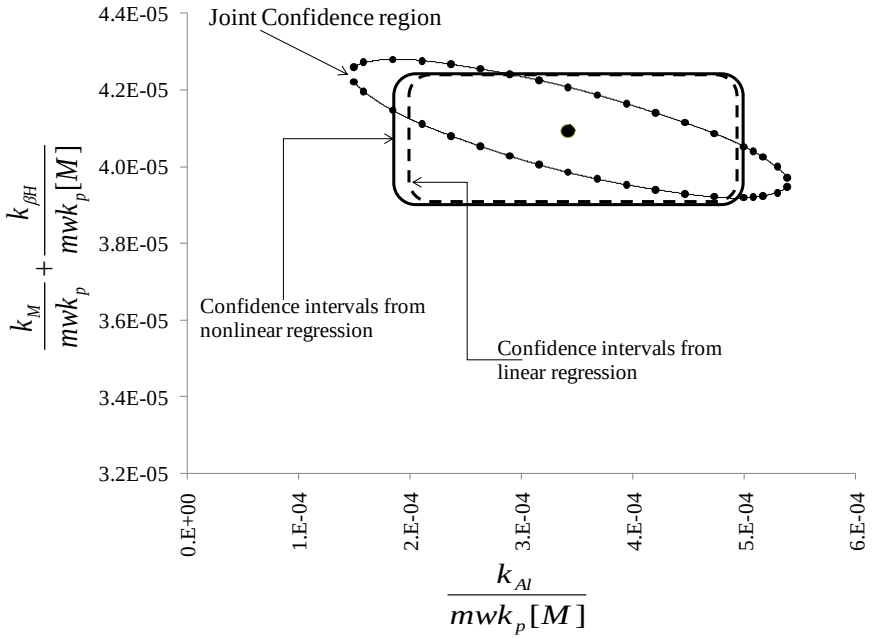

Figure 6-36. Plot of 95 % joint confidence region and individual confidence intervals for $k_{Al}/mwk_p[M]$ and $(k_M/mwk_p + k_{\beta H}/(mwk_p[M]))$.

6.4.7 Estimation of activation energy for chain transfer to monomer

The set of experiments used to estimate the effect of temperature on the polymerization constants were performed at 120 psig. In the experimental conditions adopted for these runs, $k_{Al}[Al] << k_M[M]$ (12.9 s^{-1} and 90 to 127 s^{-1}, respectively). Noting that β-hydride elimination is negligible, as demonstrated in Sections 6.4.6.1, Equation (6-32) is reduced to,

$$\frac{1}{M_n} \cong \frac{k_M[M]}{mw\ k_p[M]} \tag{6-47}$$

Taking logarithm of both sides and substituting the relevant terms from the Arrhenius law,

$$\ln(M_n) \cong -\ln\left(\frac{k_{M0}e^{-\frac{E_{aM}}{RT}}}{mw\ k_{p_0}e^{-\frac{E_{aP}}{RT}}}\right) = -\ln\left(\frac{k_{M0}}{mwk_{p0}}\right) + \frac{E_{aM} - E_{aP}}{RT} \tag{6-48}$$

where k_{M0} and k_{p0} are the frequency factors, and E_{aM} and E_{aP} are the activation energies for transfer to monomer and propagation, respectively.

Figure 6-37 shows how the ln(M_n) varies as a function of the inverse of absolute polymerization temperature. The slope of the best fit line is 1247.97 J/(mol.K), which leads to an estimated transfer to monomer activation energy of E_{aM} = 30.9 KJ/mol. The higher activation energy for transfer to monomer than for propagation (E_{aP} = 20.52 KJ/mol, see Section 6.4.5) implies that the former is more temperature sensitive than the latter. Therefore, increasing polymerization temperature causes a decrease in polymer molecular weight averages.

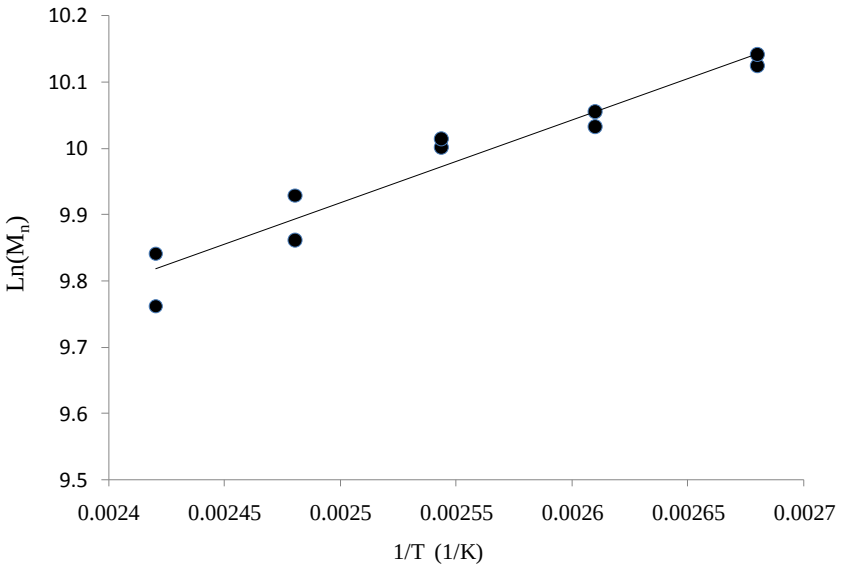

Figure 6-37. Plot of ln(M_n) as a function of reciprocal polymerization temperature.

6.4.8 Estimation of the macromonomer content in polymer

It is possible to estimate macromonomer content in a polymer if the reaction mechanism and the related reaction rate constants are known. We can also estimate macromonomer content using ^{13}C-NMR. As a final check to see if the estimated reaction rate constants are reasonable, we estimated the macromonomer content of one of the sample (3-M) using both methods.The paragraphs below explain, in detail, about these two methods.

Chain transfer to monomer leads to the production of macromonomers, while chain transfer to MAO produces Al-terminated dead polymer chains.

Transfer to monomer

$$\overset{*}{P} + M \xrightarrow{k_{M,i}} P^{=} + \overset{*}{P} \tag{6-49}$$

Transfer to cocatalyst

$$\overset{*}{P} + Al \xrightarrow{k_{Al,i}} D + C_i \tag{6-50}$$

where $P^{=}$ denotes macromonomer concentration. If we assume that the rate of LCB formation is negligible compared to the rate of transfer to monomer, the ratio of macromonomer formation via chain transfer to monomer to overall rate of chain transfer gives the mole fraction of macromonomer in the final product, as expressed by Equation (6-51).

$$Macromonomer \quad mole \quad fraction = \equiv \frac{d\overline{\overline{P}}/dt}{d\overline{\overline{P}}/dt + dD/dt} \tag{6-51}$$

Substituting the relevant rate terms in Equation (6-51) gives

$$Macromonomer \quad mole \quad fraction = \frac{k_M[M][\overset{*}{P}]}{k_M[M][\overset{*}{P}] + k_{Al}[Al][\overset{*}{P}]} = \frac{k_M[M]}{k_M[M] + k_{Al}[Al]} \tag{6-52}$$

Equation (6-52) shows that the mole fraction of macromonomer in the final product is a function of monomer and MAO concentrations. At polymerization conditions used to make Sample 3-M, [Al] = 0.0038 mol/L and [M] = 0.454 mol/L. Substituting these concentrations and the rate constants (k_M = 240.9, k_{Al} =925) in Equation (6-52), the mole fraction of macromonomer in the polymer is estimated to be equal to 0.97.

To check this estimate, Sample 3-M was analyzed by ^{13}C NMR. Figure 6-38 shows the proton decoupled ^{13}C NMR spectrum for Sample 3-M.

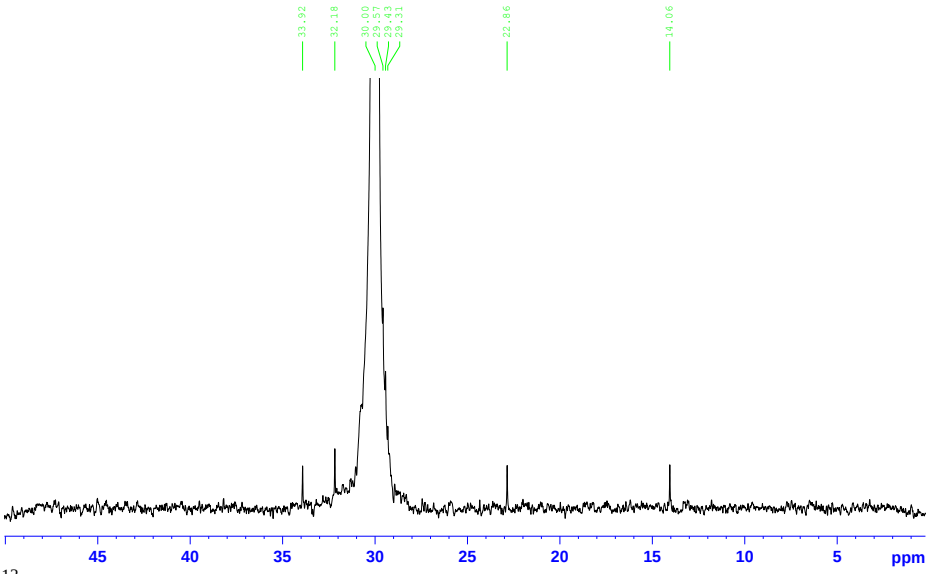

Figure 6-38. ^{13}C NMR spectra of polyethylene (Sample 3-M in Table 6-17).

Four well resolved peaks were observed, with chemical shifts positioned at 14.06, 22.86, 32.18, and 33.97 ppm. To account for the peaks observed in this spectrum, the structure shown in Figure 6-39 was assumed.

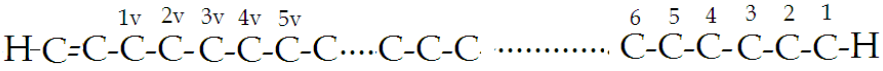

Figure 6-39. Carbon nomenclature for polymer chains with vinyl end group.

These chemical shifts corresponds to carbons 1, 2, 3 and 1v of the structure shown in Figure 6-39, based on the Grant and Paul rule.[148-149] Other types of carbon atoms (4, 5, 6 , 2v,…5v) have chemical shifts located at 30 or near 30 ppm.

The number average molecular weight can be calculated using the equation below,

$$\frac{1}{M_n} = \frac{SCED + UCED}{28{,}000} \tag{6-53}$$

where UCED is the number of unsaturated chain ends per 1 000 carbon atoms and SCED is the number of saturated chain ends per 1 000 carbon atoms. UCED and SCED are calculated using Equations (2-25) and (2-24).

UCED, SCED and M_n for Sample 3-M, calculated using Equations (2-25), (2-24), and (6-53), are equal to 0. 594, 0.599, and 23, 464. The mole fraction of macromonomer in the final product can be calculated using equation below which was found to be 0.99,

$$Macromonomer \quad mole \quad fraction = \frac{UCED}{UCED + \frac{(SCED - UCED)}{2}} \tag{6-54}$$

The mole fraction of macromonomer estimated by ^{13}C-NMR is close to the one estimated through kinetic equations confirming that the estimated kinetic parameters are satisfactory. The assumption of no LCB formation is reasonable because no LCB sign was seen in its ^{13}C NMR spectrum (Figure 6-38).

6.5 Conclusions

The results of this study show that propagation and deactivation steps are first order reaction for the solution polymerization of ethylene using rac-Et(Ind)$_2$ZrCl$_2$/MAO. Chain transfer to monomer is the main chain transfer reaction leading to the generation of vinyl-terminated polymers. Chain transfer by β-hydride elimination is negligible, while transfer to cocatalyst happens to some extent depending on the amount of MAO. However, the extent of this type of chain transfer reaction diminishes if concentration of MAO is kept low.

Increasing MAO concentration will increase polymerization activity to a maximum value of about 7.5×10^6 Kg PE/(mol Zr.hr) at Al/Zr ratio of about 1×10^6. MAO also decreases catalyst deactivation, possibly by stabilizing the active sites.

The reaction rate constants for propagation, catalyst deactivation, chain transfer to monomer and chain transfer to MAO were estimated. Their estimated values are: 213,000 L.mol^{-1}.s^{-1}, 0.001 s $^{-1}$, 241 L.mol^{-1}.s^{-1} and 925 L.mol^{-1}.s^{-1}, respectively, at 120 ^{o}C. We also estimated the activation energy for propagation, catalyst deactivation, and chain transfer to monomer. Their estimated values are 20.52, 96 and 30.9 KJ/mol, respectively.

Chapter 7

Ethylene Homopolymerization Kinetics with a Constrained Geometry Catalyst in a Solution Reactor

7.1 Summary

The solution polymerization of ethylene was studied in a semi-batch reactor using the constrained geometry catalyst (CGC) dimethylsilyl(N-tert-butylamido)-(tetramethylcyclopentadienyl)-titanium dichloride catalyst and methylaluminumoxane (MAO) as the cocatalyst. The influence of monomer concentration, temperature, MAO and catalyst concentrations on the ethylene polymerization kinetics were investigated systematically. The deactivation of the CGC/MAO system during ethylene polymerization can be described with a first order thermal deactivation mechanism that includes reversible activation and deactivation with MAO. The polymerization order with respect to ethylene varies with ethylene concentration from first to second order. The trigger mechanism was shown to describe very well the effect of ethylene concentration on polymer yield and polymerization kinetics. Low MAO concentration favors formation of polymer chains with unsaturated chain ends which in turn leads to formation of polymers with increased long chain branch density. It was also observed that the catalyst does not behave as a true single site catalyst at low MAO concentration. Finally, at low MAO concentration, low ethylene concentration increases long chain branch formation.

7.2 Introduction

Constrained geometry catalysts (CGC), a type of transition metal complexes bearing linked amido ligands, have found wide interest both in academia and industry since 1990.[150] This type of catalyst retains one of the cyclopentadienyl rings of metallocenes, but replaces the other ring with a nitrogen substituent that coordinates with the metal center, usually a group 4 metal (Zr or Ti).[8] Figure 7-1 depicts the structure of an exemplary CGC-Ti catalyst. These complexes are also known as half–sandwich complexes or Dow catalysts.

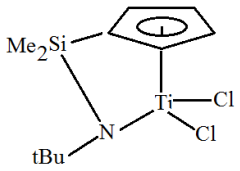

Figure 7-1. Structure of CGC-Ti catalyst.

When activated with MAO or borates, CGC can produce polyolefins with long chain branches (LCB) by the re-insertion of chains terminated with reactive double bonds (macromonomers). In the case of ethylene polymerization, vinyl-terminated chains are created by chain transfer to ethylene or β-hydride elimination

The amide donor ligand of the complex depicted in Figure 7-1 stabilizes the electrophilic metal center electronically, while the short $Me_2Si<$ bridging group causes a more open environment at the metal site compared to conventional metallocenes;[151] consequently, these types of catalysts allow the facile incorporation of bulky monomers, including 1-alkenes, cycloalkenes, and styrene[22] into random ethylene copolymers that are characterized by narrow molecular weight and chemical composition distributions.

Although several experimental studies on olefin homo- and copolymerization with CGC have been published,[63-64, 152-156] only a few investigations have dealt with polymerization kinetic studies. In one such study, ethylene was polymerized with CGC-Ti and the authors concluded that as monomer concentration increased, the polymer yield also increased, but that the MAO/CGC-Ti ratio had no effect on polymer yield; unfortunately, no information was reported on catalyst decay, which has a marked influence on polymer yield.[157] In another study,[30] the CGC $TiMe_2$/tris(pentafluorophenyl)boron/MAO system was used in a CSTR for ethylene homopolymerization. Ten polymerization runs were performed to investigate the effect of reactor residence time, polymerization temperature, ethylene and hydrogen concentrations on polymerization kinetics. Polyethylene samples with LCB frequencies from 0.07 to 0.16 were made and the CGC appeared to behave as a single site catalyst. The authors concluded that a first order catalyst decay model was not appropriate to explain the observed results, but they did not propose an alternative model to describe their data. They assumed a first order propagation step with respect to ethylene concentration and based on this assumption estimated some reaction rate constants.

In the present investigation, we polymerized ethylene with CGC-Ti/MAO system in a semibatch reactor in the solution state. Polymerization of ethylene was studied systematically by changing ethylene, catalyst, and MAO concentrations. A kinetic model, based on the trigger mechanism[32], was proposed, tested, and then refined based on monomer uptake curves and polymer yield data. First order thermal decay of the catalyst along with reversible and irreversible deactivation of the catalyst sites by MAO seemed to be satisfactory for explaining the effect of catalyst and ethylene concentration, as well as time, on ethylene uptake curves. Polymers produced at low MAO concentrations were found to have higher unsaturated chain end density and long chain branch frequencies.

7.3 Experimental

7.3.1 Materials

Methylaluminoxane (MAO, 10 wt % in toluene, Sigma-Aldrich) was used as received. Ethylene and nitrogen (Praxair) were purified by passing through molecular sieves (3 and 4-A˚) and copper(II) oxide packed beds. Toluene (EMD) was purified by distillation over an n-butyllithium/styrene/sodium system and then passed through two packed columns in series filled with molecular sieves (3, 4, and 5-A˚) and Selexorb for further purification. All air-sensitive compounds were handled under inert atmosphere in a glove box.

The catalyst, dimethylsilyl(N-tert-butylamido)-(tetramethylcyclopentadienyl)-titanium dichloride (CGC-Ti), was purchased as powder from Boulder Scientific and dissolved in toluene which was first distilled over metallic sodium and then flown through a molecular sieve bed before polymerization.

7.3.2 Polymer synthesis

The method used for polymerizations is explained in Chapter 6, Section 6.3.2.

7.3.3 Polymer characterization

7.3.3.1 Gel Permeation Chromatography (GPC)

Molecular weight distributions (MWD) were determined with a Polymer Char high-temperature gel permeation chromatographer, run at 145^{o}C under a flow rate of trichlorobenzene of 1 ml/min. Our GPC is equipped with three detectors in series (infra-red, light scattering and differential viscosimeter). The GPC was calibrated with polystyrene narrow standards.

7.3.3.2 Carbon-13 Nuclear Magnetic Resonance (^{13}C-NMR)

The ^{13}C-NMR spectrum was taken on a Bruker 500 MHz system with 5-mm tube. The probe temperature was set at 120^{o}C. The solutions were prepared for analysis by dissolution of approximately 100 mg of each sample in 650 μL of o-dichlorobenzene-d4. The samples were dissolved by heating on a hot plate at 130^{o}C for 6 hours. Acquisition parameters were 14 micro second 90^{o} pulse, inverse gated proton decoupling, 10 s delay time between pulses, and 10 000 scans for data averaging. All spectra were referenced by setting the main polyethylene chain peak to 30.00 ppm.

7.3.3.3 Fourier-Transform Infrared Spectroscopy (FT-IR)

Fourier transform–infrared spectroscopy was used to quantify the vinyl groups in the polymer chains. The spectra were recorded from 400 to 4 000 cm^{-1}, after 32 scans, with a resolution of 2 cm^{-1}. The absorption band at 910 cm^{-1}, representative of vinyl groups, was used to measure the amount of vinyl groups in the polymer. The calibration curve, Figure 5-6, was used to estimate unsaturated chain end density in polymer samples.

7.4 Results and Discussion

7.4.1 Effect of Ethylene Pressure

The effect of ethylene pressure on ethylene polymerization with CGC was investigated by varying it from 35 to 220 psig at a constant temperature of 120^{o}C. A complete randomized design with eleven monomer concentration levels and at least two replicates at each level was adopted. All polymerizations were performed at a catalyst concentration of 0.547 μmol/L, 222.8 ml of solvent, and 2.0 g of MAO solution (10 wt % in toluene). Polymer yields and molecular weight measurements are summarized in Table 7-1.

Table 7-1. Summary of polymerization runs (effect of monomer concentration).

Run	Reactor pressure (psig)	M_w	M_n	*PDI*	Polymer Yield (g)	Activity (kg PE/(mol Ti.hr))
120A	120	188 600	91 500	2.06	5.59	40 900
60A	60	121 000	52 600	2.30	1.70	12 400
100A	100	166 600	74 100	2.25	4.39	32 100
80A	80	142 800	69 900	2.04	3.01	22 000
120B	120	174 900	80 600	2.17	6.01	44 000
80B	80	150 700	68 600	2.20	2.80	20 500
60B	60	115 600	55 300	2.09	1.75	12 800
100B	100	163 100	78 100	2.09	4.10	30 000
120C	120	173 700	75 800	2.29	5.51	40 300
100C	100	167 300	74 400	2.25	4.10	30 000
45A	45	95 600	40 800	2.34	1.01	7 300
140A	140	202 600	96 500	2.10	6.70	49 000
140B	140	212 600	99 000	2.15	7.80	57 000
45B	45	110 500	48 900	2.26	0.90	6 600
140C	140	206 100	99 000	2.08	7.78	56 900
180A	180	237 300	109 600	2.17	10.40	76 100
35A	35	73 800	32 200	2.29	0.50	3 700
160A	160	216 600	105 000	2.06	8.60	62 900
160B	160	227 200	102 000	2.23	9.13	66 800
180B	180	240 400	106 900	2.25	10.44	76 300
220A	220	261 300	115 500	2.26	13.23	96 700
200A	200	247 900	102 000	2.43	12.20	89 200
220B	220	253 900	112 000	2.27	14.40	105 300
200B	200	250 700	110 200	2.27	11.69	85 500

7.4.2 Polymerization Order with Respect to Ethylene Concentration

The polymer yield versus ethylene concentration in the liquid phase is shown in Figure 7-2. The experimental results of Table 6-1 were used to calculate ethylene concentration in the liquid phase corresponding to each total reactor pressure in Table 7-1. As expected, the curve passes through the origin, but a curvature is seen at low ethylene concentrations which clearly point out to a non-first order dependence of the polymerization rate on ethylene concentration. When the polymer yield is plotted versus the square of the ethylene concentration in the reactor liquid phase for the low concentration range (Figure 7-3), a linear relation is observed, confirming a second order dependency at low ethylene concentrations. Contrarily, Figure 7-2 shows that polymer yield depends linearly on ethylene concentration for values higher than approximately 0.4 mol/L. This indicates that the propagation order with respect to ethylene concentration changes from two to one when the ethylene pressure is increased. Ethylene polymerization orders higher than one were also reported by other investigators.[158-163] We proposed the mechanism described in Equations (7-1) and (7-2) as a possible explanation for the observed change in propagation order.

$$P^* + M \underset{k_r}{\overset{k_f}{\rightleftharpoons}} P^* \cdot M \tag{7-1}$$

$$P^* \cdot M + M \xrightarrow{k_p} P^* \cdot M \tag{7-2}$$

The formulation of Equations (7-1) and (7-2) is consistent with the main assumptions of the trigger mechanism,[31-32] according to which a monomer molecule first forms a complex with the active site and insertion into the growing polymer chain can only take place if a second monomer unit approaches the active site, triggering the insertion. In the above mechanism P^* is the uncomplexed active site with a growing polymer chain of any length, while $P^* \cdot M$ is a growing polymer chain complexed with a monomer molecule. When a complexed growing polymer chain of length j reacts with a monomer unit, a complexed growing polymer chain of length $j+1$ is produced. Reversible complex formation between active site with one monomer molecule is also accepted.[164-166]

Assuming that the reaction described in Equation (7-1) is a fast equilibrium, we can write,

$$[P^* \cdot M] = \frac{k_f [M][P^*]}{k_r} \tag{7-3}$$

The total concentration of active sites, C_t, in the reactor at a given time is given by the sum of complexed and uncomplexed active sites,

$$C_t = [P^* \cdot M] + [P^*] \tag{7-4}$$

Substituting Equation (7-3) in Equation (7-4) and solving for [P*] yields,

$$[P^*] = \frac{k_r}{k_r + k_f[M]} C_t \tag{7-5}$$

Finally, combining Equations (7-5) and (7-3) gives the concentration of complexed sites in the reactor at a given time,

$$[P^* \cdot M] = \frac{k_f[M]C_t}{k_r + k_f[M]} \tag{7-6}$$

According to Equation (7-2), the polymerization rate is given by the expression,

$$R_p = k_p[P^* \cdot M][M] \tag{7-7}$$

which can be combined with Equation (7-6) to find the final expressions for the polymerization rate governed by the mechanism expressed in Equations (7-1) and (7-2),

$$R_p = \frac{k_p C_t k_f [M]^2}{k_r + k_f[M]} \tag{7-8}$$

or,

$$R_p = \frac{k_p C_t K[M]^2}{1 + K[M]} \tag{7-9}$$

where,

$$K = \frac{k_f}{k_r} \tag{7-10}$$

Consequently, at low ethylene pressures $K[M] << 1$, simplifying Equation (7-9) to,

$$R_p = k_p C_t K[M]^2 \tag{7-9.a}$$

and the polymerization order with respect to ethylene concentration approaches two. Inspection of Equations (7.8) or (7.9) will also demonstrate that the polymerization rate becomes first order with respect to ethylene concentration as [M] increases and $k[M] >> 1$. Therefore, Equations (7.8) and (7.9) can describe the change in polymerization order depicted in Figure 7-2.

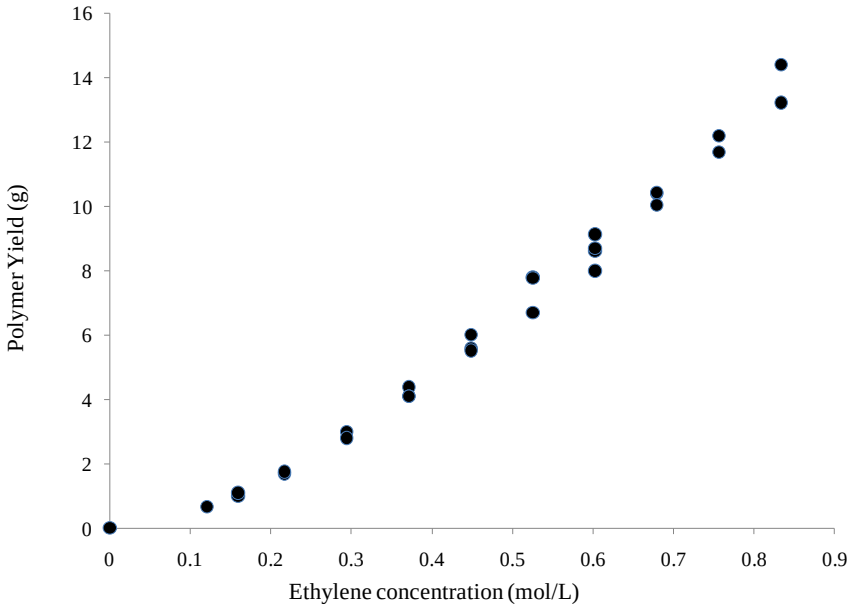

Figure 7-2. Polymer yield versus ethylene concentration in the reactor liquid phase.

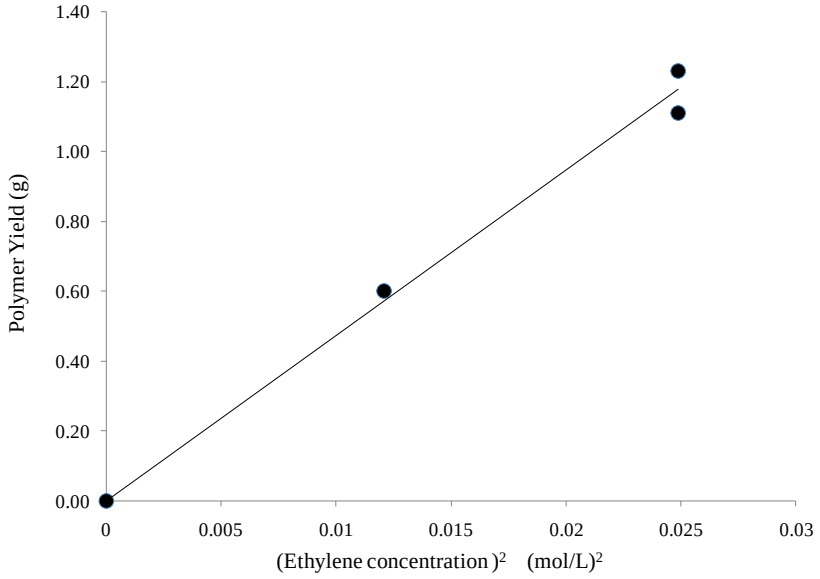

Figure 7-3. Polymer yield versus the square of ethylene concentration in the reactor liquid phase (low ethylene concentration range).

7.4.3 Catalyst Deactivation

The activation of coordination catalysts, such as CGC, by MAO involves very fast reduction and alkylation reactions yielding the catalytically active sites. After achieving a maximum polymerization activity, most coordination catalysts deactivate following a profile that depends on the catalyst type, polymerization temperature, and impurity level in the reactor. Figure 7-4 shows the ethylene consumption rates as a function of polymerization time for several ethylene pressures.

The first order catalyst decay model has been already described in Chapter 6 with Equation (6-21). However, this model fails to describe the polymerization data with CGC adequately, as shown in Figure 7-5 for a typical polymerization run.

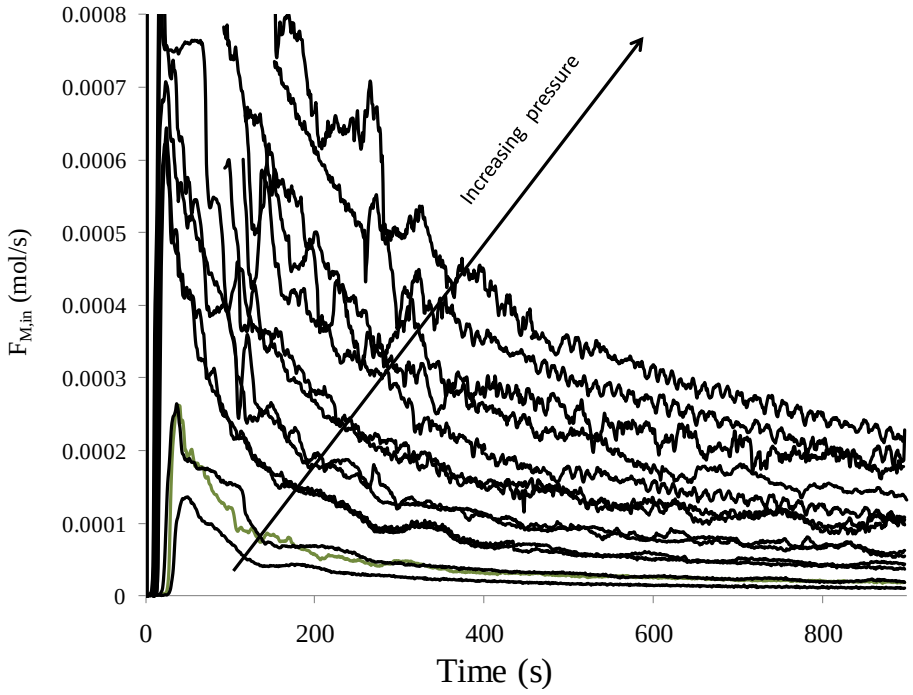

Figure 7-4. Ethylene reactor feed flow rate versus time at different total reactor pressures (For runs in Table 7-1).

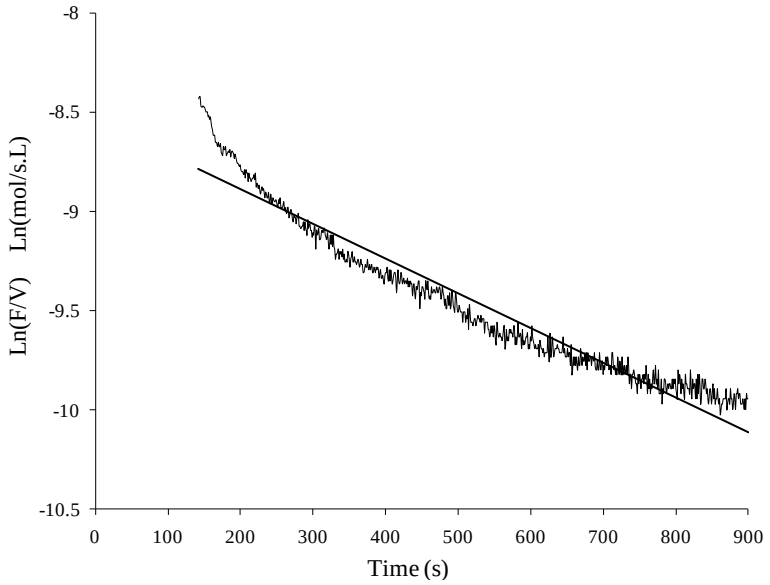

Figure 7-5. Experimental ethylene uptake curve and first order catalyst deactivation model for ethylene polymerization with CGC at total reactor pressure of 120 psig (Run 120 B in Table 7-1).

As an alternative to the first order catalyst decay model developed in Chapter 6, we propose a second order model to describe the data presented in Figure 7-4,

$$\frac{\mathrm{d}C_t}{\mathrm{d}t} = -k_d C_t^{\,2} \tag{7-11}$$

In Equation (7-11), it is assumed that the catalyst activation is instantaneous: as soon as the catalyst is injected in the reactor and comes in contact with MAO, all the catalyst sites are activated. Following a derivation similar to the one applied for *rac*-Et(Ind)$_2$ZrCl$_2$ in Chapter 6, we finally obtain the following expressions for monomer consumption rate, (more details on derivation are given in Appendix H)

$$F_{M,in} = \frac{k_p K V_R C_0 [M]^2}{(1+K[M])(1+k_d C_0 t)} \tag{7-12}$$

Rearranging gives,

$$\frac{V_R}{F_{M,in}} = \frac{(1+K[M])}{k_p K C_0 [M]^2} + \frac{(1+K[M])k_d C_0}{k_p K C_0 [M]^2} t \tag{7-13}$$

Equation (7-13) shows that, for second order catalyst decay kinetics, the plot of the reciprocal of the monomer of consumption rate versus time is linear. Figure 7-6 illustrates this behavior for some typical polymerization runs performed at different ethylene partial pressures.

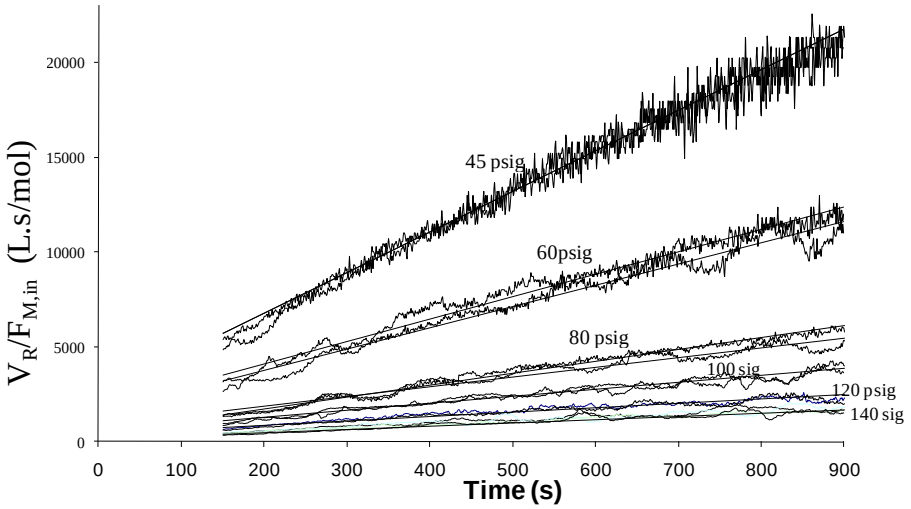

Figure 7-6. Second order decay model for CGC deactivation at several ethylene partial pressures.

Equation (7-12) can be integrated to derive an expression for the total number of moles of polymer made in the reactor after a given polymerization time,

$$n = \frac{k_p K V_R [M]^2}{(1 + K[M])k_d} \ln(1 + k_d C_0 t) \tag{7-14}$$

where *n* is polymer yield in moles. Although the polymerization curves presented in Figure 7-6 seem to be well described with a second order decay model, Equation (7-14) reveals that the polymer yield is not a linear function of catalyst concentration. However, the additional experimental results that will be reported below show that the polymer yield is indeed linearly related to catalyst concentration which contradicts the dependency found in Equation (7-14). Before proposing a modification to this deactivation mechanism in Section 7.4.5, results for the effect of catalyst concentration on the polymerization rate will be discussed.

7.4.4 Effect of Catalyst Concentration at High MAO Concentration.

7.4.4.1 Effect of Catalyst Concentration on Polymer Yield

Six polymerizations were performed at a constant MAO concentration (the same MAO concentration at which the previous set of polymerization runs, given in Table 7-1, were performed), but different catalyst concentrations and two polymerization temperatures, to investigate the effect of catalyst concentration on polymer yield at high MAO concentration. The polymerization conditions are summarized in Table 7-2. Runs 160A, 160B, 180A, and 180B have already been reported in Table 7-1 and are reproduced in Table 7-2 for easy comparison. Polymer yield and molecular weight measurements using GPC are shown in Table 7-3.

Table 7-2. Summary of polymerization conditions (effect of catalyst concentration).

Run	**Temperature (^{o}C)**	**Pressure (psig)**	**Catalyst concentration(μmol/L)**
C-3	140	120	2.55
C-2	140	120	1.89
C-1	140	120	1.22
160A	120	160	0.547
160B	120	160	0.547
160C	120	160	0.274
160D	120	160	0.274
180A	120	180	0.547
180B	120	180	0.547
180C	120	180	0.274

Table 7-3. Polymer yield and molecular weight measurement results (effect of catalyst concentration).

Run	M_n	M_w	PDI	Polymer Yield (g)
C-1	35 500	93 400	2.63	5.68
C-2	33 900	94 400	2.79	3.95
C-3	34 000	91 400	2.68	2.78
160A	105 000	216 600	2.06	8.6
160B	102 000	227 200	2.23	9.13
160C	101 700	225 400	2.22	4
160D	99 700	232 200	2.33	4.35
180A	109 600	237 300	2.17	10.4
180B	106 900	240 400	2.25	10.44
180C	105 800	247 900	2.34	5.03

The first three polymerization runs in Table 7-3 (runs C-1, C-2 and C-3) have the same polymerization conditions, except for the catalyst concentration. Figure 7-7 plots polymer yield versus catalyst concentration for these three runs, showing a clear linear relationship. Moreover, a linear extrapolation shows that it passes through the origin, as expected. Ethylene flow rate curves for these three polymerizations are shown in Figure 7-8. As a further test, we plotted the corresponding products of ethylene flow rates and catalyst ratio $C/C_{C\text{-}3}$, where $C_{C\text{-}3}$ is the catalyst concentration of run C-3, selected as the base, and C is the catalyst concentration of the other run. All curves merge into a single one, implying that ethylene flow rate is proportional to catalyst concentration in the reactor (Figure 7-9).

Comparing the yields of polymerization runs 160A and 160B with 160C and 160D shows that doubling catalyst concentration doubles polymer yield. The same conclusion is reached when the polymer yields for the runs 180A, 180B, and 180C are compared. Therefore, we have enough evidence to show that the polymer yield is proportional to the catalyst concentration in the reactor, at least at high MAO/CGC ratios and when the change in catalyst concentration is within the range

investigated in this study. These experimental findings are in disagreement with Equation (7-14), which results from the direct application of a second order decay profile for CGC.

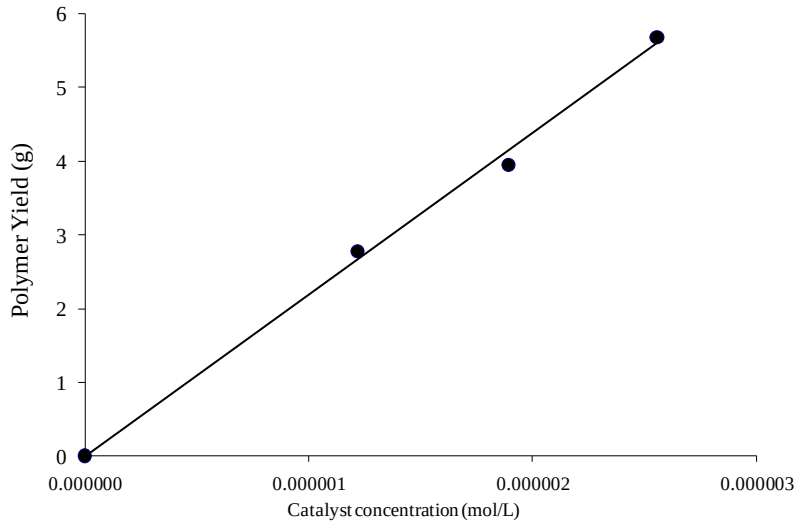

Figure 7-7. Plot of polymer yield versus catalyst concentration for runs C-1, C-2 and C-3.

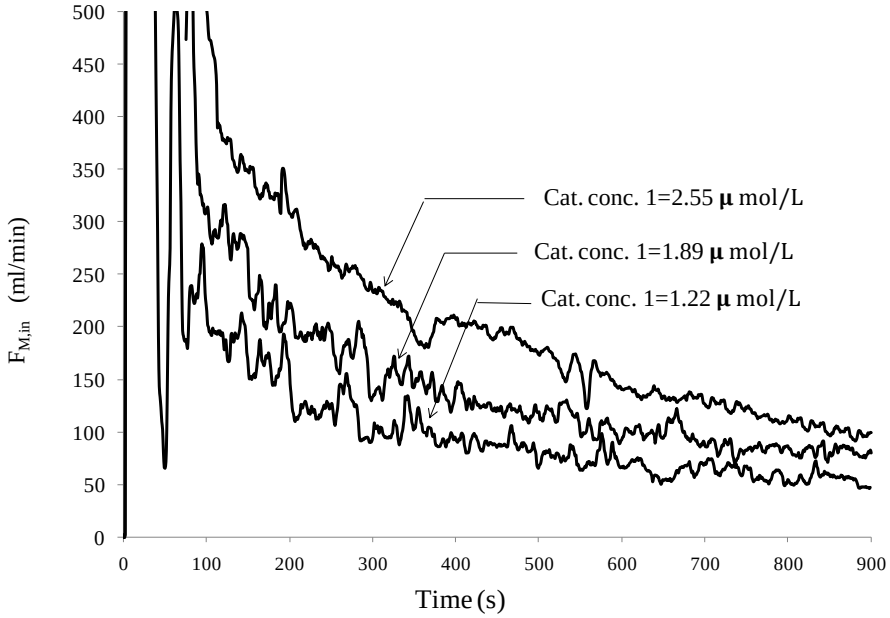

Figure 7-8. Ethylene reactor feed flow rate for runs C-1, C-2 and C-3.

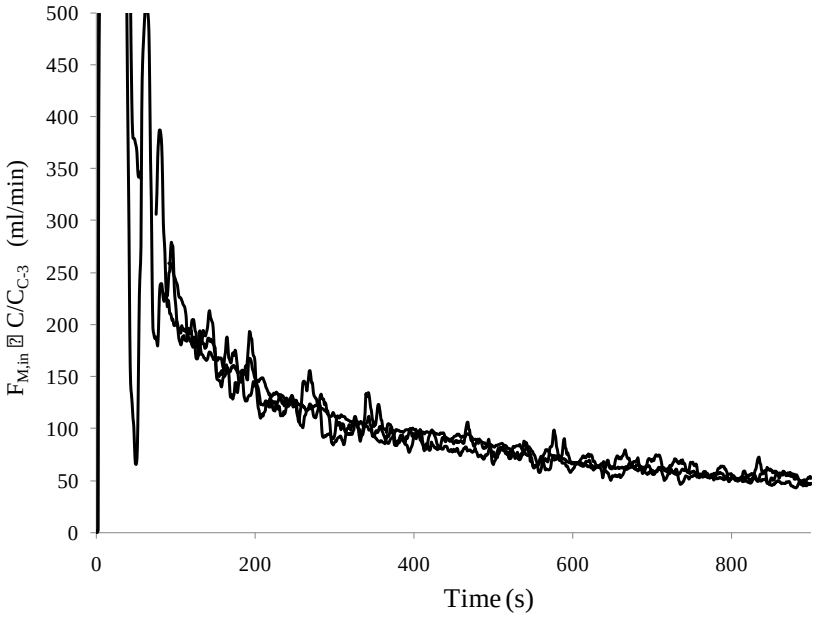

Figure 7-9. Plot of ethylene flow rate times catalyst concentration divided by catalyst concentration for run C-3 for runs C-1, C-2 and C-3.

7.4.4.2 Effect of Catalyst Concentration on Polymer Molecular Weight

A good estimate of variance for weight and number average molecular weight is necessary to check if change in catalyst concentration can affect molecular weight. Since variances for M_n and M_w are independent of ethylene concentration and they are nearly the same, combining variances using the pooled estimator of variances can provide these estimates.

The pooled estimate of the common standard deviation for M_w and M_n based on the data in Table 7-1 were found to be 5 864 and 4 200, respectively (For more details on calculation of pooled estimate of variance, see Appendix I). This variability includes errors from molecular weight measurements and polymerization replicates. The difference between the mean M_w of polyethylene samples made at two levels of catalyst concentration at 160 psig (runs 160A to 160D) is 6 931, which is less than two times of pooled estimate of the common standard deviation (2×5 864). The difference between the mean M_n of the same samples is 1150 which is again less than two times of pooled estimate of the common standard deviation for M_n (2×4 200). This means that the difference between the means of average molecular weights at the two levels of catalyst concentrations results from random error variable. A similar calculation was performed for the two levels of catalyst concentration at 180 psig, reaching

the same conclusion. Therefore, there is no evidence that changing catalyst concentration affects average molecular weights.

7.4.5 Modified Deactivation Mechanism

As shown above, a simple second order catalyst decay mechanism will not predict a linear relationship between polyethylene yield and catalyst concentration. However, the experimental results described in Section 7.4.4 show that such a linear relationship is indeed observed for the range of conditions investigated in this study. Therefore, it is necessary to propose a mechanism that can describe a non-first order catalyst decay rate and, at the same time, account for the linear relation between polymer yield and catalyst concentration in the reactor.

Let us assume that the uncomplexed and complexed active sites decay according to a first order model. Since we have assumed that the elementary reaction described in Equation (7-1) is a fast equilibrium, it is required that the deactivation rate constants for both active site states be the same, as will be explained in the short derivation below.

According to Equation (7-3), [P^*] and [$P^*{\cdot}M$] are related through the following relation,

$$[P^* \cdot M] = K[P^*][M] \tag{7-15}$$

Taking the derivative of both sides assuming that [M] is constant gives,

$$\frac{\mathrm{d}[P^* \cdot M]}{\mathrm{d}t} = K[M]\frac{\mathrm{d}[P^*]}{\mathrm{d}t} \tag{7-16}$$

Assuming that [P^*] and [$P^*{\cdot}M$] deactivate according to first order kinetics,

$$k_{d2}[P^* \cdot M] = K[M]k_{d1}[P^*] \tag{7-17}$$

and then using Equation (7-15), we conclude that $k_{d2} = k_{d1}$.

Therefore, the rate of deactivation for all catalyst sites, assuming first order decay, would follow the simple law,

$$\frac{dC_t}{dt} = -k_{d1}C_t \tag{7-18}$$

However, as we showed before, the simple first order model cannot explain the decay behavior of the CGC catalyst. Therefore, assuming that the deactivation of uncomplexed and complexed active sites occurs with different rate constants cannot be beneficial in explaining decay behavior of this catalyst. In order to model the catalyst decay behavior with CGC-Ti, we assumed that there were three elementary steps involved: thermal deactivation, and MAO-promoted deactivation and reactivation. The thermal deactivation step is given by the reaction below,

$$C_t \xrightarrow{k_{dth}} C_{dp} \tag{7-19}$$

where k_{dth} denotes the thermal deactivation rate constant, and C_{dp} are the permanently deactivated sites. MAO-promoted (or, possibly TMA contained in MAO) deactivation and reactivation reactions are represented as,

$$C_t + MAO \xrightarrow{k_d} C_d \tag{7-20}$$

$$C_d + MAO \xrightarrow{k_a} C_t \tag{7-21}$$

where C_d is a reversibly deactivated (or dormant) catalyst site that can be reactivated by reaction with MAO. This type of reversible deactivation mechanism has been used before to model the catalyst decay behavior of Cp_2ZrCl_2 for the polymerization of ethylene and propylene.[167-168]

The corresponding molar balances for C_t and C_d are given by,

$$\frac{dC_t}{dt} = -k_{dth}C_t - k_d[MAO]C_t + k_a[MAO]C_d \tag{7-22}$$

$$\frac{dC_d}{dt} = -k_a[MAO]C_d + k_d[MAO]C_t \tag{7-23}$$

Since MAO is present in excess and its concentration is much higher than the CGC-Ti concentration, $k_a[MAO]$ and $k_d[MAO]$ may be assumed to be invariant during polymerization and will be represented by the lumped constants k'_a and k'_d, respectively.

Equations (7-22) and (7-23) can be solved with Laplace transforms with the initial conditions $C_t = C_0$ and $C_d = 0$ at $t = 0$ to yield,

$$sC_t(s) - C_0 = -(k_{dth} + k_d')C_t(s) + k_a'C_d(s) \tag{7-24}$$

$$sC_d(s) = -k_a^{'}C_d(s) + k_d^{'}C_t(s) \tag{7-25}$$

Rearranging Equation (7-25),

$$C_d(s) = \frac{k_d^{'}C_t(s)}{(s + k_a^{'})} \tag{7-26}$$

and then substituting Equation (7-26) into Equation (7-24) yields,

$$C_t(s) = \frac{C_0(s + k_a^{'})}{(s + k_{dth} + k_d^{'})(s + k_a^{'}) - k_d^{'}k_a^{'}} \tag{7-27}$$

The theory of partial fractions enables us to write Equation (7-27) as,

$$C_t(s) = \frac{C_0(s_1 + k_a^{'})}{(s_1 - s_2)(s - s_1)} - \frac{C_0(s_2 + k_a^{'})}{(s_1 - s_2)(s - s_2)} \tag{7-28}$$

where s_1 and s_2 are constants defined as,

$$s_1 = \frac{1}{2}\left[\sqrt{(k_{dth} + k_d^{'} + k_a^{'})^2 - 4k_{dth}k_a^{'}} - (k_{dth} + k_d^{'} + k_a^{'})\right] \tag{7-29}$$

$$s_2 = -\frac{1}{2}\left[\sqrt{(k_{dth} + k_d^{'} + k_a^{'})^2 - 4k_{dth}k_a^{'}} + (k_{dth} + k_d^{'} + k_a^{'})\right] \tag{7-30}$$

Taking the inverse Laplace transform of Equation (7-28) gives the solution for the concentration of active sites in the time domain,

$$C_t = \frac{C_0}{(s_1 - s_2)}\left[(s_1 + k_a^{'})e^{s_1 t} - (s_2 + k_a^{'})e^{s_2 t}\right] \tag{7-31}$$

The molar balance for monomer in a semi-batch reactor is given by,

$$\frac{\mathrm{d}[M]}{\mathrm{d}t} = \frac{F_{M,in}}{V_R} - R_p \tag{7-32}$$

Since monomer concentration is kept constant, we conclude that,

$$F_{M,in} = R_p V_R \tag{7-33}$$

Combining Equations (7-9), (7-31) and (7-33) leads to the final expression for the monomer feed flow rate to the reactor for a catalyst that follows the trigger mechanism and deactivates according to the steps proposed in Equations (7-19)-(7-21),

$$F_{M,in} = \frac{k_p K[M]^2 C_0 V_R}{(1+K[M])(s_1 - s_2)}\left[(s_1 + k_a^{'})e^{s_1 t} - (s_2 + k_a^{'})e^{s_2 t}\right] \tag{7-34}$$

Finally, the polymer yield, in moles, can be obtained by the integration of Equation (7-34),

$$n = \frac{k_p K[M]^2 C_0 V_R}{(1+K[M])(s_1 - s_2)}\left[\frac{(s_1 + k_a^{'})}{s_1}(e^{s_1 t} - 1) - \frac{(s_2 + k_a^{'})}{s_2}(e^{s_2 t} - 1)\right] \tag{7-35}$$

Differently from Equation (7-14), Equation (7-35) predicts that the polymer yield depends linearly on catalyst concentration in the reactor, in agreement with the experimental findings presented in Section 7.4.4.

7.4.6 Estimation of Kinetic Parameters

Equation (7-34) can be rearranged into the following form,

$$\frac{(1+K[M])F_{M,in}}{K[M]^2} = \frac{k_p C_0 V_R}{(s_1 - s_2)}\left[(s_1 + k_a^{'})e^{s_1 t} - (s_2 + k_a^{'})e^{s_2 t}\right] \tag{7-36}$$

The right hand side (RHS) of Equation (7-36) is a function of polymerization time, catalyst concentration, reactor volume, and temperature-dependent rate constants, while the left hand side (LHS) depends on monomer concentration, reactor feed flow rate, and the equilibrium constant *K*. Therefore, if we plot Equation (7-36) LHS versus time for the runs performed at varying monomer concentrations but same catalyst concentration, reactor volume, and temperature, we expect all curves to merge into a single one, given that we have chosen a proper value for the equilibrium constant *K*.

The optimum value for *K* can be obtained by minimizing the following objective function,

$$\chi = \frac{\int\left[\left(\frac{(1+K[M])F_{M,in}}{[M]^2}\right)_{\max} - \left(\frac{(1+K[M])F_{M,in}}{[M]^2}\right)_{\min}\right]\mathrm{d}t}{\int\left[\frac{(1+K[M])F_{M,in}}{[M]^2}\right]a_v \mathrm{d}t} \tag{7-37}$$

where the subscripts 'max' and 'min' are the maximum and minimum values of Equation (7-36) LHS for all runs at time *t*, and a_v refers to its average value for all runs at time *t*. In fact, by minimizing this objective function, we are minimizing the area of the error band relative to total area under the average monomer consumption rate. Half of the value of the objective function at the optimum point would be the maximum value of the error in predicting polymer yield with Equation (7-35). The optimum *K* value estimated by minimizing the objective function defined in Equation (7-37) is 1.1.

Figure 7-10 shows the plot of Equation (7-36) LHS versus time for all the polymerization runs in Table 7-1 using K = 1.1. All curves merge relatively well into a single 'master" curve, especially taking into consideration that, due to normal random error during the polymerizations, perfect overlapping would be extremely unlikely. Since the reactor temperature and pressure fluctuate more at the beginning of the polymerization, more variability is observed at shorter polymerization times.

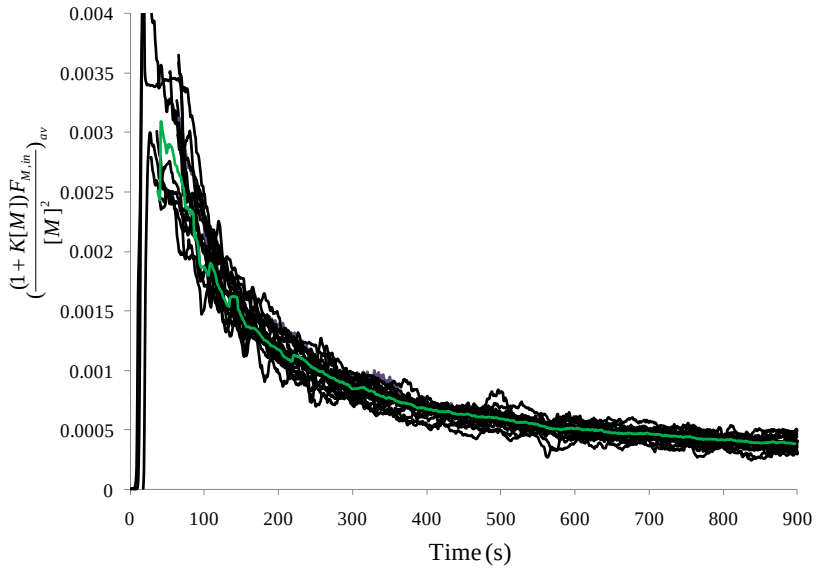

Figure 7-10. Plot $[\ (1+K[M])F_{M,in}/[M]^2]_{av}$ versus time for all the runs in Table 7-1.

Equation (7-36) was used to estimate the model parameters $k_a^{'}$, $k_pC_0V_R$, s_1 and s_2 by fitting the average value of Equation (7-36) LHS for all runs, $\left\{\frac{(1+K[M])F_{M,in}}{[M]^2}\right\}_{av}$, using the MATALB curve fit toolbox. The parameter estimates, with their approximate 95% confidence intervals, are shown in

Table 7-4. None of the confidence intervals include zero, indicating that all the parameters are significant and supporting the model's adequacy.

Figure 7-11 shows the experimental Equation (7-36) LHS for all runs $\left\{\frac{(1+K[M])F_{M,in}}{[M]^2}\right\}_{av}$ superimposed with the RHS of equation 7-36 with the estimated model parameters in Table 7-4.

Table 7-4. Summary of estimated model parameters

Parameter	**Estimated value with approximate 95% confidence interval**
$k_a^{'}$	$3.3746\times10^{-3}\pm1.5\times10^{-4}$ s^{-1}
$k_pC_0V_R$	$6.149\times10^{-3}\pm1.34\times10^{-4}$ $L.s^{-1}$
s_1	$-1.169\times10^{-2}\pm3.7\times10^{-4}$ s^{-1}
s_2	$-1.202\times10^{-3}\pm4.5\times10^{-5}$ s^{-1}

Values for k_{dth} and $k_d^{'}$ can be calculated using the equations below, obtained by solving Equations (7-29) and (7-30) simultaneously,

$$k_{dth} = \frac{s_1 s_2}{k_a^{'}} \tag{7-38}$$

$$k_d^{'} = -(s_1 + s_2) - \frac{s_1 s_2}{k_a^{'}} - k_a^{'} \tag{7-39}$$

Table 7-5 tabulates the point estimates of the all kinetic parameters required for the model represented by Equation (7-34).

Table 7-5. Estimated values of kinetic parameters for Equation (7-34).

Parameter	Estimated value
$k_a^{'}$	3.746×10^{-3} s^{-1}
k_p	5.0455×10^{4} $L.mol^{-1}.s^{-1}$
k_{dth}	3.633×10^{-3} s^{-1}
$k_d^{'}$	5.1436×10^{-3} s^{-1}
K	1.1

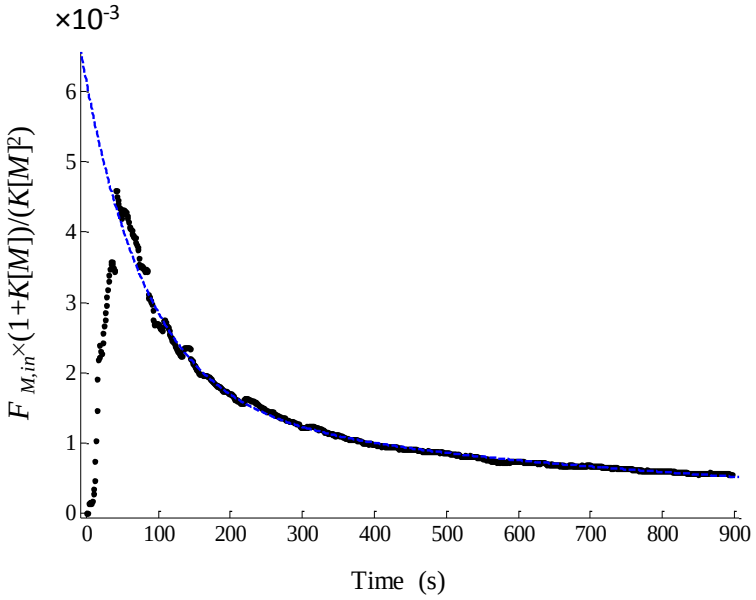

Figure 7-11. Plot of Equation (7-36) LHS, $[\ (1+K[M])F_{M,in}/[M]^2]_{av}$, versus time. The dotted curve shows the fitted curve.

Figure 7-12 shows how the experimental ethylene feed flow rates are very well represented by Equation (7-34) using the parameters reported in Table 7-5. The excellent agreement demonstrates that the proposed model can describe well the dependency of time and ethylene pressure on the monomer uptake curves.

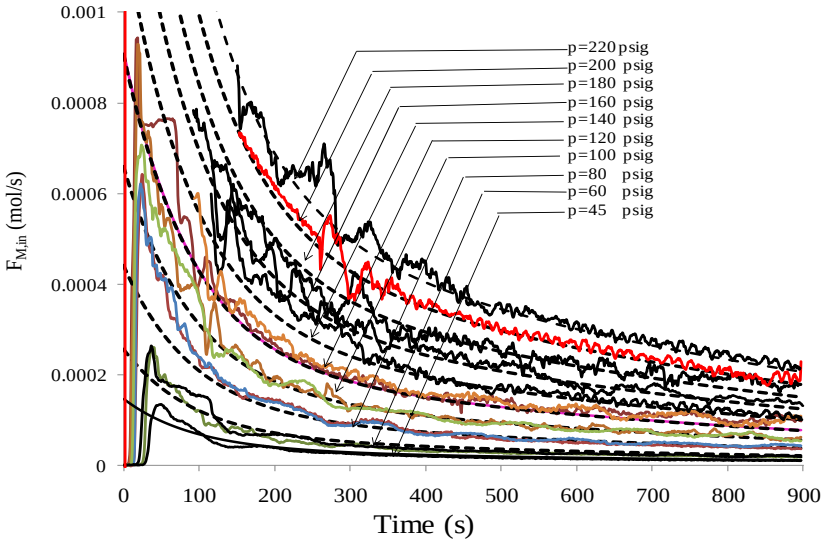

Figure 7-12. Comparison between experimental ethylene feed flow rates and model predictions with Equation (7-34) and parameters in Table 7-5.Dashed curves are model predictions.

Using the estimated kinetic parameters reported in Table 7-5 and Equation (7-35), we tried to predict the polymer yield. Figure 7-13 compares experimental and predicted polymer yields for a wide range of ethylene concentrations. Once again, good agreement was observed between experimental data and model predictions.

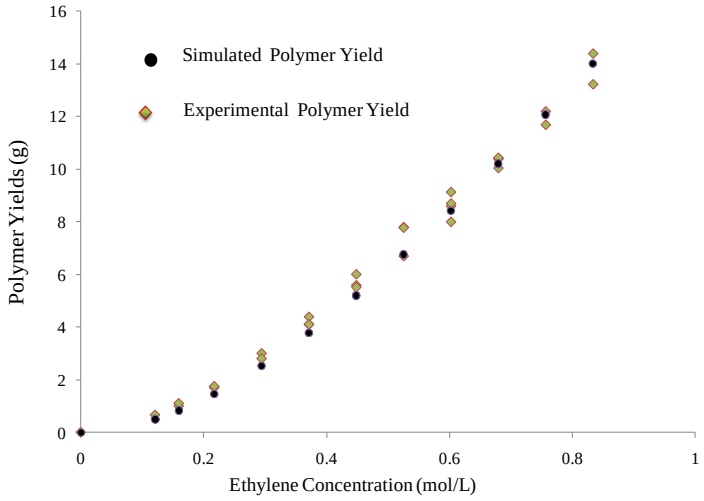

Figure 7-13. Comparison between experimental and simulated polymer yields.

The findings on decay behaviour of the CGC-Ti catalyst can be summarized as follows:

- Assuming a first order model alone (thermal decay or deactivation by impurities) cannot explain CGC deactivation. A second order model can explain CGC deactivation as a function of time, but it is unable to explain the effect of catalyst concentration.
- Assuming reversible activation and deactivation with MAO can explain the effect of catalyst concentration, but it cannot explain the effect of time because the consequence of this assumption would be the following equation for ethylene flow rate into the reactor, obtained by solving the relevant differential equations,

$$F_{M,in} = \frac{k_p K[M]^2 C_0 V_R}{(1+K[M])(k_a^{'}+k_d^{'})}\left[k_a^{'} + k_d^{'} e^{-(k_a^{'}+k_d^{'})t}\right] \tag{7-40}$$

  When time approaches infinity, the liming value for monomer flow rate reaches the limiting value'

$$F_{M,in} = \frac{k_p K[M]^2 C_0 V_R k_a^{'}}{(1+K[M])(k_a^{'}+k_d^{'})} \tag{7-41}$$

  This limiting behavior contradicts our findings because our observations were that kinetic curves go to zero as time increases.

In conclusion, in addition to reversible activation and deactivation with MAO, thermal deactivation should also be assumed to explain the effect of monomer concentration, catalyst concentration, and time on the polymerization rate of ethylene with CGC-Ti under the conditions investigated in this study.

7.4.7 Effect of Monomer Concentration on Molecular Weight

Figure 7-14 shows how M_n, M_w and *PDI* of polyethylene made with CGC-Ti vary with reactor total pressure. The *PDI* remains practically constant in all polymerizations, with values in a narrow range between 2 and 2.5, as theoretically expected for a single-site catalyst. Both M_n and M_w initially increase with polymerization pressure and then tend to constant values, which is consistent with a chain growth mechanism controlled by transfer to ethylene.

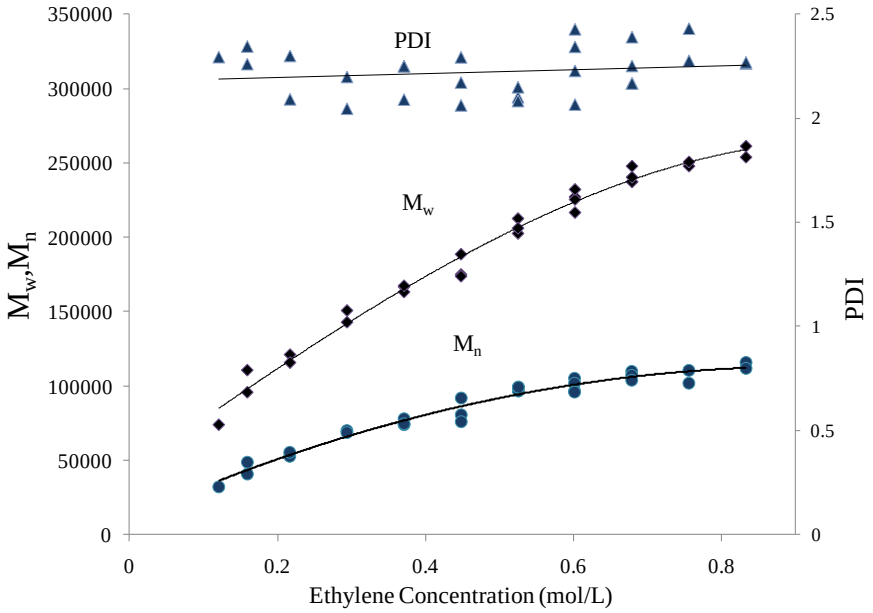

Figure 7-14. Variation of M_n, M_w and PDI with ethylene concentration.

7.4.8 Estimation of Chain Transfer Rate Constants

Transfer to monomer, to metal alkyls, to transfer agents, such as H_2, and β-hydride elimination, are among the main chain transfer mechanisms for polymerization with coordination catalyts.[31-32]

The number average molecular weight, M_n, is related to the relative rate of propagation to chain transfer reactions through the following equation,

$$\frac{mw}{M_n} = \frac{R_M + R_{\beta H} + R_{Al}}{R_P} \tag{7-42}$$

where R_P is the rate of propagation, R_M, $R_{\beta H}$ and R_{Al} are the rate of transfer to monomer, β-hydride elimination, and transfer to MAO, respectively, and mw is monomer molecular weight.

When a monomer approaches a complexed catalyst site, two reactions may take place: transfer to ethylene, forming a dead polymer chain with a terminal double bound (macromonomer) and a catalyst site attached to a single monomer unit, as described in Equation (7-43), or monomer propagation, where the monomer molecule is inserted into the growing polymer chain, as already represented in Equation (7-2),

$$P^* \cdot M + M \xrightarrow{k_M} \overline{\overline{P}} + P^* \cdot M \tag{7-43}$$

where $\overline{\overline{P}}$ denotes polymer chains with terminal double bound. Notice that we kept the trigger mechanism formalism that assumes that one monomer molecule remains complexed to the active site.

Macromonomers can also be formed via β-hydride elimination, in which the hydrogen atom attached to the β carbon in the chain is transferred to the metal center, as described in the following equation,

$$P^* \cdot M \xrightarrow{k_{\beta H}} \overline{\overline{P}} + C_i \tag{7-44}$$

The rates of macromonomer formation by these two transfer mechanisms are given by the expressions,

$$R_M = k_M [P^* \cdot M][M] \tag{7-45}$$

$$R_{\beta H} = k_{\beta H} [P^* \cdot M] \tag{7-46}$$

Substituting [*P*.M*] with Equation (7-6) into Equations (7-45) and (7-46),

$$R_M = \frac{k_M K[M]^2 C_t}{1 + K[M]} \tag{7-47}$$

$$R_{\beta H} = \frac{k_{\beta H} K[M] C_t}{1 + K[M]} \tag{7-48}$$

Similarly, for chain transfer to MAO,

$$R_{Al} = \frac{k_{Al}[Al] K[M] C_t}{1 + K[M]} \tag{7-49}$$

Finally, substituting Equations (7-9), (7-47), (7-48), and (7-49) into Equation (7-42) gives,

$$\frac{mw}{M_n} = \frac{k_M}{k_p} + \frac{k_{\beta H} + k_{Al}[Al]}{k_p} \times \frac{1}{[M]} \tag{7-50}$$

or,

$$\frac{M_n}{mw} = \frac{[M]}{\frac{k_M}{k_p}[M] + \frac{k_{\beta H} + k_{Al}[Al]}{k_p}} \tag{7-51}$$

which is, in fact, the same result we obtained in Equation (6-31). Figure 7-15 shows the plot of mw/M_n versus the reciprocal of ethylene concentration in the reactor. The slope and intercept of the line provide the point estimates for k_M / k_p and $(k_{\beta H}+k_{Al}[Al])/ k_{p,}$ respectively, which are reported in Table 7-6.

Figure 7-16 plots M_n/mw versus monomer concentration. Nonlinear regression of Equation (7-51) was performed by minimizing sum of squares of the residuals to obtain k_M / k_p and $(k_{\beta H}+k_{Al}[Al])/ k_p$. Assuming that the variability in ethylene concentration is negligible, the approximate confidence interval for the parameters can also be calculated. Table 7-6 summarizes the results of 95% confidence interval calculations for the parameters using linear regression and the corresponding approximate ones using nonlinear regressions.

Table 7-6. Summary of chain transfer parameter estimation using linear and nonlinear regression.

Parameter	**Linear Regression**	**Estimated standard error**	**Nonlinear Regression**	**Estimated Standard Error**
k_M / k_p	$1.43\times10^{-4}\pm1.8\times10^{-5}$	8.68×10^{-6}	$1.5\times10^{-4}\pm1.6\times10^{-5}$	8×10^{-6}
$(k_{\beta H}+k_{Al}[Al])/ k_p$	$8.2\times10^{-5}\pm5.6\times10^{-6}$	2.71×10^{-6}	$7.86\times10^{-5}\pm8.9\times10^{-6}$	4.33×10^{-6}

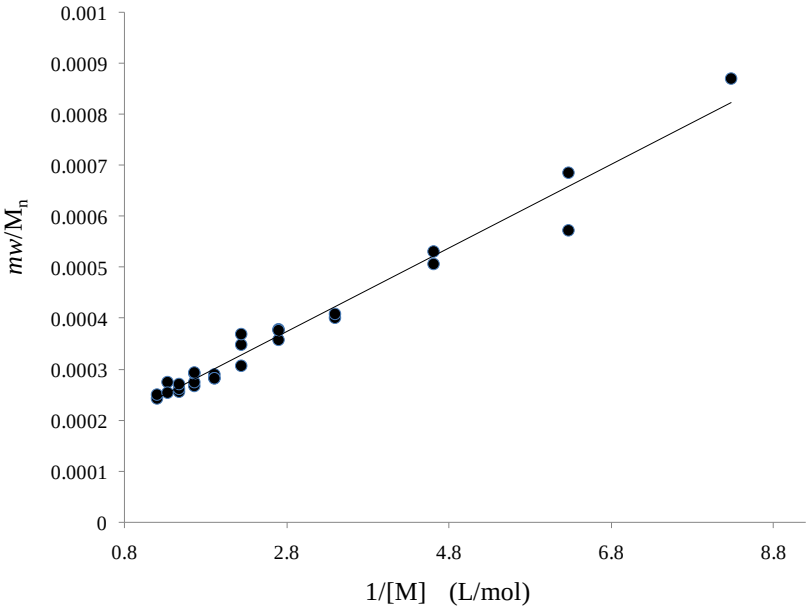

Figure 7-15. Plot of $1/M_n$ versus $1/[M]$.

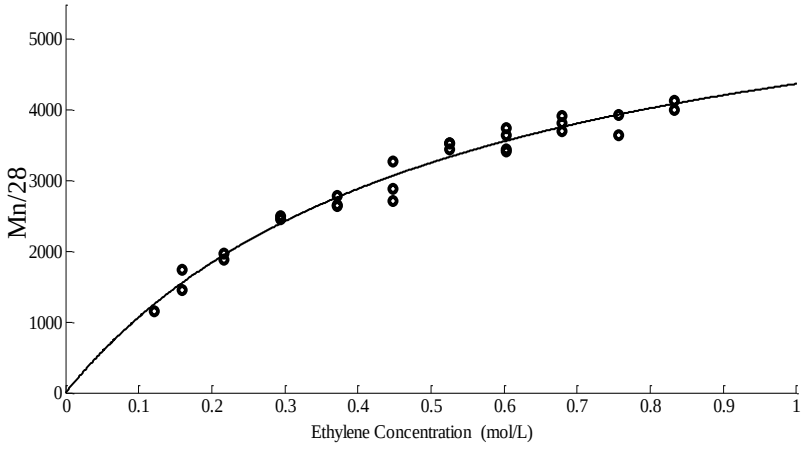

Figure 7-16. Curve fitting for M_n data using Equation (7-51).

7.4.9 Effect of MAO Concentration on Polymer Microstructure

Thirteen polymerization runs were performed to study effect of MAO concentration on microstructural properties of the resulting polymer. Temperature and pressure were kept constant during all polymerizations. Catalyst concentration was also the same for all polymerizations, except for Run 453, where it was necessary to reduce the Al/Ti to its lowest value. The summary of polymerizations conditions is given in Table 7-7.

Table 7-7. Summary of polymerization run conditions (effect of MAO).

Run	MAO (g)	Al/Ti
441	0.98	12 400
442	1.57	19 900
443	2.75	34 900
444	0.39	4 900
445	2.16	27 400
446	0.98	12 400
447	1.57	19 900
448	3.93	49 500
454	0.39	4 900
455	1.57	19 900
456	2.75	34 900
457	0.98	12 400
453[a]	0.39	1 200

Catalyst concentration: 0.62 μmol/L, polymerization temperature: 120^{o}C, polymerization pressure 120 psig.

[a]Catalyst concentration: 2.44 μmol/L

Table 7-8 summarizes molecular weight average measurements, and polymer yield.

Table 7-8. Summary of polymer yield and GPC data.

Run	M_w	M_n	PDI	Polymer Yield (g)
441	177 200	68 100	2.6	2.4
442	184 900	80 500	2.3	3.5
443	164 200	82 000	2.2	5.92
444	153 700	39 900	3.85	0.97
445	175 500	76 900	2.28	5.02
446	180 800	69 000	2.62	2.84
447	183 500	78 400	2.34	3.84
448	191 200	88 100	2.17	7.77
454	168 000	48 200	3.49	1.24
455	177 800	76 700	2.32	4.12
456	188 700	83 600	2.26	6.94
457	152 600	62 700	2.43	2.62
453	147 700	37 800	3.91	3.01

The polymer yield increases with MAO concentration in the reactor, as shown in Figure 7-17. Interestingly, the polymer yield for Sample 453, which was made at higher catalyst concentration than the other runs, does not lie on the curve showing the trend for the samples made at the same (lower) catalyst concentration but different MAO concentrations. However, if we normalize its yield by multiplying by the catalyst concentration of all other samples and then dividing by its catalyst concentration, we see that it follows the same trend. This confirms that polymer yield is linearly related to catalyst concentration, as shown before. Figure 7-18 illustrates how PDI, M_n and M_w vary with Al/Ti ratio. Decreasing Al/Ti ratio down to a certain level (about 20 000) does not affect molecular weight and PDI, while a further decrease will reduce M_n and M_w, and increase polydispersity.

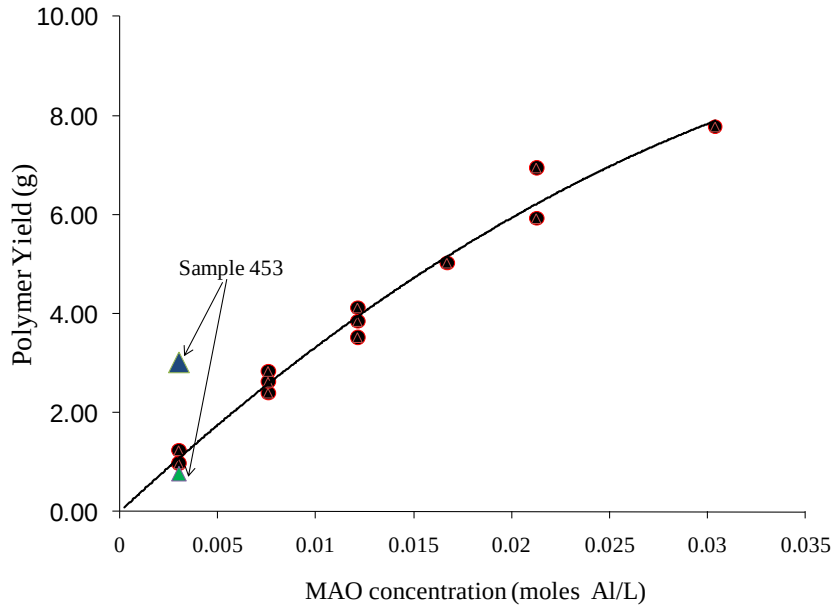

Figure 7-17. Polymer yield versus MAO concentration.

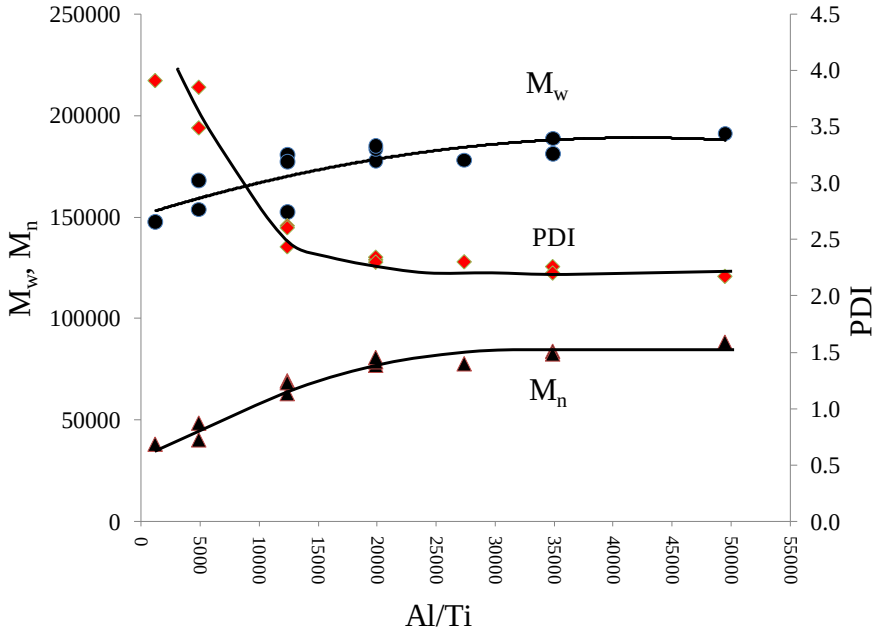

Figure 7-18. Molecular weight averages and PDI as a function Al/Ti.

7.4.10 Long Chain Branch Detection

Figure 7-19 shows the 15° light scattering signal intensity versus GPC elution volume for all the polymerization runs listed in Table 7-7. For samples made at high MAO concentration or high Al/Ti ratio (Al/Ti > 20 000), no significant shoulder or bimodality is observed. At low Al/Ti ratios (Al/Ti < 12 000 and lower) a shoulder appears at low elution volumes, becoming more significant as the Al/Ti ratio decreases. To confirm that this high molecular weight shoulder comes from long chain branching, we analyzed Sample 453, which had the lowest Al/Ti ratio of all samples shown in Table 7-7, by ^{13}C NMR. Figure 7-20 shows the proton-decoupled ^{13}C NMR spectrum for Sample 453. Seven well resolved peaks were observed with the chemical shifts positioned at 14.2, 22.9, 32.2, 34.57, 27.28, 38.2 and 33.97 ppm. To account for the peaks observed in this spectrum, the structure shown in Figure 7-21 was assumed. Based on the Grant and Paul rules, the foregoing chemical shifts correspond to carbons 1, 2, 3, α, β, *br* and 1v, respectively. Other types of carbons have chemical shifts located at 30 or near 30 ppm so they would be obscured by the main peak at 30 ppm. Inspection of the spectrum in Figure 7-20 confirms the presence of LCBs in Sample 453. The plot of log [η] versus log MW for Sample 453 depicted in Figure 7-22 further confirms the presence of LCBs in this sample.

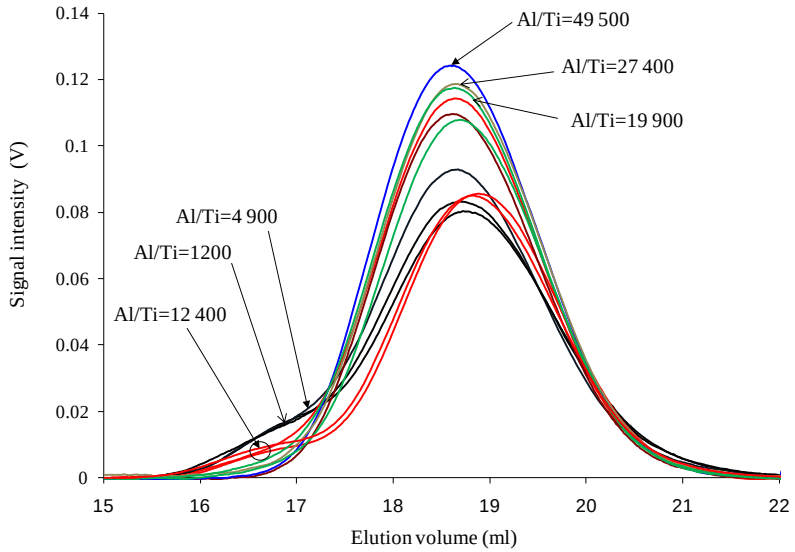

Figure 7-19. 15° Light scattering signal intensity versus GPC elution volume for samples made under different Al/Ti ratios.

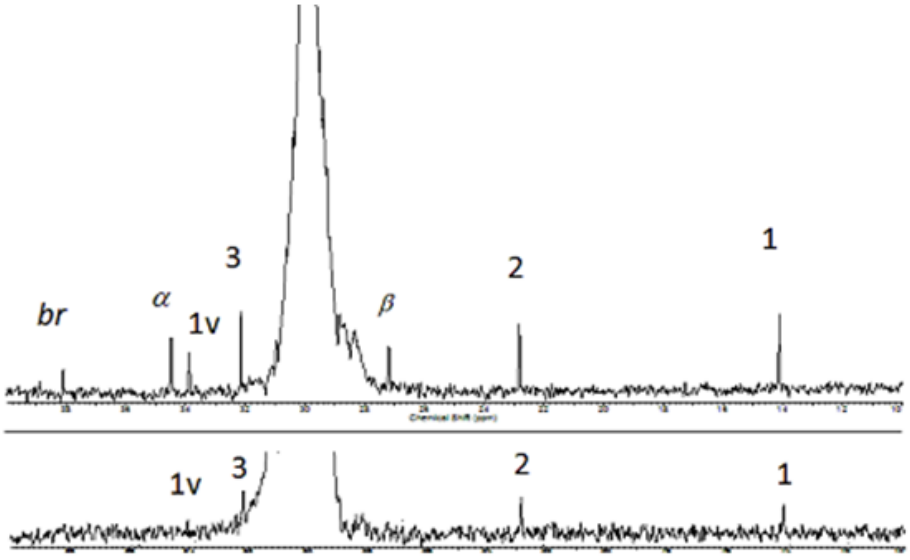

Figure 7-20. ^{13}C-NMR spectrum for Sample 453 (top) and 448 (bottom).

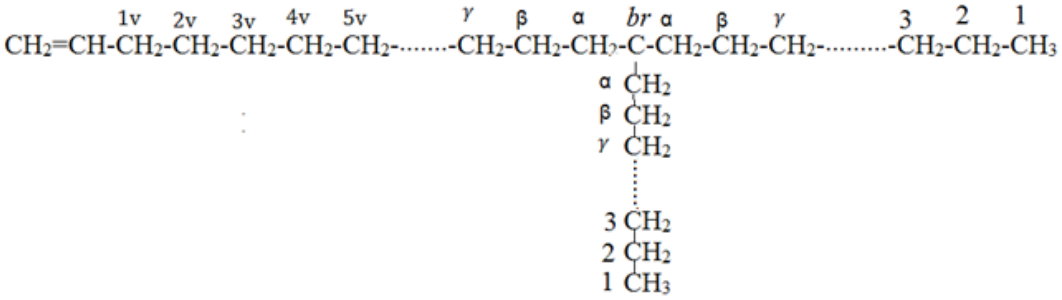

Figure 7-21. Chemical structure for long chain branched CGC-Ti polyethylene.

The increase in PDI observed when the Al/Ti ratio was reduced can be partially attributed to the formation of LCBs, as shown in ^{13}C-NMR spectra for Sample 453, but the observed increase is too high to be credited only to the presence of LCBs.

Sample 448, which was made at high Al/Ti ratio, was also analyzed using ^{13}C-NMR spectroscopy. Four peaks, corresponding to 1, 2, 3 and 1v carbons were observed, but no LCB peak was detected (Figure 7-20). In addition, its log [η] versus log MW plot was linear, indicating that LCB frequency in the sample is negligible. The summary of ^{13}C NMR analysis for the two samples is given in Table 7-9.

Table 7-9. Summary of ^{13}C-NMR analysis for the samples 453 and 448.

Sample	UCED	SCED	LCBF
453	0.39	0.78	0.23
448	0.064	0.29	0

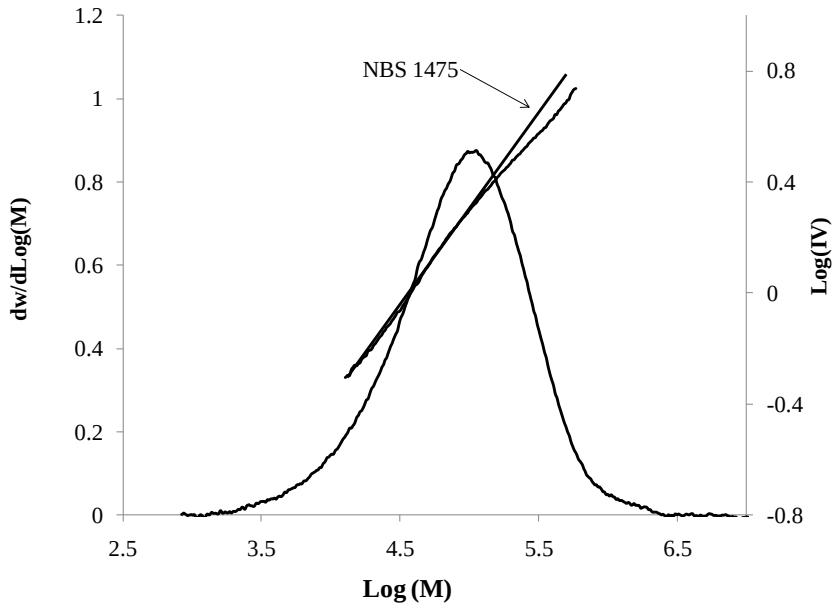

Figure 7-22. Molecular weight distribution and intrinsic viscosity plot for Sample 453.The intrinsic viscosity plot for the linear sample NBS 1475 is shown for comparison.

To better understand why molecular weight decreases when the Al/Ti ratio is reduced, the unsaturated chain end density (UCED) – the number of vinyl groups per 1000 carbon atoms in the sample – of seven randomly selected polymer samples (samples:456, 448, 445, 453, 454, 455, 446) made at

different Al/Ti ratios were measured using FTIR spectroscopy. This method was explained in detail in Chapter 5, Section 5.1.5. Figure 7-23 plots the sample UCEDs versus the Al/Ti ratio. (The multiple points at each Al/Ti level are measured replicates, not polymerization replicates, so the variability at each Al/Ti level reflects variability in UCED measurements). Since UCED for Sample 448, (made at the high Al/Ti ratio of 49 500) is low and the sample has no LCBs, it seems that high Al/Ti ratios slow down chain transfer reactions that lead to the formation of vinyl-terminated chains (macromonomers), while the rate of transfer to MAO increases. It also appears that the decrease in the rate of macromonomer formation reactions is more pronounced than the increase in the rate of chain transfer to MAO as the Al/Ti ratio is increased. The overall effect of these two rate changes is that molecular weight initially increases with increasing Al/Ti ratio until it finally levels off while, at the same time, the concentration of macromonomer decreases. Therefore, when the Al/Ti ratio decreases, the rate of macromonomer formation increases, the molecular weight decreases, and more LCBs are formed.

Figure 7-24 shows how the unsaturated chain end frequency (UCEF), or the number of unsaturated chain ends per polymer chain, varies as a function of the Al/Ti ratio. The UCEF was calculated with the expression,

$$UCEF = \frac{UCED \times M_n}{14000} \tag{7-52}$$

It is interesting to note that at low Al/Ti ratios UCEF is approximately equal to 1. This indicates that most chains in the sample have one vinyl terminal group and, consequently, that chain transfer to MAO is negligible when the Al/Ti ratio is relatively low. Since UCEF decreases with increasing Al/Ti and chain transfer to MAO does not produce vinyl terminated chains, transfer to MAO is likely to become more relevant at higher Al/Ti ratios.

Figure 7-25 compares the MWD of Sample 448 made at Al/Ti = 49 500 with those of Samples 444 and 453, produced with Al/Ti ratios of 4 900 and 1 200, respectively. The fraction of low molecular weight chains increases when the MAO concentration decreases. It can be speculated that this lower molecular weight chains are more likely to be vinyl terminated. It is also interesting to note that, for these samples, MWD depends on MAO concentration, not on Al/Ti ratio, because Samples 453 and 444 were made at the same MAO concentration but at different Al/Ti ratios of 1200 and 4200, respectively.

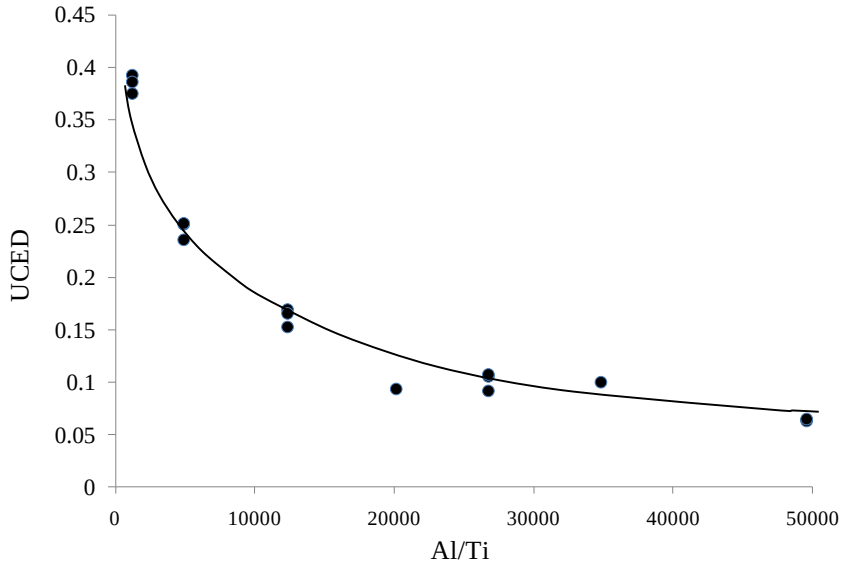

Figure 7-23. Unsaturated chain end density (UCED) as a function of Al/Ti ratio.

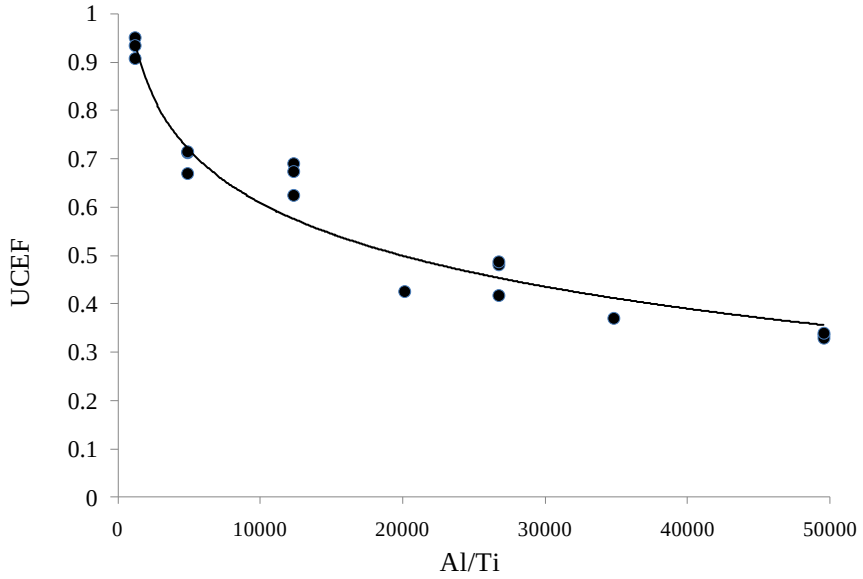

Figure 7-24. Unsaturated chain end frequency (UCEF) versus Al/Ti ratio.

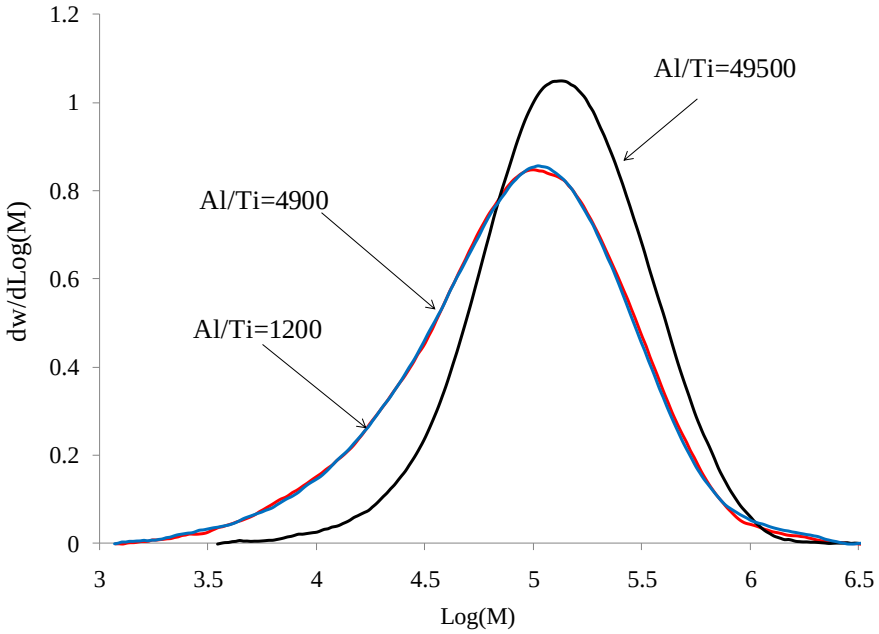

Figure 7-25. Molecular weight distributions of Samples 444, 453, and 448 made at different Al/Ti ratios.

7.4.11 Effect of Monomer Concentration on Long Chain Branching at low Al/Ti Ratio (Al/Ti=916)

Long chain branch formation with metallocene catalysts is simply copolymerization with macromonomers; thus, decreasing ethylene concentration in the reactor is expected to increase LCB formation. The experimental results shown in the previous section show that low MAO concentration favors the formation of macromonomers, which is a pre-requisite for LCB formation. In this section we analyze the effect of changing ethylene concentration at low MAO concentration on LCB formation.

The effect of ethylene concentration was investigated by varying the total reactor pressure from 40 to 210 psig at a temperature of 120^{o}C. Nine polymer samples were made at five different pressures (Table 7-10). MAO and catalyst concentration, polymerization time and temperature were kept the same in all runs. Molecular weight averages, polymer yields, and LCB estimations are presented in Table 7-11.

Table 7-10. Summary of polymerization runs (Effect of monomer concentration at Al/Ti=916).

Run	733	734	735	736	737	738	741	742	745
Total reactor pressure (psig)	120	160	80	80	120	205	120	40	40

Catalyst concentration: 4.9 μmole/L, Temperature: 120°C, Al/Ti: 916.

Table 7-11. Summary of GPC results and polymer yields (Effect of monomer concentration at Al/Ti=916).

Run	**Pressure (psig)**	M_w	M_n	**PDI**	**Polymer Yield (g)**	**LCBF**[a]
733	120	142200	40200	3.5	4.57	0.2
734	160	176700	46400	3.8	6.64	0
735	80	113400	31400	3.6	2.04	0.27
736	80	113600	32400	3.5	2.50	0.25
737	120	137600	38600	3.6	4.79	0.21
741	120	158900	46300	3.4	4.69	0.18
742	40	94000	23400	4.0	0.65	0.32
738	205	195300	55100	3.5	10.22	0
745	40	105200	24900	4.2	0.77	0.3

[a] Estimated using Zimm-Stockmeyer equation.

Figure 7-26 plots polymer yield versus monomer concentration. As observed for high Al/Ti (see Figure 7-1), a non-first order dependence on monomer concentration is also noticed.

Plots of the 15° GPC light scattering detector signal intensity versus elution volume for all polymer samples are shown in Figure 7-27. At an ethylene pressure of 120 psig, a shoulder is observed on the low elution volume region (high molecular weight), which corresponds to long chain branched polymer chains, as demonstrated in Section 7.4.8.1. Decreasing ethylene pressure accentuates this bimodality. The area under the high molecular weight peak (low elution volume) increases as ethylene pressure decreases, implying that LCB formation is more significant at lower pressures.

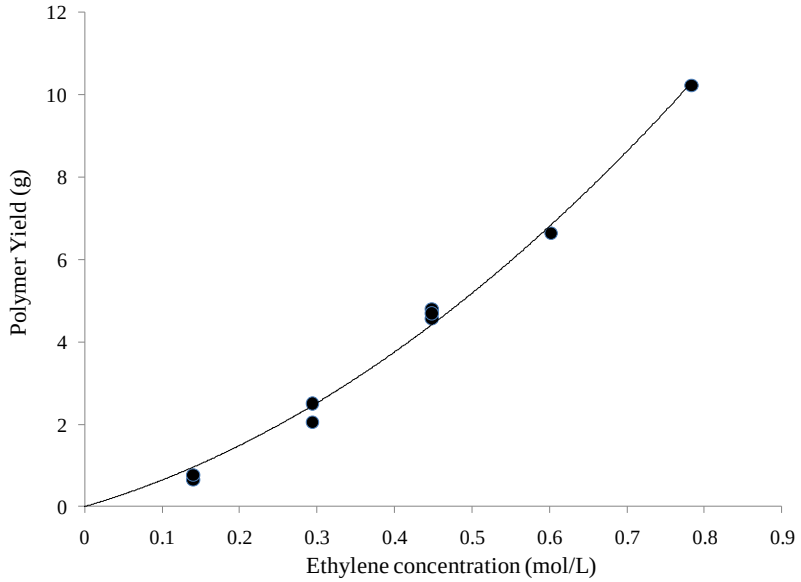

Figure 7-26. Polymer yield as a function of ethylene concentration (Al/Ti=916).

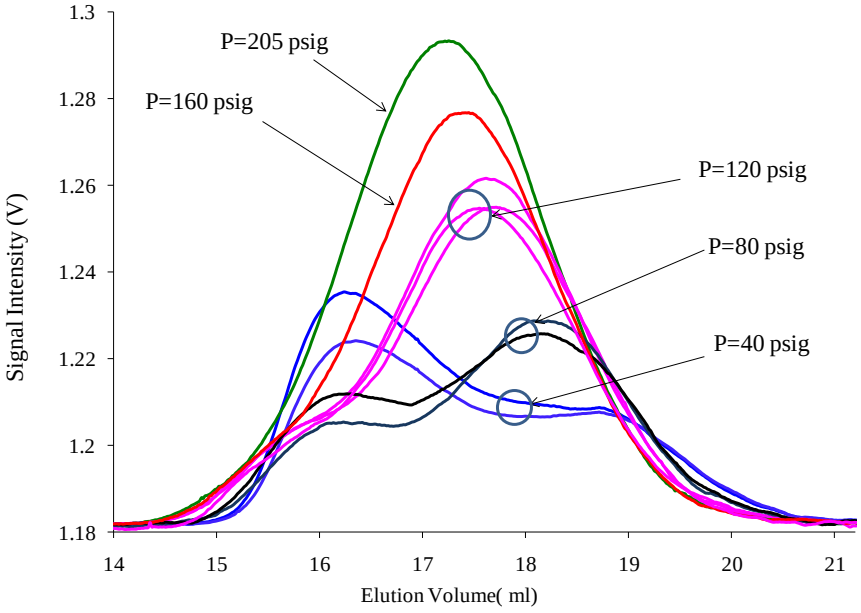

Figure 7-27. 15° GPC light scattering detector signal intensity versus elution volume for samples in Table 7-10.

Figure 7-28 compares the MWDs for all samples, and log [η] versus log MW plots for the linear polyethylene standard NBS 1475 and Sample 745 (made at 40 psig). The nonlinear log [η] versus log MW curve for Sample 745 is a clear indication of the presence of LCBs. The high molecular weight shoulders seen for the samples made at 120, 80, and 40 psig are also indications of LCB chains. Zimm-Stockmayer equations, introduced in Chapter 5, were used to estimate the LCB frequency for these samples (Table 7-11), confirming that decreasing ethylene pressure in the reactor leads to more long chain branching in the polymer.

Figure 7-29 shows how M_n, M_w and PDI vary with ethylene concentration. PDI is almost constant at high ethylene concentrations, but starts to increase for values lower than 0.4 mol/L. This change in PDI at lower ethylene concentrations can be attributed to an increase in the rate of LCB formation due to the decreasing ethylene concentration. Although at high ethylene concentrations (ethylene pressures of 160 psig and higher) no sign of LCB was observed by the GPC viscometer, PDI still remains higher that the theoretical value of two expected for polyethylene made with single-site catalysts at uniform conditions, which indicates that not all increase in PDI can be attributed to long chain branching. In fact, a true single site behavior is not observed when MAO concentration is low.

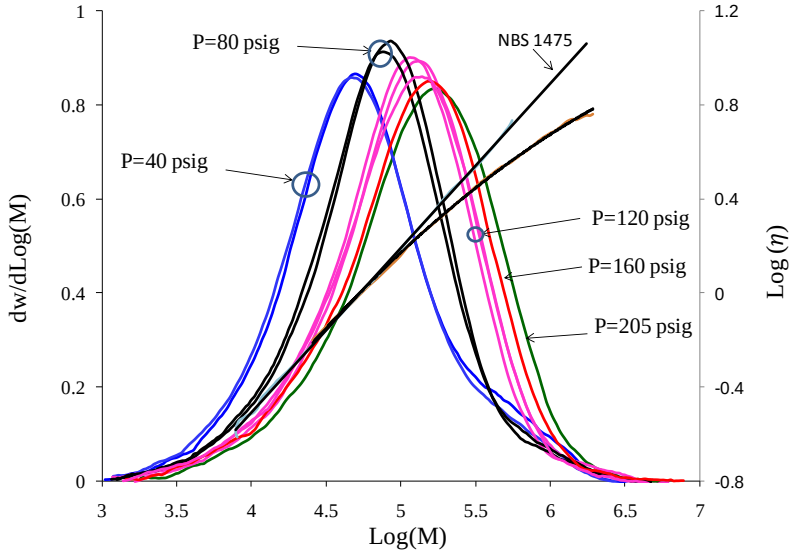

Figure 7-28. Molecular weight distribution of the polyethylene samples made at low Al/Ti ratio and Plot of log [η] versus log MW for Sample 745 (P =40 psig) and NBS 1475.

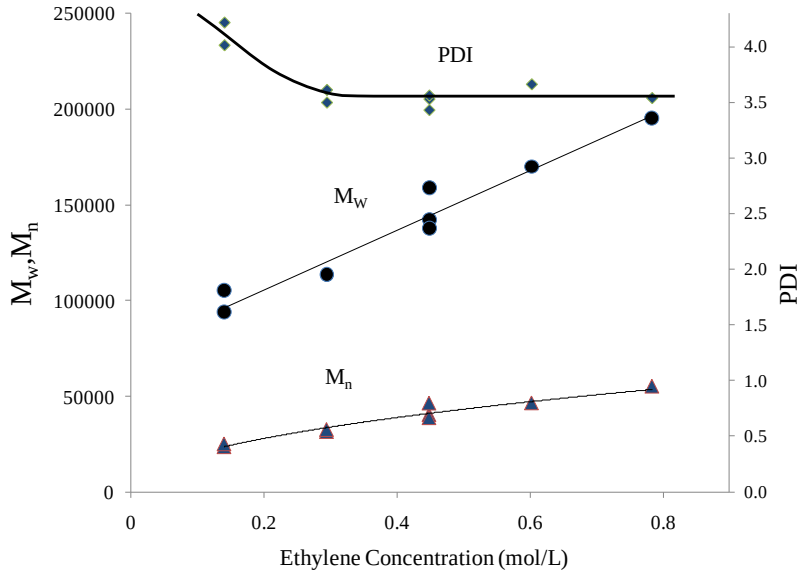

Figure 7-29. Effect of ethylene concentration on M_n, M_w and PDI (Low MAO concentration)

Finally, Figure 7-30 compares M_n and M_w for the two sets of samples made at low and high Al/Ti ratios. Weight and number averages are higher when the polymers are made at larger Al/Ti ratios, but this difference decreases for lower ethylene pressures.

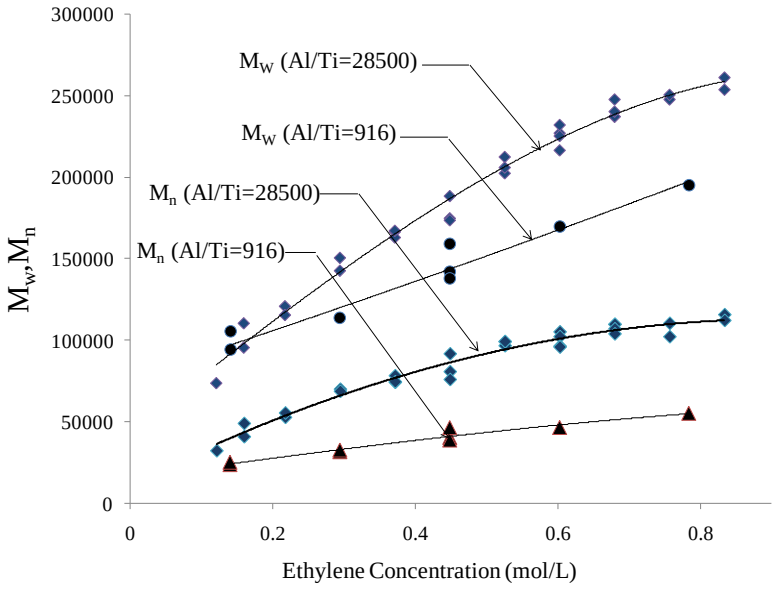

Figure 7-30. Effect of ethylene concentration and Al/Ti ratio on molecular weight.

7.5 Conclusions

The kinetics of ethylene solution polymerization using the CGC/MAO system was studied in a semibatch reactor at high temperature. The propagation reaction order was found to be first order with respect to catalyst concentration, whilst the order with respect to ethylene concentration changed from 1 to 2. Assuming reversible activation and deactivation with MAO along with thermal deactivation can explain the effect of time, monomer and catalyst concentration on the propagation rate.

Decrease in MAO concentration leads to the production of polymer chains with terminal vinyl groups, which may be subsequently incorporated into growing polymer chains to produce long chain branched polymers. Polymer molecular weight is decreased by lowering MAO concentration, whilst PDI increases. Part of the increase in PDI due to the lowering of MAO concentration can be attributed to LCB formation, whereas the rest results from non single site behavior of the catalyst at low MAO concentration. Decrease in monomer concentration leads to the production of polymer chains with increased LCB frequencies while the MAO concentration is low.

Chapter 8

Kinetic Study on Homopolymerization of Ethylene Using a Combination of Two Single Site Catalysts in a Solution Reactor

8.1 Summary

The homopolymerization of ethylene and copolymerization of ethylene and 1-octene was studied in a semi-batch solution reactor using a combination of dimethylsilyl(N-tert-butylamido)-(tetramethylcyclopentadienyl)-titanium dichloride (CGC-Ti) and *rac*-Et(Ind)$_2$ZrCl$_2$ catalyst and MAO as cocatalyst. Polymerizations were performed either at high (0.013 mol Al/L) and low (0.003 mol Al/L) MAO concentrations. The results show that catalyst sites act independently of each other and no increase in long chain branch formation was observed. Based on Crystaf profiles of the copolymerization runs, reactivity ratios for ethylene\1-octene using *rac*-Et(Ind)$_2$ZrCl$_2$ and CGC-Ti were determined.

8.2 Introduction

Increasing polymer molecular weight improves physical properties of unimodal MWD polyolefin resins at the expense of decrease in processability. One way of overcoming this problem is to use bimodal MWD resins. Bimodal resins have both high and low molecular weight polymer chains. Low molecular weight polymer chains enhance processability and the high molecular weight ones enhance physical properties. The common method for making bimodal resins is to use two reactors in series (tandem reactor technology). Metallocene catalyst technology has made it possible to produce bimodal resins in a single reactor by using two metallocenes that make polymer chains with significantly different average molecular weights. Intimate mixing of high and low molecular weight portions, less process complexity, and lower investment costs are among the advantages of using metallocene catalysts for making bimodal MWD resins. Another way to increase processablity is to introduce long chain branches into unimodal MWD resins. Combined metallocene catalysts can also be used to make bimodal resins with long chain branches. In this chapter, we investigate the combination of *rac*-Et(Ind)$_2$ZrCl$_2$ and CGC-Ti to make polyethylene with increased long chain branching. Three cases were tested: homopolymerization at high and low MAO concentration, and copolymerization at high MAO concentration.

8.3 Experimental

8.3.1 Materials

Methylaluminoxane (MAO, 10 wt % in toluene, Sigma-Aldrich) was used as received. 1-Octene was passed through a packed column filled with molecular sieves (3, 4, and 5-Å). The purification process for ethylene, nitrogen, and toluene was explained in Chapter 6, Section 6.3.1. The catalysts, CGC-Ti and *rac*-Et$(Ind)_2ZrCl_2$ were purchased as powders from Boulder Scientific and dissolved in toluene which was first distilled over metallic sodium and then flown through a molecular sieve bed before polymerization.

8.3.2 Polymer Synthesis and Characterization

The method used for homopolymerization was explained in Chapter 6, Section 6.3.2. Catalysts were mixed in a vial and then transferred to the catalyst injection assembly about 10 minutes before transferring into the reactor. For copolymerization with the combined catalyst system, 1-octene was transferred into the reactor after MAO injection.

Methods used for polymer characterizations were explained in Chapter 7, Section 7.3.3.

8.4 Results and Discussion

8.4.1 Ethylene Homopolymerization with $Et(Ind)_2ZrCl_2$/CGC-Ti at High MAO Concentration

The simulation results presented in Chapter 3 show that when ethylene is polymerized with two single site catalysts, one capable of producing macromonomers and the other of incorporating macromonomers, the long chain branching frequency can be increased. The results reported in Chapter 6 show that *rac*-Et$(Ind)_2ZrCl_2$ is an excellent catalyst for the production of polyethylene macromonomers. As dicussed in Chapter 7, some of the polymer samples made with CGC-Ti contained long chain branches. To check whether the macromoners produced by *rac*-Et$(Ind)_2ZrCl_2$ could be incorporated into the growing polymer chains produced by CGC-Ti, ethylene was polymerized with a combination of these two catalysts at high MAO concentration. Fourteen polymerizations were run at seven different molar catalyst ratios. Table 8-1 summarizes the polymerization conditions for these runs. Molecular weights and polymer yields for all these runs are listed in Table 8-2.

Table 8-1. Polymerization conditions for combined catalyst system at high MAO concentration.

Run	CGC Concentration (nmol)	*rac*-Et(Ind)$_2$ZrCl$_2$ Concentration (nmol)	x'	Polymer Yield (g)
274	0	11.5	0	5.15
276	608	0	1	5.87
277	304	5.8	0.5	5.44
278	203	7.6	0.34	5.37
279	506	1.9	0.83	5.47
280	104	9.6	0.17	5.39
281	400	4	0.65	5.99
282	400	4	0.65	4.94
283	304	5.8	0.5	4.93
284	0	11.5	0	4.59
285	608	0	1	4.81
286	104	9.6	0.17	4.9
287	506	1.9	0.83	5.1
288	304	5.8	0.5	5.12

Polymerization Temperature:120 ^{0}C, Polymerization Pressure : 120 psig. Polymerization time: 15 min, MAO concentration: 0.013 mol Al/L.

Average polymer yield per mole of *rac*-Et(Ind)$_2$ZrCl$_2$ catalyst, calculated from polymer yield data for runs 274 and 284, using Equation I-2 in Appendix I, with 95% confidence interval is :

$$\frac{(5.15+4.59)}{(2\times 1000\times 11.5\times 10^{-9})} \pm \frac{t_{(0.025,14-7)} \times 0.48}{(1000\times 11.5\times 10^{-9})\sqrt{2}} = 423500 \pm 69800 \quad \frac{Kg}{mole} \tag{8-1}$$

Similarly, the average polymer yield per mole of CGC-Ti catalyst, calculated from polymer yield data for runs 276 and 285, with 95% confidence interval is:

$$\frac{(5.87+4.81)}{(2\times 1000\times 608\times 10^{-9})} \pm \frac{2.36\times 0.48}{(1000\times 608\times 10^{-9})\sqrt{2}} = 8783 \pm 1320 \quad \frac{Kg}{mole} \tag{8-2}$$

In order to estimate 95% confidence intervals in the above calculations, we assumed that the same phenomena were generating random error at each level of catalysts combination; therefore, the polymer yield standard deviations at all levels were pooled to obtain a single estimate of the standard deviation, equal to 0.48 g (for more details on pooled standard deviation, see Appendix I).

Comparing polymer yields for rac-Et(Ind)$_2$ZrCl$_2$ and CGC-Ti shows that the polymer yield per mole of rac-Et(Ind)$_2$ZrCl$_2$ is about 50 times of the polymer yield per mole of CGC-Ti under the same polymerization conditions. Consequently, using catalyst mole fraction is not a convenient variable for displaying polymer yield data for this combined system. A modified catalyst mole fraction, x', defined by the equation below was introduced,

$$x' = \frac{\dfrac{\text{moles of CGC - Ti}}{\text{maximum moles of CGC - Ti}}}{\dfrac{\text{moles of rac - Et(Ind)}_2\text{ZrCl}_2}{\text{maximum moles of rac - Et(Ind)}_2\text{ZrCl}_2} + \dfrac{\text{moles of CGC - Ti}}{\text{maximum moles of CGC - Ti}}} \qquad (8\text{-}3)$$

The parameters, maximum moles of CGC-Ti, and, maximum *rac*-Et(Ind)$_2$ZrCl$_2$, introduced in Equation 8-3 are 608 and 11.5 nmol, respectively, which are the moles of catalyst injected into the reactor for the Runs 276 and 274. The fourth column of Table 8-1 gives x' values for each run.

Table 8-2. Molecular weight averages and polymer yields for runs listed in Table 8-1.

Run	M_w	M_n	***PDI***	**Polymer Yield (g)**	w_c**×100**	w_{GPC}**×100**
274	48 800	23 400	2.09	5.15	0	0
276	191 000	79 000	2.41	5.87	100	100
277	149 200	39 600	3.77	5.44	52	63
278	116 000	31 600	3.68	5.37	36	43
279	171 800	57 200	3.00	5.47	85	87
280	87 500	27 700	3.16	5.39	18	21
281	162 800	45 400	3.58	5.99	68	73
282	155 800	45700	3.41	4.94	68	71
283	142 000	38 200	3.72	4.93	52	57
284	46 900	23 600	1.99	4.59	0	0
285	186 400	79 200	2.35	4.81	100	100
286	78 500	26 100	3.01	4.9	18	20.4
287	162 000	54 000	3	5.1	85	83
288	136 800	37 700	3.63	5.12	52	58

Figure 8-1 plots the polymer yield versus the modified CGC-Ti mole fraction, x'. The linear trend observed indicates that activities of these two catalysts are additive and do not affect each other. Visual inspection of the polymer yield data in Figure 8-1 also shows that the polymer yield variance does not depend on CGC-Ti fraction, supporting the use of pooled standard deviation.

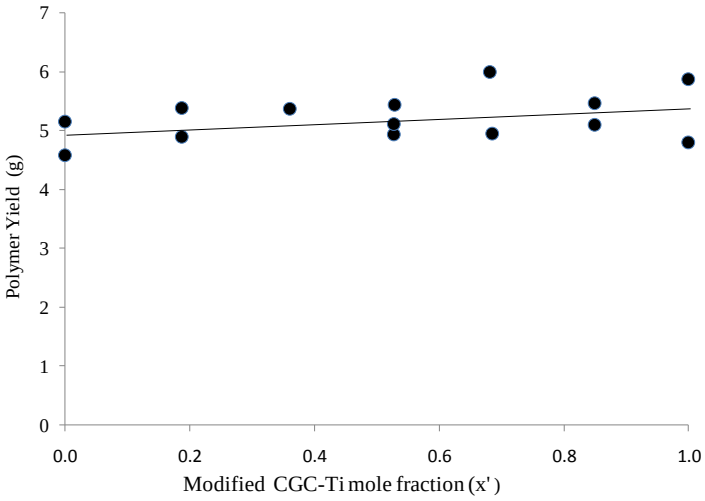

Figure 8-1.Polymer yield versus modified catalyst mole fraction *x´*

The Mark-Houwink plot and ^{13}C NMR analysis were used to determine whether combining these two catalysts increase long chain branching. Figure 8-2 shows the MWD of all samples overlaid with their corresponding log [η] versus log *M* plots. The linear trends observed in their intrinsic viscosity plots indicate lack of long chain branching. To support these observations, we analyzed samples 274 and 277, containing zero and 50 weight % CGC-Ti polymer, respectively, by ^{13}C NMR. Their spectra showed resonances related to saturated and vinyl carbons, but any peaks indicative of the presence of long chain branches were not detected (Figure 8-3).

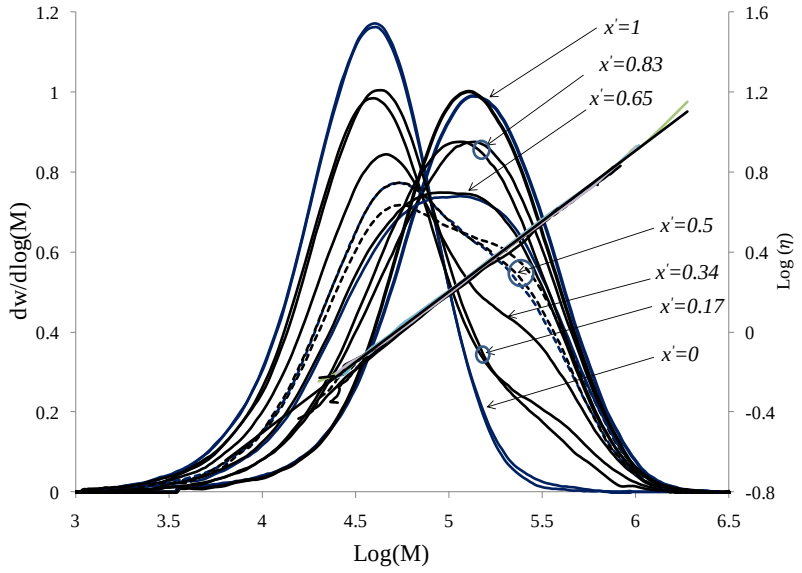

Figure 8-2. MWDs and Mark-Houwink plots for the sample listed in Table 8-1.

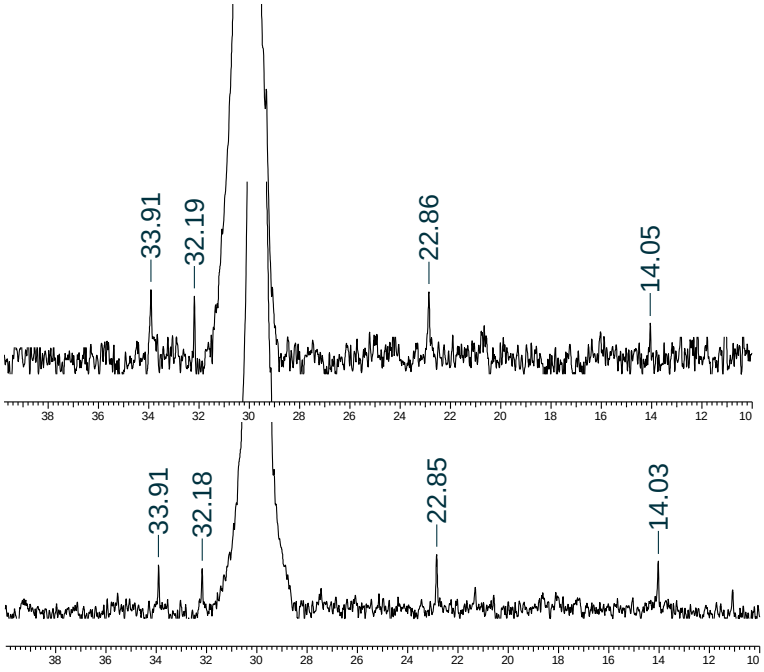

Figure 8-3. ^{13}C-NMR spectra for sample 277 (top) and sample 274(bottom).

8.4.1.1 Determination of Weight Fraction of CGC-Ti Polymer Using GPC.

It is possible to calculate the weight percent of polymer made with each catalyst type using the molecular weight distribution of polymers produced with the combined catalyst system. The following paragraph explains how this calculation was performed.

Polymers made using individual *rac*-Et(Ind)$_2$ZrCl$_2$ and CGC-Ti were mixed in different proportions and their MWDs were measured by GPC. Seven 20 mg polymer blends containing 0, 20, 40, 50, 60, 80 and 100 wt% CGC-Ti polymer were prepared using a precision scale, with accuracy of ±0.0001 g. The weight fraction of the CGC-Ti polymer in the samples (we refer to this weight fraction as w_{GPC} afterwards) listed in Table 8-2 was measured by interpolating between the MWD of those seven polymer blends. Figure 8-4 compares the MWD of sample 283 with the two polymer blends prepared by adding CGC-Ti and *rac*-Et(Ind)$_2$ZrCl$_2$ polymers. The w_{GPC} for those two blends were 50 and 60 (**w50** and **w60** samples, respectively). As shown in Figure 8-4, the MWD for sample 283 lies between the MWDs of **w50** and **w60** samples. Therefore, the w_{GPC} for sample 283 should be between 50 and 60 %. The precise w_{GPC} for sample 283 can be obtained by a trial and error procedure based on the MWDs of the samples **w50**, **w60,** and 283 using the following MWD linear interpolation expression,

$$dw_{\text{int}} = \frac{(dw_{60} - dw_{50})}{(0.6 - 0.5)}(x - 0.5) + dw_{50} \tag{8-4}$$

where dw_{50} and dw_{60} are the weight fractions of the slices coming out of the GPC columns at molecular weight M for samples **w50** and **w60,** respectively, dw_{int} is the interpolated weight fraction of the slice at the same molecular weight, M, and x is the w_{GPC} for sample 283, which is unknown and should be determined by trial and error. If we choose the correct value of x, we expect the MWD for sample 283 to coincide with the interpolated MWD (Figure 8-4). The w_{GPC} for sample 283 determined by this method was 0.565. The same method was applied to obtain the w_{GPC} for other samples, shown in the last column of Table 8.2.

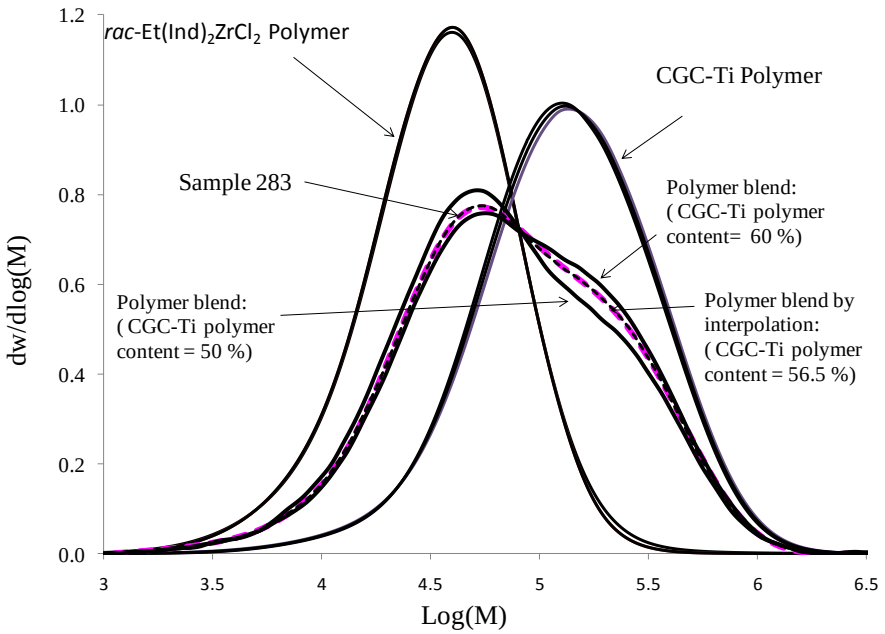

Figure 8-4. MWD for sample 283, **w50**, **w60**, and interpolated MWD with 56.5 wt% content of CGC-Ti polymer and polymers made using individual CGC-Ti and *rac*-Et(Ind)$_2$ZrCl$_2$ catalysts.

We can also predict the weight fraction of the CGC-Ti polymer in the polymer samples using the average polymer yield per mole of the individual catalysts, calculated in Section 8.4.1, Equations 8-1 and 8-2, and moles of individual catalysts used in the polymerization. Henceforth, we refer to this weight fraction as w_c.

Equation below was used to calculate w_c .

$$w_c = \frac{n_{c,CGC-Ti} \times a_{CGC-Ti}}{n_{c,CGC-Ti} \times a_{CGC-Ti} + n_{c,Et-ind} \times a_{Et-ind}} \quad (8\text{-}5)$$

where $n_{c,CGC\text{-}Ti}$ and $n_{c,Et\text{-}ind}$ are the moles of CGC-Ti and *rac*-Et(Ind)$_2$ZrCl$_2$ catalysts injected into the reactor, respectively, and $a_{CGC\text{-}Ti}$ and $a_{Et\text{-}ind}$ are their corresponding average polymer yield per mole of catalyst. The sixth column of Table 8-2 tabulates the values calculated for w_c.

Figure 8-5 plots w_{GPC} for the samples, versus w_c, for all the runs listed in Table 8-1. A positive deviation ($w_{GPC} > w_C$) is observed, which may be attributed to the effect of change in Al/Ti ratio on polymer yield. For example, in sample 283, CGC-Ti and *rac*-Et(Ind)$_2$ZrCl$_2$ concentrations in the reactor are half of those in samples 276 and 274, respectively. When CGC-Ti concentration is reduced, the Al/Ti ratio increases; therefore, an increase in the activity of CGC-Ti is expected as shown in Chapter 7, Figure 7-17. On the other hand, for *rac*-Et(Ind)$_2$ZrCl$_2$ an increase in yield is not expected because the MAO concentration is so high that a further increase in MAO concentration has no effect on its activity, as shown in Figure 6-32 in Chapter 6.

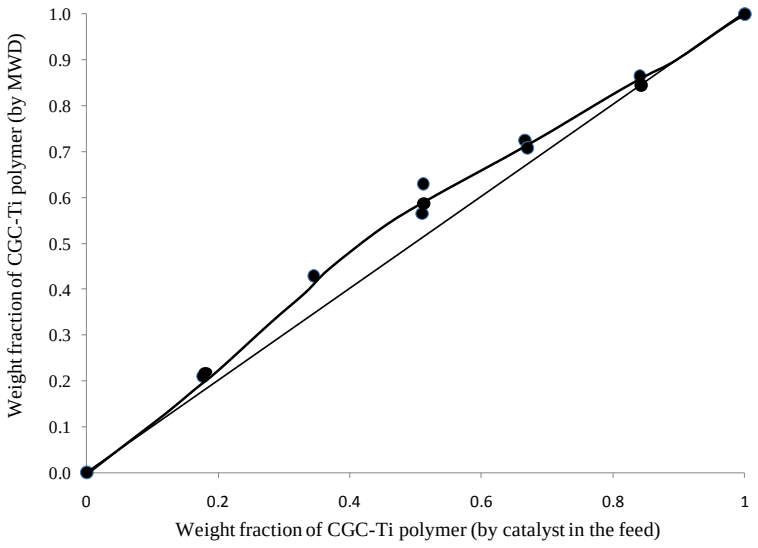

Figure 8-5. Plot of w_{GPC} versus w_c

Figure 8-6 plots M_w, M_n and *PDI* versus w_{GPC}. The linear relation observed in the Mw plot seems to support that no macromonomer produced by rac-Et(Ind)2ZrCl2 is incorporated by CGC-Ti. The

maximum increase in PDI is achieved when the weight fraction of CGC-Ti polymer is about 0.5, as also expected.

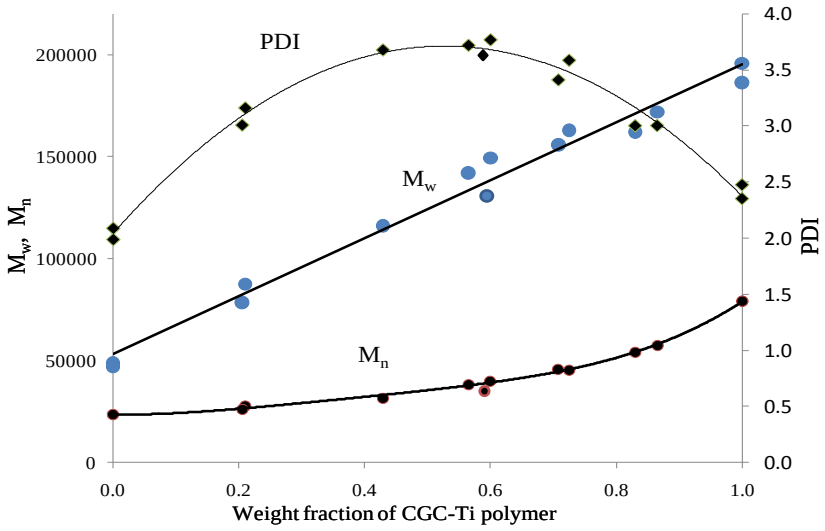

Figure 8-6. Molecular weight averages and PDI versus weight fraction of CGC-Ti polymer (w_{GPC}).

Since, in Case study 1 in Chapter 3, we assumed that both catalysts have the same propagation and deactivation rate constants, the immediate consequence is that the LCB catalyst mole fraction and LCB catalyst weight fraction are equivalent. Therefore it is reasonable to compare the trends in Figure 8-6 with those in Figures 3-6, 3-7, and 3-8. As it was shown in Figure 3-7, weight average chain length is a linear function of LCB catalyst mole fraction which is consistent with the trend observed in Figure 8-6 for M_w. A nonlinear increasing trend is seen for M_n in Figutre 8-6 which is again in consistent with the simulation trend observed in Figure 3-8 for the number average chain length. Polydispersity index passes a maximum at LCB catalyst mole fraction of 0.5 which was also observed in Figure 8-6.

8.4.2 Copolymerization of Ethylene and 1-Octene Using $Et(Ind)_2ZrCl_2$/CGC-Ti at High MAO Concentration.

A total of nine polymerizations were run, in random order, at seven different and equally spaced 1-octene concentration levels to investigate 1-octene incorporating ability of the two

catalysts under the same polymerization conditions. Except for 1-octene concentration, all reaction variables were kept the same during the polymerizations. Table 8.3 indicates the conditions used for each experiment.

Crystaf was used to analyze the 1-octene incorporation in the copolymer samples. The Crystaf profiles for all the runs in Table 8-3 are illustrated in Figures 8-7 and 8-8. Two full replicates (runs 408 and 412) were performed to show the repeatability of the bimodal Crystaf profiles. With the exception of samples 413 and 415, made without 1-octene, all Crystaf profiles were bimodal, showing that the reactivity ratios for *rac*-Et$(Ind)_2ZrCl_2$ and CGC-Ti are very different: the high temperature peaks correspond to copolymer chains made with *rac*-Et$(Ind)_2ZrCl_2$, while the low temperature ones are related to copolymers formed on CGC-Ti. Since no intermediate Crystaf peak was observed for any sample, we may conclude that copolymer chains made with *rac*-Et$(Ind)_2ZrCl_2$ were not significantly incorporated on chains made with CGC-Ti.

Table 8-3. Copolymerization conditions using combined metallocene catalysts.

Run	**CGC-Ti nanomoles**	***rac*-Et$(Ind)_2ZrCl_2$ (nanomoles)**	**1-octene (g)**	**Yield (g)**
407	106.3	2.97	8	7.92
408	106.3	2.97	4	8.76
409	106.3	2.97	12	7.52
410	106.3	2.97	6	8.67
415	106.3	0	0	3.6
412	106.3	2.97	4	6.8
411	106.3	2.97	10	7.1
414	106.3	2.97	2	7.13
413	106.3	2.97	0	6.3

MAO concentration = 0.013 mol Al/L, toluene volume = 222.8 ml, polymerization temperature = 120^{o}C, total reactor pressure = 120 psig, polymerization time = 15 min.

Figure 8-9 shows MWD and hexyl branch distribution (HBD) for four samples covering the whole range of 1-octene loading into the reactor. For all three copolymer samples (407,408,409), HBD is low for the low molecular weight components, where most of the polymer chains were formed by *rac*-Et$(Ind)_2ZrCl_2$, while increasing to higher values for the high molecular weight components, made

with CGC-Ti. This type of distribution is called reverse comonomer incorporation, meaning that the comonomer content of the copolymer increases as the molecular weight of the polymer chains increases. Polymers with reverse comonomer incorporation are useful in improving the characteristics that govern long term creep-related properties like slow crack growth resistance.[169]

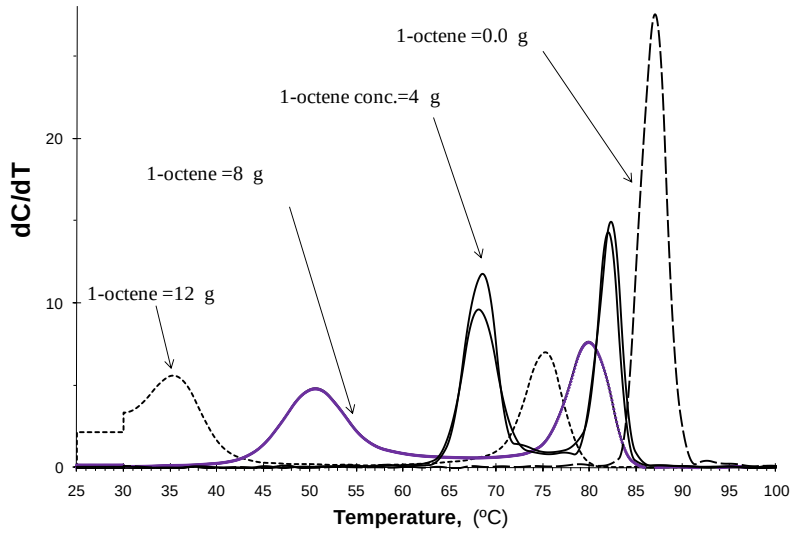

Figure 8-7. Crystaf profiles for samples 413, 408, 412, 407 and 409.

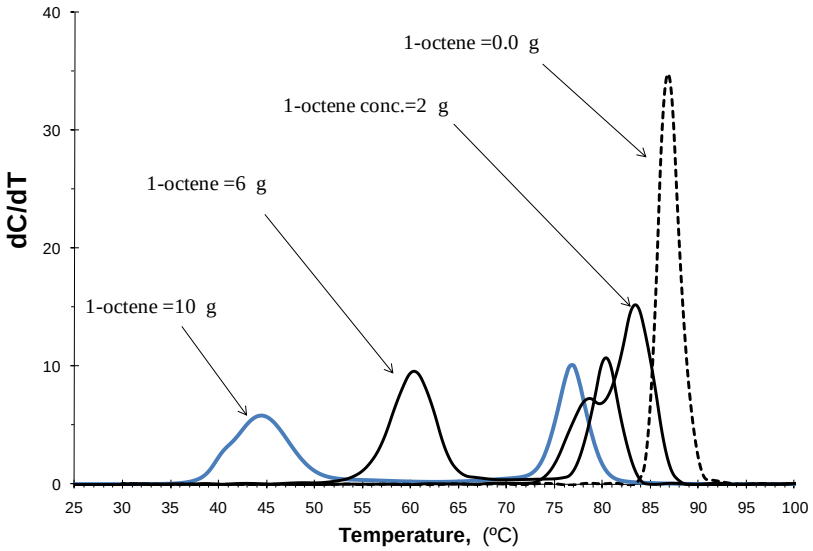

Figure 8-8. Crystaf profiles for samples 410, 411, 414 and 415.

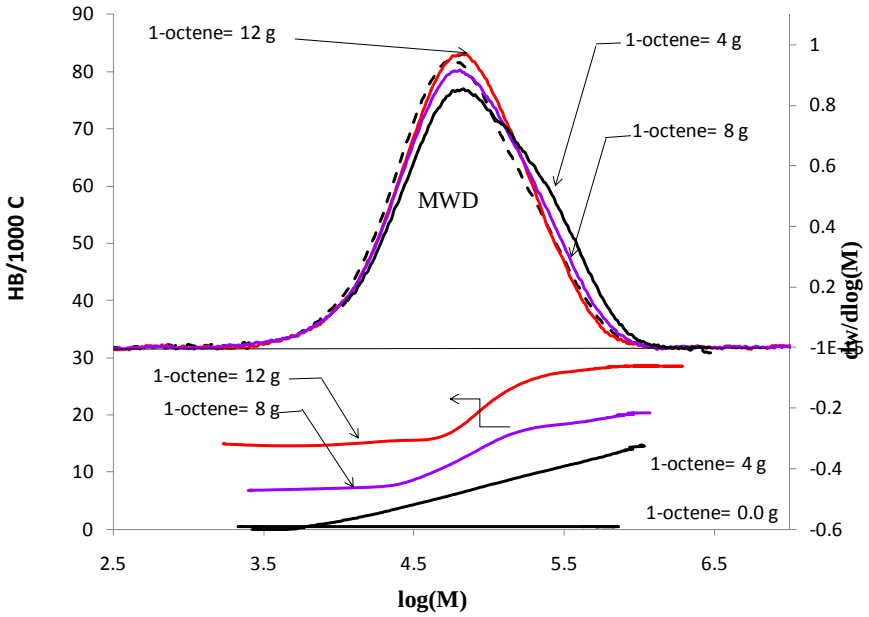

Figure 8-9. MWD and HBD for samples 407 (8 g 1-octene), 408 (4 g 1-octene), 409 (12 g 1-octene) and 413 (0.0 g 1-octene). The dashed curve shows MWD for sample 413.

Table 8-4 summarizes the GPC results of the samples shown in Figure 8-9, and sample 415 which was made using CGC-Ti catalyst alone. Although the HBD of the three copolymer samples differ significantly, their MWDs and molecular weight averages are nearly the same.

Table 8-4. Summary of GPC results for some selected samples from Table-8-3

Run	HBD	M_w	M_n	*PDI*
407	13.1	110 700	40 500	2.73
408	7.1	128 400	41 800	3.1
409	21.3	100 330	40 800	2.46
413	0	100 200	36 500	2.74
415	0	183 300	80 900	2.26

When the peak crystallization temperature, T_{peak}, for both Crystaf profile peaks shown in Figures 8-7 and 8-8 are plotted versus the mass of 1-octene added to the reactor, two linear relationships are observed, showing that both catalyst sites compete for 1-octene incorporation (Figure 8-10).

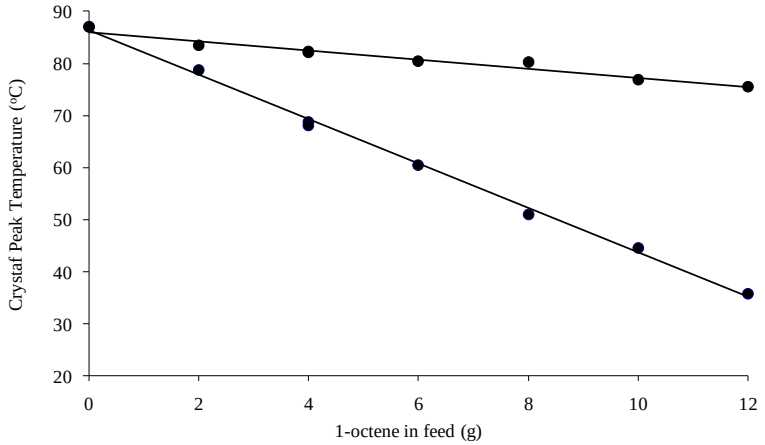

Figure 8-10. Crystaf peak temperature versus 1-octene mass added to the reactor for the runs listed in the Table 8-3.

8.4.2.1 Reactivity Ratio Estimation

Crystaf peak temperature data (Figure 8-10), Crystaf calibration curve (Figure 5-4), the Mayo-Lewis equation, and a method to estimate 1-octene and ethylene concentration in the reactor liquid phase at the polymerization conditions were used to estimate the reactivity ratios for ethylene/1-octene using CGC-Ti and *rac*-Et(Ind)$_2$ZrCl$_2$.

The Mayo-Lewis equation, relating the mole fraction of ethylene in copolymer, F_1, to ethylene mole fraction in the reactor, f_1, is given by,

$$F_1 = \frac{r_1 f_1^2 + f_1 f_2}{r_1 f_1^2 + 2 f_1 f_2 + r_2 f_2^2} \tag{8-6}$$

The variable f_1 can be calculated using ethylene, M_1, and α-olefin, M_2, molar concentrations in the reactor,

$$f_1 = 1 - f_2 = \frac{M_1}{M_1 + M_2} \tag{8-7}$$

Finally, r_1 and r_2 are the reactivity ratios given by the expressions,

$$r_1 = \frac{k_{11}}{k_{12}} \tag{8-8}$$

$$r_2 = \frac{k_{22}}{k_{21}} \tag{8-9}$$

where k_{11} and k_{21} are the propagation rate constants when M_1 reacts with polymer chains ending with M_1, or M_2, respectively, and k_{12} and k_{22} are the corresponding propagation rate constants when M_2 reacts with polymer chains ending with M_1 and M_2, respectively.

Aspen Plus was used to estimate ethylene, 1-octene, and toluene concentrations in the reactor liquid phase. The Peng-Robison equation of state was selected to estimate the fugacity coefficients of each component in both vapor and liquid phases. Table 8-5 lists the output results of Aspen Plus for concentration of ethylene, 1-octene, and toluene in the liquid phase.

Table 8-5. Liquid phase composition of ethylene/1-octene/toluene mixtures at 120°C and 120 psig as estimated by Aspen Plus using the Peng-Robison equation of state.

	Liquid phase composition			
1-octene in the feed (g)	1-octene (mol/L)	Ethylene (mol/L)	Toluene (mol/L)	f_1
0	0.0000	0.4480	8.073	1.000
2	0.0678	0.4480	7.970	0.869
4	0.1339	0.4479	7.869	0.770
6	0.1983	0.4479	7.771	0.693
8	0.2611	0.4478	7.675	0.632
10	0.3225	0.4477	7.582	0.581
12	0.3823	0.4476	7.491	0.539

Toluene volume: 222.8 ml

The relationship between the mass of 1-octene added to the reactor and the resulting concentration in the liquid phase is almost linear, as is illustrated in Figure 8-11.

Table 8-6 lists the T_{peak} for Figure 8-7 and 8-8 and their corresponding 1-octene contents, calculated using Equation (5-6), and F_1 values. Since there are two Crystaf peaks for copolymers made in the combined catalysts runs, two values are reported for 1-octene and ethylene mole fractions.The Percent conversion of 1-octene can also be calculated based on the Crystaf profiles, polymer yields and Crystaf calibration curves as it is explained below for sample 410.

The percent area under the CGC-Ti peak in the Crystaf profile for sample 410 is 58.2 which was calculated by numerical integration. The 1-octene mole% of the two peaks of Crystaf profiles for sample 410 can be converted to 1-octene wt %, and then since polymer yield is known, mass of 1-octen in the final polymer is calculated. 1-octene conversion is the mass of 1-octene incorporated divided by the initial mass of 1-octene in the liquid phase which can be calculated by multiplying the 1-octene concentration in the liquid phase and volume of liquid phase estimated using the phase equilibrium calculation through Aspen Plus (Table 8-7, third column). Calculation for sample 410 is given below.

Mass of 1-octene in the polymer:

$$=8.67\times0.58\times10.56/100 + 8.67\times(1-0.58)\times1.82/100=0.53+0.066=0.596\ \text{g} \quad (8\text{-}10)$$

$$\text{Initial mass of 1-octene in the liquid phase} = 0.267\times0.1983\times112.2=5.94\ \text{g} \quad (8\text{-}11)$$

$$\text{1-octene fractional conversion}=0.596/5.94=0.101 \quad (8\text{-}12)$$

Summary of the calculations for the other samples are given in Table 8-7. 1-Octene conversions for all runs were low; therefore, it is reasonable to assume that the 1-octene concentration remains practically the same throughout the polymerization.

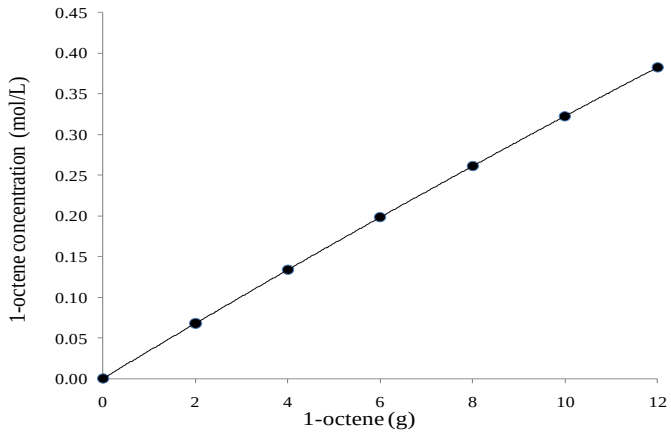

Figure 8-11. Relationship between 1-octene concentration in the reactor liquid phase and the amount of 1-octene added to the reaction mixture (estimated by Aspen Plus).

Table 8-6. Copolymerization runs for samples made using a combination of CGC-Ti and *rac*-Et(Ind)$_2$ZrCl$_2$.

Run	CGC-Ti Peak (^{o}C)	*rac*-Et(Ind)$_2$ZrCl$_2$ peak (^{o}C)	1-octene mole % in polymer (CGC-Ti peak)	1-octene mole % in polymer (*rac*-Et(Ind)$_2$ZrCl$_2$ peak)	F_1 (CGC-Ti)	F_1 (*rac*-Et(Ind)$_2$ZrCl$_2$)
407	51	80.2	3.991	0.484	0.9601	0.9952
408	68.1	82.1	1.937	0.256	0.9815	0.9974
409	35.7	75.5	5.828	1.049	0.9417	0.9895
410	60.4	80.4	2.862	0.460	0.9714	0.9954
415	87.1	NA	0	NA	1	NA
412	68.1	82.3	1.937	0.232	0.9806	0.9977
411	44.6	76.9	4.76	0.880	0.9524	0.9912
414	78.7	83.4	0.664	0.1	0.9934	0.9990
413	87	87	0	0	1	1

Table 8-7. Summary of calculation results for 1-octene conversion.

Run	CG wt% by Crstaf	Liquid phase volume (L)	1-octene wt% in CGC-Ti polymer peak	1-octene wt% in *rac*-Et(Ind)$_2$ZrCl$_2$ polymer peak	1-octene Conversion (%)
407	51	0.271	14.28	1.91	8.2
408	54	0.261	7.33	1.02	9.8
409	58	0.277	19.87	4.07	8.4
410	58	0.267	10.56	1.82	10.1
412	50	0.261	7.33	0.92	7.2
411	47	0.274	16.69	3.44	6.9
414	50*	0.261	2.61	0.40	5.4
413	0.00	0.257	0.00	0.00	0.0

* Due to overlapping of the Crystaf peaks, a tentative value of 50 wt% was assumed.

Crystaf peak temperature data and their corresponding 1-octene contents for a set of ten copolymerization runs conducted at exactly the same polymerization conditions of the runs listed in Table 8-3, except using *rac*-Et(Ind)$_2$ZrCl$_2$ catalyst instead of using combined catalysts, are also given in Table 8-8. Their corresponding Crystaf profiles are shown in Figure 8-12.

Table 8-8.Summary of copolymerization run results for samples made using *rac*-Et(Ind)$_2$ZrCl$_2$

Run	1-octene in feed (g)	T_{peak} (^oC)	1-octene mole % in copolymer	f_1	F_1
397	0	87	0	1.0000	1.0000
398	4	82.8	0. 17	0.7699	0.9983
399	12	75	1.11	0.5393	0.9889
400	0	86.5	0	1.0000	1.0000
401	8	79.1	0. 62	0.6316	0.9938
402	12	75.6	1.04	0.5393	0.9896
403	8	78.9	0. 64	0.6316	0.9936
404	4	83.1	0. 14	0.7699	0.9986
405	8	78.6	0. 68	0.6316	0.9932
406	4	82.9	0. 16	0.7699	0.9984

T=120 ^{o}C, P=120 psig, MAO concentration=0.015

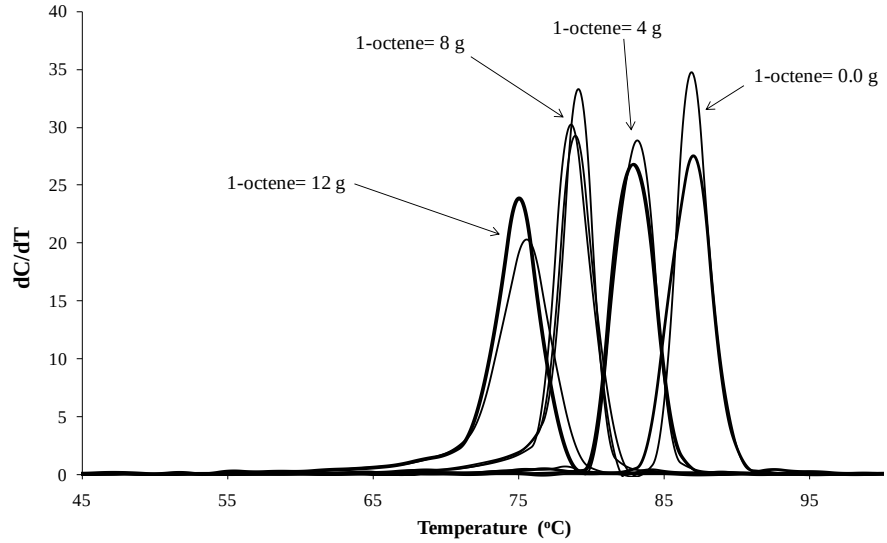

Figure 8-12. Crystaf profiles for the samples made with *rac*-Et(Ind)$_2$ZrCl$_2$ listed in Table 8-8.

Figure 8-13 plots the 1-octene mole fraction in the polymer versus 1-octene concentration (mol/L) in the liquid phase for the combined catalyst system. The line with the higher slope corresponds to copolymer chains formed on CGC-Ti and the lower line is related to copolymer chains formed on *rac*-Et(Ind)$_2$ZrCl$_2$. The corresponding plot, related to samples made with to *rac*-Et(Ind)$_2$ZrCl$_2$ alone is also given in Figure 8-13 and is indistinguishable from samples made with *rac*-Et(Ind)$_2$ZrCl$_2$ in the

combined catalyst system, implying that presence of CGC-Ti has not affected 1-octene incorporation by *rac*-Et(Ind)$_2$ZrCl$_2$. Therefore, to calculate the reactivity ratio for *rac*-Et(Ind)$_2$ZrCl$_2$, we used both sets of data, *rac*-Et(Ind)$_2$ZrCl$_2$ alone and in combination with CGC-Ti. The ratio of the slopes of the upper to the lower line in Figure 8-13 is 6.1; it is a measure of the reactivity towards 1-octene incorporation of CGC-Ti relative to *rac*-Et(Ind)$_2$ZrCl$_2$.

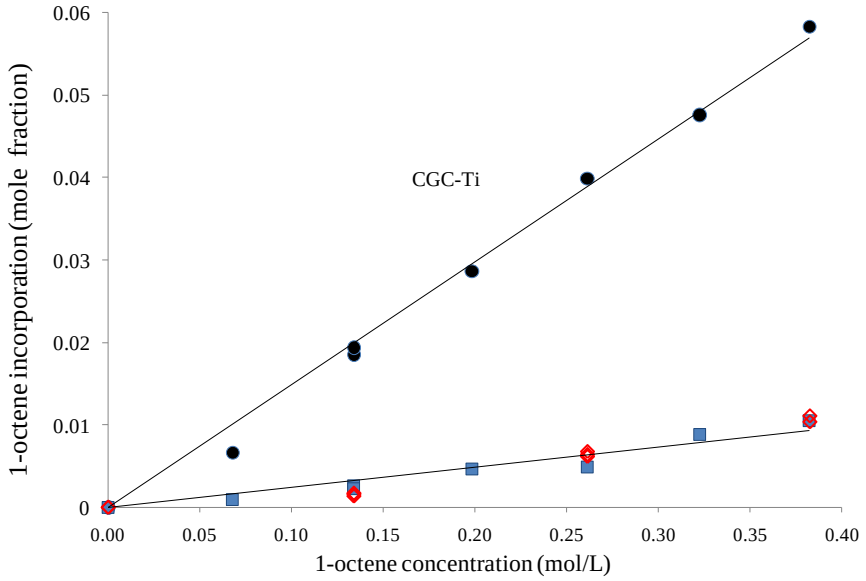

Figure 8-13. 1-octene content in polymer (mole fraction) versus 1-octene concentration in the liquid phase (mol/L) for combined catalyst system and *rac*-Et(Ind)$_2$ZrCl$_2$ alone (red diamond symbols).

Estimates of the reactivity ratios, r_1 and r_2, for *rac*-Et(Ind)$_2$ZrCl$_2$ were obtained by fitting Equation (8-6) to the experimental data and minimizing the sum of square of residuals using Newton's method. MATLAB curve fit toolbox was used for nonlinear regression. Table 8-9 summarizes the results of the curve fitting.

Table 8-9. Reactivity ratios for ethylene/1-octene using *rac*-Et(Ind)$_2$ZrCl$_2$/MAO.

Parameter	Value	Lower confidence limit	Higher confidence limit
r_1	133.6	97.3	169.9
r_2	0.79	0.2	1.38

Sum of squares of residuals=4.9×10^{-6}, R^2=0.98

Similar calculations were performed to estimate the reactivity ratios for CGC-Ti (Table 8-10).

Finally, Figure 8-14 shows the Mayo–Lewis equation fit for the copolymer composition as a function of ethylene molar fraction in the initial monomer mixture for the *rac*-Et(Ind)$_2$ZrCl$_2$ and CGC-Ti systems.

Table 8-10. Reactivity ratios for ethylene/1-octene using CGC-Ti/MAO catalyst system (combined catalyst system) .

Parameter	Value	Lower confidence limit	Higher confidence limit
r_1	17.06	14.39	19.73
r_2	0.356	0.085	0.627

Sum of squares of residuals=1.03×10^{-5}, R^2=0.996

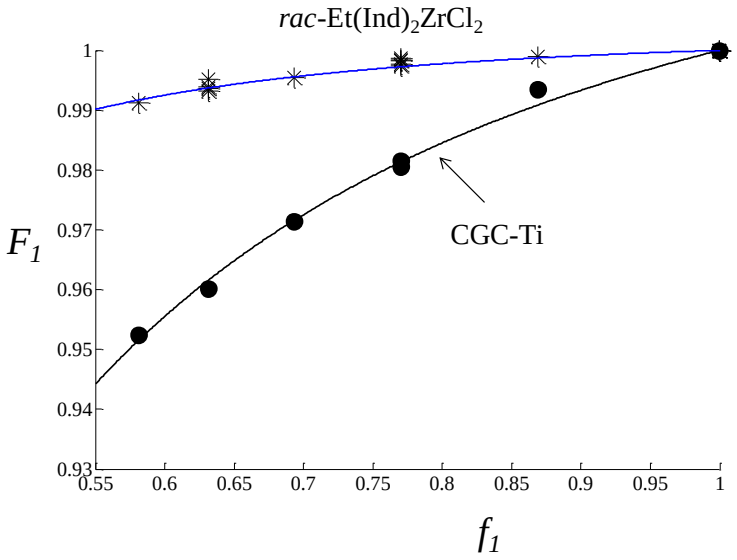

Figure 8-14. Copolymer composition versus liquid phase composition for *rac*-Et(Ind)$_2$ZrCl$_2$ and CGC-Ti systems.

Estimates of the reactivity ratios, r_1 and r_2, for *rac*-Et(Ind)$_2$ZrCl$_2$ have wider confidence intervals than CGC-Ti. This is due to high variability in the F_1 measurements compared to the total change in F_1 covered which is about 0.01.To decrease the confidence intervals, a wider range of f_1 values should be covered for *rac*-Et(Ind)$_2$ZrCl$_2$ catalyst or we should use ^{13}C-NMR instead of Crystaf calibration curve, to reduce the variability in the F_1 measurements.

8.4.3 Ethylene Homopolymerization with Combined Metallocene Catalysts at Low MAO Concentration (0.003 mol Al/L)

Similar to the set of polymerization runs shown in Table 8-1, another set of polymerizations were conducted at low MAO concentration (0.003 mol Al/L). Polymerization temperature and pressure, MAO concentration, and polymerization time were kept the same. Table 8-11 summarizes the polymerization conditions for these runs. The variable x' in Table 8-11 is the modified catalyst mole fraction, as defined by Equation (8-3).

Table 8-11. Polymerization conditions using combined metallocene catalysts ([MAO] = 0.003 molAl/L).

Run	CGC-Ti (nanomoles)	*rac*-Et(Ind)$_2$ZrCl$_2$ (nanomoles)	x'	Yield
507	0	3	0.00	3.89
509	546	0	1.00	4
510	546	3	0.50	7.46
511	546	2.04	0.59	4.77
512	182	3	0.25	4.41
513	546	1.01	0.75	3.93
514	364	3	0.40	5.85

Total reactor pressure=120 psig, Temperature= 120 ^{o}C, Polymerization time =15 min.

Figure 8-15 shows MWDs for all samples overlaid with their corresponding log [η] versus log M plots. Except for sample 509 (dashed curve), for which a slight departure from linearity is seen in its viscosity plot, all the other samples follow a linear trend indicating that there is no detectable long chain branching. Samples 507, 509 and 510 were also analyzed by ^{13}C-NMR (Figure 8-16). No peaks related to long chain branches (α, β or *br* carbons) were observed for samples 507 and 510; however, peaks related to α and β carbons, which are indicative of LCB, were observed in the spectra for sample 509 which was made using only CGC-Ti. The peak related to the *br* carbon was not observed, likely because the intensity of this carbon peak is almost one third of the other two. The long chain branch frequency estimated based on these two peaks was about 0.11 LCB per chain.

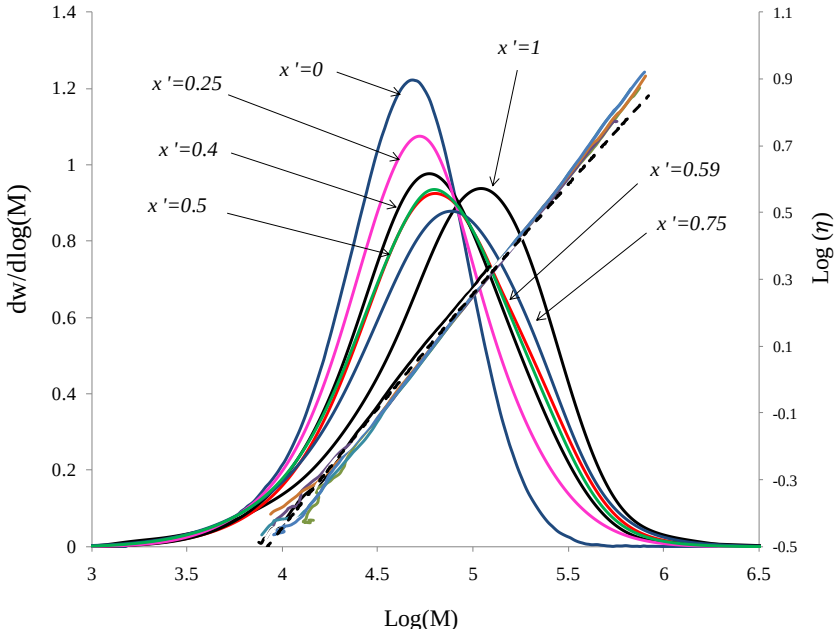

Figure 8-15. Molecular weight distributions and Mark-Houwink plots for samples listed in Table 8-11.

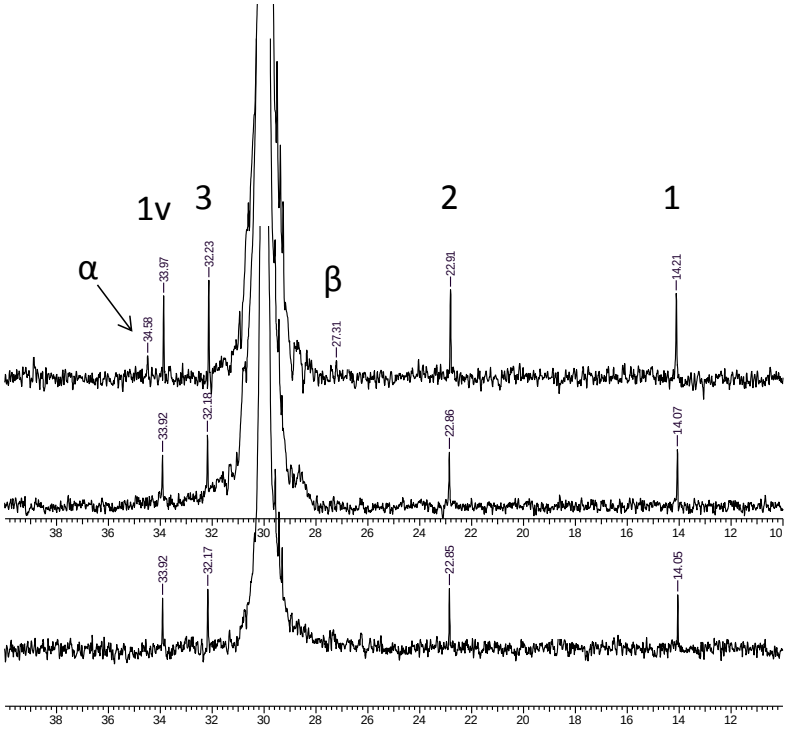

Figure 8-16. ^{13}C-NMR spectra for samples 509 (above), 510 (middle) and 507 (below).

Table 8-12 summarizes the molecular weight averages and polymer yields for this set of samples. The CGC-Ti polymer content for the samples, listed in the last column, were determined using Equation (8-13) below, which is analogous to Equation (8-4). The variables dw_{100} and dw_0 are the weight fractions of the slices coming out of the GPC columns at molecular weight M for samples 509 and 507, containing 100 and 0 % CGC-Ti polymer, respectively.

$$dw_{\text{int}} = dw_{100} + (1 - x) \times dw_0 \tag{8-13}$$

Figure 8-17 illustrates MWDs of samples 507, 509, 510, and the hypothetical polymer blend containing 50 wt% CGC-Ti polymer. The full overlap of the MWDs for sample 510 and the hypothetical polymer blend containing 50 wt% CGC-Ti supports the hypothesis that macromonomers produced by *rac*-Et(Ind)$_2$ZrCl$_2$ catalyst sites have not been incorporated into polymer chains formed by CGC-Ti catalyst. This type of exact match for the MWDs was also seen for the other samples in this set.

Table 8-12. Polymer yields and GPC results of samples listed in Table 8-11.

Run	M_w	M_n	**PDI**	**Yield**	w_c	**Wt fraction of CGC-Ti polymer in sample determined by MWD**
507	55 500	27 600	1.99	3.89	0	0
509	121 500	39 300	3.10	4	1	1
510	104 100	36 700	2.83	7.46	0.51	0.60
511	95 300	33 800	2.82	4.77	0.60	0.56
512	73 400	31 300	2.35	4.41	0.26	0.27
513	117 300	34 900	3.36	3.93	0.75	0.71
514	94 800	34 800	2.72	5.85	0.41	0.5

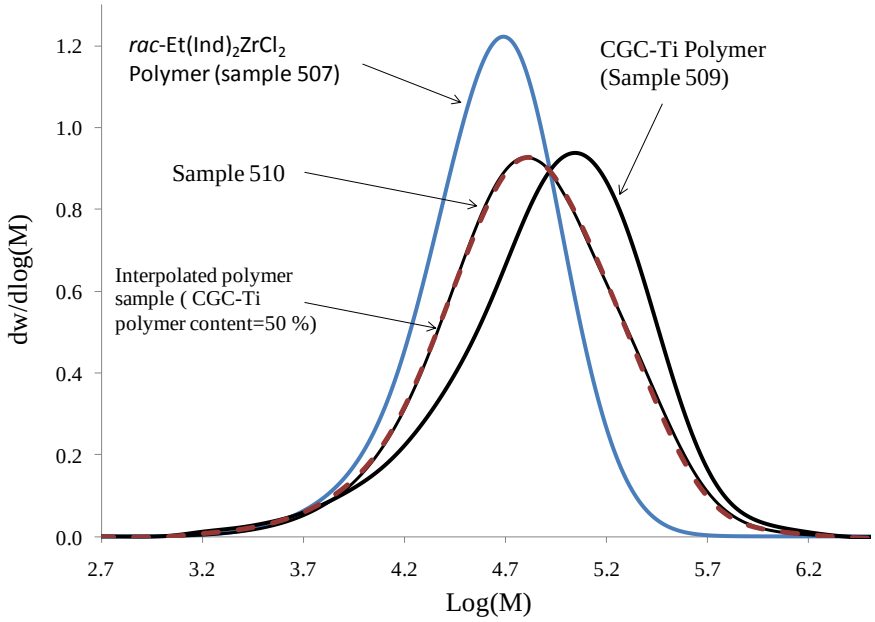

Figure 8-17. Molecular weight distributions of samples 507, 509, 510 and a hypothetical polymer sample with 50% CGC-Ti polymer content.

Figure 8-18 plots the weight fraction of the CGC-Ti polymer in the polymer samples, determined by GPC, versus weight fraction of the CGC-Ti polymer in the polymer samples, w_c, estimated through catalyst mole fractions in the feed. Unlike the case of homopolymerization using the combined catalyst system at high MAO concentration (0.013 mol Al/L), a positive deviation was not observed. This seems reasonable because, at low MAO concentration, neither catalyst had reached their maximum activity, so their catalyst activities were affected by change in Al/catalyst ratio. The overall effect was such that no deviation was observed.

This data can be examined from another point of view, by plotting the actual polymer yield and the theoretical polymer yield (yields when the effect of MAO concentration on polymer yield is neglected, so that the polymer yields from each catalyst are additive) versus x', as shown in Figure 8-19. The theoretical polymer yield, m_{th}, was calculated based on the activity of the individual catalysts using equation below.

$$m_{th} = n_{c,CGC-Ti} \times a_{CGC-Ti} + n_{c,Et-ind} \times a_{Et-ind} \quad (8\text{-}14)$$

For all catalyst combinations, the actual polymer yield (dashed curve) is lower than the theoretical yield (solid curve) implying that catalyst activities have decreased. By increasing catalyst concentration, while MAO concentration is constant, the ratio of Al to catalyst sites decreases causing decrease in catalyst activities which in turn decreases polymer yield.

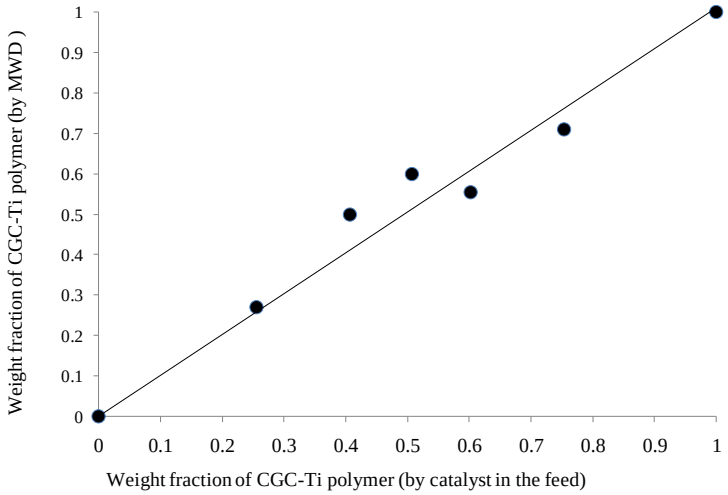

Figure 8-18. Weight fraction of CGC-Ti in polymer estimated using MWD versus the corresponding weight fraction using the concentration of the catalysts injected in the reactor ([MAO] = 0.003 mol Al/L).

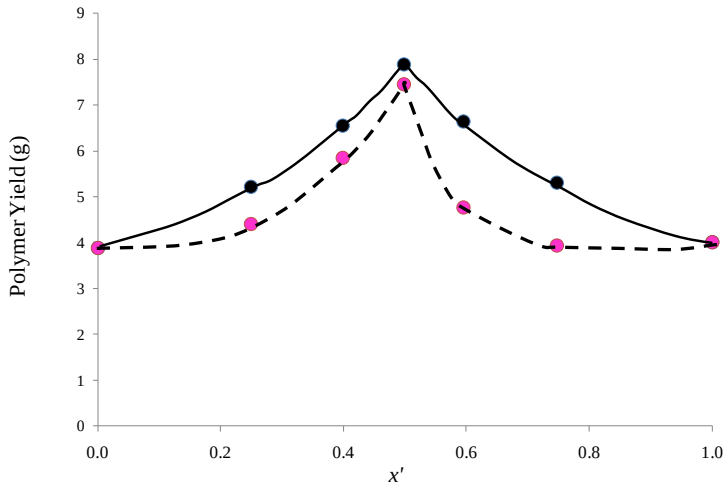

Figure 8-19. Actual polymer yield (dashed curve) and theoretical polymer yield (solid curve) versus modified catalyst mole fraction x'.

8.5 Conclusions

Ethylene homopolymerization and copolymerization with 1-octene were conducted using a combined catalysts system (CGC-Ti and *rac*-Et(Ind)$_2$ZrCl$_2$) at low and high MAO concentrations (0.003 and 0.013 mol Al/L, respectively). Polymer samples with bimodal MWDs were obtained at high MAO concentration but no LCB was detected in the samples using ^{13}C NMR and a in-line GPC viscosity detector. The CGC-Ti polymer content of the samples were higher than expected based on the moles of the catalysts injected. This could be due to effect of MAO/catalyst ratio on polymer yield.

We also copolymerized ethylene and 1-octene using the combined catalysts system. Using the Crystaf calibration curve and Crystaf profiles of the copolymer samples, the reactivity ratios for ethylene/1-octene were estimated. For CGC-Ti catalyst, estimates of r_1 and r_2 with approximate 95% confidence intervals are 17.1 ± 2.7 and 0.356 ± 0.271, respectively, whereas for *rac*-Et(Ind)$_2$ZrCl$_2$ their corresponding values are 133.6 ± 36.3 and 0.79 ± 0.59.

Chapter 9

Production of Ethylene/α-Olefin/1,9-Decadiene Copolymers with Complex Microstructures Using a Two-Stage Polymerization Process

9.1 Summary

Ethylene was copolymerized with 1,9-octadiene using methylaluminoxane-activated *rac*-Et-Ind_2ZrCl_2 at 120°C to produce macromonomers with pendant and terminal vinyl groups, with frequencies up to 6.5 vinyls per polymer chain. The macromonomer pendant vinyl group content is linearly related to the diene concentration added to the reactor. The macromonomers were then terpolymerized with ethylene and 1-butene or 1-octene using a constrained geometry catalyst (dimethylsilyl(N-tert-butylamido)-(tetramethylcyclopentadienyl)-titanium dichloride) at 120°C in toluene. The resulting branched polymers showed three distinct populations during crystallization analysis fractionation, indicating the formation of a new fraction produced by the incorporation of macromonomer chains into ethylene/1-butene or ethylene/1-octene copolymer chains.

9.2 Introduction

Metallocene catalysts enable the production of polyolefins with narrow molecular weight distribution and uniform comonomer distribution. Certain metallocenes, such as constrained geometry catalysts, can also form polymers with long chain branches (LCB) and good processability, while keeping the molecular weight distribution (MWD) quite narrow. The use of mixed metallocene catalysts results in more degrees of freedom to make polyethylene resins with designed microstructural properties. Dual metallocene systems have been used to produce polyolefins with bimodal distributions of molecular weight and chemical composition,[132-133, 137-138, 170-171] to maximize the LCB formation in polyethylene,[28, 94, 172] and to produce branched and linear olefin block copolymers.[85, 116, 135] Similar products can also be made with a single metallocene in two reactors operated in series under different polymerization conditions.

It has been shown that by the proper selection of catalysts pairs, comonomer types, and polymerization conditions, it is possible to make copolymers displaying characteristics of thermoplastic elastomers.[135, 173] Olefin copolymerization with dienes opens up the possibility of

creating chains with pendant double bonds that act as macromonomers with increased likelihood of being incorporated into a growing polymer chain formed on another catalyst site.

Several articles have been published on the copolymerization of ethylene and 1,5-hexadiene with homogeneous metallocenes, showing that 1,5-hexadiene is preferentially incorporated into the polymer backbone as five-membered rings instead of generating pendant vinyl groups.[174-178] Selectivity toward cyclization was reported to decrease when diene concentration increased over 50 mol%.[175]

Ethylene copolymerization with 1,7-octadiene using constrained geometry catalysts (CGC) has also been reported, with the conclusion that diene insertion was in the form of cyclic structures like 1,3-cycloheptane and 1,5-cyclononane in the main polyethylene chain, with 1,5-cyclononane being the dominant ring structure.[179-180] Several bridged and non-bridged zirconocene catalysts were also investigated for copolymerization of ethylene and 1,7-octadiene at 40^{o}C to conclude that zironocene catalysts with indenly ligands produced copolymers having 1,3-disubstituted cycloheptane units, while zirconocene catalysts with cyclopentadienyl or pentamethylcclopentadienyl ligands gave 1-hexenyl pendant branches along the main polymer chain or 1,3-disubstituted cycloheptane units.[181] Finally, the copolymerization of ethylene and 1,9-decadiene was shown to generate 1-octenyl branches or loosely crosslinked polyethylene, depending on the type of metallocene used during the polymerization.[181]

In this chapter, we copolymerized ethylene and 1,9-decadiene to make macromonomers with different number of pendant vinyl groups in a separate reactor using *rac*-Et(Ind)$_2$ZrCl$_2$, and then terpolymerized these macromonomers with ethylene and α-olefins (1-butene and 1-octene) on a second polymerization step, using CGC-Ti, to create complex polymers with branched structures composed of three main components: a high-crystallinity fraction (macromonomers), a low-crystallinity (or amorphous) fraction (α-olefin copolymer), and a third component resulting from the crosslinking of the two previous components (*cross-product*). Figure 9-1 illustrates this classification. The whole product made after the second stage of polymerization will be referred to as *Branch-block copolymer*.

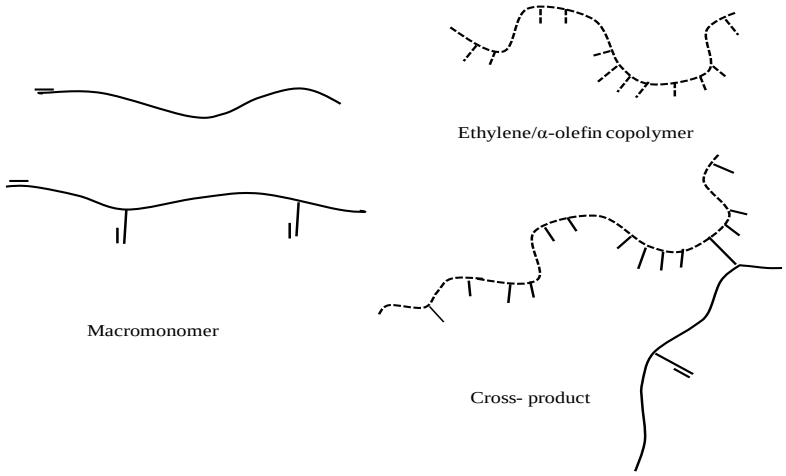

Figure 9-1. Microstructure classification.

9.3 Experimental

9.3.1 Materials

Methylaluminoxane (MAO, 10 wt % in toluene, Sigma-Aldrich) was used as received. Ethylene and nitrogen (Praxair) were purified by passing through molecular sieves (3 and 4-A˚) and copper(II)oxide packed beds. Toluene (EMD) was purified by distillation over a n-butyllithium/styrene/sodium system and then passed through two packed columns in series filled with molecular sieves (3, 4, and 5-A˚) and Selexorb for further purification. All air-sensitive compounds were handled under inert atmosphere in a glove box.

The catalysts, rac-ethenebis(indenyl) zirconium dichloride (rac-Et$[Ind]_2ZrCl_2$) and dimethylsilyl(N-tert-butylamido)-(tetramethylcyclopentadienyl)-titanium dichloride (CGC-Ti), were purchased as powders from Sigma-Aldrich and Boulder Scientific, respectively, and were dissolved in toluene which was first distilled over metallic sodium and then flown through a molecular sieve bed before polymerization.

9.3.2 Polymer Synthesis

All polymerizations were performed in a 500 ml Parr autoclave reactor operated in semi-batch mode. The polymerization temperature was controlled using an electrical band heater and internal cooling coils. The reaction medium was mixed using a pitched-blade impeller connected to a magneto-driver

stirrer, rotating at 2000 rpm. Prior to use, the reactor was heated to 125°C, evacuated, and refilled with nitrogen six times to reduce the oxygen concentration in the reactor, then 250 ml of toluene along with 0.5 g of triisobutyl aluminum was charged into the reactor. The temperature was then increased to 120°C and kept constant for 20 minutes for stabilization. Finally, the reactor contents were blown out under nitrogen pressure. This procedure ensures excellent removal of impurities from the reactor walls.

To make macromonomer, first 200 ml of toluene was charged into the reactor, followed by 0.58 g of MAO (10 wt%), introduced via a 5 ml tube and a 20 ml sampling cylinder connected in series with an ethylene pressure differential of 50 psig. A specified volume of toluene was placed in the sampling cylinder before injection to wash the tube wall from any MAO solution. Then the band heater was powered on to commence heating of the reactor up to 120°C. Ethylene was introduced to the reactor until the solvent was saturated with ethylene and the total pressure in the reactor reached 120 psig. After approximately 10 minutes, when the reactor temperature set point was reached and kept at a stable value, catalyst solution was injected using the same method for MAO injection, but with a lower pressure differential to ensure a minimum pressure increase in the reactor at the start of the polymerization, but still enough to transfer the catalyst solution completely to the reactor. Ethylene was supplied on demand to maintain a constant reactor pressure of 120 psig and monitored with a mass flow meter. With the exception of a 1–2°C exotherm upon catalyst injection, the temperature was kept at 120°C ± 0.15°C throughout all polymerizations. After 15 minutes, the polymerization was stopped by closing the ethylene valve and immediately blowing out the reactor contents into a 2-L beaker filled with 400 ml of ethanol. The polymer produced was then kept overnight, filtered, washed five times cross-currently with ethanol, dried in air, and further dried under vacuum.

9.3.3 Synthesis of Branch-Block Copolymers

The branch-block copolymers were made separately from the macromonomers (sequential process[124]). After charging the reactor with a specified amount of macromonomer and removing air from the reactor by alternating vacuum and nitrogen purging cycles, solvent was added and the reactor was heated to 120°C with high stirring to dissolve the macromonomer followed by the addition of cocatalyst. An appropriate amount of comonomer (1-butene or 1-octene) was then added to the reactor. Finally, the reactor was pressurized with ethylene up to the desired polymerization pressure. The reactor was equilibrated at 120°C for 10 minutes. Catalyst was injected using a 5 ml

catalyst injection tube connected to a 20 ml sampling cylinder filled with a specified volume of toluene to wash the tube walls from any catalyst solution and guarantee that catalyst transfer was complete. After 10 to15 minutes of polymerization time, the reactor contents were forced out of the reactor (using nitrogen pressure) into a beaker containing ethanol to stop reaction immediately. Washing and drying of the polymer were performed the same way as for macromonomers.

9.3.4 Polymer Characterization

The polymer molecular weight averages and molecular weight distribution (MWD) were measured at 135^{o}C with a Polymer Char high-temperature gel permeation chromatographer (GPC), under a flow rate of trichlorobenzene of 1 ml/min. A column bank of three PLgel Olexis 13 μm mixed pore type 300×7.5 mm columns were used for GPC separations. The GPC was equipped with three detectors in series (infra-red, light scattering 15^{0} angle and differential viscometer). The GPC was calibrated with polystyrene narrow standards.

The ^{13}C NMR spectrum was taken on a Bruker 500 MHz system. The probe temperature was set at 120^{o}C. Acquisition parameters were optimized for quantitative NMR, including a 14 microsecond 90^{o} pulse, inverse gated proton decoupling and 10 s delay time between pulses. 10000 scans was used for data averaging of homopolymers and 5000 for copolymers. The biggest peak was referenced to 30.0 ppm. Deuterated ortho dichlorobenzene was used to obtain the field-frequency lock.

Crystallization analysis fractionation (Crystaf) was performed using a Polymer Char Crystaf model 200. Polymer sample was dissolved in 47 ml of 1,2,4 trichlorobenzene at a concentration of 0.6 mg/ml. The polymer solution was heated to 160^{o}C, held for 2 hours to ensure complete dissolution, followed by decreasing the temperature to 105^{o}C and stabilizing for another 55 minutes. A constant cooling rate of 0.1^{o}C/min was applied during all analyses until the temperature reached 30^{o}C. Polymer concentration in the solution phase was monitored using an in-line infrared detector.

Ethyl and hexyl branch distribution were determined using infrared detectors of the GPC. The details of this method are given in Chapter 5, Section 5.1.6. The Zimm-Stockmeyer approach was used to determine the degree of long chain branching, as detailed in Chapter 5, Section 5.2.6.

9.4 Results and Discussion

9.4.1 Macromonomer Synthesis

Ethylene was copolymerized with different amounts of 1,9-decadiene using rac-Et[Ind]$_2$ZrCl$_2$/MAO in toluene at 120^{o}C and a total reactor pressure of 120 psig to make macromonomers with different fractions of pendant vinyl groups. Twelve polymerization runs were performed at five different decadiene concentrations and polymerization time of 15 minutes. The run order was randomized to avoid possible biases in the experimental results. Table 9-1 summarizes molecular weight measurements and polymer yields for these runs. It is hard to deduce any conclusive effect by just glancing at the weight average molecular weights in Table 9-1, or even by plotting their molecular weight distributions, as shown in Figure 9-1. However, inferential statistics can be used to conclude that macromonomers made with higher decadiene concentrations also had higher weight average molecular weights, as will be explained in the following paragraphs.

Table 9-1. Molecular weight measurements for ethylene/1,9-decadiene copolymers.

Run	1,9 decadiene in feed (mmol/L)	M_w	M_n	PDI	Polymer Yield (g)
1	0.114	52 300	25 500	2.05	4.8
2	0.077	51 900	26 100	1.99	5.6
3	0	50 500	25 000	2.02	7.7
4	0.039	50 900	25 400	2.00	6.45
5	0.114	52 700	24 800	2.13	5.26
6	0.077	50 800	25 300	2.00	5.85
7	0	51 000	25 500	2.00	7.47
8	0.152	54 100	25 500	2.13	4.8
9	0.039	50 500	25 200	2.00	6.16
10	0.114	52 900	25 900	2.04	5.65
11	0	51 400	25 800	1.99	7.5
12	0.077	51 500	25 100	2.05	6.27

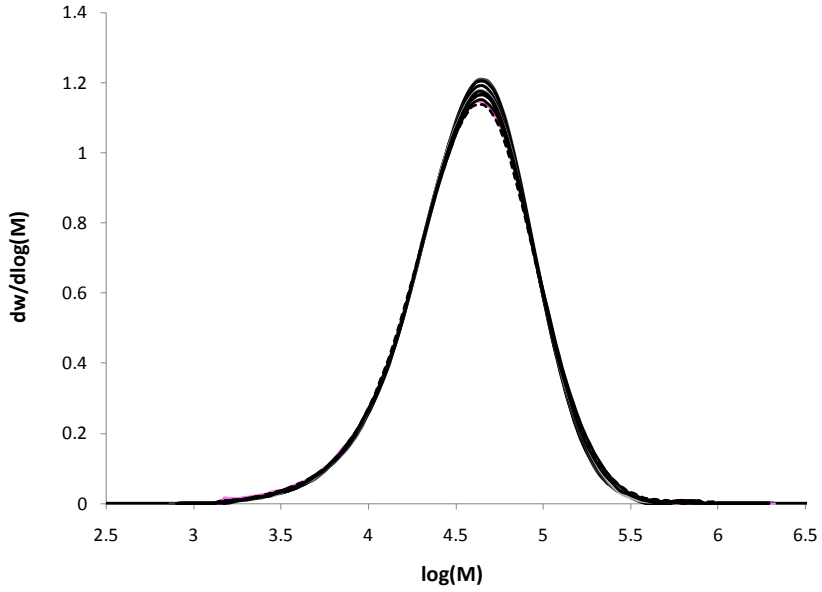

Figure 9-2. Molecular weight distribution of the ethylene/1,9-decadiene copolymers .

Molecular weight measurements can be described with the single-factor ANOVA model,[144]

$$Y_{i,j} = \mu + \tau_i + \varepsilon_{i,j} \tag{9-1}$$

where $Y_{i,j}$ is the $i \times j^{th}$ measurement, μ is the overall mean, τ_i is a parameter associated with the i^{th} treatment level (called the treatment effect – in the present case, weight average molecular weight) and $\varepsilon_{i,j}$ is a random error component arising from all sources of variability. The null hypothesis is $H_0 : \tau_1 = \tau_2 = ... \tau_n = 0$ (where n = 5, conc. of decadiene in the reactor) and the alternative hypothesis is $H_1 : \tau_i \neq 0$ for at least one value of i.

Since the number of replicates are not the same in all treatments levels (see Table 9-1), an unbalanced design[144] approach was used to perform the analysis of variance, as summarized in Table 9-2. The test statistic F_0, which is the ratio of the treatment mean square to error mean square, was used to test the null hypothesis. Because F_0 = 16.058 is greater than $F_{0.05\ 4,\ 7}$ = 4.12, we reject the null hypothesis and conclude it is unlikely that the treatment means are equal. In other words, the 1,9-decadiene concentration affects the molecular weight averages of the ethylene/1,9-decadiene copolymers.

Table 9-2. Analysis of variance for weight average molecular weight.

Source of Variation	Sum of Squares	Degrees of Freedom	Mean Square	F_0	P-Value
Diene concentration	12 153 518	4	3 038 379	16.058	0.0012
Error	1 324 493	7	189 213		
Total	13 478 011	11			

The analysis of variance assumes that the measurements are normally and independently distributed with the same variance for each factor level. The normality assumption can be checked by constructing a normal probability plot of the residuals. The normal probability plot of the residuals for weight average molecular weight measurements is shown in Figure 9-3. The impression from examining this display is that the error distribution is normal, despite the fact that it is likely with small samples to see moderate departures from normality. The plots of the residuals versus run order and diene amount in the reactor also do not show any pattern, with the approximately uniform spread of residuals supporting the assumption of equal variances (these figures were not shown herein for the sake of brevity).

In Figure 9-4, weight and number average molecular weights were plotted versus decadiene mass added to the reactor. A slight, but statistically significant increase in M_w is observed. The reason for increasing M_w with the increase in the diene content in the reactor can be attributed to the higher probability of macromonomer incorporation (LCB formation reactions) onto the growing polymer chains because of the increase in pendant vinyl group concentration in the macromonomer chains. This increase is also confirmed by the log [η] versus log M plot shown in Figure 9-5, since samples with higher diene content have a more marked deviation from linearity in the high molecular weight region. However, the LCB frequency was not high because the MWD shown in Figure 9-2 are not significantly affected.

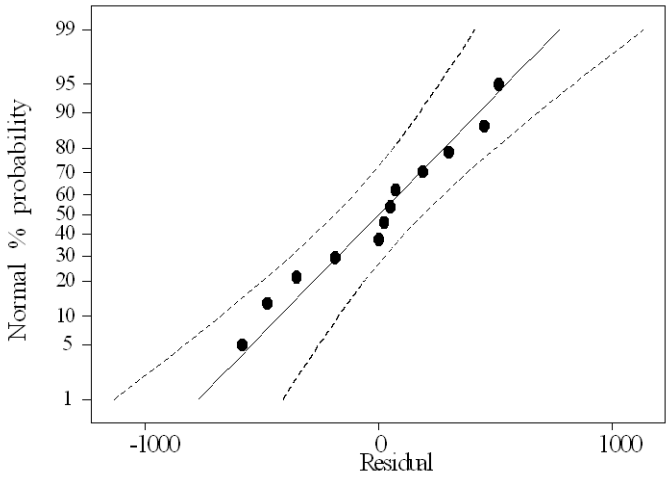

Figure 9-3. Normal probability plot of residuals for weight average molecular weight measurements.

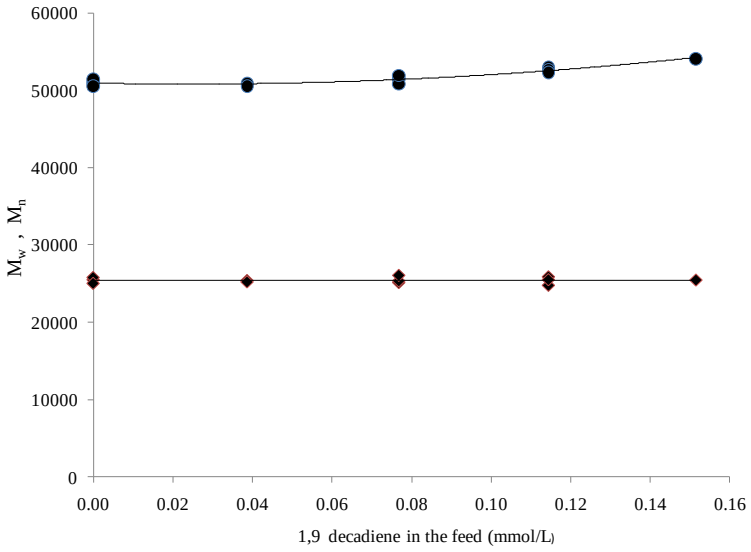

Figure 9-4. Number and weight average molecular weight measurements versus concentration of 1,9-decadiene in the reactor.

The Crystaf profiles for these macromonomers are shown in Figure 9-6. It is clear that, as the diene content increases in the macromonomer chains, their Crystaf peak temperatures decrease as expected, since the incorporation of the diene molecules generates short chain branches (SCB) that decrease the crystallizabilities of the macromonomer chains.

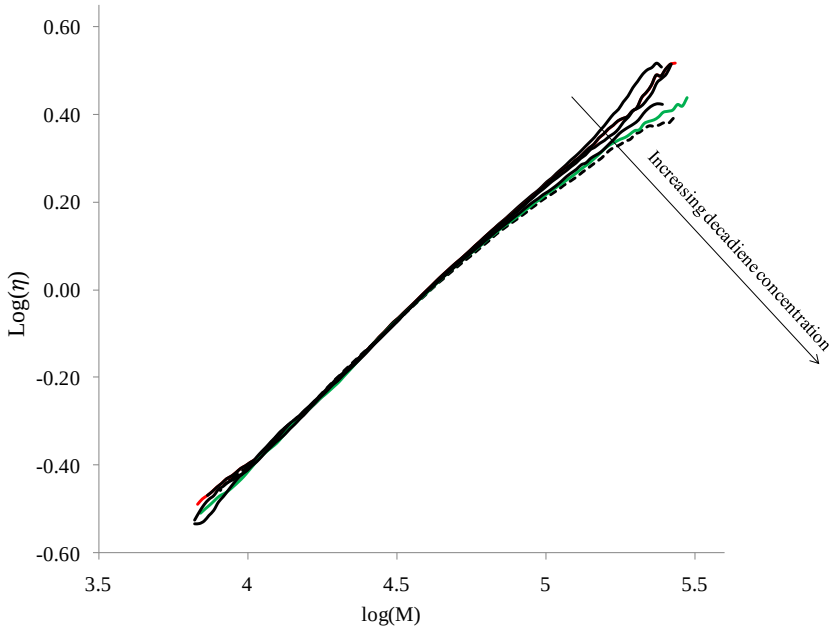

Figure 9-5. Intrinsic viscosity plot for ethylene/1,9-decadiene copolymers.

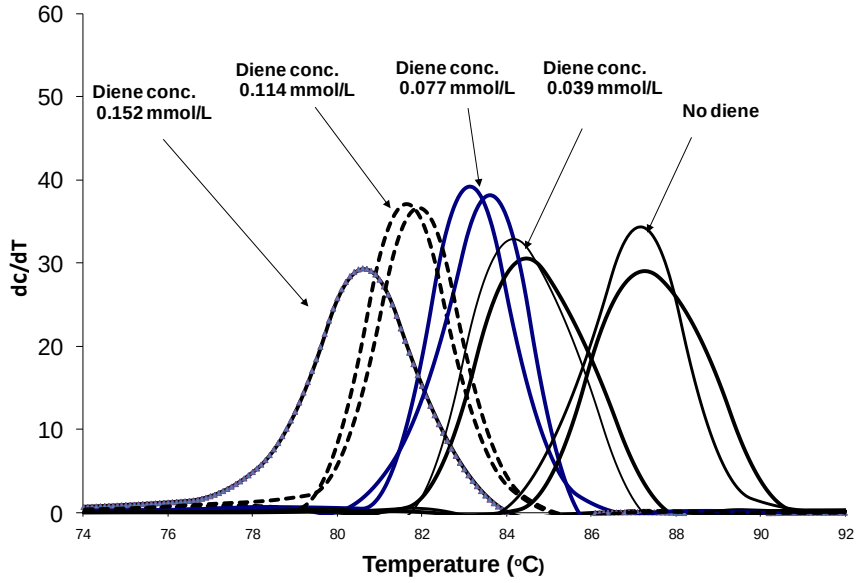

Figure 9-6. Crystaf profiles for ethylene/1,9-decadiene copolymers.

9.4.1.1 Macromonomer structure investigation by ^{13}C NMR

Five samples with different diene molar fractions were selected randomly from the resins made for further study using nuclear magnetic resonance spectroscopy.

Figure 9-7 illustrates the ^{13}C NMR spectrum of an ethylene/1,9-decadiene copolymer (Run 4, Table 9-1). Based on the peaks observed in its spectrum, the structure shown in Scheme 9-1 was proposed for the ethylene/1,9-decadiene copolymers. Using the Grant and Paul rules,[148-149] we obtained the assignments listed in Table 9-3.

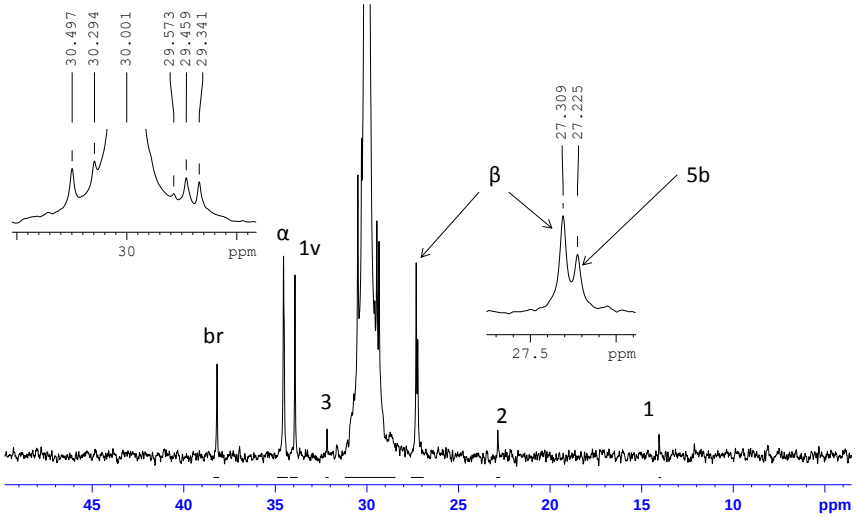

Figure 9-7. ^{13}C NMR spectra of poly(ethylene-*co*-1,9-decadiene) (Run 4).

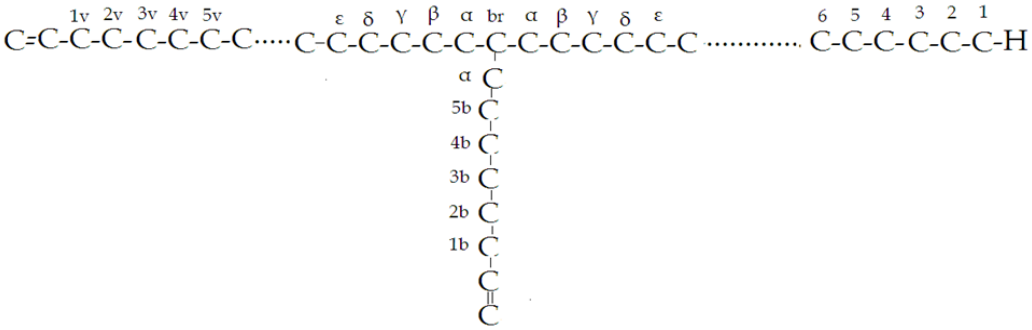

Scheme 9-1. Carbon nomenclature for chemical shift assignments.

Table 9-3. ^{13}C NMR chemical shifts for poly(ethylene-co-1,9-decadiene) made with *rac*-Et-$(Ind)_2ZrCl_2$.

Resonance peak	Chemical shift calculated (δ) (ppm)	Chemical shift observed (δ) (ppm)
1	14.07	14.05
2	22.68	22.85
3	32.46	32.17
4	29.58	29.57
br	38	38.18
α	34.89	34.55
β	27.56	27.31
γ	30.44	30.5
δ	30.07	30
ε	30.01	30
5b	27.13	27.22
4b	30.41	30.29
3b	30.42	30.5
2b	29.58	29.57
1b	34.07	33.92
1v	34.07	33.93
2v	29.58	29.57
3v	30.3	30.3

The following equations were developed to calculate the pendant unsaturated chain end density (PUCED, number of pendant vinyl groups per 1000 carbon atoms), assuming that all pendant groups are the source of branch points in the polymer chains,

$$PUCED = 1000\frac{(IA_{\alpha} + IA_{\beta} + IA_{5b})}{6 \times IA_{Tot}} \tag{9-2}$$

or

$$PUCED = 1000\frac{(IA_{\alpha} + IA_{\beta} + IA_{5b} + IA_{br})}{7 \times IA_{Tot}} \tag{9-3}$$

where IA_α, IA_β, IA_{5b} and IA_{br} are the areas of the peaks for α, β, 5b and tertiary carbon atoms, respectively. The 5b carbon atom has a lower chemical shift than the β carbon (27.22 versus 27.31), which explains the double peak at approximately 27 ppm shown in Figure 9-7. The deconvolution of this peak using Lorentzian functions gives an average area ratio of 1.9 for all four samples, which shows that the chemical shift assignment is correct (allowing for small deconvolution and integration errors). Therefore, to calculate $IA_\beta + IA_{5b}$ we just integrate the bimodal peak from 27 to 27.5 ppm.

The number average molecular weight is calculated with a modified version of Equation (6-59) to account for pendant vinyl groups,

$$\frac{1}{M_n} = \frac{SCED + UCED - PUCED}{28{,}0000} \tag{9-4}$$

The unsaturated chain end density, UCED, calculated using Equation (2-25), gives the total number of pendant and terminal vinyl groups per 1,000 carbons; the difference between UCED and PUCED is the number of terminal vinyl bonds at the end of the polymer chains per 1,000 carbon atoms. Table 9-4 summarizes the result of these calculations for selected polymer samples. The last column in Table 9-4 also lists the number average molecular weights determined using GPC, demonstrating that they are in good agreement with those determined using ^{13}C NMR.

Table 9-4. ^{13}C NMR results for poly(ethylene-*co*-1,9-decadiene) copolymers

Run	**1,9 decadiene in feed (mmol/L)**	**UCED×10**	**SCBD×10**	**PUCED[a]×10**	**PUCED[b]×10**	M_n [c]	M_n [d]
3	0	5.95	5.99	0.00	0.00	23 464	25 020
4	0.039	14.69	5.34	8.18	7.56	23 625	25 400
6	0.077	22.76	4.73	15.75	15.37	23 834	25 346
5	0.114	29.84	6.12	24.40	24.11	24 224	24 759
8	0.152	37.92	5.94	32.24	31.37	24 089	25 460

[a] PUCED calculated using Equation 9-2, [b] PUCED calculated using Equation 9-3, [c] Determined using ^{13}C NMR, [d] Determined using GPC.

Figure 9-8 shows the proton decoupled ^{13}C NMR spectrum for Run 3 (Table 9-1, no diene). To account for the peaks observed in this spectrum, the structure for ethylene homopolymer shown in Scheme 9-2 was assumed.

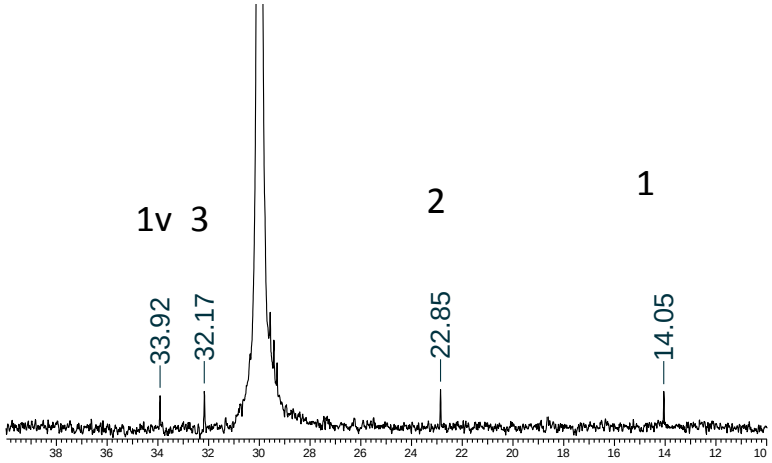

Figure 9-8. ^{13}C NMR spectra of linear polyethylene (Run 3 in Table 1).

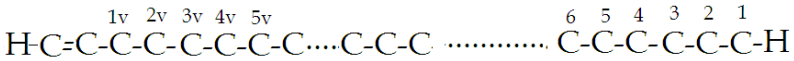

Scheme 9-2. Carbon nomenclature for ethylene homopolymer (Sample 3)

Four well resolved peaks are expected for carbons 1, 2, 3 and 1v if this structure is present. Based on the Grant and Paul rules,[148-149] we can estimate the chemical shift positions of those four carbons (Table 9-5). The calculation of the chemical shift positions for the other carbons using the same rule shows that they are very close to 30 ppm and, since they are obscured by the main spectrum peak, related to methylene carbon, centered at 30 ppm, we cannot get useful information from those carbons. Of course, this does not produce any difficulty because the resonances of the unambiguous carbons can be used to extract useful microstructural information.

Table 9-5. Chemical shift assignments for polyethylene made with rac-Et-$(Ind)_2ZrCl_2$.

Resonance peak	Chemical shift calculated (δ) (ppm)	Chemical shift observed (δ) (ppm)
1	14.07	14.05
2	22.68	22.85
3	32.46	32.17
1v	34.07	33.92

The unsaturated chain-end density (UCED, number of unsaturated chain ends per 1000 carbon atoms), the saturated chain end density (SCED, number of saturated chain ends per 1000 carbon atoms), and number average molecular weight, M_n, were calculated using the Equations (2-25), (2-24) and (6-53) for this sample (Table 9-4, Run 3). In the derivation of Equation (6-53), we have assumed that all chains have a terminal vinyl unsaturation. This assumption is acceptable for the homopolymer made in Run 3 (Table 9-1) because its UCED and SCED are practically the same.

Figure 9-9 shows how UCED and SCED vary with the concentration of 1,9-decadiene in the reactor. Higher diene concentrations increase the polymer vinyl group density linearly, while the SCED remains unaffected, implying that one end of the polymer chains is saturated and the other end has a terminal vinyl group. On the other hand, as the concentration of decadiene in the reactor is increased, the number of these unsaturated pendant groups in the polymer also increases.

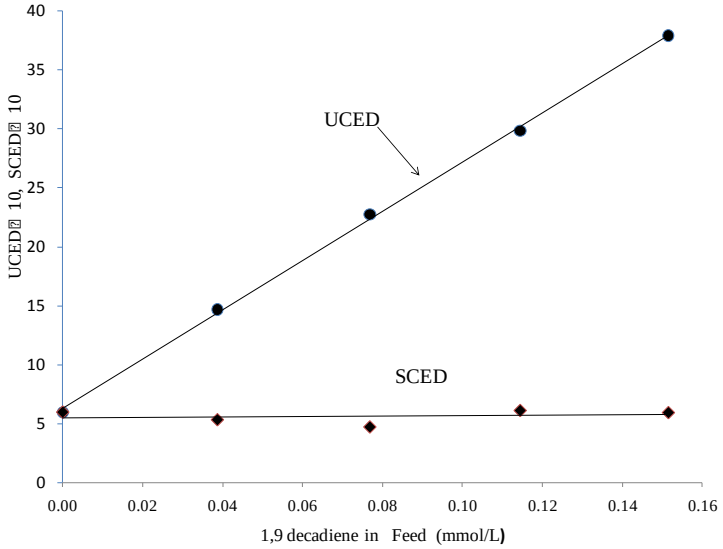

Figure 9-9. Dependency of UCED and SCED with 1,9-decadiene concentration in the reactor.

Figure 9-10 shows that PUCED increases linearly with 1,9-decadiene concentration in the reactor. These macromonomer chains, functionalized with pendant vinyl groups, have increased the possibility of being incorporated onto a growing chain made on another catalyst site (or in another reactor), leading to the formation of chains with long chain branches, as will be demonstrated below.

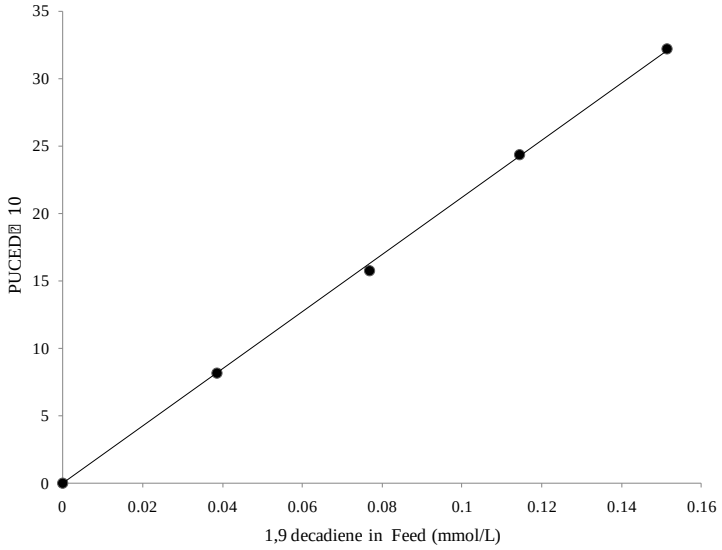

Figure 9-10. PUCED versus 1,9-decadiene concentration in feed.

Three other important macromonomer microstructural characteristics are the average ethylene sequence length between diene units, n, average pendant vinyl groups per polymer chain, λ, and average unsaturated chain ends per polymer chain, γ. Equations for calculating these properties are given below,

$$n = \frac{M_n - \frac{M_n \times PUCED \times 111}{14{,}000}}{\left(\frac{M_n \times PUCED}{14{,}000} + 1\right) \times 28} \tag{9-5}$$

$$\lambda = \frac{PUCED \times M_n}{14{,}000} \tag{9-6}$$

$$\gamma = \frac{UCED \times M_n}{14{,}000} \tag{9-7}$$

Table 9-6 summarizes these calculations for the five selected samples.

Table 9-6. Summary of calculations for microstructural properties of ethylene-1,9-decadiene copolymers.

Run	1,9 decadiene in feed (mmol/L)	n	λ	γ
3	0	838	0	0.997
4	0.039	352	1.38	2.479
6	0.077	228	2.68	3.876
5	0.114	162	4.22	5.103
8	0.152	128	5.55	6.525

Increasing the diene concentration in the reactor causes a linear increase in the pendant unsaturated chain end frequency (λ) and the unsaturated chain end frequency (γ) as shown in Figure 9-11. Figure 9-12 illustrates how the average ethylene sequence length between diene units decreases with increasing diene concentration in the reactor.

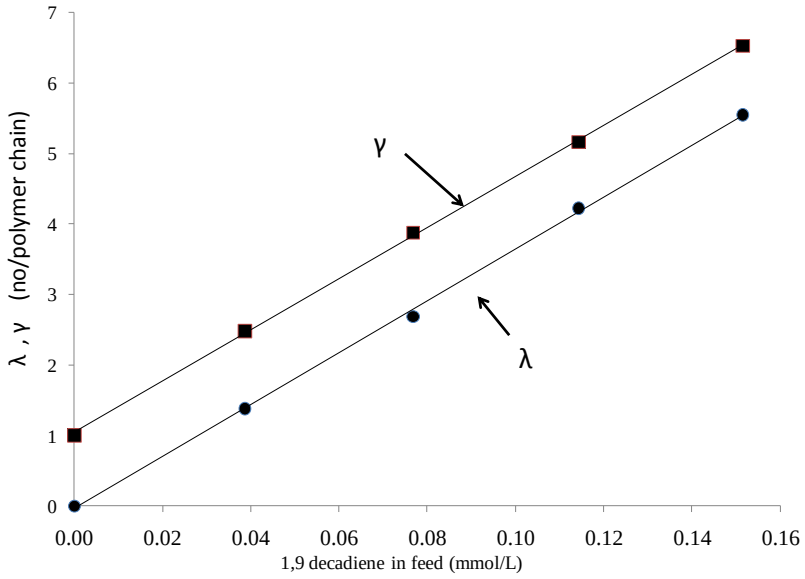

Figure 9-11. Pendant (λ) and unsaturated (γ) chain end frequency variation with 1,9-decadiene concentration in the reactor.

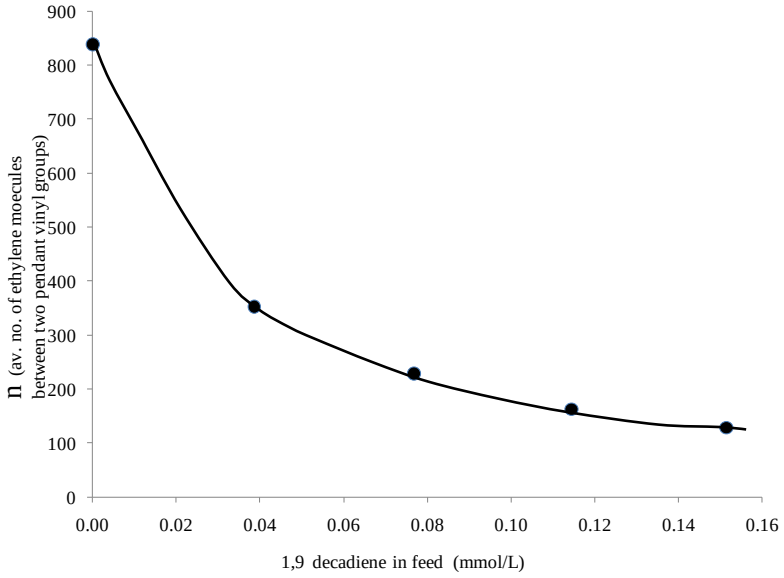

Figure 9-12. Average ethylene sequence length between diene units in the copolymer versus concentration of 1,9-decadiene in the reactor.

Figure 9-13 shows the Crystaf peak temperature versus pendant unsaturated chain end frequency of the copolymer. A linear trend was observed, indicating that the 1,9-decadiene molecules incorporated in the polyethylene chain decreased its crystallizability, as would also be observed for α-olefin incorporation.

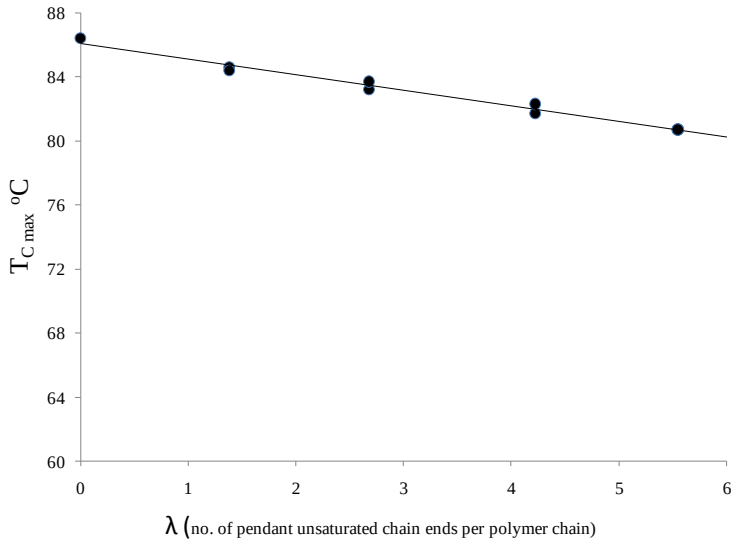

Figure 9-13. Crystaf peak temperature versus pendant unsaturated chain end frequency in the copolymer.

9.4.2 Synthesis of Branch-Block Copolymers

Two procedures may be used for the production of branch-block copolymers: simultaneous or sequential synthesis. In the simultaneous synthesis, two catalysts are added to the reactor at the same time to produce branch-block copolymers, while in the sequential synthesis approach, macromonomers are produced separately and then introduced in another reactor to be terpolymerized with ethylene and α-olefins with a catalyst capable of incorporating macromonomers into the growing copolymer chains. In this investigation, we adopted the sequential approach because it leads to higher macromonomer incorporation, as shown in our previous simulation studies.[116, 124] The procedure for making the macromonomers containing terminal and pendant vinyl groups was explained in the previous section.

The comonomers used were 1-butene and 1-octene. Reaction variables tested included polymerization time, ethylene pressure, and catalyst concentration. The catalyst used for macromonomer incorporation was CGC-Ti.

9.4.2.1 Brach-Block Copolymers Made with 1-Butene

9.4.2.1.1 Effect of Degree of Unsaturation in Macromonomer

In the first set of runs, three polymerization were performed, each starting with macromonomers of different vinyl group densities to produce branch–block copolymers. Table 9-7 summarizes the polymerization conditions for these runs.

Table 9-7. Ethylene/1-butene polymerization conditions.

Sample	Macromonomer concentration (g/L)	Macromonomer UCED×10	Number of vinyl groups per macromonomer chain	Total polymer weight (g)[a]	Weight of polymer Formed (g)	Polymerization time (min)
A	13.47	5.95	1	10.9	7.9	15
B	13.47	22.76	3.88	15.07	12.07	15
C	13.47	37.92	6.53	9.36	6.36	15

Polymerization conditions: Temperature= 120 ^{o}C, pressure= 120 psig, Toluene=222.8 ml, 1-butene=0.62 mol/L

a:Total polymer weight = macromonomer weight + weight of polymer formed

Molecular weights and short chain branch frequencies for the polymers made with macromonomers A, B, and C are summarized in Table 9-8.

Figure 9-14 shows the Crystaf profile for samples A, B and C. Samples B and C, made with macromonomers having higher vinyl group density, are trimodal, while sample A is bimodal. The high crystallization temperature peak corresponds to unreacted macromonomer, while the low crystallinity (or soluble) peak is formed by ethylene/1-butene low crystallinity (or amorphous) copolymer. The intermediate peak observed in samples B and C results from the incorporation of macromonomers into growing copolymer chains (cross-product). For sample C, the intermediate Crystaf peak and the macromonomer peak superimpose because the macromonomer has lower crystallizability due to its higher 1,9-decadiene incorporation, as already illustrated in Figure 9-6.

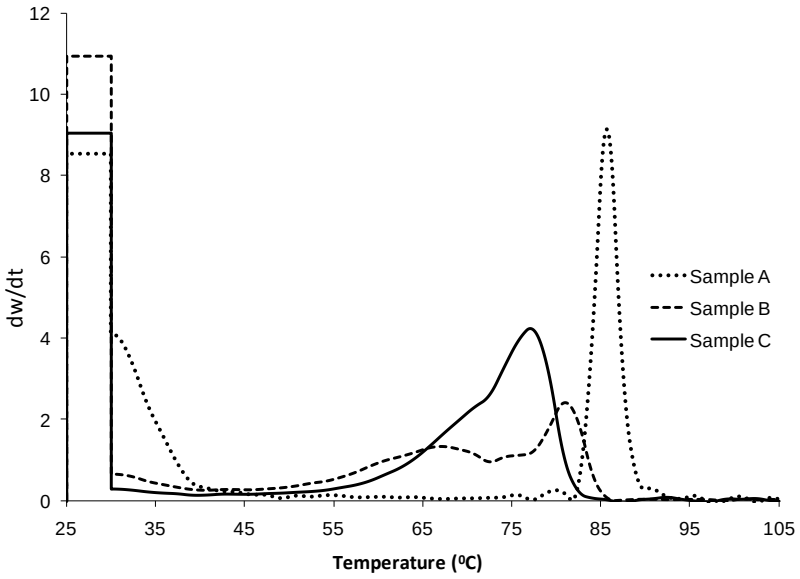

Figure 9-14. Crystaf profiles for samples A, B and C.

Figure 9-15 presents the log [η] versus log M plot overlaid on the MWDs for samples A, B and C**.** Due to polymer coil contraction resulting from 1-butene SCBs, the intrinsic viscosity of sample A is lower than that for the NBS 1475 standard with no SCBs, but it follows the linear trend characteristic of polymers without LCBs. This measurement confirms our observation in Figure 9-14 that no cross-

product was formed in sample A, which is simply a blend of two linear polymers. The log η versus log *MW* plots for samples B and C, on the other hand, show a clear departure from linearity at higher molecular weight values, indicating that those samples contain LCBs. This supports our conclusion that the intermediate Crystaf peak is formed by macromonomer chains grafted onto ethylene/1-butene copolymer chains.

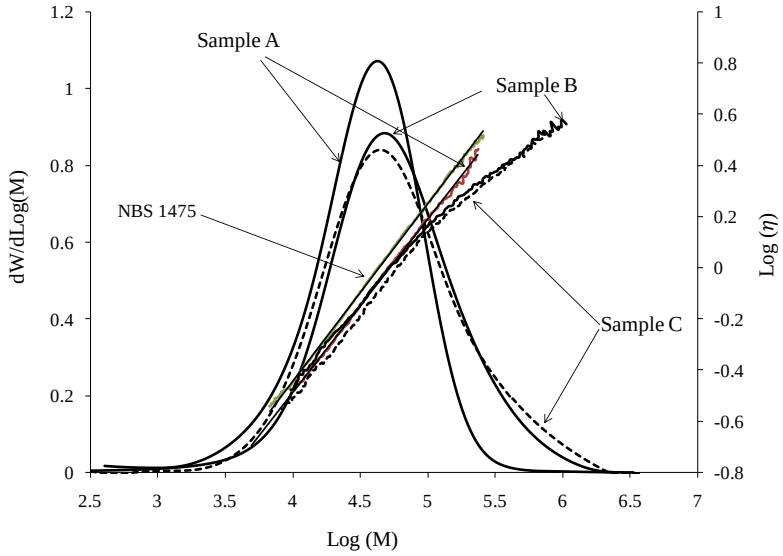

Figure 9-15. MWD and intrinsic viscosity plot for sample A. Dashed curves are related to sample C.

The LCBF and LCBD for samples A, B and C were also calculated using the method developed in Chapter 5, Section 5.2.6 (Table 9-8). A ε value of 0.75 was used in Equation (5-13) to relate g to g'.[130] Although the exact value for ε is not known for our branch-block copolymers, assuming ε = 0.75 enables us to estimate their approximate LCB frequencies and it is a useful measure for comparing variation among polymer samples.

Table 9-8. Molecular weight measurements using GPC and long chain branch calculation using Zimm-Stockmayer equation.

Sample	M_w	M_n	***PDI***	**EBD**	***LCBF* for the whole polymer[a]**	***LCBD* for the whole polymer[b]**
A	50 400	21 000	2.4	29	0	0
B	108 400	27 300	3.9	36.8	0.2	0.103
C	115 800	27 800	4.2	35.7`	0.74	0.37

[a]*LCBF*: number of long chain branches per polymer chain (short chain branch correction was applied).
[b]*LCBD*: number of long chain branches per 1,000 carbon atoms.

The result of LCBF calculations shows that an increase in pendant vinyl group frequency of the macromonomer leads to production of polymers with higher long chain branch frequencies (Table 9-8).

Finally, if we compare the MWDs of the three samples, we observe that polymers made with macromonomers with higher diene density have broader MWDs caused by LCB formation reactions resulting in the production of cross-product chains of higher molecular weight.

9.4.2.1.2 Effect of Polymerization Time and Catalyst Concentration

Four polymerization runs were performed to investigate effect of polymerization time and catalyst concentration on cross-product formation. The polymerization conditions are summarized in Table 9-9.

The polymerization procedure was the same as used in the previous runs. The UCED of the macromonomer used in the terpolymerization was 2.28 per 1000 carbons. Run F in Table 9-9 is just an ethylene/1-butene copolymerization under the same conditions to locate the Crystaf peak for the ethylene/1-butene copolymer alone.

Runs D and G were performed to investigate the effect of polymerization time on cross-product formation. Their polymerization conditions were the same, except for polymerization time, which was 7 minutes for run D and 15 minutes for run G. Similarly, runs E and G were performed under the same polymerization conditions, except that in run E the amount of CGC injected in the polymerization reactor was lower than in run G. Table 9-10 summarizes molecular weight results for these polymers.

Table 9-9. Polymerization conditions and summary results for runs D through G.

Sample	Polymerization time (min)	Macromonomer concentration (g/L)	Total polymer weight (g)	Polymer formed (g)	Weight% of macromonomer	CGC Catalyst (µmole/L)
D	7	13.47	13.3	10.3	22.6	8.98
E	15	13.47	6.84	3.86	48.4	6.7
F	15	0	6.5	6.5	0	1.8
G	15	13.47	18.6	15.6	16.1	8.98

Polymerization conditions: Temperature = 120^{o}C, pressure = 120 psig, toluene volume = 222.8 ml, 1-butene Conc. = 0.4 mol/L. The UCED of the macromonomers used in these polymerizations was 2.28.

Table 9-10. GPC-IR results for samples D-G and macromonomer.

Sample	M_w	M_n	*PDI*	Ethyl branch/1000C of the whole polymer	LCBF of the whole polymer[a]
D	187 300	41 300	4.54	25	0.62
E	73 300	25 300	2.9	19	0.16
F	96 000	38 200	2.5	29	0
G	273 300	42 100	6.5	26.3	1.03
Macromonomer	54 100	26 000	2.08	0	0.083

a: Calculated using Zimm-Stockmeyer equation

Figure 9-16 overlays the Crystaf profiles of polymers D, F, G, and macromonomer, while Figure 9-17 shows their corresponding MWDs. As discussed above, if no cross-product is formed during polymerization, two Crystaf peaks are expected: one high-temperature peak for the macromonomer, and another low-temperature peak for the ethylene/1-butene copolymer (equivalent to that of polymer F). Interestingly, an intermediate third peak was observed for the samples D and G, which indicates the formation of cross-product chains.

The MWD plots in Figure 9-17 also strongly support the presence of branched cross-products because of the observed broadening of the MWD. Increase in time of polymerization increases molecular weight and long chain branch frequency of the whole polymer, as shown in Table 9-10. The ethylene branch density of the whole polymer also increases because the mass fraction of the cross-product increases (Table 9-10).

Figure 9-18 shows the log [η] versus log *MW* plots for polymers D, F, G, macromonomer and linear NBS standard 1475. Sample F exhibits simple power law behavior described by the Mark-Houwink equation, which is indicative of linear polymers, while the curvature of the corresponding curves for samples D and G imply the presence of LCBs. The actual structure of these LCBs is likely to be of two polymer chains connected through a bridge six carbons long, resulting from the polymerization of the pendant double bond of 1,9-decadiene units. The "main" branch is an amorphous ethylene/1-butene chain with high 1-butene content (about 40 ethyl branches per 1000 carbon atoms), while the macromonomer branch is more crystalline, with about three SCBs per polymer chain.

Long chain branch frequencies (LCBF) for the polymer samples were also calculated and are shown in Table 9-10. Although these numbers are not absolute, they are useful to compare the extent of LCB

formation in the samples. The results in Table 9-10 show that increasing polymerization time leads to higher LCBF values for the whole polymer, which is the expected result for this type of polymerization.

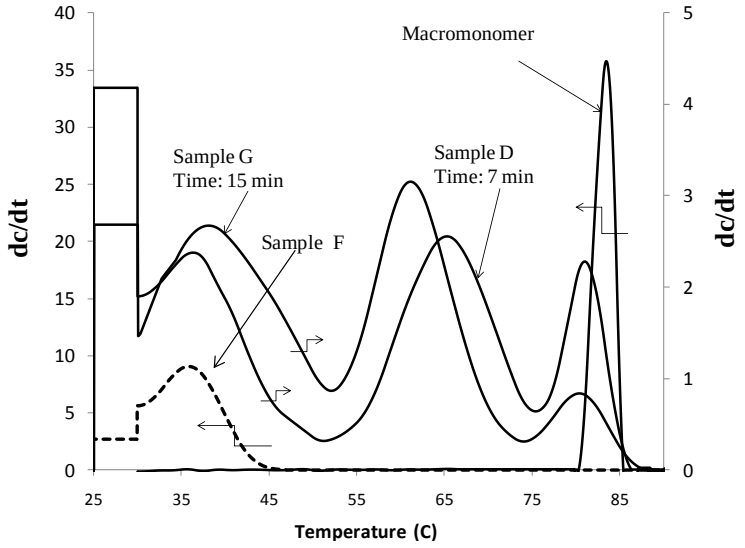

Figure 9-16. Crystaf profiles for samples D, F and G. The dashed line is for sample F (ethylene/1-butene copolymer).

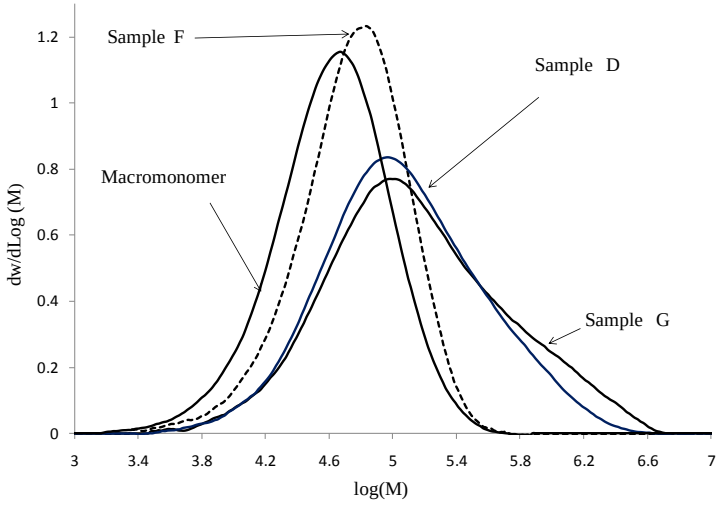

Figure 9-17. Molecular weight distributions for samples D, F, G and macromonomer.

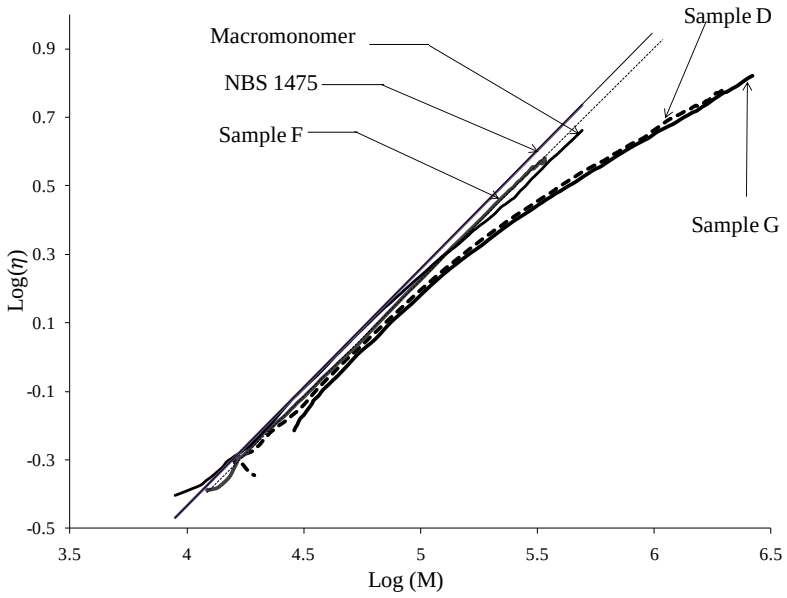

Figure 9-18 . Intrinsic viscosity versus molecular weight for samples D, F, G, macromonomer, and NBS 1475.

Samples E and G were made at different CGC concentrations. Figure 9-19 shows the effect of changing CGC concentration on the MWD of the resulting terpolymer. Increasing CGC concentration leads to more macromonomer incorporation (for the same polymerization time), which in turn broadens the MWD with the formation of higher molecular weight polymer. In Run E, despite the lower CGC concentration, LCBs are still formed (as shown by the deviation from linearity in the log $[\eta]$ versus log *MW* plot in Figure 9-20), but not enough to produce a noticeable Crystaf peak, only a slight shoulder (Figure 9-21).

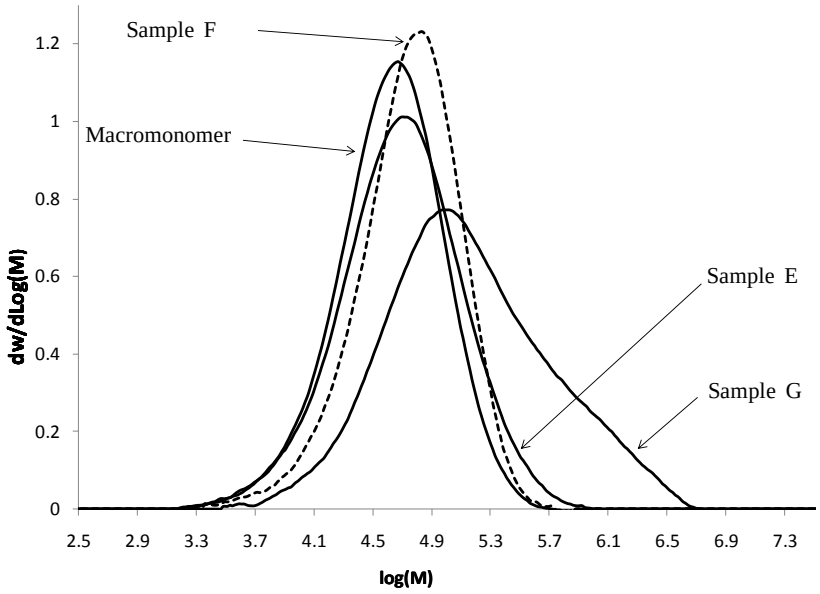

Figure 9-19. Molecular weight distributions for samples E, G, F and macromonomer.

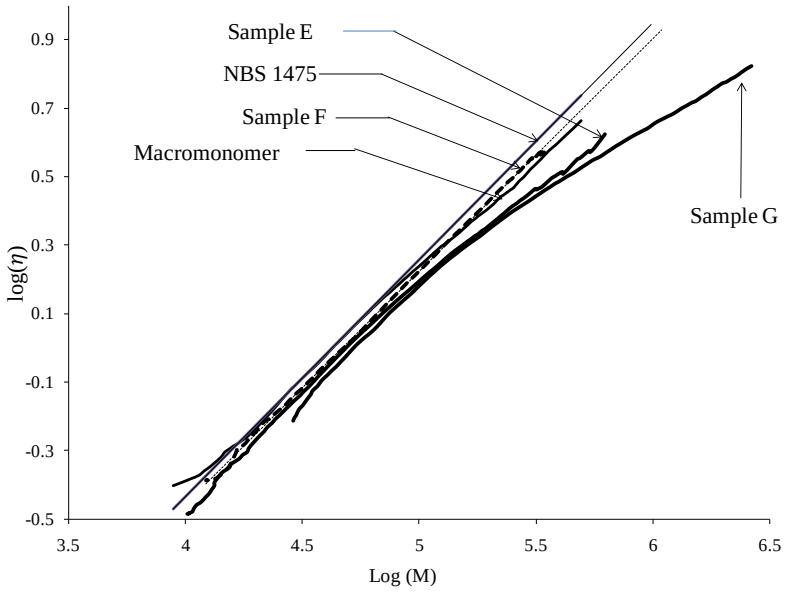

Figure 99-20. Plot of intrinsic viscosity versus molecular weight for samples E, F, G, macromonomer, and NBS 1475.

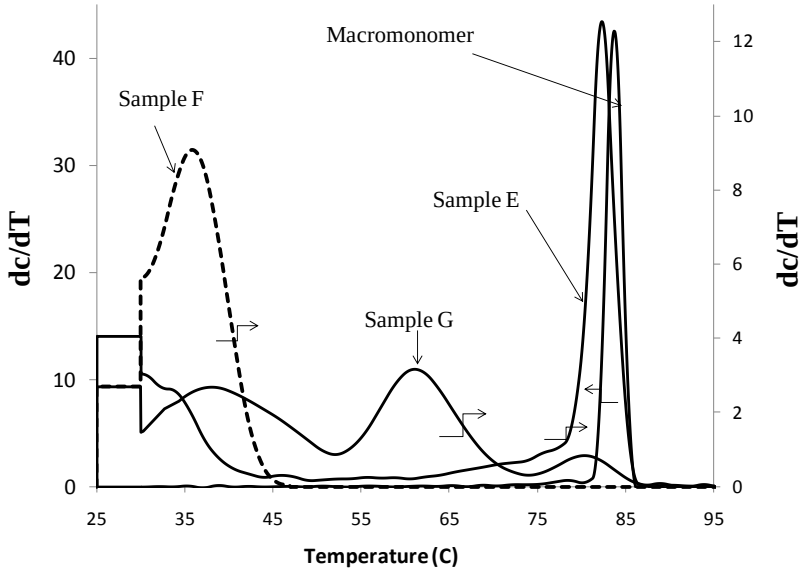

Figure 9-21. Crystaf profiles for samples E, F, G, and macromonomer.

9.4.2.1.3 Ethylene Pressure Effect

The effect of ethylene pressure on the microstructural properties of the resulting terpolymers was investigated at three different ethylene partial pressures during polymerization. The UCED of the macromonomer used was approximately 2.3 (2.68 pendant vinyl groups per chain). CGC and cocatalyst loadings were the same for all three runs. Polymerization temperature and time were also the same, except for the highest ethylene pressure run, for which the polymerization time had to be decreased to approximately three minutes to reduce the polymer mass to an acceptable range and avoid mass and heat transfer limitations (polymer yield is directly proportional to ethylene pressure). The polymerization conditions are summarized in Table 9-11. Average molecular weights and SCB frequencies are shown in Table 9-12 .

Table 9-11. Polymerization conditions for samples H, I, and J.

Sample	Total pressure during polymerization (psig)	Macromonomer UCED×10	CGC Catalyst (μmole/L)	Total polymer weight (g)	Polymer Formed (g)	Time (min)
H	46	22.76	12.25	4.6	1.6	15
I	120	22.76	12.25	11.76	8.76	15
J	200	22.76	12.25	14.04	11.04	2.8

Polymerization conditions: Temperature = 120 ^{o}C, , Toluene=222.8 ml, 1-butene=0.63 mol/L.

Table 9-12. Average molecular masses, SCBD and long chain branch frequency for samples H, I and J

Run	M_w	M_n	PDI	Average Ethyl branch/1000C for the whole polymer	Average Ethyl branch/1000C for the polymer formed by adding CGC	LCBF corrected for SCB	LCBD of the X-product
H	58 900	14 300	4.1	40.5	117	0.054	0.0003
I	84 400	22 600	3.7	35.5	48	0.17	0.126
J	119100	37 100	3.2	18.5	23.5	0.16	0. 65
Macromonomer	54100	26 000	2.08	0.0	-	0.081	n/a

The overlay of the Crystaf profiles for samples H, I and J is shown in Figure 9-22. Sample H, made at the lowest ethylene pressure, does not show an intermediate peak. For sample I, the left side shoulder of the macromonomer peak is attributed to macromonomer incorporation into the copolymer chains by the CGC catalyst. The intermediate peak for the sample J is formed by a similar mechanism. It may seem counterintuitive that increasing ethylene pressure would favor macromonomer incorporation, but this behavior seems to be related to the 1-butene fraction in the chains made by the CGC catalyst. As the ethylene pressure increases in the reactor for the same 1-butene concentration, the fraction of 1-butene in the copolymer decreases, as clearly seen in the Crystaf profiles depicted in Figure 9-22 (the copolymer peak move to higher crystallization temperature). Due to steric effects, it is more likely that a macromonomer chain will be inserted into the growing chain terminated in an

ethylene, rather than a butene, unit. Therefore, increasing the ethylene pressure at the same 1-butene concentration will indirectly favor macromonomer insertion, as illustrated in Figure 9-22.

Figure 9-23 shows the SCB distribution across the MWD for sample H, which was made at the lowest ethylene pressure. A bimodal MWD peak is observed and since the high molecular weight peak for that sample coincides with the macromonomer peak (dashed curve in Figure 9-23), it seems that the high molecular weight peak results from the unreacted macromonomer. This conclusion is also supported by SCBD versus molecular weight plot shown in Figure 9-23 because the SCBD for high molecular weight polymer is very low, practically in the experimental range of SCBD measured for the macromonomer alone.

Figure 9-23 also depicts the log [η] versus log MW plot across the MWD for sample H and macromonomer. The log [η] versus log MW plot deviates from linearity at both low and high molecular weight regions. The deviation at the low molecular weight may be attributed to the presence of higher SCB frequency chains. Since the difference between the log [η] versus log MW plots for macromonomer and sample H is small, the LCB in sample H is not high, as already noticed by inspection of its Crystaf profile. Therefore, the small deviation at the high molecular weight region may be attributed to the presence of LCBs in the unreacted macromonomer itself. As proposed above, the high short chain branch frequency (117 SCB/1000 for lower molecular weight region) of the polymer backbone growing on CGC in sample H might cause steric hindrances which decrease the rate of macromonomer incorporation.

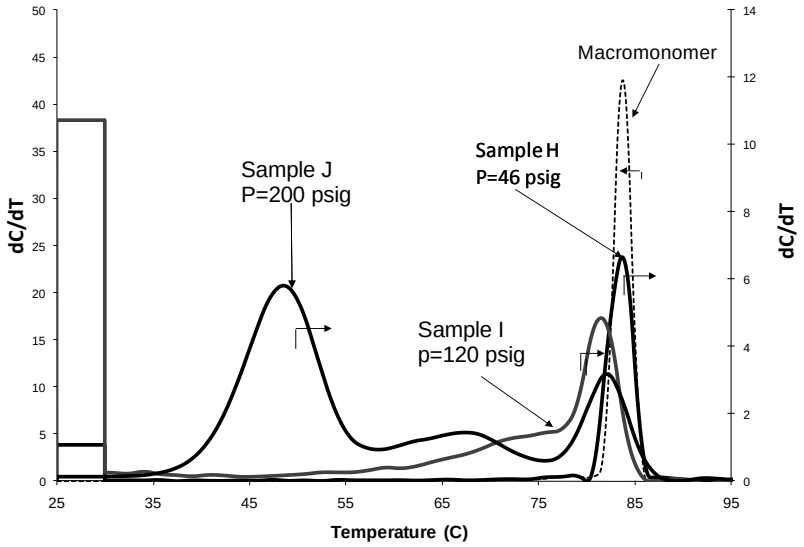

Figure 9-22. Crystaf profile for samples H, I, J, and macromonomer.

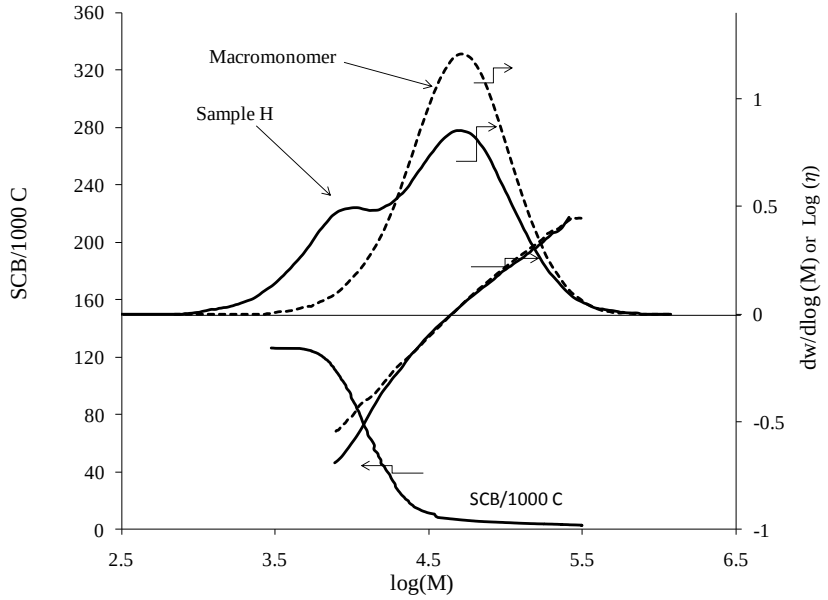

Figure 9-23. MWD, SCB distribution and intrinsic viscosity plot for the sample H and macromonomer. Dashed lines and solid lines are related to macromonomer and sample H, respectively.

Figure 9-24 show analytical results for sample I, made at total pressure of 120 psig. This figure clearly shows the presence of LCBs in sample I, since log [η] versus log MW plots deviates from linearity significantly. Comparing the SCB distribution of this sample (Figure 9-24) with the one made at the lowest pressure (Figure 9-23) shows a gradual, not sudden, decrease in SCB. This happens because the molecular weight of the copolymer made at higher ethylene pressure increases, making the MWD unimodal and "merging" the MWD distributions for each component in the polymer.

Figure 9-25 shows the log [η] versus log MW plot for sample J. The LCB frequency of sample J is similar to that of sample I (Table 9-12). We can speculate that a low ethylene pressure favors the formation of LCBs but, at the same time, the higher SCB frequency in ethylene/1-butene copolymers made at lower ethylene pressures makes it harder for macromonomers to be incorporated into these chains; these two factors, acting in opposing directions, cause the LCBF of the samples I and J, polymerized at 120 and 200 psig, to be approximately the same.

The SCB distribution as a function of molecular weight for sample J, as shown in Figure 9-25, is very interesting because it initially increases with molecular weight, reaches a maximum, and then

decreases. This apparently abnormal behavior is easy to explain: the copolymer made at higher ethylene pressure has higher molecular weight averages than those of the macromonomer, consequently, the low MW region is mostly composed of macromonomer with low SCB content; the intermediate MW region is mostly formed by ethylene/1-butene copolymer with high SCB frequency; finally, the high MW region contains most of the cross-product, which is formed by copolymer (high SCB) and macromonomer (low SCB) chains linked by covalent bonds.

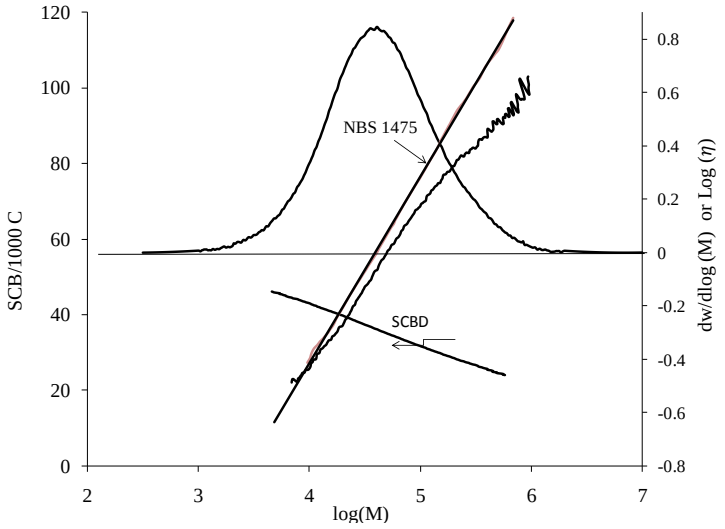

Figure 9-24. MWD, intrinsic viscosity plot and SCB distribution for sample I.

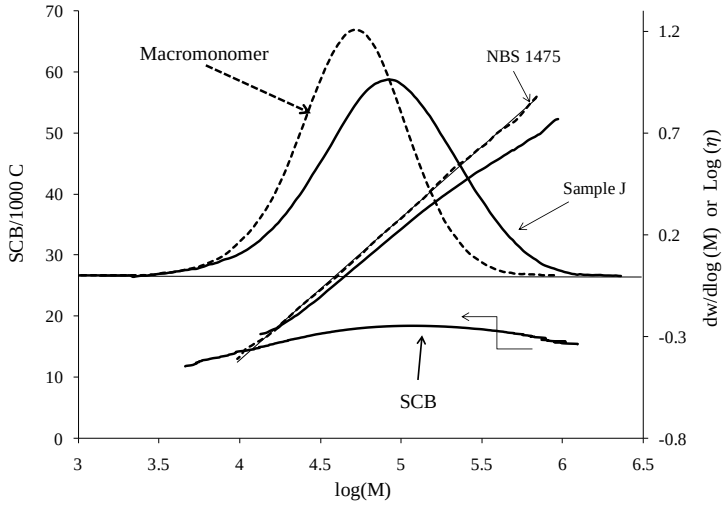

Figure 9-25. MWD and intrinsic viscosity plot for samples J and macromonomer. Dashed lines are related to macromonomer and solid lines refer to sample J.

9.4.2.2 Branch-Block Copolymers Made with 1-Octene

Similar experiments were conducted with 1-octene instead of 1-butene to synthesize branch-block copolymers. The polymerization procedure was analogous to the one used for ethylene/1-butene copolymerizations. Two factors were investigated: 1-octene concentration and degree of unsaturation in macromonomer. Table 9-13 summarizes the conditions for these polymerization runs and Table 9-14 lists some polymer properties and yields.

Table 9-13. Polymerization conditions for samples L, M, L-n and M-n.

Sample	Initial macromonomer concentration in the reactor (g/L)	Macromonomer γ	1-octene concentration in the reactor (mol/L)	Polymerization time (min)	CGC Catalyst concentration In the reactor (μmole/L)
L	13.47	5.1	0.36	15	2.44
M	13.47	5.1	0.48	15	2.44
L-n	13.47	1	0.36	15	2.44
M-n	13.47	1	0.48	15	2.44

T=120 ^{0}C, P=120 psig

Table 9-14. Summary of GPC results and LCBs calculations for samples L, M, M-O, L-O, M-n and L-n

Sample	Total Polymer weight (g)	Polymer formed by adding CGC (g)	M_w	M_n	PDI	HBD whole polymer	HBD polymer formed by CGC	LCBF
Macromonomer			53 000	24 800	2.1	0		0.09
L	13.15	10.15	275 200	56 521	4.9	11.1	14.4	0.89
M	13.1	10.1	217 334	53 425	4.1	14.6	18.9	0.31
M-O			121 200	55 000	2.2	24	24	0
L-O			128 000	59 000	2.2	17.3	18.9	0
M-n	13.15	10.6	45 800	112 800	2.5	12.4	17.4	0
L-n	11.46	8.46	50 900	137 000	2.7	9.8	13.3	0

Effect of 1-Octene Concentration

Polymerization runs L and M were both done at the same macromonomer concentration, having identical average unsaturated chain ends per polymer chain, but with different concentrations of 1-octene in the reactor. All other reaction conditions were the same. Two ethylene-1-octene copolymers were also made under the same 1-octene concentrations used for making samples L and M to indentify the Crystaf peaks when no macromonomer was added to the reactor (samples L-O and M-O).

Figure 9-26 illustrates the Crystaf profiles of samples L, M, L-O, M-O, and macromonomer.

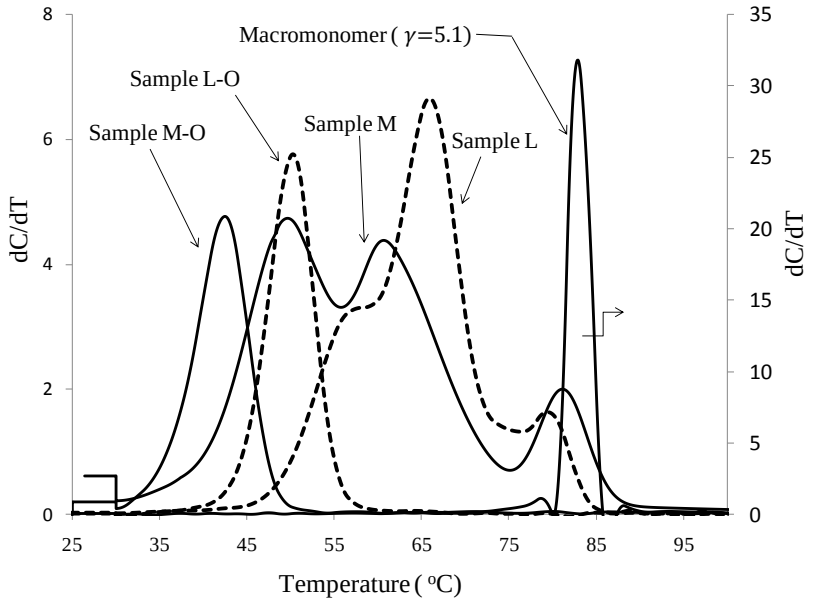

Figure 9-26. Crystaf profiles for samples M, L, M-O, L-O, and macromonomer.

Both L and M samples have intermediate Crystaf peaks due to the incorporation of macromonomer into the growing ethylene/1-octene copolymer chains. A few interesting observations can be made regarding these Crystaf profiles. First, polymers made under lower 1-octene concentration seem to produce more cross-product, as indicated by the higher area under the intermediate Crystaf peaks for samples L and M. This is in agreement with the previous observation that decreasing ethylene pressure, and thus increasing the 1-butene fraction in the copolymer, led to the production of less cross-product in the ethylene/1-butene copolymerization experiments. Second, it appears that there is

a competition for insertion between 1-octene and macromonomer; the presence of macromonomer seems to decrease the relative rate of 1-octene insertion. This is clear when comparing the positions for the L-O and M-O peaks with the lower crystallinity peaks for samples L and M, respectively. We suggest that 1-octene is less likely to be polymerized after a macromonomer insertion due to steric effects (that is, the reactivity ratio for 1-octene/macromonomer is small), effectively lowering 1-octene incorporation in the copolymer.

Figure 9-27 shows the MWD and log [η] versus log M plot for samples L and M. The log [η] versus log M curves for both samples deviate from linearity at high molecular weight, confirming the presence of long chain branching in these polymers.

If we assume that there is no interaction between macromonomer and the CGC-produced copolymer chains, we can predict the MWD of the resulting polymer by superposition of the MWDs of the macromonomer and of the ethylene/1-octene copolymer. Figure 9-27 compares these hypothetical MWDs with the ones actually measured for samples L and M, clearly showing that significant chemical bonding between macromonomer and ethylene/1-octene chains took place during the polymerization.

Since the initial mass of macromonomer and the final mass of polymer are known, the mass of ethylene/1-octene copolymer made in the second stage of polymerization can be calculated. Therefore, we can calculate the hexyl branch density of the ethylene/1-octene copolymer made in the second stage of polymerization (second last column of the table 9-14). The following shows typical calculation for sample M.

$$3\times0.0+HBD\times10.1=13.1\times14.6 \qquad (9\text{-}8)$$

Therefore, the hexyl branch density (HBD) of the ethylene/1-octene copolymer made in the second stage of polymerization would be 18.9.

The hexyl branch density calculated for the ethylene/1-octene copolymer made in the second stage of polymerization of sample M is lower than the corresponding hexyl branch density of sample M-O. This means that the ability of CGC to incorporate 1-octene is affected by the presence of macromonomer. The same conclusion can be drawn when HBD of the ethylene/1-octene copolymer made in the second stage of polymerization for samples L and L-O are compared. Comparing the Crystaf profiles of samples M and M-O, which were made at identical 1-octene concentration, shows that their far left peaks do not overlap which support the aforementioned conclusion.

The long chain branch frequency for sample L, calculated using the Zimm-Stocymayer approach (Table 9-14), is higher than the long chain branch frequency for sample M. Since the hexyl branch

density in the copolymer chains of sample M is 18.9 which is higher than hexyl branch density in sample L, 14.4, it can be concluded that steric hindrances of the hexyl branches might be the reason for reduced amount of LCB in sample M.

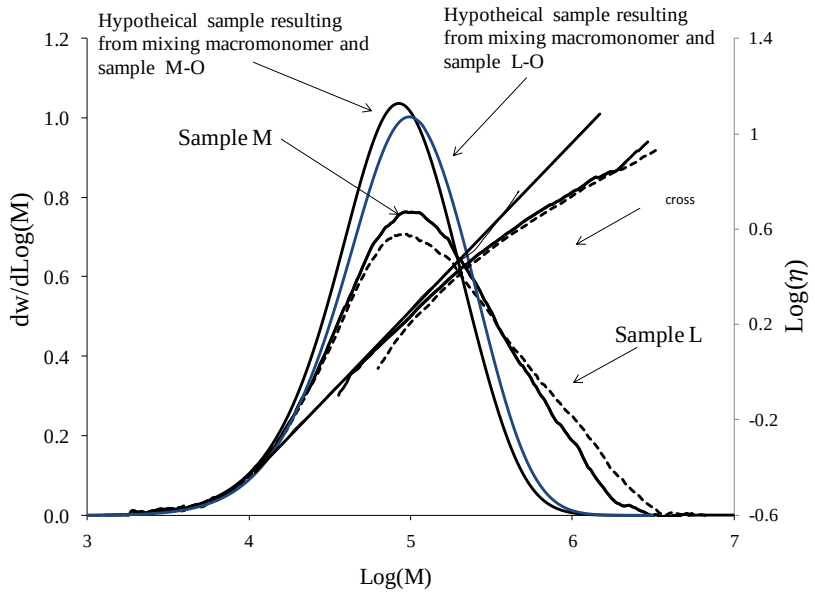

Figure 9-27. MWD and intrinsic viscosity plot for samples L and M. The viscosity plots for samples L and M are the SCB corrected ones.

Effect of degree of unsaturation in macromonomer

It has been demonstrated above that polyethylene macromonomers having vinyl pendant double bonds resulting from ethylene/1,9-decadiene copolymerization were very effective in forming cross-product chains. To investigate whether it was possible to make similar polymers using macromonomers that contained only terminal unsaturations (no diene incorporation), we synthesized two more samples (L-n and M-n) using macromonomers produced in the absence of 1,9-decadiene. Tables 9-13 and 9-14 show the polymerization conditions and polymer properties for these resins. Sample L-n was made under polymerization conditions similar to those used to make sample L, with the exception that the macromonomer had only terminal vinyl groups. A similar approach applies to sample M-n as compared to sample M. Figure 9-28 illustrates the Crystaf profiles of samples L, M, L-n and M-n.

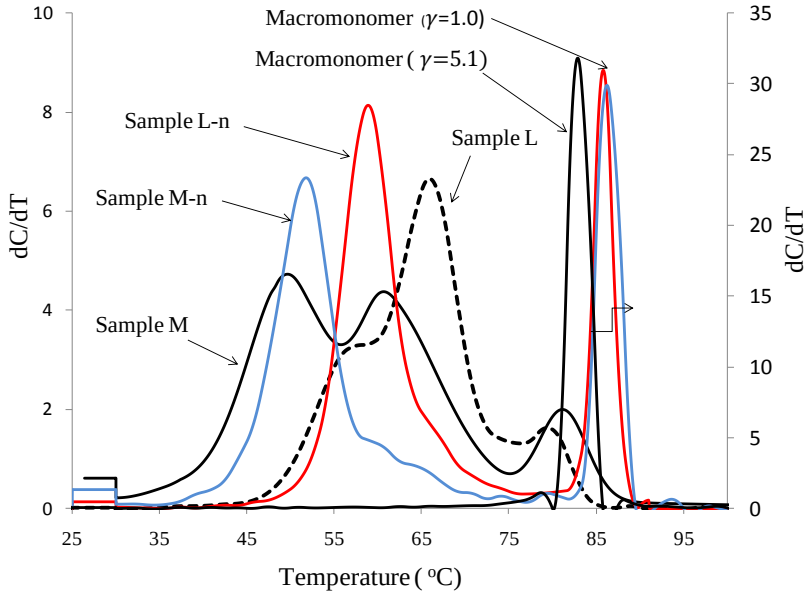

Figure 9-28. CRSTAF profile for samples L, M, M-n, L-n and macromonomers

The low crystallinity Crystaf peaks of samples L and M overlap with the corresponding low crystallinity peaks of samples L-n and M-n, respectively, since they correspond to ethylene/1-octene copolymer chains that have not reacted with the macromonomer chains.

Figure 9-29 shows the MWD overlaid with hexyl branch distribution for sample L-n. No LCB formation is apparent in this sample, as its log $[\eta]$ versus log M plot is linear and overlaps the corresponding plot for the linear polyethylene NBS 1475 standard after short chain branch correction. The lack of intermediate Crystaf peak in Figure 9-28 for this sample also confirms that long chain branching is negligible.

The HBD for low molecular chains is zero, increasing gradually until reaching a maximum value of 13.5 SCB/1000C, and remaining constant for higher molecular weights. This observation indicates that macromonomer chains (with no hexyl branches) are located in the low molecular region of the MWD.

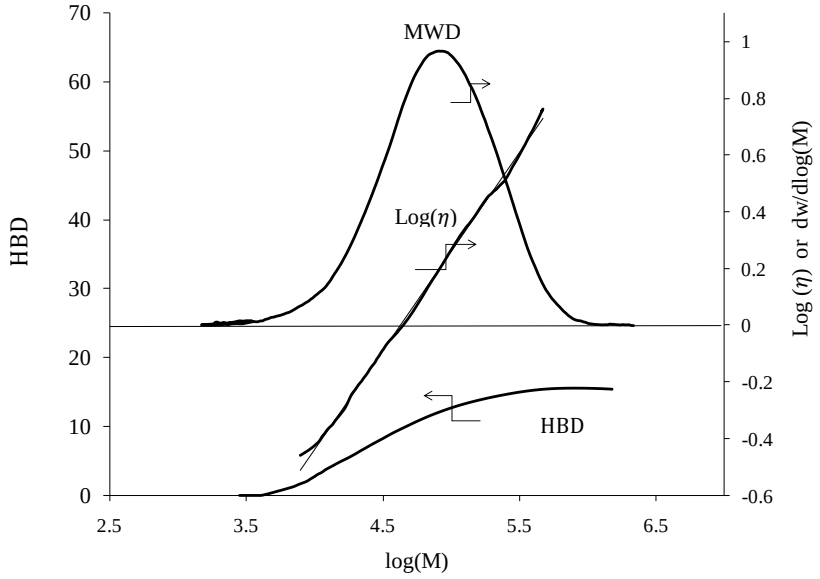

Figure 9-29. Molecular weight distribution, hexyl branch distribution, and viscosity plot for sample L-n.

The log [η] versus log *M* plot for the sample M-n also indicate that the polymer is linear (see Figure 9-30) and no cross-product peak was observed in its Crystaf profile in Figure 9-28. Both observations imply that long chain branching in these polymers is below the detection range of the online GPC viscometer detector and Crystaf.

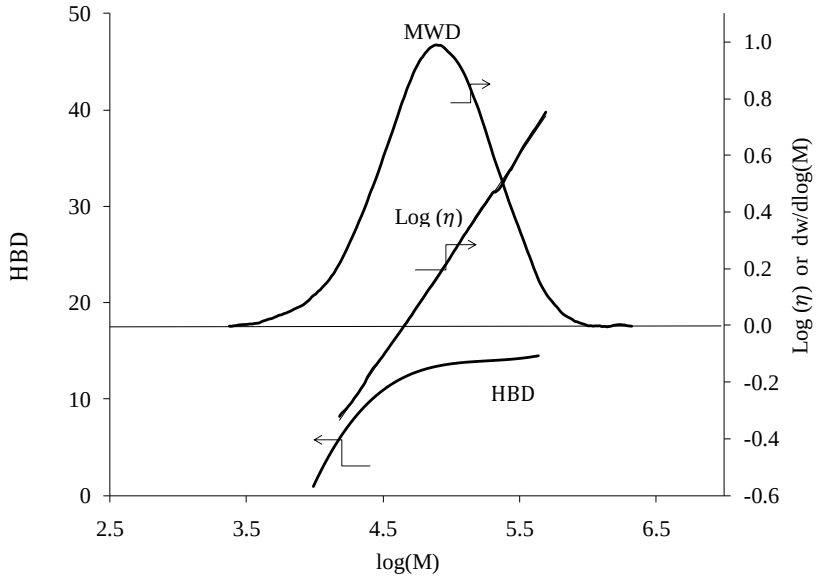

Figure 9-30. MWD, hexyl branch distribution, and viscosity plot for sample M-n.

9.5 Conclusions

Branch-block copolymers can be made in two polymerization stages. Stage 1 is used to produce linear macromonomers with pendant vinyl groups. Stage 2 is employed to make ethylene/α-olefin/macromonomer terpolymers. The proportions of the different components in the polymer (high crystallinity, low crystallinity, and cross-product) can be regulated by varying reactor residence time, catalyst concentration, diene fraction, and ethylene/α-olefin ratio.

The copolymerization of ethylene with 1,9-decadiene using MAO-activated rac-Et-Ind$ZrCl_2$ catalyst was used to produce macromonomers containing pendant 1-octenyl branches. Increasing the diene concentration in the reactor at a constant ethylene pressure causes a linear increase in the frequency of pendant 1-octenyl branches in the macromonomer, while the molecular weight average of the polymer increases only slightly.

Under the experimental conditions covered in this investigation, we were not able to make branch-block copolymers with macromonomers having only terminal unsaturations (no diene), although the homopolymer made using rac-Et-Ind$ZrCl_2$ had about one terminal vinyl group per chain. Introducing a certain amount of pendant vinyl group into the copolymer made by rac-Et-$(Ind)_2ZrCl_2$, however, facilitated the production of branch-block copolymer with CGC and produced a material with considerable fractions of cross-product.

When macromonomers containing pendant double groups were present in the second stage of polymerization, longer polymerization times and higher CGC concentrations increased the weight fraction of cross-product. Increasing the ethylene pressure during the second polymerization stage at a constant 1-butene concentration produced copolymer chains with higher crystallinity and favored the formation of cross-product, likely due to steric effects associated with the sequential insertion or 1-butene and macromonomer.

When 1-octene was used as the comonomer, it was observed that increase in 1-octene concentration decreased long chain branching, whereas Increase in pendant vinyl group frequency of the macromonomer led to increased long chain branching.

Chapter 10
Conclusions and Recommendations

10.1 Conclusions

Significant contributions to polymer science and polymer reaction engineering have been made in this research:

1) For the first time, a mathematical model was developed for a system of two continuous stirred tank reactors in series using a combination of two single site catalysts that produced LCB polymers. Population balances and the method of the moments were used to develop the model. The model can predict average weight fractions, molecular weights, average chain lengths, polydispersity and long chain branch density for different polymer populations. This model can be used to guide polymer reactor engineers formulate new products with complex microstructures.
2) A similar model was developed for semibatch reactors to predict change in microstructural properties with time. Simulation results show that CSTRs are more efficient than semibatch reactors in producing branch-block polymers.
3) A systematic methodology for olefin polymerization kinetics determination with metallocenes was introduced for semibatch reactors that can be used to obtain kinetic parameters and statistically test polymerization mechanism.
4) An in-depth study on ethylene homopolymerization kinetics with *rac*-Et$(Ind)_2ZrCl_2$/MAO system was performed for the first time, revealing that the catalyst decays according to a first order model, chain transfer to monomer is the dominant transfer reaction, followed by chain transfer to MAO, and that macromonomers can be prepared at low MAO concentrations.
5) For the first time, a polymerization kinetics model was developed for the homopolymerization of ethylene with CGC-Ti/MAO system at high MAO concentration. Unlike *rac*-Et$(Ind)_2ZrCl_2$/MAO, increase in MAO concentration leads to an increase in molecular weights. Decrease in monomer pressure and MAO concentration favors formation of polymer with long chain branches.
6) Polymer microstructures with defined pendant 1-octenyl branches frequency were made using *rac*-Et$(Ind)_2ZrCl_2$/MAO catalyst, which can be used as macromonomer for further copolymerization reactions.

7) Polymer chains with complex microstructures were made by incorporating macromonomers with two to five pendant vinyl groups into ethylene/1-butene or ethylene/1-octene copolymers. These long chain branched materials were called cross-product. The cross-product compatibilizes the low crystallinity or amorphous copolymer chains with the high crystallinity macromonomer molecules, forming a long-range network bound by physical crosslinks.

10.2 Recommendations for Future Work

We did a systematic investigation study on making branch block copolymer made using 1,9 decadiene, ethylene and 1-butene or 1-octene. An interesting research topic could arise from making isotactic blocks of propylene with sterospecific metallocene catalysts having pendant 1-octenyl branches and then incorporating them to copolymer chains of ethylene and 1-octene or 1-butene to make thermoplastic elastomers with enhanced properties.

Mathematical modeling of the polymerization for a semibatch reactor with initial presence of macromonomer having pendant vinyl groups could help to understand and expedite the experimental part.

Experimental study to increase the amount of cross products for TPEs made using isotactic propylene and α-olefin copolymers. Surface response methodology would be a fast and most convenient method to achieve this goal.

Another subject that needs to be investigated is to do kinetic study on homopolymerization using CGC and borate as cocatalyst and comparing the results with present study to figure out which cocatalyst is more efficient in producing polymers with more LCBs.

References

1. Direct, G.M., *http://www.prlog.org/10272416-the-global-demand-for-polyethylene-has-increased-by-565-pa.html*. 2009.
2. Yan, D., W.J. Wang, and S. Zhu, *Effect of long chain branching on rheological properties of metallocene polyethylene.* Polymer, 1999. **40**(7): p. 1737-1744.
3. Doak, K.W., *Encyclopedia of Polymer Science and Engineering*. 1986, Wiely-intersience: New York.
4. Cudby, M.E.A. and A. Bunn, *Determination of Chain-Branching in Low-Density Polyethylene by C-13 Nuclear Magnetic-Resonance and Infrared Spectroscopy.* Polymer, 1976. **17**(4): p. 345-347.
5. Randall, J.C., *C-13 Nmr of Ethylene-1-Olefin Copolymers - Extension to Short-Chain Branch Distribution in a Low-Density Polyethylene.* Journal of Polymer Science Part B-Polymer Physics, 1973. **11**(2): p. 275-287.
6. Dorman, D.E., F.A. Bovey, and E.P. Otocka, *C-13 Observations of Nature of Short-Chain Branches in Low-Density Polyethylene.* Macromolecules, 1972. **5**(5): p. 574-&.
7. Bovey, F.A., et al., *Short-Chain and Long-Chain Branching in Low-Density Polyethylene.* Macromolecules, 1976. **9**(1): p. 76-80.
8. Odian, G., *Principles of Polymerization*. 4 ed. 2004, New Jersy: John Wiely & Sons
9. Ebewele, R., *Polymer Science and Technology*. 2000, New York: CRC Press.
10. Fried J, R., *Polymer Science and Technology*. 1995, New Jersy: Prentice Hall.
11. Soares, J.B.P., Simon L. C., *Handbook of Polymer Reaction Engineering*. 2005, Weinheim: Wiley-VCH Verlag GmbH & Co KGaA.
12. Lappin, G.R., Sauer J. D., *Alpha olefins Applications Handbook*. 1989, New York and Basel: Marcel Decker Inc.
13. Kashiwa, N., *The discovery and progress of MgCl2-supported TiCl4 catalysts.* Journal of Polymer Science; part A: Polymer Chemistry, 2004. **42**: p. 1-8.
14. Kaminsky, W. and A. Laban, *Metallocene catalysis.* Applied Catalysis A: General, 2001. **222**(1-2): p. 47-61.
15. Natta, G., et al., *Crystalline High Polymers of Alpha-Olefins.* Journal of the American Chemical Society, 1955. **77**(6): p. 1708-1710.
16. Breslow, D.S. and N.R. Newburg, *Bis-(Cyclopentadienyl)-Titanium Dichloride-Alkylaluminum Complexes as Catalysts for the Polymerization of Ethylene.* Journal of the American Chemical Society, 1957. **79**(18): p. 5072-5073.
17. PatentDE3007725., *Verfahren Zur Herstellung Von Polyethylene, Polypropylen und Copolymeren* 1980.
18. Kaminsky, W., *The Discovery of Metallocene Catalysts and Their Present State of the Art.* Journal of Polymer Science; Part A :Polymer Chemistry, 2004. **42**: p. 3911-3921.
19. Kaminsky, W., *New polymers by metallocene catalysis.* Macromolecular Chemistry and Physics, 2003. **197**: p. 3907-3945.
20. Wang, B., *Ansa-metallocene polymerization catalysts: Effects of the bridges on the catalytic activities* Coordination Chemistry Review, 2006. **250**: p. 242-258.
21. Braunschweig, H. and F.M. Breitling, *Constrained geometry complexes - Synthesis and applications.* Coordination Chemistry Reviews, 2006. **250**(21-22): p. 2691-2720.
22. McKnight, A.L. and R.M. Waymouth, *Group 4 ansa-cyclopentadienyl-amido catalysts for olefin polymerization.* Chemical Reviews, 1998. **98**(7): p. 2587-2598.

23. Kaminsky, W., F. Muller, and O. Sperber, *Comparison of olefin polymerization processes with metallocene catalysts.* Macromolecular Materials and Engineering, 2005. **290**(4): p. 347-352.
24. Coates, G.W., *Precise control of polyolefin stereochemistry using single-site metal catalysts.* Chemical Reviews, 2000. **100**(4): p. 1223-1252.
25. Horvath, I.T., *Encyclopedia of Catalysis*. 2003, Wiely-interscience: New York. p. 725-768.
26. Ittel, S.D., L.K. Johnson, and M. Brookhart, *Late-metal catalysts for ethylene homo- and copolymerization.* Chemical Reviews, 2000. **100**(4): p. 1169-1203.
27. Simon, L.C., et al., *Effect of polymerization temperature and pressure on the microstructure of Ni-diimine-catalyzed polyethylene: parameter identification for Monte-Carlo simulation.* Chemical Engineering Science, 2001. **56**(13): p. 4181-4190.
28. Soares, J.B.P., *Polyolefins with Long Chain Branches Made with Single-Site Coordination Catalysts: A Review of Mathematical Modeling Techniques for Polymer Microstructure.* Macromolecular Materials and Engineering, 2004. **289**(1): p. 70-87.
29. Iedema, P.D., H.C.J. Hoefsloot, and J. Smit, *Predicting the Molecular Weight Distribution of Polyethylene for Mixed Systems with a Constrained-Geometry Metallocene Catalyst in a Semibatch Reactor.* Industrial and Engineering Chemistry Research, 2004. **43**(1): p. 36-50.
30. Wang, W.-J., et al., *Kinetics of long chain branching in continuous solution polymerization of ethylene using constrained geometry metallocene.* Macromolecules, 1998. **31**(25): p. 8677-8683.
31. Hamielec, A.E. and J.B.P. Soares, *Polymerization reaction engineering - Metallocene catalysts.* Progress in Polymer Science, 1996. **21**(4): p. 651-706.
32. Huang, J. and G.L. Rempel, *Ziegler-Natta Catalysts for Olefin Polymerization - Mechanistic Insights from Metallocene Systems.* Progress in Polymer Science, 1995. **20**(3): p. 459-526.
33. Scheirs, J., Kaminsky, W., *Metallocene-based polyolefins*. Vol. 1. 2000, New York: John Weily & Sons.
34. Sinn, H., *Proposals for Structure and Effect of Methylalumoxane Based on Mass Balances and Phase-Separation Experiments.* Macromolecular Symposia, 1995. **97**: p. 27-52.
35. Kaminsky, W. and R. Steiger, *Polymerization of Olefins with Homogeneous Zirconocene Alumoxane Catalysts.* Polyhedron, 1988. **7**(22-23): p. 2375-2381.
36. Tritto, I., et al., *H-1 and C-13 Nmr Spectroscopic Study of Titanium Metallocene-Aluminoxane Catalysts for Olefin Polymerizations.* Macromolecules, 1993. **26**(26): p. 7111-7115.
37. Kaminsky, W., *Metallocenes for Polymer Catalysis.* Advances in Polymer Science, 1997. **127**: p. 143-187.
38. Eisch, J.J., et. al., Macromolecular Rapid Communications, 1994. **15**: p. 217.
39. Santos, J.H.Z.D., *Comparative Study of (nBuCp)2ZrCl2 Performance in Ethylene Polymerization: Homogeneous and Supported Catalysts.* The Azo Journal of Material Science online 2006. **2**: p. http://www.azom.com/Details.asp?ArticleID=3290.
40. Giannetti, E., Nicoletti, G. M., *Homogeneous Ziegler–Natta catalysis. II. Ethylene polymerization by IVB transition metal complexes/methyl aluminoxane catalyst systems.* Journal of Polymer Science: Polymer Chemistry Edition, 1985. **23**(8): p. 217-2134.
41. Woo, T.K., L. Fan, and T. Ziegler, *A Density-Functional Study of Chain Growing and Chain Terminating Steps in Olefin Polymerization by Metallocene and Constrained Geometry Catalysts.* Organometallics, 1994. **13**(6): p. 2252-2261.
42. Ziegler, T., E. Folga, and A. Berces, *A Density Functional-Study on the Activation of Hydrogen Hydrogen and Hydrogen Carbon Bonds by Cp2sc-H and Cp2sc-Ch3.* Journal of the American Chemical Society, 1993. **115**(2): p. 636-646.

43. Kaminsky, W. and H. Luker, *Influence of Hydrogen on the Polymerization of Ethylene with the Homogeneous Ziegler System Bis(Cyclopentadienyl)Zirconiumdichloride Aluminoxane.* Makromolekulare Chemie-Rapid Communications, 1984. **5**(4): p. 225-228.
44. Weng, W.Q., E.J. Markel, and A.H. Dekmezian, *Synthesis of vinyl-terminated isotactic poly(propylene).* Macromolecular Rapid Communications, 2000. **21**(16): p. 1103-1107.
45. Resconi, L., et al., *Olefin Polymerization at Bis(Pentamethylcyclopentadienyl)Zirconium and Hafnium Centers - Chain-Transfer Mechanisms.* Journal of the American Chemical Society, 1992. **114**(3): p. 1025-1032.
46. Resconi, L., *Chain transfer and isomerization reactions in propylene polymerization with isospecific metallocene catalysts.* Abstracts of Papers of the American Chemical Society, 1999. **217**: p. U406-U406.
47. Kokko, E., *Metallocene-Catalyzed Ethene Polymerization: Long-Chain Branched Polyethene*, in *Department of Chemical Technology*. 2002, Hesinki University of Technology: Helsinki.
48. D 'Agnillo, L., J.B.P. Soares, and A. Penlidis, *Effect of operating conditions on the molecular weight distribution of polyethylene synthesized by soluble metallocene/methylaluminoxane catalysts.* Macromolecular Chemistry and Physics, 1998. **199**(6): p. 955-962.
49. Soares, J.B.P. and A.E. Hamielec, *Effect of hydrogen and of catalyst prepolymerization with propylene on the polymerization kinetics of ethylene with a non-supported heterogeneous Ziegler-Natta catalyst.* Polymer, 1996. **37**(20): p. 4599-4605.
50. Carvill, A., et al., *Polymer microstructure as a probe into hydrogen activation effect in ansa-zirconocene/methylaluminoxane catalyzed propene polymerizations.* Macromolecules, 1997. **30**(23): p. 7056-7062.
51. Tsutsui, T., N. Kashiwa, and A. Mizuno, *Effect of Hydrogen on Propene Polymerization with Ethylenebis(1-Indenyl)Zirconium Dichloride and Methylalumoxane Catalyst System.* Makromolekulare Chemie-Rapid Communications, 1990. **11**(11): p. 565-570.
52. Shiono, T. and K. Soga, *Synthesis of Terminally Aluminum-Functionalized Polypropylene.* Macromolecules, 1992. **25**(13): p. 3356-3361.
53. Chung, J.S., *Polymer-supported metallocene catalysts for gas-phase ethylene polymerization* Korean Journal of Chemical Engineering, 2002. **19**(4): p. 597-600.
54. Roos, P., Gerben, B., *Gas phase polymerization of ethylene with a silicasupported metallocene catalyst: influence of temperature on deactivation.* Macromol. Rapid Commun., 1997. **18**: p. 319-324.
55. Dornik, H.P., et al., *Deactivation kinetics of metallocene-catalyzed ethene polymerization at high temperature and elevated pressure.* Macromolecular Materials and Engineering, 2004. **289**(5): p. 475-479.
56. Soares, J.B.P. and A.E. Hamielec, *Bivariate chain length and long chain branching distribution for copolymerization of olefins and polyolefin chains containing terminal double-bonds.* Macromolecular Theory and Simulations, 1996. **5**(3): p. 547-572.
57. Wang, W.J., et al., *Long chain branching in ethylene polymerization using constrained geometry metallocene catalyst.* Macromolecular Chemistry and Physics, 1998. **199**(11): p. 2409-2416.
58. Nele, M. and J.B.P. Soares, *Long-chain branching with metallocene catalysts: Is a purely kinetic mechanism for terminal branching sufficient?* Macromolecular Theory and Simulations, 2002. **11**(9): p. 939-943.
59. Hatzikiriakos, S.G., *Long chain branching and polydispersity effects on the rheological properties of polyethylenes.* Polymer Engineering and Science, 2000. **40**(11): p. 2279-2287.

60. Doerpinghaus, P.J. and D.G. Baird, *Separating the effects of sparse long-chain branching on rheology from those due to molecular weight in polyethylenes.* Journal of Rheology, 2003. **47**(3): p. 717-736.
61. Costeux, S., P. Wood-Adams, and D. Beigzadeh, *Molecular structure of metallocene-catalyzed polyethylene: Rheologically relevant representation of branching architecture in single catalyst and blended systems.* Macromolecules, 2002. **35**(7): p. 2514-2528.
62. Wang, W.-J., et al., *Dynamic mechanical and rheological properties of metallocene-catalyzed long-chain-branched ethylene/propylene copolymers.* Polymer, 2004. **45**(16): p. 5497-5504.
63. Wen-Jun, W., et al., *Dynamic mechanical and rheological properties of metallocene-catalyzed long-chain-branched ethylene/propylene copolymers.* Polymer, 2004. **45**(16): p. 5497-5504.
64. Yan, D., W.J. Wang, and S. Zhu, *Effect of long chain branching on rheological properties of metallocene polyethylene.* Polymer, 1999. **40**(7): p. 1737-44.
65. Bubeck, R.A., *Structure-property relationships in metallocene polyethylenes.* Materials Science & Engineering R-Reports, 2002. **39**(1): p. 1-28.
66. Wood-Adams, P. and S. Costeux, *Thermorheological behavior of polyethylene: Effects of microstructure and long chain branching.* Macromolecules, 2001. **34**(18): p. 6281-6290.
67. Wood-Adams, P.M., et al., *Effect of molecular structure on the linear viscoelastic behavior of polyethylene.* Macromolecules, 2000. **33**(20): p. 7489-7499.
68. Piel, C., et al., *Structure-property relationships of linear and long-chain branched metallocene high-density polyethylenes and SEC-MALLS.* Macromolecular Chemistry and Physics, 2006. **207**(1): p. 26-38.
69. Raju, V.R., et al., *Properties of Amorphous and Crystallizable Hydrocarbon Polymers .1. Melt Rheology of Fractions of Linear Polyethylene.* Journal of Polymer Science Part B-Polymer Physics, 1979. **17**(7): p. 1183-1195.
70. Rachapudy, H., et al., *Properties of Amorphous and Crystallizable Hydrocarbon Polymers .3. Studies of the Hydrogenation of Polybutadiene.* Journal of Polymer Science Part B-Polymer Physics, 1979. **17**(7): p. 1211-1222.
71. Vega, J.F., et al., *Comparison of the rheological properties of metallocene-catalyzed and conventional high-density polyethylenes.* Macromolecules, 1996. **29**(3): p. 960-965.
72. Shroff, R.N. and H. Mavridis, *Long-chain-branching index for essentially linear polyethylenes.* Macromolecules, 1999. **32**(25): p. 8454-8464.
73. Wood-Adams, P.M., *The effect of long chain branches on the shear flow behavior of polyethylene.* Journal of Rheology, 2001. **45**(1): p. 203-210.
74. Gabriel, C. and H. Munstedt, *Influence of long-chain branches in polyethylenes on linear viscoelastic flow properties in shear.* Rheologica Acta, 2002. **41**(3): p. 232-244.
75. Gabriel, C., et al., *Analytical and rheological characterization of long-chain branched metallocene-catalyzed ethylene homopolymers.* Polymer, 2002. **43**(24): p. 6383-6390.
76. Lohse, D.J., et al., *Well-defined, model long chain branched polyethylene. 2. Melt rheological behavior.* Macromolecules, 2002. **35**(8): p. 3066-3075.
77. Kolodka, E., et al., *Rheological and thermomechanical properties of long-chain-branched polyethylene prepared by slurry polymerization with metallocene catalysts.* Journal of Applied Polymer Science, 2004. **92**(1): p. 307-316.
78. Shroff, R.N. and H. Mavridis, *Assessment of NMR and rheology for the characterization of LCB in essentially linear polyethylenes.* Macromolecules, 2001. **34**(21): p. 7362-7367.

79. Rodríguez, H., et. al. , *Determination of the molecular characteristics of commercial polyethylenes with different architectures and the relation with the melt flow index.* Journal of Applied Polymer Science, 2007. **104**(3): p. 1572-1578.
80. Bersted, B.H., *On the Effects of Very Low-Levels of Long-Chain Branching on Rheological Behavior in Polyethylene.* Journal of Applied Polymer Science, 1985. **30**(9): p. 3751-3765.
81. ASTM, *Standard Test Method for Determining Molecular Weight Distribution and Molecular Weight Average of Polyolefins by High Temperature Gel Permeation Chromatography*. Designation D 6474-99. Vol. 08.03. 2005: American Society for Testing Materials
82. Sun, T., et al., *Effect of short chain branching on the coil dimensions of polyolefins in dilute solution.* Macromolecules, 2001. **34**(19): p. 6812-6820.
83. Wang, W.J., et al., *Triple-detector GPC characterization and processing behavior of long-chain-branched polyethylene prepared by solution polymerization with constrained geometry catalyst.* Polymer, 2004. **45**(19): p. 6495-6505.
84. Beigzadeh, D., *Long chain-branching in Ethylene Polymerization using Combined metallocene catalyst systems*, in *Chemical Engineering Department*. 2000, Thesis, (PhD). University of Waterloo: Waterloo.
85. Dekmezian, A.H., et al., *Characterization and modeling of metallocene-based branch-block copolymers.* Macromolecules, 2002. **35**(25): p. 9586-9594.
86. Nele, M., J.B.P. Soares, and J.C. Pinto, *Evolution of molecular weight and long chain branch distributions in olefin-diene copolymerization.* Macromolecular Theory and Simulations, 2003. **12**(8): p. 582-592.
87. Campbell, D., *Polymer Characterization*. 2000, Cheltenham: Stanley Thornes (Publishers) Ltd. .
88. Grubisic, Z., P. Rempp, and H. Benoit, *A Universal Calibration for Gel Permeation Chromatography.* Journal of Polymer Science Part B-Polymer Letters, 1967. **5**(9pb): p. 753-
89. Yau, W.W., *Modern Size-Exclusion Liquid Chromatography*. 1979, New York: John Wiely & Sons.
90. Wood-Adams, P.M. and J.M. Dealy, *Using rheological data to determine the branching level in metallocene polyethylenes.* Macromolecules, 2000. **33**(20): p. 7481-7488.
91. Janzen, J. and R.H. Colby, *Diagnosing long-chain branching in polyethylenes.* Journal of Molecular Structure, 1999. **485**: p. 569-584.
92. Robertson, C.G.e.a., *Extent of branching from linear viscoelasticity of long-chain-branched polymers.* Journal of polymer science Part B, Polymer Phisics, 2004. **42**: p. 1671-1684.
93. American Society for Testing Materials., *ASTM D5017-96(2009)e1 Standard Test Method for Determination of Linear Low Density Polyethylene (LLDPE) Composition by Carbon-13 Nuclear Magnetic Resonance*. 2009.
94. Beigzadeh, D., J.B.P. Soares, and T.A. Duever, *Production of polyolefins with controlled long chain branching and molecular weight distributions using mixed metallocene catalysts.* Macromolecular Symposia, 2001. **173**: p. 179-194.
95. Zimm, B.H. and W.H. Stockmayer, *The Dimensions of Chain Molecules Containing Branches and Rings.* Journal of Chemical Physics, 1949. **17**(12): p. 1301-1314.
96. Mendelso.Ra, W.A. Bowles, and F.L. Finger, *Effect of Molecular Structure on Polyethylene Melt Rheology .1. Low-Shear Behavior.* Journal of Polymer Science Part a-2-Polymer Physics, 1970. **8**(1pa2): p. 105-&.
97. Zimm, B.H. and R.W. Kilb, *Dynamics of Branched Polymer Molecules in Dilute Solution.* Journal of Polymer Science, 1959. **37**(131): p. 19-42.

98. Morton, M., et al., *Preparation and Properties of Monodisperse Branched Polystyrene.* Journal of Polymer Science, 1962. **57**(165): p. 471-&.
99. Noda, I., et al., *Solution Properties of Comb-Shaped Polystyrenes.* Macromolecules, 1970. **3**(6): p. 795-&.
100. Mendelso.Ra, W.A. Bowles, and F.L. Finger, *Effect of Molecular Structure on Polyethylene Melt Rheology .2. Shear-Dependent Viscosity.* Journal of Polymer Science Part a-2-Polymer Physics, 1970. **8**(1pa2): p. 127-&.
101. Monrabal, B., *Crystallization Analysis Fractionation - a New Technique for the Analysis of Branching Distribution in Polyolefins.* Journal of Applied Polymer Science, 1994. **52**(4): p. 491-499.
102. Sarzotti, D.M., J.B.P. Soares, and A. Penlidis, *Ethylene/1-hexene copolymers synthesized with a single-site catalyst: Crystallization analysis fractionation, modeling, and reactivity ratio estimation.* Journal of Polymer Science Part B-Polymer Physics, 2002. **40**(23): p. 2595-2611.
103. Britto, L.J.D., et al., *Polyolefin analysis by single-step crystallization fractionation.* Journal of Polymer Science Part B-Polymer Physics, 1999. **37**(6): p. 539-552.
104. Soares, J.B.P., *Crystallizability of ethylene homopolymers by crystallization analysis fractionation.* Journal of Polymer Science Part B: Polymer Physic 2001. **39**: p. 1616-1628.
105. American Society for Testing Materials., *ASTM D5576 - 00(2006) Standard Practice for Determination of Structural Features in Polyolefins and Polyolefin Copolymers by Infrared Spectrophotometry (FT-IR).* 2006.
106. Kirk-Othmer, *Encyclopedia of Chemical Technology*. 2007: John Wiley & Sons.
107. Erman, B., Mark J. E.,, *Structure and Properties of Rubberlike Networks*. 1997, New York: Oxford University Press.
108. Legge, N.R., Holden, H. E., *Thermoplastic Elastomers: A comprehensive Review*. 1988, New York: Hansser Verlag.
109. Carlson, E.D., et al., *Rheological and thermal properties of elastomeric polypropylene.* Macromolecules, 1998. **31**(16): p. 5343-5351.
110. Gauthier, W.J., et al., *Elastomeric Poly(Propylene) - Influence of Catalyst Structure and Polymerization Conditions on Polymer Structure and Properties.* Macromolecules, 1995. **28**(11): p. 3771-3778.
111. Collette, J.W., et al., *Elastomeric Polypropylenes from Alumina-Supported Tetraalkyl Group-Ivb Catalysts .2. Chain Microstructure, Crystallinity, and Morphology.* Macromolecules, 1989. **22**(10): p. 3858-3866.
112. Nele, M., et al., *Two-state models for olefin polymerization using metallocene catalysts. 1. Application to fluxional metallocene catalyst systems.* Macromolecules, 2000. **33**(20): p. 7249-7260.
113. Shiono, T., S.M. Azad, and T. Ikeda, *Copolymerization of atactic polypropene macromonomer with propene by an isospecific metallocene catalyst.* Macromolecules, 1999. **32**(18): p. 5723-5727.
114. Dekmezian, E.J., *Elastomeric propylene polymers* U.S. Patent, Editor. 1999, Exxon Chemical Patents.
115. Nele, M. and J.B.P. Soares, *Molecular weight and long chain branch distributions of branch-block olefinic thermoplastic elastomers.* Macromolecular Theory and Simulations, 2003. **12**(6): p. 386-400.
116. Mehdiabadi, S., J.B.P. Soares, and A.H. Dekmezian, *Simulation of polymerization and long chain branch formation in a semi-batch reactor using two single-site catalysts.* Macromolecular Reaction Engineering, 2008. **2**(1): p. 37.

117. Woo, T.K., et al., *Static and ab initio molecular dynamics study of the titanium(IV)-constrained geometry catalyst (CpSiH2NH)Ti-R+ .2. Chain termination and long chain branching.* Organometallics, 1997. **16**(15): p. 3454-3468.
118. Jensen, M.H., J. Myers, A. Hummel, A., *What is driving changes in polyolefin catalysts and catalyst technology?* Hydrocarbon Processing, 2008. **87**(4): p. 81-84.
119. Tse, M.F., A.J. Dias, and H.C. Wang, *Characterization and physical properties of new isobutylene-based graft copolymers.* Rubber Chemistry and Technology, 1998. **71**(4): p. 803-819.
120. Collette, J.W., et al., *Elastomeric Polypropylenes from Alumina-Supported Tetraalkyl Group-Ivb Catalysts .1. Synthesis and Properties of High Molecular-Weight Stereoblock Homopolymers.* Macromolecules, 1989. **22**(10): p. 3851-3858.
121. Dietrich, U., et al., *Control of stereoerror formation with high-activity "dual-side" zirconocene catalysts: A novel strategy to design the properties of thermoplastic elastic polypropenes.* Journal of the American Chemical Society, 1999. **121**(18): p. 4348-4355.
122. Coates, G.W. and R.M. Waymouth, *Oscillating Stereocontrol - a Strategy for the Synthesis of Thermoplastic Elastomeric Polypropylene.* Science, 1995. **267**(5195): p. 217-219.
123. Hotta, A., et al., *Semicrystalline thermoplastic elastomeric polyolefins: Advances through catalyst development and macromolecular design.* Proceedings of the National Academy of Sciences of the United States of America, 2006. **103**(42): p. 15327-15332.
124. Mehdiabadi, S., J.B.P. Soares, and A.H. Dekmezian, *Production of Long-Chain Branched Polyolefins with Two Single-Site Catalysts: Comparing CSTR and Semi-Batch Performance.* Macromolecular Reaction Engineering, 2008. **2**(6): p. 529-550.
125. Depooter, M., et al., *Determination of the Composition of Common Linear Low-Density Polyethylene Copolymers by C-13-Nmr Spectroscopy.* Journal of Applied Polymer Science, 1991. **42**(2): p. 399-408.
126. Paul, J.D., et. al., *Quantifying short chain branching microstructures in ethylene1-olefins copolymers using size exclusion chromatography and Fourier transform infrared spectroscopy (SEC-FTIR).* Polymer 2002. **43**: p. 159-170.
127. Tribe, K., G. Saunders, and R. Meissner, *Characterization of branched polyolefins by high temperature GPC utilizing function specific detectors.* Macromolecular Symposia, 2006. **236**: p. 228-234.
128. Fox, J.J. and A.E. Martin, *Investigations of infra-red spectra-absorption of some hydroxy compounds in the region of 3 mu.* Proceedings of the Royal Society of London Series a-Mathematical and Physical Sciences, 1937. **162**(A910): p. 0419-0441.
129. Slader, P.E., ed. *polymer molecular weights*. 1 ed. Vol. 4. 1975, Marcel Dekker Inc.: New York. 623.
130. Roovers, J., *Encyclopedia of polymer Science and Engineering*. second ed, ed. H.F. Mark. Vol. 2. 1985: Wiely-Interscience publisher.
131. Sun, T., et al., *A study of the separation principle in size exclusion chromatography.* Macromolecules, 2004. **37**(11): p. 4304-4312.
132. Kim, J.D., J.B.P. Soares, and G.L. Rempel, *Use of hydrogen for the tailoring of the molecular weight distribution of polyethylene in a bimetallic supported metallocene catalyst system.* Macromolecular Rapid Communications, 1998. **19**(4): p. 197-199.
133. Kim, J.D. and J.B.P. Soares, *Copolymerization of ethylene and 1-hexene with supported metallocene catalysts: Effect of support treatment.* Macromolecular Rapid Communications, 1999. **20**(6): p. 347-350.
134. Weng, W., et al., *Long chain branched isotactic polypropylene.* Macromolecules, 2002. **35**(10): p. 3838-3843.

135. Arriola, D.J., et al., *Catalytic production of olefin block copolymers via chain shuttling polymerization.* Science, 2006. **312**(5774): p. 714-719.
136. Soares, J.B.P. and J.D. Kim, *Copolymerization of ethylene and alpha-olefins with combined metallocene catalysts. I. A formal criterion for molecular weight bimodality.* Journal of Polymer Science Part a-Polymer Chemistry, 2000. **38**(9): p. 1408-1416.
137. Kim, J.D. and J.B.P. Soares, *Copolymerization of ethylene and alpha-olefins with combined metallocene catalysts. II. Mathematical modeling of polymerization with single metallocene catalysts.* Journal of Polymer Science Part A: Polymer Chemistry, 2000. **38**(9): p. 1417-1426.
138. Kim, J.D. and J.B.P. Soares, *Copolymerization of ethylene and alpha-olefins with combined metallocene catalysts. III. Production of polyolefins with controlled microstructures.* Journal of Polymer Science Part A: Polymer Chemistry, 2000. **38**(9): p. 1427-1432.
139. Mehdiabadi, S. and J.B.P. Soares, *Influence of Metallocene Type on the Order of Ethylene Polymerization and Catalyst Deactivation Rate in a Solution Reactor.* Macromolecular Symposia, 2009. **285**: p. 101-114
140. Smith, J.M., *Chemical Engineering Thermodynamics*. sixth ed. 2001, New York: Mc Graw Hill.
141. Glen, N.F., Johns, A., *Determination of the Density of Toluene in the Range from (293 to 373) K and from (0.1 to 30) MPa* J. Chem. Eng. Data, 2009. **54**(9): p. 2538-2545.
142. Mcgarry, J., *Correlation and Prediction of the Vapor-Pressures of Pure Liquids over Large Pressure Ranges.* Industrial & Engineering Chemistry Process Design and Development, 1983. **22**(2): p. 313-322.
143. Monogomery, D.C., *Design and Analysis of Experiments*. 6 ed. 2005, New York: John Wiely & Sons.
144. Montgomery D. C., *Applied statistics and propability for engineers* third ed. 2003: John Wiely and Sons Inc.
145. Cox, A.R.F., et al., *Coordination complexes bearing potentially tetradentate phenoxyamine ligands.* Dalton Transactions, 2006(42): p. 5014-5023.
146. Boekel, V., *Statistical Aspects of Kinetic Modeling for Food Science Problems.* Journal of Food Science 1996. **61**: p. 477.
147. Seber, G.A., Wild, C. J., *Nonlinear Regression*. 1989, New York: John Wiely & Sons.
148. Grant, D.M. and E.G. Paul, *Carbon-13 Magnetic Resonance .2. Chemical Shift Data for Alkanes.* Journal of the American Chemical Society, 1964. **86**(15): p. 2984-+.
149. Paul, E.G. and D.M. Grant, *Additivity Relationships in Carbon-13 Chemical Shift Data for Linear Alkanes.* Journal of the American Chemical Society, 1963. **85**(11): p. 1701-&.
150. Braunschweig, *Constrained geometry complexes—Synthesis and applications* Coordination Chemistry Reviews, 2006. **250**(21-22): p. 29.
151. Chen, Y.X., et al., *A novel phenolate "constrained geometry" catalyst system. Efficient synthesis, structural characterization and alpha-olefin polymerization catalysis.* Organometallics, 1997. **16**(26): p. 5958-5963.
152. Beigzadeh, D., J.B.P. Soares, and A.E. Hamielec, *Recipes for synthesizing polyolefins with tailor-made molecular weight, polydispersity index, long-chain branching frequencies, and chemical composition using combined metallocene catalyst systems in a CSTR at steady state.* Journal of Applied Polymer Science, 1999. **71**(11): p. 1753-1770.
153. Wang, W.-J., et al., *Triple-detector GPC characterization and processing behavior of long-chain-branched polyethylene prepared by solution polymerization with constrained geometry catalyst.* Polymer, 2004. **45**(19): p. 6495-6505.

154. Wang, W.-J., S. Zhu, and S.-J. Park, *Long chain branching in ethylene/propylene solution polymerization using constrained geometry catalyst.* Macromolecules, 2000. **33**(16): p. 5770-5776.
155. Kolodka, E., et al., *Copolymerization of propylene with poly(ethylene-co-propylene) macromonomer and branch chain-length dependence of rheological properties.* Macromolecules, 2002. **35**(27): p. 10062-10070.
156. Beigzadeh, D., J.B.P. Soares, and T.A. Duever, *Effect of cocatalyst on the chain microstructure of polyethylene made with CGC-Ti/MAO/B(C6F5)3.* Journal of Polymer Science, Part A: Polymer Chemistry, 2004. **42**(12): p. 3055-3061.
157. Young, M.J. and C.C.M. Ma, *Polymerization kinetics and modeling of solution PE process with metallocene catalysts.* Journal of Polymer Engineering, 2002. **22**(2): p. 75-93.
158. Chakravarti, S. and W.H. Ray, *Kinetic study of olefin polymerization with a supported metallocene catalyst. III. Ethylene homopolymerization in slurry.* Journal of Applied Polymer Science, 2001. **81**(12): p. 2901-2917.
159. Chakravarti, S. and W.H. Ray, *Kinetic study of olefin polymerization with a supported metallocene catalyst. II. Ethylene/1-hexene copolymerization in gas phase.* Journal of Applied Polymer Science, 2001. **80**(8): p. 1096-1119.
160. Xu, Z.G., S. Chakravarti, and W.H. Ray, *Kinetic study of olefin polymerization with a supported metallocene catalyst. I. Ethylene/propylene copolymerization in gas phase.* Journal of Applied Polymer Science, 2001. **80**(1): p. 81-114.
161. Chien, J.C.W., et al., *Polymerizations of olefins and diolefins catalyzed by monocyclopentadienyltitanium complexes containing a (dimethylamino)ethyl substituent and comparison with ansa-zirconocene systems.* Journal of Polymer Science Part a-Polymer Chemistry, 1998. **36**(2): p. 319-328.
162. Kissin, Y.V., et al., *Kinetics and mechanism of ethylene homopolymerization and copolymerization reactions with heterogeneous Ti-based Ziegler-Natta catalysts.* Topics in Catalysis, 1999. **7**(1-4): p. 69-88.
163. Bergstra, M.F. and G. Weickert, *Ethylene polymerization kinetics with a heterogeneous metallocene catalyst - Comparison of gas and slurry phases.* Macromolecular Materials and Engineering, 2005. **290**(6): p. 610-620.
164. Bohm, L.L., *Homopolymerization and Copolymerization with a Highly-Active Ziegler-Natta Catalyst.* Journal of Applied Polymer Science, 1984. **29**(1): p. 279-289.
165. Shaffer, W.K.A. and W.H. Ray, *Polymerization of olefins through heterogeneous catalysis .18. A kinetic explanation for unusual effects.* Journal of Applied Polymer Science, 1997. **65**(6): p. 1053-1080.
166. Schnauss, A. and K.H. Reichert, *Modeling the Kinetics of Ethylene Polymerization with Ziegler-Natta Catalysts.* Makromolekulare Chemie-Rapid Communications, 1990. **11**(7): p. 315-320.
167. Fischer, D. and R. Mulhaupt, *Reversible and Irreversible Deactivation of Propene Polymerization Using Homogeneous Cp2zrcl2 Methylaluminoxane Ziegler-Natta Catalysts.* Journal of Organometallic Chemistry, 1991. **417**(1-2): p. C7-C11.
168. Jiang, S., et al., *New kinetic model of ethene polymerization with CP2ZrCl2/MAO catalyst.* Macromolecular Theory and Simulations, 2002. **11**(1): p. 77-83.
169. Garcia, R., *Slow crack growth resistance in resin blends of chromium and metallocene catalyzed ethylene-hexene copolymers for pipe applications.* Polymer Engineering and science, 2008. **48**: p. 925-933.

170. Soares, J.B.P. and J.D. Kim, *Copolymerization of ethylene and alpha-olefins with combined metallocene catalysts. I. A formal criterion for molecular weight bimodality.* Journal of Polymer Science Part A: Polymer Chemistry, 2000. **38**(9): p. 1408-1416.
171. Kim, J.D., J.B.P. Soares, and G.L. Rempel, *Synthesis of tailor-made polyethylene through the control of polymerization conditions using selectively combined metallocene catalysts in a supported system.* Journal of Polymer Science Part A: Polymer Chemistry, 1999. **37**(3): p. 331-339.
172. Sperber, O. and W. Kaminsky, *Synthesis of long-chain branched comp-structured polyethylene from ethylene by tandem action of two single-site catalysts.* Macromolecules, 2003. **36**(24): p. 9014-9019.
173. Markel, E.J., et al., *Metallocene-based branch-block thermoplastic elastomers.* Macromolecules, 2000. **33**(23): p. 8541-8548.
174. Choo, T.N. and R.M. Waymouth, *Cyclocopolymerization: A mechanistic probe for dual-site alternating copolymerization of ethylene and alpha-olefins.* Journal of the American Chemical Society, 2002. **124**(16): p. 4188-4189.
175. Pietikainen, P., T. Vaananen, and J.V. Seppala, *Copolymerization of ethylene and non-conjugated dienes with Cp2ZrCl2/MAO catalyst system.* European Polymer Journal, 1999. **35**(6): p. 1047-1055.
176. Pietikainen, P., et al., *Copolymerization of ethylene and non-conjugated dienes with Cp2ZrCl2/MAO catalyst system: effect of polymerization temperature on the copolymer structure.* European Polymer Journal, 2000. **36**(1): p. 183-192.
177. Jin, H.J., et al., *Copolymerization of ethylene/nonconjugated dienes over a bis(2-methyl indenyl) zirconium dichloride/methylaluminoxane catalyst system.* Journal of Applied Polymer Science, 2002. **84**(5): p. 1048-1058.
178. Kim, I., et al., *Copolymerization of ethylene and 1,5-hexadiene by stereospecific metallocenes in the presence of Al(iBU)(3)/[Ph3C][B(C6F5)(4)]*. Polymer, 2001. **42**(23): p. 9393-9403.
179. Naga, N. and A. Toyota, *Unique insertion mode of 1,7-octadiene in copolymerization with ethylene by constrained-geometry catalyst.* Macromolecular Rapid Communications, 2004. **25**(18): p. 1623-1627.
180. Sarzotti, D.M., et al., *Microstructural characterization of molecular weight fractions of ethylene/1,7-octadiene copolymers made with a constrained geometry catalyst.* Macromolecular Materials and Engineering, 2005. **290**(6): p. 584-591.
181. Naga, N. and Y. Imanishi, *Copolymerization of Ethylene and 1,7-Octadiene, 1,9-Decadiene with Zirconocene Catalysts.* Macromolecular Chemistry and Physics, 2002. **203**(15): p. 2155.

APPENDICES

Appendix A

Population Balances and Moment Equations (CSTR 1)

The n^{th} moment, M^n, of a generic distribution $f(x)$ is given by the equation:

$$\mathrm{M}^n = \sum_{x=0}^{\infty} x^n f(x) \tag{A-1}$$

The following convention was adopted for the moments: x_i, x_i^I, x_i^{II} are the zero[th], first and second moments of linear chains; $\bar{x}_i, \bar{x}_i^I, \bar{x}_i^{II}$ are the zero[th], first and second moments of homogeneous-branched chains; $\bar{\bar{x}}_i, \bar{\bar{x}}_i^I, \bar{\bar{x}}_i^{II}$ are the zero[th], first and second moments of cross-product chains; the subscript i indicates catalyst type; moments of living polymer chains are represented by Y, of macromonomers by Θ, and of dead polymers by Q.

Living Chains

The population balance for linear living chains with length larger than 2, $r \geq 2$, is given by

$$\begin{aligned}\frac{\mathrm{d}P_{i,r}}{\mathrm{d}t} &= k_{p,i}M(P_{i,r-1} - P_{i,r}) - (k_{\beta,i} + k_{\beta-CH_3,i} + k_{Al,i}Al + k_{H,i}H_2 + k_{M,i}M)P_{i,r} - k_{d,i}P_{i,r} \\ &\quad - k_{b,i}P_{i,r}\sum_{s=2}^{\infty}(\mu_{i,s} + \mu_{j,s} + \bar{\mu}_{i,s} + \bar{\mu}_{j,s} + \bar{\bar{\mu}}_s) - sP_{i,r}\end{aligned} \tag{A-2}$$

where s is the reciprocal of the average residence time in the CSTR .

This equation will be used in a more compact form as

$$\frac{\mathrm{d}P_{i,r}}{\mathrm{d}t} = k_{p,i}M(P_{i,r-1} - P_{i,r}) - (\sigma_i + k_{b,i}\tilde{\Theta})P_{i,r} \tag{A-3}$$

where the following lumped parameters were defined

$$\sigma_i = K_{t,i} + k_{d,i} + s \tag{A-4}$$

$$K_{t,i} = K_{t.i}^{=} + K_{t.i}^{s} \tag{A-5}$$

$$K_{t,i}^{=} = k_{\beta,i} + k_{M,i}M + k_{\beta-CH_3,i} \tag{A-6}$$

$$K_{t,i}^{s} = k_{Al,i}Al + k_{H,i}H_2 \tag{A-7}$$

$$\tilde{\Theta} = \sum_{r=2}^{\infty}(\mu_{i,r} + \mu_{j,r} + \bar{\mu}_{i,r} + \bar{\mu}_{j,r} + \bar{\bar{\mu}}_r) \tag{A-8}$$

A slightly different equation is required for chains of unity length, $r = 1$

$$\frac{dP_{i,1}}{dt} = k_{p,i}M(C_i - P_{i,1}) - (\sigma_i + k_{b,i}\tilde{\Theta})P_{i,1} + \sum_{r=1}^{\infty}(P_{i,r} + \bar{P}_{i,r} + \bar{\bar{P}}_{i,r})k_{M,i}M \tag{A-9}$$

$$\frac{dP_{i,1}}{dt} = k_{p,i}M(C_i - P_{i,1}) - (\sigma_i + k_{b,i}\tilde{\Theta})P_{i,1} + k_{M,i}M\tilde{Y}_i \tag{A-10}$$

where

$$\tilde{Y}_i = \sum_{r=1}^{\infty}P_{i,r} + \sum_{r=2}^{\infty}\bar{P}_{i,r} + \sum_{r=2}^{\infty}\bar{\bar{P}}_{i,r} \tag{A-11}$$

The dynamic equation for the zero[th] moment of linear living polymer made on catalyst *i* is

$$\frac{dY_i}{dt} = \frac{dP_{i,1}}{dt} + \sum_{r=2}^{\infty}\frac{dP_{i,r}}{dt} \tag{A-12}$$

Substituting Equations (A-3) and (A-10) into Equation (A-12) and simplifying the resulting expression, we obtain the equation for the zero[th] moment of linear living chains

$$\frac{dY_i}{dt} = k_{p,i}C_iM - (\sigma_i + k_{b,i}\tilde{\Theta})\,Y_i + k_{M,i}M\tilde{Y}_i \tag{A-13}$$

The equation for the first moment is

$$Y_i^I = \sum_{r=1}^{\infty}rP_{i,r} \tag{A-14}$$

Differentiating Equation (4A-14) yields

$$\frac{\mathrm{d}Y_i^I}{\mathrm{d}t} = \frac{\mathrm{d}P_{i,1}}{\mathrm{d}t} + \sum_{r=2}^{\infty} r \frac{\mathrm{d}P_{i,r}}{\mathrm{d}t} \tag{A-15}$$

Substituting Equations (A-3) and (A-10) into Equation (A-15)

$$\begin{aligned}\frac{\mathrm{d}Y_i^I}{\mathrm{d}t} &= k_{p,i}(C_i - P_{i,1})M - (\sigma_i + k_{b,i}\widetilde{\Theta})P_{i,1} \\ &+ \sum_{r=2}^{\infty} r[k_{p,i}(P_{i,r-1} - P_{i,r})M - (\sigma_i + k_{b,i}\widetilde{\Theta})P_{i,r}] + k_{M,i}M\widetilde{Y}_i\end{aligned} \tag{A-16}$$

Simplifying Equation (A-16), leads to the first moment equation for the linear living chains

$$\frac{\mathrm{d}Y_i^I}{\mathrm{d}t} = k_{p,i}M(C_i + Y_i) - (\sigma_i + k_{b,i}\widetilde{\Theta})Y_i^I + k_{M,i}M\widetilde{Y}_i \tag{A-17}$$

Finally, for the second moment

$$\frac{\mathrm{d}Y_i^{II}}{\mathrm{d}t} = \frac{\mathrm{d}P_{i,1}}{\mathrm{d}t} + \sum_{r=2}^{\infty} r^2 \frac{\mathrm{d}P_{i,r}}{\mathrm{d}t} \tag{A-18}$$

Substituting Equations (A-3) and (A-10) into Equation (A-18) we get

$$\begin{aligned}\frac{\mathrm{d}Y_i^{II}}{\mathrm{d}t} &= k_{p,i}(C_i - P_{i,1})M - (\sigma_i + k_{b,i}\widetilde{\Theta})P_{i,1} + k_{M,i}M\widetilde{Y} + \\ &\sum_{r=2}^{\infty} r^2[k_{p,i}(P_{i,r-1} - P_{i,r})M - (\sigma_i + k_{b,i}\widetilde{\Theta})P_{i,r}]\end{aligned} \tag{A-19}$$

After some algebraic manipulation, the following equation for the second moment of linear living polymer is obtained

$$\frac{\mathrm{d}Y_i^{II}}{\mathrm{d}t} = k_{p,i}C_iM - (\sigma_i + k_{b,i}\widetilde{\Theta})Y_i^{II} + k_{p,i}(Y_i + 2Y_i^I)M + k_{M,i}M\widetilde{Y}_i \tag{A-20}$$

We will consider only chains with $r \geq 2$ as branched chains, since chains with $r = 1$ must necessarily be linear. This is just a convention and does not affect the final calculation results for long chains, but it simplifies the next derivation steps.

The population balance for homogenous-branched living chains is

$$\frac{\mathrm{d}\overline{P}_{i,r}}{\mathrm{d}t} = k_{p,i}M(\overline{P}_{i,r-1} - \overline{P}_{i,r}) - (\sigma_i + k_{b,i}\widetilde{\Theta})\overline{P}_{i,r} + k_{b,i}\sum_{s=2}^{r-1}\overline{P}_{i,r-s}(\mu_{i,s} + \overline{\mu}_{i,s}) + k_{b,i}\sum_{s=2}^{r-1}P_{i,r-s}(\mu_{i,s} + \overline{\mu}_{i,s}) \tag{A-21}$$

The equation for the zero[th] moment is obtained by substituting Equation (A-21) into Equation (A-12) and ignoring the first term on the right-hand side for $r = 1$

$$\frac{\mathrm{d}\overline{Y}_i}{\mathrm{d}t} = k_{p,i}M\left(\sum_{r=2}^{\infty}\overline{P}_{i,r-1} - \sum_{r=2}^{\infty}\overline{P}_{i,r}\right) - (\sigma_i + k_{b,i}\widetilde{\Theta})\sum_{r=2}^{\infty}\overline{P}_{i,r} + k_{b,i}\sum_{r=2}^{\infty}\sum_{s=2}^{r-1}\overline{P}_{i,r-s}(\mu_{i,s} + \overline{\mu}_{i,s}) + k_{b,i}\sum_{r=2}^{\infty}\sum_{s=2}^{r-1}P_{i,r-s}(\mu_{i,s} + \overline{\mu}_{i,s}) \tag{A-22}$$

This expression can be simplified to obtain the final equation for the zero[th] moment of homogeneous-branched living chains

$$\frac{\mathrm{d}\overline{Y}_i}{\mathrm{d}t} = k_{b,i}Y_i(\Theta_i + \overline{\Theta}_i) - [\sigma_i + k_{b,i}(\Theta_j + \overline{\Theta}_j + \overline{\overline{\Theta}})]\ \overline{Y}_i \tag{A-23}$$

The equation for the first moment is obtained by substituting Equation (A-21) into Equation (A-15), summing from $r = 2$ to ∞, and using the identities

$$\sum_{r=2}^{\infty} r\overline{P}_{i,r-1} - \sum_{r=2}^{\infty} r\overline{P}_{i,r} = \overline{Y}_i \tag{A-24}$$

$$\sum_{r=2}^{\infty}\sum_{s=1}^{r-1} rP_{r-s}D_s = Y\ Q^I + Y^I Q \tag{A-25}$$

Finally, the equation for the first moment of homogeneous-branched living chains is

$$\frac{\mathrm{d}\overline{Y}_i^I}{\mathrm{d}t} = k_{p,i}M\overline{Y}_i + k_{b,i}[(Y_i + \overline{Y}_i)(\Theta_i^I + \overline{\Theta}_i^I) + Y_i^I(\Theta_i + \overline{\Theta}_i)] - [\sigma_i + k_{b,i}(\Theta_j + \overline{\Theta}_j + \overline{\overline{\Theta}})]\overline{Y}_i^I \tag{A-26}$$

The equation for the second moment is obtained by substituting Equation (A-21) into Equation (A-18) and using the following expressions

$$\sum_{r=2}^{\infty} r^2 \overline{P}_{i,r-1} - \sum_{r=2}^{\infty} r^2 \overline{P}_{i,r} = \overline{Y}_i + 2\overline{Y}_i^I \tag{A-27}$$

$$\sum_{r=2}^{\infty} \sum_{s=1}^{r-1} r^2 P_{r-s} D_s = Y\ Q^{II} + 2Y^I Q^I + Y^{II} Q \tag{A-28}$$

Finally, the equation for the second moment of homogeneous-branched living chains becomes

$$\begin{aligned} \frac{\mathrm{d}\overline{Y}_i^{II}}{\mathrm{d}t} &= k_{p,i} M (\overline{Y}_i + 2\overline{Y}_i^I) - [\sigma_i + k_{b,i}(\Theta_j + \overline{\Theta}_j + \overline{\overline{\Theta}})]\overline{Y}_i^{II} \\ &\quad + k_{b,i}[(\overline{Y}_i + Y_i)(\Theta_i^{II} + \overline{\Theta}_i^{II}) + 2(\overline{Y}_i^I + Y_i^I)(\Theta_i^I + \overline{\Theta}_i^I) + Y_i^{II}(\Theta_i + \overline{\Theta}_i)] \end{aligned} \tag{A-29}$$

For cross-product chains, we will also adopt the convention that $r > 2$ during all derivations.

The population balance for cross-product chains is

$$\begin{aligned} \frac{\mathrm{d}\overline{\overline{P}}_{i,r}}{\mathrm{d}t} &= k_{p,i} M (\overline{\overline{P}}_{i,r-1} - \overline{\overline{P}}_{i,r}) - (\sigma_i + k_{b,i}\tilde{\Theta})\overline{\overline{P}}_{i,r} \\ &\quad + k_{b,i} \sum_{s=2}^{r-1} \begin{bmatrix} \overline{\overline{P}}_{i,r-s}(\mu_{i,s} + \mu_{j,s} + \overline{\mu}_{i,s} + \overline{\mu}_{j,s} + \overline{\overline{\mu}}_s) + \\ (\overline{P}_{i,r-s} + P_{i,r-s})(\mu_{j,s} + \overline{\mu}_{j,s} + \overline{\overline{\mu}}_s) \end{bmatrix} \end{aligned} \tag{A-30}$$

The equation for the zero[th] moment is obtained by substituting Equation (A-30) into Equation (A-12)

$$\begin{aligned} \frac{\mathrm{d}\overline{\overline{Y}}_i}{\mathrm{d}t} &= k_{p,i} M \left(\sum_{r=2}^{\infty} \overline{\overline{P}}_{i,r-1} - \sum_{r=2}^{\infty} \overline{\overline{P}}_{i,r} \right) - (\sigma_i + k_{b,i}\tilde{\Theta}) \sum_{r=2}^{\infty} \overline{\overline{P}}_{i,r} \\ &\quad + k_{b,i} \sum_{r=2}^{\infty} \sum_{s=2}^{r-1} \begin{bmatrix} \overline{\overline{P}}_{i,r-s}(\mu_{i,s} + \mu_{j,s} + \overline{\mu}_{i,s} + \overline{\mu}_{j,s} + \overline{\overline{\mu}}_s) + \\ (\overline{P}_{i,r-s} + P_{i,r-s})(\mu_{j,s} + \overline{\mu}_{j,s} + \overline{\overline{\mu}}_s) \end{bmatrix} \end{aligned} \tag{A-31}$$

This expression can be reduced to the more convenient form

$$\begin{aligned} \frac{\mathrm{d}\overline{\overline{Y}}_i}{\mathrm{d}t} &= k_{p,i} M (\overline{\overline{Y}}_i - \overline{\overline{Y}}_i) - (\sigma_i + k_{b,i}\tilde{\Theta})\overline{\overline{Y}}_i \\ &\quad + k_{b,i} \begin{bmatrix} \sum_{r=2}^{\infty} \overline{\overline{P}}_{i,r} \sum_{s=2}^{\infty} (\mu_{i,s} + \mu_{j,s} + \overline{\mu}_{i,s} + \overline{\mu}_{j,s} + \overline{\overline{\mu}}_s) + \\ \sum_{r=2}^{\infty} (\overline{P}_{i,r} + P_{i,r}) \sum_{s=2}^{\infty} (\mu_{j,s} + \overline{\mu}_{j,s} + \overline{\overline{\mu}}_s) \end{bmatrix} \end{aligned} \tag{A-32}$$

or

$$\frac{\mathrm{d}\overline{\overline{Y}}_i}{\mathrm{d}t} = k_{b,i}(\overline{Y}_i + Y_i)(\Theta_j + \overline{\Theta}_j + \overline{\overline{\Theta}}) - \sigma_i \overline{\overline{Y}}_i \tag{A-33}$$

The equation for the first moment is calculated by substituting Equation (A-30) into Equation (A-15) and simplifying the resulting equation using Equations (A-24) and (A-25)

$$\frac{\mathrm{d}\overline{\overline{Y}}_i^I}{\mathrm{d}t} = k_{p,i} M \overline{\overline{Y}}_i - \sigma_i \overline{\overline{Y}}_i^I + k_{b,i} \begin{bmatrix} \overline{\overline{Y}}_i (\Theta_i^I + \Theta_j^I + \overline{\Theta}_i^I + \overline{\Theta}_j^I + \overline{\overline{\Theta}}^I) \\ + (\overline{Y}_i + Y_i)(\Theta_j^I + \overline{\Theta}_j^I + \overline{\overline{\Theta}}^I) \\ + (\overline{Y}_i^I + Y_i^I)(\Theta_j + \overline{\Theta}_j + \overline{\overline{\Theta}}) \end{bmatrix} \tag{A-34}$$

The equation for the second moment is derived by substituting Equation (A-30) into Equation (A-18) and then applying Equations (A-24) and (A-25) to simplify the result

$$\begin{aligned} \frac{\mathrm{d}\overline{\overline{Y}}_i^{II}}{\mathrm{d}t} &= k_{p,i} M (\overline{\overline{Y}}_i + 2\overline{\overline{Y}}_i^I) - \sigma_i \overline{\overline{Y}}_i^{II} \\ &+ k_{b,i} \begin{bmatrix} \overline{\overline{Y}}_i (\Theta_i^{II} + \Theta_j^{II} + \overline{\Theta}_i^{II} + \overline{\Theta}_j^{II} + \overline{\overline{\Theta}}^{II}) + 2\overline{\overline{Y}}_i^I (\Theta_i^I + \Theta_j^I + \overline{\Theta}_i^I + \overline{\Theta}_j^I + \overline{\overline{\Theta}}^I) \\ + (\overline{Y}_i + Y_i)(\Theta_j^{II} + \overline{\Theta}_j^{II} + \overline{\overline{\Theta}}^{II}) + 2(\overline{Y}_i^I + Y_i^I)(\Theta_j^I + \overline{\Theta}_j^I + \overline{\overline{\Theta}}^I) \\ + (\overline{Y}_i^{II} + Y_i^{II})(\Theta_j + \overline{\Theta}_j + \overline{\overline{\Theta}}) \end{bmatrix} \end{aligned} \tag{A-35}$$

Macromonomers

The population balance for linear macromonomers is given by

$$\frac{\mathrm{d}\mu_{i,r}}{\mathrm{d}t} = K_{t,i}^{=} P_{i,r} - k_{b,i}(Y_i + \overline{Y}_i + \overline{\overline{Y}}_i)\mu_{i,r} - k_{b,j}(Y_j + \overline{Y}_j + \overline{\overline{Y}}_j)\mu_{i,r} - s\mu_{i,r} \tag{A-36}$$

Defining $\tilde{\tilde{Y}}_i$ as the zero[th] moment of the population of all living chains growing on catalyst type *i*

$$\tilde{\tilde{Y}}_i = Y_i + \overline{Y}_i + \overline{\overline{Y}}_i \tag{A-37}$$

leads to a more compact representation of the population balance of linear macromonomers

$$\frac{\mathrm{d}\mu_{i,r}}{\mathrm{d}t} = K_{t,i}^{=} P_{i,r} - (k_{b,i}\tilde{Y}_i + k_{b,j}\tilde{Y}_j + s)\,\mu_{i,r} \tag{A-38}$$

Substitution of Equation (A-38) into Equation (A-12) leads to the expression for the zero[th] moment of linear macromonomers

$$\frac{\mathrm{d}\Theta_i}{\mathrm{d}t} = K_{t,i}^{=} Y_i - (k_{b,i}\tilde{Y}_i + k_{b,j}\tilde{Y}_j + s)\,\Theta_i \tag{A-39}$$

Similarly, substitution of Equation (A-38) into Equation (A-15) results in the expression for the first moment

$$\frac{\mathrm{d}\Theta_i^I}{\mathrm{d}t} = K_{t,i}^{=} Y_i^I - (k_{b,i}\tilde{Y}_i + k_{b,j}\tilde{Y}_j + s)\,\Theta_i^I \tag{A-40}$$

Finally, combining Equations (A-38) and (A-18) leads to the expression for the second moment

$$\frac{\mathrm{d}\Theta_i^{II}}{\mathrm{d}t} = K_{t,i}^{=} Y_i^{II} - (k_{b,i}\tilde{Y} + k_{b,j}\tilde{Y}_j + s)\,\Theta_i^{II} \tag{A-41}$$

The population balance for homogeneous-branched macromonomers is

$$\frac{\mathrm{d}\overline{\mu}_{i,r}}{\mathrm{d}t} = K_{t,i}^{=} \overline{P}_{i,r} - (k_{b,i}\tilde{Y}_i + k_{b,j}\tilde{Y}_j + s)\overline{\mu}_{i,r} \tag{A-42}$$

Substituting Equation (A-42) into Equations (A-12), (A-15) and (A-18) leads to the expressions for the zero[th], first and second moments of homogeneous-branched macromonomers

$$\frac{\mathrm{d}\overline{\Theta}_i}{\mathrm{d}t} = K_{t,i}^{=} \overline{Y}_i - (k_{b,i}\tilde{Y}_i + k_{b,j}\tilde{Y}_j + s)\,\overline{\Theta}_i \tag{A-43}$$

$$\frac{\mathrm{d}\overline{\Theta}_i^I}{\mathrm{d}t} = K_{t,i}^{=} \overline{Y}_i^I - (k_{b,i}\tilde{Y}_i + k_{b,j}\tilde{Y}_j + s)\,\overline{\Theta}_i^I \tag{A-44}$$

$$\frac{\mathrm{d}\overline{\Theta}_i^{II}}{\mathrm{d}t} = K_{t,i}^{=} \overline{Y}_i^{II} - (k_{b,i}\tilde{Y}_i + k_{b,j}\tilde{Y}_j + s)\,\overline{\Theta}_i^{II} \tag{A-45}$$

Similarly, the population balance for cross-product macromonomers is

$$\frac{\mathrm{d}\overline{\overline{\mu}}_r}{\mathrm{d}t} = \overline{K}_{t,i}\overline{\overline{P}}_{i,r} + \overline{K}_{t,j}\overline{\overline{P}}_{j,r} - (k_{b,i}\tilde{Y}_i + k_{b,j}\tilde{Y}_j + s)\overline{\overline{\mu}}_r \tag{A-46}$$

Consequently, the equations for the zero[th], first, and second moments are

$$\frac{\mathrm{d}\overline{\overline{\Theta}}}{\mathrm{d}t} = \overline{K}_{t,i}\overline{\overline{Y}}_i + \overline{K}_{t,j}\overline{\overline{Y}}_j - (k_{b,i}\tilde{Y}_i + k_{b,j}\tilde{Y}_j + s)\overline{\overline{\Theta}} \tag{A-47}$$

$$\frac{\mathrm{d}\overline{\overline{\Theta}}^{I}}{\mathrm{d}t} = \overline{K}_{t,i}\overline{\overline{Y}}_i^{I} + \overline{K}_{t,j}\overline{\overline{Y}}_j^{I} - (k_{b,i}\tilde{Y}_i + k_{b,j}\tilde{Y}_j + s)\overline{\overline{\Theta}}^{I} \tag{A-48}$$

$$\frac{\mathrm{d}\overline{\overline{\Theta}}^{II}}{\mathrm{d}t} = \overline{K}_{t,i}\overline{\overline{Y}}_i^{II} + \overline{K}_{t,j}\overline{\overline{Y}}_j^{II} - (k_{b,i}\tilde{Y}_i + k_{b,j}\tilde{Y}_j + s)\overline{\overline{\Theta}}^{II} \tag{A-49}$$

Dead Chains

The derivation of population balance and moment equations for dead polymers follows the same approach used for the macromonomers. Only the final equations will be shown below.

$$\frac{\mathrm{d}D_{i,r}}{\mathrm{d}t} = (K_{t,i}^{s} + k_{d,i})P_{i,r} - sD_{i,r} \tag{A-50}$$

$$\frac{\mathrm{d}Q_i}{\mathrm{d}t} = (K_{t,i}^{s} + k_{d,i})Y_i - sQ_i \tag{A-51}$$

$$\frac{\mathrm{d}Q_i^{I}}{\mathrm{d}t} = (K_{t,i}^{s} + k_{d,i})Y_i^{I} - sQ_i^{I} \tag{A-52}$$

$$\frac{\mathrm{d}Q_i^{II}}{\mathrm{d}t} = (K_{t,i}^{s} + k_{d,i})Y_i^{II} - sQ_i^{II} \tag{A-53}$$

$$\frac{\mathrm{d}\overline{D}_{i,r}}{\mathrm{d}t} = (K_{t,i}^{s} + k_{d,i})\overline{P}_{i,r} - s\overline{D}_{i,r} \tag{A-54}$$

$$\frac{\mathrm{d}\overline{Q}_i}{\mathrm{d}t} = (K_{t,i}^{s} + k_{d,i})\overline{Y}_i - s\overline{Q}_i \tag{A-55}$$

$$\frac{\mathrm{d}\overline{Q}_i^I}{\mathrm{d}t} = (K_{t,i}^s + k_{d,i})\,\overline{Y}_i^I - s\overline{Q}_i^I \tag{A-56}$$

$$\frac{\mathrm{d}\overline{Q}_i^{II}}{\mathrm{d}t} = (K_{t,i}^s + k_{d,i})\,\overline{Y}_i^{II} - s\overline{Q}_i^{II} \tag{A-57}$$

$$\frac{\mathrm{d}\overline{\overline{D}}_r}{\mathrm{d}t} = (K_{t,i}^s + k_{d,i})\,\overline{\overline{P}}_{i,r} + (K_{t,j}^s + k_{d,j})\,\overline{\overline{P}}_{j,r} - s\overline{\overline{D}}_{i,r} \tag{A-58}$$

$$\frac{\mathrm{d}\overline{\overline{Q}}}{\mathrm{d}t} = (K_{t,i}^s + k_{d,i})\,\overline{\overline{Y}}_i + (K_{t,j}^s + k_{d,j})\,\overline{\overline{Y}}_j - s\overline{\overline{Q}} \tag{A-59}$$

$$\frac{\mathrm{d}\overline{\overline{Q}}^I}{\mathrm{d}t} = (K_{t,i}^s + k_{d,i})\,\overline{\overline{Y}}_i^I + (K_{t,j}^s + k_{d,j})\,\overline{\overline{Y}}_j^I - s\overline{\overline{Q}}^I \tag{A-60}$$

$$\frac{\mathrm{d}\overline{\overline{Q}}^{II}}{\mathrm{d}t} = (K_{t,i}^s + k_{d,i})\,\overline{\overline{Y}}_i^{II} + (K_{t,j}^s + k_{d,j})\,\overline{\overline{Y}}_j^{II} - s\overline{\overline{Q}}^{II} \tag{A-61}$$

Appendix B

Steady-State Solution of the Moment Equations (CSTR 1)

The steady-state solution for the moment equations is obtained, as usual, by setting the time derivatives in the right-hand side of the moment equations derived in Appendix A to zero and solving for the unknown moments.

Zeroth Moments

The equation for the zeroth moment of all living chains growing on catalyst type *i* is given by the expression

$$\frac{\mathrm{d}\tilde{Y}_i}{\mathrm{d}t} = k_{p,i}C_iM - (K_{t,i} + k_{d,i})\tilde{Y}_i + k_{M,i}M\tilde{Y} = k_{p,i}C_iM - \sigma_i\tilde{Y}_i + k_{M,i}M\tilde{Y}_i \tag{B-1}$$

At steady state

$$k_{p,i}C_iM - \sigma_i\tilde{Y}_i + k_{M,i}M\tilde{Y}_i = 0 \tag{B-2}$$

$$\tilde{Y}_i = \frac{k_{p,i}C_iM}{\sigma_i - k_{M,i}M} \tag{B-3}$$

The molar balance for catalytic active sites of type *i* is given by

$$\frac{\mathrm{d}C_i}{\mathrm{d}t} = (k_{\beta,i} + K^s_{t.i})\tilde{Y}_i - (k_{p,i}M + k_{d,i} + s)\,C_i + C_i^{in} \tag{B-4}$$

or

$$\frac{\mathrm{d}C_i}{\mathrm{d}t} = (k_{\beta,i} + K^s_{t.i})(Y_i + \bar{Y}_i + \bar{\bar{Y}}_i) - (k_{p,i}M + k_{d,i} + s)\,C_i + C_i^{in} \tag{B-5}$$

where C_i^{in} is molar flow rate of catalyst per unit volume to the reactor. Using Equation (B-3) to eliminate $\tilde{Y}_i$ from Equation (B-4) and solving for C_i

$$C_i = \frac{C_i^{in}}{\{1-(k_{\beta,i} + K^s_{t.i})/(\sigma_i - k_{M,i}[M])\}k_{p,i}M + k_{d,i} + s} \tag{B-6}$$

where the parameter α_i is defined as

$$\alpha_i = \frac{K_{t,i}}{\sigma_i} \tag{B-7}$$

The concentration of all macromonomer chains ($\tilde{\Theta}$) can be calculated with the equation

$$\tilde{\Theta} = \Theta_i + \Theta_j + \bar{\Theta}_i + \bar{\Theta}_j + \bar{\bar{\Theta}} \tag{B-8}$$

Taking derivatives of both sides of Equation (B-8) substituting Equations (A-39), (A-44), and (A-47), leads to the following equation for the steady-state zero[th] moment of all macromonomers in the reactor

$$\frac{\mathrm{d}\tilde{\Theta}}{\mathrm{d}t} = K_{t,i}^{=}\tilde{Y}_i + K_{t,j}^{=}\tilde{Y}_j - k_{b,i}\tilde{Y}_i\tilde{\Theta} - k_{b,j}\tilde{Y}_j\tilde{\Theta} - s\tilde{\Theta} = 0 \tag{B-9}$$

$$\tilde{\Theta} = \frac{K_{t,i}^{=}\tilde{Y}_i + K_{t,j}^{=}\tilde{Y}_j}{k_{b,i}\tilde{Y}_i + k_{b,j}\tilde{Y}_j + s} \tag{B-10}$$

Assuming that the concentrations of monomer (*M*), hydrogen (H_2), and cocatalyst (*Al*), are known, $\tilde{Y}_i$, C_i, and $\tilde{\Theta}$ can be calculated with Equations (B-3), (B-6) and (B-10), respectively. The values for Y_i and Θ_i are also easily found from the steady-state solutions of Equations (A-13) and (A-37), respectively

$$Y_i = \frac{k_{p,i}C_iM + k_{M,i}M\tilde{Y}_i}{k_{b,i}\tilde{\Theta} + \sigma_i} \tag{B-11}$$

$$\Theta_i = \frac{K_{t,i}^{=}Y_i}{k_{b,i}\tilde{Y}_i + k_{b,j}\tilde{Y}_j + s} \tag{B-12}$$

The steady-state equations for the zero[th] moments of branched living chains and macromonomers have to be solved simultaneously. We used a simple Gauss-Seidel iteration approach with first estimate $\bar{\Theta}_i = \bar{\bar{\Theta}} = 0$ to calculate $\bar{Y}_i$ and $\bar{\bar{Y}}_i$. These values were used to re-estimate $\bar{\Theta}_i$ and $\bar{\bar{\Theta}}$, and the iterations were repeated until convergence was achieved using the following equations

$$\overline{Y}_i = \frac{k_{b,i} Y_i (\Theta_i + \overline{\Theta}_i)}{k_{b,i}(\Theta_j + \overline{\Theta}_j + \overline{\overline{\Theta}}) + \sigma_i} \tag{B-13}$$

$$\overline{\overline{Y}}_i = \frac{k_{b,i}(Y_i + \overline{Y}_i)(\Theta_j + \overline{\Theta}_j + \overline{\overline{\Theta}})}{\sigma_i} \tag{B-14}$$

$$\overline{\Theta}_i = \frac{K_{t,i}^{=} \overline{Y}_i}{k_{b,i}\tilde{Y}_i + k_{b,j}\tilde{Y}_j + s} \tag{B-15}$$

$$\overline{\overline{\Theta}} = \frac{K_{t,i}^{=} \overline{\overline{Y}}_i + K_{t,j}^{=} \overline{\overline{Y}}_j}{k_{b,i}\tilde{Y}_i + k_{b,j}\tilde{Y}_j + s} \tag{B-16}$$

Finally, the zero[th] moment equations for the dead polymer chains can be solved sequentially

$$Q_i = \frac{(K_{t,i}^{s} + k_{d,i})\, Y_i}{s} \tag{B-17}$$

$$\overline{Q}_i = \frac{(K_{t,i}^{s} + k_{d,i})\, \overline{Y}_i}{s} \tag{B-18}$$

$$\overline{\overline{Q}} = \frac{(K_{t,i}^{s} + k_{d,i})\, \overline{\overline{Y}}_i + (K_{t,j}^{s} + k_{d,j})\, \overline{\overline{Y}}_j}{s} \tag{B-19}$$

First Moments

The steady state equations for the first moments can be solved sequentially after the solution for the zero[th] moments. After some algebraic manipulation, the following solutions are derived

$$Y_i^I = \frac{k_{p,i} M (C_i + Y_i) + k_{M,i} M \tilde{Y}_i}{\sigma_i + k_{b,i}\tilde{\Theta}} \tag{B-21}$$

$$\overline{Y}_i^I = \frac{\{k_{p,i} M \overline{Y}_i + k_{b,i}[(Y_i + \overline{Y}_i)\Theta_i^I + Y_i^I(\Theta_i + \overline{\Theta}_i)]\}(k_{b,i}\tilde{Y}_i + k_{b,j}\tilde{Y}_j + s)}{[\sigma_i + k_{b,i}(\Theta_j + \overline{\Theta}_j + \overline{\overline{\Theta}})](k_{b,i}\tilde{Y}_i + k_{b,j}\tilde{Y}_j + s) - k_{b,i}(Y_i + \overline{Y}_i)K_{t,i}^{=}} \tag{B-22}$$

$$\overline{\overline{Y}}_i^I = \frac{1}{\sigma_i}\left\{ k_{p,i} M \overline{\overline{Y}}_i + k_{b,i} \begin{bmatrix} \overline{\overline{Y}}_i (\Theta_i^I + \Theta_j^I + \overline{\Theta}_i^I + \overline{\Theta}_j^I + \overline{\overline{\Theta}}^I) \\ + (\overline{Y}_i + Y_i)(\Theta_j^I + \overline{\Theta}_j^I + \overline{\overline{\Theta}}^I) \\ + (\overline{Y}_i^I + Y_i^I)(\Theta_j + \overline{\Theta}_j + \overline{\overline{\Theta}}) \end{bmatrix} \right\} \tag{B-23}$$

$$\Theta_i^I = \frac{K_{t,i}^{=} Y_i^I}{k_{b,i}\tilde{\tilde{Y}}_i + k_{b,j}\tilde{\tilde{Y}}_j + s} \tag{B-24}$$

$$\overline{\Theta}_i^I = \frac{K_{t,i}^{=} \overline{Y}_i^I}{k_{b,i}\tilde{\tilde{Y}}_i + k_{b,j}\tilde{\tilde{Y}}_j + s} \tag{B-25}$$

$$\overline{\overline{\Theta}}^I = \frac{\begin{array}{l} a_i \left\{ k_{p,i} M \overline{\overline{Y}}_i + k_{b,i} \begin{bmatrix} \overline{\overline{Y}}_i (\Theta_i^I + \Theta_j^I + \overline{\Theta}_i^I + \overline{\Theta}_j^I) + (\overline{Y}_i + Y_i)(\Theta_j^I + \overline{\Theta}_j^I) \\ + (\overline{Y}_i^I + Y_i^I)(\Theta_j + \overline{\Theta}_j + \overline{\overline{\Theta}}) \end{bmatrix} \right\} + \\ a_j \left\{ k_{p,j} M \overline{\overline{Y}}_j + k_{b,j} \begin{bmatrix} \overline{\overline{Y}}_j (\Theta_i^I + \Theta_j^I + \overline{\Theta}_i^I + \overline{\Theta}_j^I) + (\overline{Y}_j + Y_j)(\Theta_i^I + \overline{\Theta}_i^I) \\ + (\overline{Y}_j^I + Y_j^I)(\Theta_i + \overline{\Theta}_i + \overline{\overline{\Theta}}) \end{bmatrix} \right\} \end{array}}{1 - a_i k_{b,i}\tilde{\tilde{Y}}_i - a_j k_{b,j}\tilde{\tilde{Y}}_j} \tag{B-26}$$

$$Q_i^I = \frac{(K_{t,i}^s + k_{d,i}) Y_i^I}{s} \tag{B-27}$$

$$\overline{Q}_i^I = \frac{(K_{t,i}^s + k_{d,i}) \overline{Y}_i^I}{s} \tag{B-28}$$

$$\overline{\overline{Q}}^I = \frac{(K_{t,i}^s + k_{d,i}) \overline{\overline{Y}}_i^I + (K_{t,j}^s + k_{d,j}) \overline{\overline{Y}}_j^I}{s} \tag{B-29}$$

where

$$a_i = \frac{A_i}{\sigma_i} \tag{B-30}$$

Second Moments

The steady state equations for the second moments can be solved sequentially after the solution for the zero[th] and first moments with the following expressions

$$Y_i^{II} = \frac{k_{p,i}M\left(Y_i + 2Y_i^I + C_i\right) + k_{M,i}M\tilde{Y}_i}{\sigma_i + k_{b,i}\tilde{\Theta}} \tag{B-31}$$

$$\bar{Y}_i^{II} = \frac{\begin{array}{l}\{k_{p,i}M(\bar{Y}_i + 2\bar{Y}_i^I) + k_{b,i}[(\bar{Y}_i + Y_i)\Theta_i^{II} + 2(Y_i^I + \bar{Y}_i^I)(\Theta_i^I + \bar{\Theta}_i^I) \\ + Y_i^{II}(\Theta_i + \bar{\Theta}_i)]\} \times (k_{b,i}\tilde{Y}_i + k_{b,j}\tilde{Y}_j + s)\end{array}}{[\sigma_i + k_{b,i}(\Theta_j + \bar{\Theta}_j + \bar{\bar{\Theta}})](k_{b,i}\tilde{Y}_i + k_{b,j}\tilde{Y}_j + s) - k_{b,i}(\bar{Y}_i + Y_i)K_{t,i}^{=}} \tag{B-32}$$

$$\bar{\bar{Y}}_i^{II} = \frac{k_{p,i}}{\sigma_i}M(\bar{\bar{Y}}_i + 2\bar{\bar{Y}}_i^I) + \frac{k_{b,i}}{\sigma_i}\begin{bmatrix}\bar{\bar{Y}}_i(\Theta_i^{II} + \Theta_j^{II} + \bar{\Theta}_i^{II} + \bar{\Theta}_j^{II} + \bar{\bar{\Theta}}^{II}) \\ + 2\bar{\bar{Y}}_i^I(\Theta_i^I + \Theta_j^I + \bar{\Theta}_i^I + \bar{\Theta}_j^I + \bar{\bar{\Theta}}^I) + \\ (\bar{Y}_i + Y_i)(\Theta_j^{II} + \bar{\Theta}_j^{II} + \bar{\bar{\Theta}}^{II}) \\ + 2(\bar{Y}_i^I + Y_i^I)(\Theta_j^I + \bar{\Theta}_j^I + \bar{\bar{\Theta}}^I) + \\ (\bar{Y}_i^{II} + Y_i^{II})(\Theta_j + \bar{\Theta}_j + \bar{\bar{\Theta}})\end{bmatrix} \tag{B-33}$$

$$\Theta_i^{II} = \frac{K_{t,i}^{=}Y_i^{II}}{k_{b,i}\tilde{Y} + k_{b,j}\tilde{Y}_j + s} \tag{B-34}$$

$$\bar{\Theta}_i^{II} = \frac{K_{t,i}^{=}\bar{Y}_i^{II}}{k_{b,i}\tilde{Y}_i + k_{b,j}\tilde{Y}_j + s} \tag{B-35}$$

$$\overline{\overline{\Theta}}^{II} = \frac{\begin{bmatrix} a_i k_{p,i} M(\overline{\overline{Y}}_i + 2\overline{\overline{Y}}_i^{I}) + a_i k_{b,i} \begin{bmatrix} \overline{\overline{Y}}_i(\Theta_i^{II} + \Theta_j^{II} + \overline{\Theta}_i^{II} + \overline{\Theta}_j^{II}) \\ + 2\overline{\overline{Y}}_i^{I}(\Theta_i^{I} + \Theta_j^{I} + \overline{\Theta}_i^{I} + \overline{\Theta}_j^{I} + \overline{\overline{\Theta}}^{I}) + \\ (\overline{Y}_i + Y_i)(\Theta_j^{II} + \overline{\Theta}_j^{II}) \\ + 2(\overline{Y}_i^{I} + Y_i^{I})(\Theta_j^{I} + \overline{\Theta}_j^{I} + \overline{\overline{\Theta}}^{I}) + \\ (\overline{Y}_i^{II} + Y_i^{II})(\Theta_j + \overline{\Theta}_j + \overline{\overline{\Theta}}) \end{bmatrix} \\ + a_j k_{p,j} M(\overline{\overline{Y}}_j + 2\overline{\overline{Y}}_j^{I}) + a_j k_{b,j} \begin{bmatrix} \overline{\overline{Y}}_j(\Theta_i^{II} + \Theta_j^{II} + \overline{\Theta}_i^{II} + \overline{\Theta}_j^{II}) \\ + 2\overline{\overline{Y}}_j^{I}(\Theta_i^{I} + \Theta_j^{I} + \overline{\Theta}_i^{I} + \overline{\Theta}_j^{I} + \overline{\overline{\Theta}}^{I}) + \\ (\overline{Y}_j + Y_j)\left(\Theta_i^{II} + \overline{\Theta}_i^{II}\right) \\ + 2(\overline{Y}_j^{I} + Y_j^{I})\left(\Theta_i^{I} + \overline{\Theta}_i^{I} + \overline{\overline{\Theta}}^{I}\right) + \\ (\overline{Y}_j^{II} + Y_j^{II})(\Theta_i + \overline{\Theta}_i + \overline{\overline{\Theta}}) \end{bmatrix} \end{bmatrix}}{1 - a_i k_{b,i} \widetilde{Y}_i - a_j k_{b,j} \widetilde{Y}_j} \tag{B-36}$$

$$Q_i^{II} = \frac{(K_{t,i}^{s} + k_{d,i}) Y_i^{II}}{s} \tag{B-37}$$

$$\overline{Q}_i^{II} = \frac{(K_{t,i}^{s} + k_{d,i}) \overline{Y}_i^{II}}{s} \tag{B-38}$$

$$\overline{\overline{Q}}^{II} = \frac{(K_{t,i}^{s} + k_{d,i}) \overline{\overline{Y}}_i^{II} + (K_{t,j}^{s} + k_{d,j}) \overline{\overline{Y}}_j^{II}}{s} \tag{B-39}$$

Appendix C

Model Equations for CSTR 2

The moment equations for CSTR 1 are derived with a simple modification of the equations for CSTR 1 to allow for the flow of species from CSTR 1 to CSTR 2. The procedure will be illustrated for the equation of the zero[th] moment of linear living polymer and, for the sake of brevity, just final results for all other moments, along with the methodology for solving them, will be presented.

For CSTR 2, we must modify Equation (A-13) to allow for the flow of zero[th] moment (polymer molar concentration) from CSTR1 to CSTR 2

$$\frac{\mathrm{d}Y_i}{\mathrm{d}t} = k_{p,i}C_i M - (\sigma_i + k_{b,i}\tilde{\Theta})\,Y_i \; + Y_i^* \frac{\dot{\upsilon}_{out,1}}{V_1} + k_{M,i}M\tilde{Y}_i \tag{C-1}$$

The volumes of CSTR 1 and CSTR 2 are represented by ν_1 and ν_2, respectively, and were assumed to be the same with no change in the volume of the reaction mixtures during the polymerization. C_1^{in}, C_2^{in} *are* molar flow rates of catalysts 1 and 2 per unit volume of the reactor. The volumetric flow rates entering and leaving CSTR 1 are denoted by $\dot{\upsilon}_{in,1}$ and $\dot{\upsilon}_{out,1}$ and for CSTR 2 by $\dot{\upsilon}_{in,2}$ and $\dot{\upsilon}_{out,2}$.

where Y_i^* is the zero[th] moment of living linear polymer leaving CSTR 1.

Since the average residence time in the reactor is given by the ratio $\frac{\dot{\upsilon}_{out,1}}{V_1}$, Equation (C-1) becomes

$$\frac{\mathrm{d}Y_i}{\mathrm{d}t} = k_{p,i}C_i M - (\sigma_i + k_{b,i}\tilde{\Theta})\,Y_i \; + \frac{Y_i^*}{t_r^*} + k_{M,i}M\tilde{Y}_i \tag{C-2}$$

where t_r^* is the average residence time in CSTR 1.

The steady-state solution of Equation (C-2) is

$$Y_i = \frac{k_{p,i}C_i M + Y_i^* s^* + k_{M,i}M\tilde{Y}_i}{\sigma_i + k_{b,i}\tilde{\Theta}} \tag{C-3}$$

where s^* is the reciprocal of the average residence time in CSTR 1.

Similar equations for all the other moments can be developed in an analogous way. Their final expressions are listed below.

Zeroth Moments

The following equations can be solved sequentially

$$C_i = \frac{C_i^{in} + C_i^* s^* + (k_{\beta,i} + K_{t.i}^s)/(\sigma_i - k_{M,i}[M])\tilde{Y}_i^*}{\{1-(k_{\beta,i} + K_{t.i}^s)/(\sigma_i - k_{M,i}[M])\}k_{p,i}M + k_{d,i} + s} \tag{C-4}$$

$$\tilde{Y}_i = \frac{k_{p,i}C_i M + \tilde{Y}_i^* s^*}{\sigma_i - k_{M,i}[M]} \tag{C-5}$$

$$\tilde{\Theta} = \frac{K_{t,i}^{=}\tilde{Y}_i + K_{t,j}^{=}\tilde{Y}_j + \tilde{\Theta}^* s^*}{k_{b,i}\tilde{Y}_i + k_{b,j}\tilde{Y}_j + s} \tag{C-6}$$

$$Y_i = \frac{k_{p,i}C_i M + k_{M,i}[M]\tilde{Y}_i + Y_i^* s^*}{k_{b,i}\tilde{\Theta} + \sigma_i} \tag{C-7}$$

$$\Theta_i = \frac{K_{t,i}^{=}Y_i + \Theta_i^* s^*}{k_{b,i}\tilde{Y}_i + k_{b,j}\tilde{Y}_j + s} \tag{C-8}$$

The following equations need be solved simultaneously

$$\bar{Y}_i = \frac{k_{b,i}Y_i(\Theta_i + \bar{\Theta}_i) + \bar{Y}_i^* s^*}{k_{b,i}(\Theta_j + \bar{\Theta}_j + \bar{\bar{\Theta}}) + \sigma_i} \tag{C-9}$$

$$\bar{\bar{Y}}_i = \frac{k_{b,i}(Y_i + \bar{Y}_i)(\Theta_j + \bar{\Theta}_j + \bar{\bar{\Theta}}) + \bar{\bar{Y}}_i^* s^*}{\sigma_i} \tag{C-10}$$

$$\bar{\Theta}_i = \frac{K_{t,i}^{=}\bar{Y}_i + \bar{\Theta}_i^* s^*}{k_{b,i}\tilde{Y}_i + k_{b,j}\tilde{Y}_j + s} \tag{C-11}$$

$$\overline{\overline{\Theta}} = \frac{K_{t,i}^{=}\overline{\overline{Y}}_i + K_{t,j}^{=}\overline{\overline{Y}}_j + \overline{\overline{\Theta}}^{*} s^{*}}{k_{b,i}\widetilde{Y}_i + k_{b,j}\widetilde{Y}_j + s} \tag{C-12}$$

Finally, the moment equations for the dead polymers can be solved sequentially

$$Q_i = \frac{(K_{t,i}^{s} + k_{d,i})\, Y_i + Q_i^{*} s^{*}}{s} \tag{C-13}$$

$$\overline{Q}_i = \frac{(K_{t,i}^{s} + k_{d,i})\, \overline{Y}_i + \overline{Q}_i^{*} s^{*}}{s} \tag{C-14}$$

$$\overline{\overline{Q}} = \frac{(K_{t,i}^{s} + k_{d,i})\, \overline{\overline{Y}}_i + (K_{t,j}^{s} + k_{d,j})\, \overline{\overline{Y}}_j + \overline{\overline{Q}}^{*} s^{*}}{s} \tag{C-15}$$

First Moments

All first moment equations can be solved sequentially.

$$Y_i^{I} = \frac{k_{p,i}[M]\left(C_i + Y_i\right) + Y_i^{I^{*}} s^{*} + k_{M,i} M \widetilde{Y}_i}{\sigma_i + k_{b,i}\widetilde{\Theta}} \tag{C-16}$$

$$\overline{Y}_i^{I} = \frac{\begin{array}{l}\{k_{p,i} M \overline{Y}_i + k_{b,i}[(Y_i + \overline{Y}_i)\Theta_i^{I} + Y_i^{I}(\Theta_i + \overline{\Theta}_i)] + \overline{Y}_i^{I^{*}} s^{*}\} \\ (k_{b,i}\widetilde{Y}_i + k_{b,j}\widetilde{Y}_j + s) + k_{b,i}(Y_i + \overline{Y}_i)\overline{\Theta}_i^{I^{*}} s^{*}\end{array}}{\begin{array}{l}[\sigma_i + k_{b,i}(\Theta_j + \overline{\Theta}_j + \overline{\overline{\Theta}})](k_{b,i}\widetilde{Y}_i + k_{b,j}\widetilde{Y}_j + s) \\ - k_{b,i}(Y_i + \overline{Y}_i)K_{t,i}^{=}\end{array}} \tag{C-17}$$

$$\overline{\overline{Y}}_i^{I} = \frac{1}{\sigma_i}\left\{\begin{array}{l} k_{p,i} M \overline{\overline{Y}}_i + k_{b,i}\left[\begin{array}{l}\overline{\overline{Y}}_i(\Theta_i^{I} + \Theta_j^{I} + \overline{\Theta}_i^{I} + \overline{\Theta}_j^{I} + \overline{\overline{\Theta}}^{I}) \\ + (\overline{Y}_i + Y_i)(\Theta_j^{I} + \overline{\Theta}_j^{I} + \overline{\overline{\Theta}}^{I}) \\ + (\overline{Y}_i^{I} + Y_i^{I})(\Theta_j + \overline{\Theta}_j + \overline{\overline{\Theta}})\end{array}\right] \\ + \overline{\overline{Y}}_i^{I^{*}} s^{*}\end{array}\right\} \tag{C-18}$$

$$\Theta_i^I = \frac{K_{t,i}^{=} Y_i^I + \Theta_i^{I*} s^*}{k_{b,i}\tilde{Y}_i + k_{b,j}\tilde{Y}_j + s} \tag{C-19}$$

$$\bar{\Theta}_i^I = \frac{K_{t,i}^{=} \bar{Y}_i^I + \bar{\Theta}_i^{I*} s^*}{k_{b,i}\tilde{Y}_i + k_{b,j}\tilde{Y}_j + s} \tag{C-20}$$

$$a_i \left\{ k_{p,i} M \overline{\overline{Y}}_i + k_{b,i} \left[\begin{array}{l} \overline{\overline{Y}}_i (\Theta_i^I + \Theta_j^I + \bar{\Theta}_i^I + \bar{\Theta}_j^I) \\ + (\bar{Y}_i + Y_i)(\Theta_j^I + \bar{\Theta}_j^I) \\ + (\bar{Y}_i^I + Y_i^I)(\Theta_j + \bar{\Theta}_j + \overline{\overline{\Theta}}) \end{array} \right] + \overline{\overline{Y}}_i^{I*} s^* \right\} +$$

$$a_j \left\{ k_{p,j} M \overline{\overline{Y}}_j + k_{b,j} \left[\begin{array}{l} \overline{\overline{Y}}_j (\Theta_i^I + \Theta_j^I + \bar{\Theta}_i^I + \bar{\Theta}_j^I) \\ + (\bar{Y}_j + Y_j)(\Theta_i^I + \bar{\Theta}_i^I) \\ + (\bar{Y}_j^I + Y_j^I)(\Theta_i + \bar{\Theta}_i + \overline{\overline{\Theta}}) \end{array} \right] + \overline{\overline{Y}}_i^{I*} s^* \right\} +$$

$$\overline{\overline{\Theta}}^I = \frac{\overline{\overline{\Theta}}^{I*} s^*}{k_{b,i}\tilde{Y}_i + k_{b,j}\tilde{Y}_j + s} \Big/ \left(1 - a_i k_{b,i}\tilde{Y}_i - a_j k_{b,j}\tilde{Y}_j\right) \tag{C-21}$$

$$Q_i^I = \frac{(K_{t,i}^s + k_{d,i}) Y_i^I + Q_i^{I*} s^*}{s} \tag{C-22}$$

$$\bar{Q}_i^I = \frac{(K_{t,i}^s + k_{d,i}) \bar{Y}_i^I + \bar{Q}_i^{I*} s^*}{s} \tag{C-23}$$

$$\overline{\overline{Q}}^I = \frac{(K_{t,i}^s + k_{d,i}) \overline{\overline{Y}}_i^I + (K_{t,j}^s + k_{d,j}) \overline{\overline{Y}}_j^I + \overline{\overline{Q}}^{I*} s^*}{s} \tag{C-24}$$

Second Moments

All second moment equations are solved sequentially.

$$Y_i^{II} = \frac{k_{p,i}[M]\left(Y_i + 2Y_i^I + C_i\right) + k_{M,i} M \tilde{Y} + Y_i^{II*} s^*}{\sigma_i + k_{b,i}\tilde{\Theta}} \tag{C-25}$$

$$
\begin{aligned}
&\{k_{p,i}M(\overline{Y}_i + 2\overline{Y}_i^I) + k_{b,i}[(\overline{Y}_i + Y_i)\Theta_i^{II} \\
&+ 2(Y_i^I + \overline{Y}_i^I)(\Theta_i^I + \overline{\Theta}_i^I) + Y_i^{II}(\Theta_i + \overline{\Theta}_i)] + \overline{Y}_i^{II*} s^*\} \\
\overline{Y}_i^{II} = &\frac{\times (k_{b,i}\tilde{Y}_i + k_{b,j}\tilde{Y}_j + s) + k_{b,i}(\overline{Y}_i + Y_i)\overline{\Theta}_i^{II*} s^*}{[\sigma_i + k_{b,i}(\Theta_j + \overline{\Theta}_j + \overline{\overline{\Theta}})](k_{b,i}\tilde{Y}_i + k_{b,j}\tilde{Y}_j + s)} \\
&- k_{b,i}(\overline{Y}_i + Y_i)K_{t,i}^{=}
\end{aligned}
\tag{C-26}
$$

$$
\Theta_i^{II} = \frac{K_{t,i}^{=} Y_i^{II} + \Theta_i^{II*} s^*}{k_{b,i}\tilde{Y} + k_{b,j}\tilde{Y}_j + s} \tag{C-27}
$$

$$
\overline{\Theta}_i^{II} = \frac{K_{t,i}^{=} \overline{Y}_i^{II} + \overline{\Theta}_i^{II*} s^*}{k_{b,i}\tilde{Y}_i + k_{b,j}\tilde{Y}_j + s} \tag{C-28}
$$

$$
\begin{aligned}
&a_i k_{p,i} M(\overline{\overline{Y}}_i + 2\overline{\overline{Y}}^{I}_i) \\
&+ a_i k_{b,i} \begin{bmatrix} \overline{\overline{Y}}_i(\Theta^{II}_i + \Theta^{II}_j + \overline{\Theta}^{II}_i + \overline{\Theta}^{II}_j) \\ + 2\overline{\overline{Y}}^{I}_i(\Theta^{I}_i + \Theta^{I}_j + \overline{\Theta}^{I}_i + \overline{\Theta}^{I}_j + \overline{\overline{\Theta}}^{I}) + \\ (\overline{Y}_i + Y_i)(\Theta^{II}_j + \overline{\Theta}^{II}_j) \\ + 2(\overline{Y}^{I}_i + Y^{I}_i)(\Theta^{I}_j + \overline{\Theta}^{I}_j + \overline{\overline{\Theta}}^{I}) + \\ (\overline{Y}^{II}_i + Y^{II}_i)(\Theta_j + \overline{\Theta}_j + \overline{\overline{\Theta}}) \end{bmatrix} + a_i \overline{\overline{Y}}^{II*}_i s^* \\
&+ a_j k_{p,j} M(\overline{\overline{Y}}_j + 2\overline{\overline{Y}}^{I}_j) \\
&+ a_j k_{b,j} \begin{bmatrix} \overline{\overline{Y}}_j(\Theta^{II}_i + \Theta^{II}_j + \overline{\Theta}^{II}_i + \overline{\Theta}^{II}_j) \\ + 2\overline{\overline{Y}}^{I}_j(\Theta^{I}_i + \Theta^{I}_j + \overline{\Theta}^{I}_i + \overline{\Theta}^{I}_j + \overline{\overline{\Theta}}^{I}) + \\ (\overline{Y}_j + Y_j)\left(\Theta^{II}_i + \overline{\Theta}^{II}_i\right) \\ + 2(\overline{Y}^{I}_j + Y^{I}_j)\left(\Theta^{I}_i + \overline{\Theta}^{I}_i + \overline{\overline{\Theta}}^{I}\right) + \\ (\overline{Y}^{II}_j + Y^{II}_j)(\Theta_i + \overline{\Theta}_i + \overline{\overline{\Theta}}) \end{bmatrix} + a_j \overline{\overline{Y}}^{II*}_j s^* \\
&+ \overline{\overline{\Theta}}^{II*} s^*
\end{aligned}
$$

$$
\overline{\overline{\Theta}}^{II} = \frac{}{k_{b,i}\tilde{\overline{Y}}_i + k_{b,j}\tilde{\overline{Y}}_j + s} \Big/ \left(1 - a_i k_{b,i}\tilde{\overline{Y}}_i - a_j k_{b,j}\tilde{\overline{Y}}_j\right) \tag{C-29}
$$

$$
Q^{II}_i = \frac{(K^s_{t,i} + k_{d,i})Y^{II}_i + Q^{II*}_i s^*}{s} \tag{C-30}
$$

$$
\overline{Q}^{II}_i = \frac{(K^s_{t,i} + k_{d,i})\overline{Y}^{II}_i + \overline{Q}^{II*}_i s^*}{s} \tag{C-31}
$$

$$
\overline{\overline{Q}}^{II}_i = \frac{(K^s_{t,i} + k_{d,i})\overline{\overline{Y}}^{II}_i + (K^s_{t,j} + k_{d,j})\overline{\overline{Y}}^{II}_j + \overline{\overline{Q}}^{II*} s^*}{s} \tag{C-32}
$$

$$
\begin{aligned}
\overline{\overline{Y}}_i^{II} &= \frac{k_{p,i}}{\sigma_i} M(\overline{\overline{Y}}_i + 2\overline{\overline{Y}}_i^{I}) \\
&+ \frac{k_{b,i}}{\sigma_i}\left[\begin{array}{l}
\overline{\overline{Y}}_i(\Theta_i^{II} + \Theta_j^{II} + \overline{\Theta}_i^{II} + \overline{\Theta}_j^{II} + \overline{\overline{\Theta}}^{II}) \\
+ 2\overline{\overline{Y}}_i^{I}(\Theta_i^{I} + \Theta_j^{I} + \overline{\Theta}_i^{I} + \overline{\Theta}_j^{I} + \overline{\overline{\Theta}}^{I}) + \\
(\overline{Y}_i + Y_i)(\Theta_j^{II} + \overline{\Theta}_j^{II} + \overline{\overline{\Theta}}^{II}) \\
+ 2(\overline{Y}_i^{I} + Y_i^{I})(\Theta_j^{I} + \overline{\Theta}_j^{I} + \overline{\overline{\Theta}}^{I}) + \\
(\overline{Y}_i^{II} + Y_i^{II})(\Theta_j + \overline{\Theta}_j + \overline{\overline{\Theta}})
\end{array}\right] + \frac{\overline{\overline{Y}}_i^{II*} s^*}{\sigma_i}
\end{aligned}
\qquad \text{(C-33)}
$$

Appendix D

Additional Reactor and Polymer Property Equations for CSTR 1

The molar balance for monomer is given by

$$\frac{\mathrm{d}M}{\mathrm{d}t} = -[k_{p,i}C_i + k_{p,j}C_j + s]M - k_{p,i}M\tilde{Y}_i - k_{p,j}M\tilde{Y}_j - k_{M,i}M\tilde{Y}_i - k_{M,j}M\tilde{Y}_j + M^{in} \tag{D-1}$$

where M^{in} is the molar flow rate of monomer to the reactor per reactor volume

$$M^{in} = \frac{F_{M,in,1}}{V_1} \tag{D-2}$$

The steady-state solution of Equation (C-1) is

$$\frac{F_{M,in,1}}{v_1} = M[k_{p,i}C_i + k_{p,j}C_j + s + (k_{p,i} + k_{M,i})\tilde{Y}_i + (k_{p,j} + k_{M,j})\tilde{Y}] \tag{D-3}$$

Chain length averages are given by the ratio of two moments. For living linear chains made on catalyst *i*

$$r_n = \frac{Y_i^I}{Y_i} \tag{D-4}$$

$$r_w = \frac{Y_i^{II}}{Y_i^I} \tag{D-5}$$

$$pdi = \frac{r_w}{r_n} \tag{D-6}$$

Similar equations are used to calculate the chain length averages of other polymer populations present in the reactor.

Molar percentages are calculated from the zero[th] moments. For instance, the molar percentage of linear living chains made on catalyst *i* is given by

$$n\,\% = \frac{Y_i}{\left(\begin{array}{l} Y_i + Y_j + \overline{Y}_i + \overline{Y}_j + \overline{\overline{Y}}_i + \overline{\overline{Y}}_j + \\ \Theta_i + \Theta_j + \overline{\Theta}_i + \overline{\Theta}_j + \overline{\overline{\Theta}}_i + \overline{\overline{\Theta}}_j + \\ Q_i + Q_j + \overline{Q}_i + \overline{Q}_j + \overline{\overline{Q}}_i + \overline{\overline{Q}}_j \end{array}\right)} \times 100 \tag{D-7}$$

Similarly, weight percentages are calculated using the first moments

$$w\,\% = \frac{Y_i^I}{\left(\begin{array}{l} Y_i^I + Y_j^I + \overline{Y}_i^I + \overline{Y}_j^I + \overline{\overline{Y}}_i^I + \overline{\overline{Y}}_j^I + \\ \Theta_i^I + \Theta_j^I + \overline{\Theta}_i^I + \overline{\Theta}_j^I + \overline{\overline{\Theta}}_i^I + \overline{\overline{\Theta}}_j^I + \\ Q_i^I + Q_j^I + \overline{Q}_i^I + \overline{Q}_j^I + \overline{\overline{Q}}_i^I + \overline{\overline{Q}}_j^I \end{array}\right)} \times 100 \tag{D-8}$$

Analogous expressions are used to calculate the molar and weight percentages of the other polymer populations in the reactor.

Two types of LCB averages will be calculated: the number of LCBs per 1000 carbon atoms (λ or LCBD) and the number of LCBs per chain (B_n). The general expressions for these averages are

$$\lambda = 500 \frac{\text{rate of LCB formation}}{\text{rate of polymerization}} \tag{D-9}$$

The number of LCBs per chain is calculated with the equation

$$B_n = \frac{\lambda \times r_n}{500} \tag{D-10}$$

Therefore, for homogeneous-branched chains

$$\lambda_i = 500 \frac{k_{b,i}(\Theta_i + \overline{\Theta}_i)}{k_{p,i} M} \tag{D-11}$$

for cross-product chains

$$\lambda_c = 500 \frac{\begin{array}{c} k_{b,1}[(Y_1 + \overline{Y}_1)(\Theta_2 + \overline{\Theta}_2 + \overline{\overline{\Theta}}) + \overline{\overline{Y}}_1 \widetilde{\Theta}] \\ + k_{b,2}[(Y_2 + \overline{Y}_2)(\Theta_1 + \overline{\Theta}_1 + \overline{\overline{\Theta}}) + \overline{\overline{Y}}_2 \widetilde{\Theta}] \end{array}}{(k_{p,1}\overline{\overline{Y}}_1 + k_{p,2}\overline{\overline{Y}}_2)M} \tag{D-12}$$

and, finally, for the overall polymer:

$$\lambda_O = 500 \frac{(k_{b,1}\widetilde{Y}_1 + k_{b,2}\widetilde{Y}_2)\widetilde{\Theta}}{(k_{p,1}\widetilde{Y}_1 + k_{p,2}\widetilde{Y}_2)M} \tag{D-13}$$

Appendix E

Long Chain Branch Averages for CSTR 2

Additional equations are needed to calculate LCB averages for CSTR 2. Since their derivations are lengthy, just final equations are shown here.

Parameters $[M]_i$ and x_i are monomer concentration and conversion in CSTR 1 (i = 1) or CSTR 2 (i = 2).

The monomer conversion in CSTR 1 can be calculated with the equation

$$x_1 = \frac{F_{M,in,1} - F_{M,out,1}}{F_{M,in,1}} \quad \text{(E-1)}$$

which, after some substitutions, becomes

$$x_1 = \frac{\frac{F_{M,in,1}}{V_1} - \frac{V_1[M]_1 s^*}{V_1}}{\frac{F_{M,in,1}}{V_1}} = \frac{[M]_1[k_{p,i}C_i + k_{p,j}C_j + s^* + (k_{p,i} + k_{M,i})\tilde{Y}_i + (k_{p,j} + k_{M,j})\tilde{Y}] - [M]_1 s^*}{[M]_1[k_{p,i}C_i + k_{p,j}C_j + s^* + (k_{p,i} + k_{M,i})\tilde{Y}_i + (k_{p,j} + k_{M,j})\tilde{Y}]} \quad \text{(E-2)}$$

Monomer conversion for CSTR 2 is given by

$$x_2 = \frac{[M]_1 s^* + \frac{F_{M,in,2}}{v_2} - [M]_2 s_2}{[M]_1 s^* + \frac{F_{M,in,2}}{V_2}} \quad \text{(E-3)}$$

Where s_2 *is* the reciprocal of the residence time in the CSTR 2

$$x_2 = \frac{[M]_2[k_{p,i}C_i + k_{p,j}C_j + s_2 + (k_{p,i} + k_{M,i})\tilde{Y}_i + (k_{p,j} + k_{M,j})\tilde{Y}] - [M]_2 s_2}{[M]_2[k_{p,i}C_i + k_{p,j}C_j + s_2 + (k_{p,i} + k_{M,i})\tilde{Y}_i + (k_{p,j} + k_{M,j})\tilde{Y}]} \quad \text{(E-4)}$$

The LCB density for the polymer exiting CSTR 2 ($\lambda_{overall,out,2}$) was calculated using the equation

$$\lambda_{overall,out,2} = \frac{\lambda_{overall,out,1}\dfrac{F_{M,in,1}x_1}{V_1}}{\dfrac{F_{M,in,1}x_1}{V_1} + \left([M]_1 s^* + \dfrac{F_{M,in,2}}{V_2}\right)x_2} + \frac{\lambda_{overall,inst,2}\left([M]_1 s^* + \dfrac{F_{M,in,2}}{V_2}\right)x_2}{\dfrac{F_{M,in,1}x_1}{V_1} + \left([M]_1 s^* + \dfrac{F_{M,in,2}}{V_2}\right)x_2} \tag{E-5}$$

where $\lambda_{overall,inst,2}$ is the instantaneous LCB density of the overall polymer within CSTR 2 if there was no flow from CSTR 1, calculated with Equation (D-13) with the corresponding monomer and population concentrations in CSTR 2. The parameter $\lambda_{overall,out,1}$ is the LCB density of the polymer exiting CSTR 1, which is again calculated with Equation (D-13) using monomer and populations concentrations in CSTR 1.

The equation for calculating the LCB density of the cross-product exiting CSTR 2 is

$$\lambda_{cross,out,2} = \frac{\lambda_{cross,out,1}\dfrac{F_{M,in,1}x_1}{V_1}\dfrac{n_{cross,out,1}r_{n,cross,out,1}}{r_{n,overall,out,1}}}{\left\{\dfrac{F_{M,in,1}x_1}{V_1} + \left([M]_1 s^* + \dfrac{F_{M,in,2}}{V_2}\right)x_2\right\}\dfrac{n_{cross,out,2}r_{n,cross,out,2}}{r_{n,overall,out,2}}} + \frac{\lambda_{cross,inst,2}\left([M]_1 s^* + \dfrac{F_{M,in,2}}{V_2}\right)x_2}{\left\{\dfrac{F_{M,in,1}x_1}{V_1} + \left([M]_1 s^* + \dfrac{F_{M,in,2}}{V_2}\right)x_2\right\}} \tag{E-6}$$

Where $n_{cross,out,1}$ and $n_{cross,out,2}$ denote the mole fraction of the cross-product exiting CSTR 1 and CSTR 2, respectively. Their corresponding number average chain lengths are $r_{n,cross,out,1}$ and $r_{n,cross,out,2.}$ In the same way, $r_{n,overall,out,1}$ and $r_{n,overall,out,2}$ represent the number average chain lengths of the overall polymer exiting CSTR 1 and CSTR 2.

Finally, the LCB density of homogeneous-branched chains is:

$$\lambda_{homo,out,2} = \frac{\lambda_{homo,out,1} \dfrac{F_{M,in,1} x_1}{V_1} \dfrac{n_{homo,out,1} r_{n,homo,out,1}}{r_{n,overall,out,1}}}{\left\{ \dfrac{F_{M,in,1} x_1}{V_1} + \left([M]_1 s^* + \dfrac{F_{M,in,2}}{V_2} \right) x_2 \right\} \dfrac{n_{homo,out,2} r_{n,homo,out,2}}{r_{n,overall,out,2}}} + \frac{\lambda_{homo,inst,2} \left([M]_1 s^* + \dfrac{F_{M,in,2}}{V_2} \right) x_2}{\left\{ \dfrac{F_{M,in,1} x_1}{V_1} + \left([M]_1 s^* + \dfrac{F_{M,in,2}}{V_2} \right) x_2 \right\}} \tag{E-7}$$

Appendix F

Relative standard deviation (*RSD*) is defined as the standard deviation, *s*, divided by the mean value. When experimental data involved are related through products and quotients like product below.

$$y = a \times b \times c \tag{F-1}$$

The relative standard deviation of the result y, s_y/y, is obtained by summing the squares of the relative standard deviations of *a*, *b* and *c* and extracting the square root of the sum given that variables involved are independent.

$$\frac{s_y}{y} = \sqrt{\left(\frac{s_a}{a}\right)^2 + \left(\frac{s_b}{b}\right)^2 + \left(\frac{s_c}{c}\right)^2} \tag{F-2}$$

We can estimate confidence interval for k_M and $k_{\beta H} + k_{Al}[Al]$ using equation F-2 and the estimated standard errors from nonlinear regression (last column of Table 6-16) . For $k_{M,}$ we can write

$$k_M = \left(\frac{k_M}{mw \times k_p}\right) \times k_p \times mw \tag{F-3}$$

Since *mw* is a constant , *RSD(mw)* would be zero. Therefore, we can write equation below

$$\left(\frac{s_{k_M}}{k_M}\right)^2 = \left(\frac{s_{\left(\frac{k_M}{mw \times k_p}\right)}}{\frac{k_M}{mw \times k_p}}\right)^2 + \left(\frac{s_{k_p}}{k_p}\right)^2 \tag{F-4}$$

or

$$RSD(k_M) = \sqrt{(RSD(\frac{k_M}{mwk_P}))^2 + (RSD(k_P))^2} \tag{F-5}$$

Similarly, for $k_{\beta H} + k_{Al}[Al]$

$$RSD(k_{\beta H} + k_{Al}[Al]) = \sqrt{(RSD(\frac{k_{\beta H} + k_{Al}[Al]}{mwk_P}))^2 + (RSD(k_P))^2} \tag{F-6}$$

Substituting the relevant parameters into the equations F-5 and F-6 gives

$$RSD(k_M) = \sqrt{(\frac{5.6\times10^{-7}}{4.04\times10^{-5}})^2 + (\frac{3450}{213000})^2} = 2.13\times10^{-2} \quad \text{(F-7)}$$

$$RSD(k_{\beta H} + k_{Al}[Al]) = \sqrt{(\frac{2\times10^{-7}}{1.17\times10^{-6}}))^2 + (\frac{3450}{213000})^2} = 0.172 \quad \text{(F-8)}$$

The 95% confidence intervals estimates for k_M and $k_{\beta H} + k_{Al}[Al]$ are

$$k_M = 240.94 \pm t_{0.25,19-2} \times 2.13\times10^{-2} \times 240.94 = 240.94 \pm 10.83 \quad \frac{\text{L}}{\text{mol.s}} \quad \text{(F-9)}$$

$$k_{\beta H} + k_{Al}[Al] = 6.978 \pm t_{0.25,19-2} \times 0.172 \times 6.978 = \quad 6.98 \pm \quad 2.53 \quad 1/s \quad \text{(F-10)}$$

Appendix G

The standard deviation of the sum of two random variables can be related to their individual standard deviations and the covariance between them.

$$SD(X+Y)=\sqrt{\text{var}(X)+\text{var}(Y)+2\,\text{cov}(X,Y)} \tag{G-1}$$

If the random variables are independent, then their covariance is zero, so

$$SD(X+Y)=\sqrt{\text{var}(X)+\text{var}(Y)} \tag{G-2}$$

Similar to equation G-1, we can write

$$SD\left[k_M/mwk_p+k_{\beta H}/(mwk_p[M])\right]=\sqrt{\left[SD(k_M/mwk_p)\right]^2+\left[SD(k_{\beta H}/(mwk_p[M]))\right]^2} \tag{G-3}$$

Substituting the relevant terms for k_M/mwk_p, and $k_M/mwk_p+k_{\beta H}/(mwk_p[M])$ from Tables 6-16 and 6-22 into equation G-3 gives,

$$SD\left(\frac{k_{\beta H}}{mwk_p[M]}\right)=\sqrt{(6.67\times10^{-7})^2+(5.6\times10^{-7})^2}=8.71\times10^{-7}\quad\frac{mol}{g} \tag{G-4}$$

and its approximate 95% confidence interval is,

$$\frac{k_{\beta H}}{mwk_p[M]}==5.2\times10^{-7}\pm1.96\times8.71\times10^{-7}=5.2\times10^{-7}\pm17.1\times10^{-7}\quad\frac{mol}{g} \tag{G-5}$$

The relative standard deviation for k_{Al} was calculated using Equation G-6 and the previously estimated values of k_p,(Section 6.4.3), monomer concentration (Section 6.4.1) and $k_{Al}/(mwk_p[M])$ (Table 6-22) .

$$RSD(k_{Al})=\sqrt{(RSD(k_p))^2+(RSD([M]))^2+(RSD(k_{Al}/mwk_p[M]))^2} \tag{G-6}$$

$$RSD(k_{Al})=\sqrt{\left(\frac{3446}{213000}\right)^2+\left(\frac{0.0046}{0.4537}\right)^2+\left(\frac{7.27\times10^{-5}}{3.419\times10^{-4}}\right)^2}=\sqrt{0.00026+0.0001+0.045}=0.21\frac{L}{mol.s} \tag{G-7}$$

The approximate 95 % confidence interval for the kinetic parameter k_{Al} is,

$$k_{Al}=925\pm t_{0.025,15-2.}\times0.21\times925=925\pm420\quad\frac{L}{mol.s} \tag{G-8}$$

Appendix H

The concentration of complexed active sites is given by equation 7-6 rewritten below

$$[P^* \cdot M] = \frac{k_f [M] C_t}{k_r + k_f [M]} \tag{H-1}$$

or

$$[P^* \cdot M] = \frac{K[M] C_t}{1 + K[M]} \tag{H-2}$$

The propagation rate is:

$$R_p = k_p [P^*.M][M] \tag{H-3}$$

Substituting equation (H-2) in (H-3) gives equation below

$$R_p = \frac{k_p C_t K[M]^2}{1 + K[M]} \tag{H-4}$$

If we assume that catalyst sites decay according to the second order model given below

$$\frac{\mathrm{d}C_t}{\mathrm{d}t} = -k_d C_t^{\,2} \tag{H-5}$$

Integration of the equation (H-5) yields

$$\frac{1}{C_t} = \frac{1}{C_0} + k_d t \tag{H-6}$$

Rearranging lead to

$$C_t = \frac{C_0}{1 + k_d C_0 t} \tag{H-7}$$

If we now substitute equation (H-7) in (H-4), we get the expression below

$$R_p = \frac{k_p C_0 K[M]^2}{(1 + K[M])(1 + k_d C_0 t)} \tag{H-8}$$

The molar balance for monomer in a semi-batch reactor is given by,

$$\frac{\mathrm{d}[M]}{\mathrm{d}t} = \frac{F_{M,in}}{V_R} - R_p \tag{H-9}$$

Since monomer concentration is kept constant, we conclude that,

$$F_{M,in} = R_p V_R \tag{H-10}$$

Substituting equation (H-8) in (H-10) leads to equation below

$$F_{M,in} = \frac{k_p K V_R C_0 [M]^2}{(1+K[M])(1+k_d C_0 t)} \tag{H-11}$$

Appendix I

Pooled standard deviation

In statistics, a problem often arises when there are several series of measurements performed under similar conditions and it is desired to achieve an improved estimate of the variability of the process. If we assume that the same phenomena are generating random error at every level of independent variable, although their means may differ, so standard deviations can be pooled to express a single estimate of the standard deviation called pooled standard deviation. The reason for using pooled standard deviation is to avoid numerous repeated tests required at each value of x, which sometimes causes the expense of testing to become prohibitive. The pooled standard deviations s_p from k series of measurements can be calculated as

$$s_p^2 = \frac{\sum_i^r (n_i - 1) s_i^2}{\sum_i^r (n_i - 1)} \tag{I-1}$$

The suffices 1, 2, ... i refer to the different series of measurements. In this case it is assumed that there exists a single underlying standard deviation s of which the pooled standard deviation s_p is a better estimate than the individual calculated standard deviations s_1, s_2, ... s_r.

The 95% confidence interval for the mean of the ith factor level is calculated by:

$$Mean_i \pm t_{(\alpha/2, N-r)} \times \frac{s_p}{\sqrt{n_i}} \tag{I-2}$$

N is the total number of observations

r is the number of factor levels

n_i is the number of observations for the ith factor level

Difference in means of two normal distribution

Test for equality of variances

Suppose that two independent normal populations are of interest, where the population means and variances, say, μ_1 , σ_1^2 , μ_2 and σ_2^2 , are unknown. If s_1^2 and s_2^2 are the sample variances and samples sizes are n_1 and n_2, respectively, then the following test procedure can be applied to test for equality of variances[144].

Null hypothesis: $\sigma_1^2 = \sigma_2^2$ (I-3)

Alternative hypothesis: $\sigma_1^2 \neq \sigma_2^2$ (I-4)

Test statistic: $f_0 = \frac{s_1^2}{s_2^2}$ (I-5)

The null hypothesis will be rejected If $f_0 > f_{\alpha/2, n_1-1, n_2-1}$ (I-6)

where $f_{\alpha/2, n_1-1, n_2-1}$ is the upper α/2 percentage point of the *F* distribution with n_1-1 numerator and n_2 -1 denominator degrees of freedom.

Confidence interval for difference in means when variances are unequal

The confidence interval for the difference in means can be calculated from the equation below.

$$\bar{x}_1 - \bar{x}_2 - t_{\alpha/2,\nu}\sqrt{\frac{s_1^2}{n_1} + \frac{s_2^2}{n_2}} \leq \mu_1 - \mu_2 \leq \bar{x}_1 - \bar{x}_2 + t_{\alpha/2,\nu}\sqrt{\frac{s_1^2}{n_1} + \frac{s_2^2}{n_2}} \quad \text{(I-7)}$$

Where

$$\nu = \frac{(\frac{s_1^2}{n_1} + \frac{s_2^2}{n_2})^2}{\frac{(\frac{s_1^2}{n_1})^2}{n_1 - 1} + \frac{(\frac{s_2^2}{n_2})^2}{n_2 - 1}} \quad \text{(I-8)}$$

Confidence interval for difference in means when variances are equal

The confidence interval for the difference in means of two normal distributions, when their variances are equal, can be calculated from the equation below.

$$\bar{x}_1 - \bar{x}_2 - t_{\alpha/2, n_1+n_2-2} s_p \sqrt{\frac{1}{n_1} + \frac{1}{n_2}} \leq \mu_1 - \mu_2 \leq \bar{x}_1 - \bar{x}_2 + t_{\alpha/2, n_1+n_2-2} s_p \sqrt{\frac{1}{n_1} + \frac{1}{n_2}} \quad \text{(I-9)}$$

Where

$$s_p = \sqrt{\frac{(n_1 - 1)s_1^2 + (n_2 - 1)s_2^2}{n_1 + n_2 - 2}} \qquad \text{(I-10)}$$